Numerical Models of Galaxy Evolution: Black Hole Feedback and Disk Heating

by

Jackson Eugene DeBuhr

A dissertation submitted in partial satisfaction of the

requirements for the degree of

Doctor of Philosophy

in

Physics

in the

Graduate Division

of the

University of California, Berkeley

Committee in charge:

Professor Chung-Pei Ma, Co-Chair

Professor Eliot Quataert, Co-Chair

Professor Christopher McKee

Professor Leo Blitz

Spring 2012

Numerical Models of Galaxy Evolution: Black Hole Feedback and Disk Heating

Jackson Eugene DeBuhr

Abstract

Numerical Models of Galaxy Evolution: Black Hole Feedback and Disk Heating

by

Jackson Eugene DeBuhr

Doctor of Philosophy in Physics

University of California, Berkeley

Professor Chung-Pei Ma, Co-Chair

Professor Eliot Quataert, Co-Chair

This thesis explores two topics in contemporary galaxy evolution using numerical models and N-body simulation: feedback in active galactic nuclei and the heating of stellar disks.

Two numerical models of feedback from active galactic nuclei are developed and applied to the case of a major merger between two disk galaxies. Accretion into central black holes is modeled via a subgrid prescription based on angular momentum transport on unresolved scales. Feedback from black holes is modeled in two ways, both of which deposit a momentum $\tau L/c$ into the surroundings, where L is the luminosity of radiation produced by the galactic nucleus. In the first model, the momentum is divided equally among the nearby gas particles to model processes like the absorption of ultraviolet light by dust grains. The second model deposits the same amount of momentum into the surroundings, but it does so by launching a wind with a fixed speed, which only has a direct effect on a small fraction of the gas in the black hole's vicinity. Both models successfully regulate the growth of the black hole, reproducing, for example, the $M_{BH} - \sigma$ relationship, albeit for large amounts of momentum deposition (large τ). This regulation is largely independent of the fueling model employed, and thus is 'demand limited' black hole growth, rather than a 'supply limited' mode. However, only the model that implements an active galactic nucleus wind explicitly has an effect on large scales, quenching star formation in the host galaxy, and driving a massive galaxy-scale outflow.

In a separate set of calculations, a method for including a stellar disk in cosmological zoom-in simulation is presented and applied to a set of realistic dark matter halos taken from the Aquarius suite of simulations. The halos are adiabatically adjusted from $z = 1.3$ to $z = 1.0$ by a rigid disk potential, at which point the rigid potential is replaced with a live stellar disk of particles. The halos respond to the disks, in every orientation simulated, by contracting in their central regions and by becoming oblate instead of prolate. The resulting disks, with few exceptions, form large bars which contain a fair fraction of the mass of the disk. These bars buckle and

dominate the dynamics of the disk, increasing not only the scale height of the disk, but also the vertical velocity dispersion. During the simulations, the disks tumble coherently with their host halo, but can leave the outermost edges of the disk behind, creating streams that are far out of the plane of the disk. Some first steps are taken to relate the evolution of the disk to the substructure in the halo, but the situation is complicated by the massive bar.

To Theresa

Contents

Acknowledgments

Many people and institutions contributed to the work presented in this thesis and are richly deserving of thanks. First and foremost are my advisors, Chung-Pei Ma and Eliot Quataert, without whom this work would not exist, and whose guidance was instrumental for my time as a graduate student. Some early technical assistance was provided by Ian Parrish and Prateek Sharma, who are thus at least mildly responsible for me having completed any calculations. Some initial effort for the work in Chapter 5 was done by Onsi Fakhouri, who has my thanks. Considerable effort was undertaken with Michael Aumer to understand the unintuitive conventions of GADGET's units.

The contents of Chapters 2-4 of this thesis were previously published by the Monthly Notices of the Royal Astronomical Society. Chapter 2 was originally published as DeBuhr et al. (2010), and was performed in collaboration with Eliot Quataert, Chung-Pei Ma and Philip Hopkins. Chapter 3 and 4 were originally published as DeBuhr et al. (2011) and DeBuhr et al. (2012) respectively, and were performed in collaboration with Eliot Quataert and Chung-Pei Ma. The work in Chapter 5 of this thesis was performed in Collaboration with Chung-Pei Ma and Simon White, and though it is not published, that is certainly the intent.

This thesis used many computing resources around the country, including: the Abe, Steele and Ranger systems, managed through the TeraGrid collaboration, and its successor, the XSEDE collaboration; the systems Carver, Franklin, Hopper and Jacquard administered by the National Energy Research Scientific Computing Center; and the Henyey cluster at UC Berkeley supported by the NSF AST grant 0905801.

Chapter 1

Introduction

1.1 Overview

This thesis explores two topics in contemporary galaxy evolution theory: the feedback hypothesis and the heating of disks due to the impact of halo substructure. The feedback hypothesis states that feedback, for example the energy produced in winds and radiation from active galactic nuclei (AGN), can regulate the growth of supermassive black holes (BH) and their host galaxies producing the observed BH-galaxy relations. Disk heating is a process by which the stellar disks of galaxies thicken due to an increase in the random motions of the stars comprising the disk because of, for example, halo substructure impact.

These topics have been explored through observation, theory and numerical simulation. This thesis adds to the numerical work for both of these topics, so to place this work in context, what follows is a brief review of the observational, theoretical and numerical treatments of these problems to date.

1.2 AGN Feedback

Supermassive black holes at the centers of galaxies have often been invoked as an explanation for many problems in galaxy formation. Among these are the suggestion that feedback on the surrounding gas could not only regulate the growth of the black hole itself, but might also quench star formation in the host galaxy, and that this feedback might drive gas out of the host and affect the properties of the intergalactic medium.

The question of whether feedback from active galactic nuclei can perform all the roles that have been suggested is an important one. Observationally conclusions are hard to draw because interpreting the results of measurements often relies on modeling assumptions that are themselves difficult to verify. This is further complicated by the fact that theoretical treatments often make simplifying assumptions which might have

a large effect on the final dynamics. Numerically, the problem is recently becoming more tractable, but the simulations often involve a vast range of time and distance scales that are difficult to treat properly.

1.2.1 Observational Results

Across a wide range of masses and types, galaxies show strong nuclear activity. The hallmark of an active galactic nucleus is its electromagnetic output over a wide range of wavelengths. Unlike a normal galaxy with a spectrum comprised primarily of the thermal emission of the sum of all its stars, an active galaxy shows continuum emission with a non-thermal spectrum. Active galaxies often show emission lines, both with broad line widths ($> 2000\,\mathrm{km\,s^{-1}}$) and narrow line widths ($< 500\,\mathrm{km\,s^{-1}}$) (Sulentic et al., 2000, Netzer, 2008). Strong radio emission (Wadadekar, 2004), sometimes in large lobes a significant distance from the center of the galaxy (Bridle and Perley, 1984), are another indication of a galaxy's activity. Another hallmark of an active galaxy is strong emission in x-rays (Suchkov et al., 2006, Shen et al., 2006), which is typically absent at the same level in star forming galaxies.

The wide variety of radiation mechanisms in active galaxies reflects an underlying variety in physical processes by which the radiation interacts with the material in those galaxies. The presence of broad and narrow emission lines indicates the presence of two classes of clouds which intercept and interact with the AGN's radiation (Netzer, 2008). Often intense infrared emission from a galaxy, as from LIRGs and ULIRGs, is present indicating that interactions with dust can play an important part in an AGN (Sanders, 1999). The presence of x-rays in a spectrum is often taken to be due to Compton up-scatter of lower energy photons by hot electrons (Sunyaev and Titarchuk, 1980). The 'big blue bump' (Sanders et al., 1989) is often taken to be thermal emission from a disk which might feed the power source for an AGN (Laor and Netzer, 1989)

The intense radiation from an AGN leads immediately to the question of what could possibly power such an extraordinary energy output. High resolution measurements of the nuclei of nearby active galaxies puts the problem in sharper relief: how can a region the size of the Solar System produce the light of a trillion stars? The best candidate for the power source of an AGN is accretion onto a supermassive black hole.

The best evidence for the existence of a supermassive black hole is in our own Galaxy (which is not itself particularly active). High resolution imaging of the Galactic center has allowed researchers to track the orbits of a number of stars in the central cluster in our Galaxy (Ghez et al., 2008). From the fitted orbits, the mass of the central object, $\sim 4 \times 10^6 \mathrm{M}_\odot$, and the size of the region in which it must be confined, ~ 120 AU, can be determined which leaves a black hole as essentially the only possibility.

Outside of our local universe, the evidence is more inferential. Among the methods

of finding masses for central objects are dynamical modeling of the stellar kinematics (McConnell et al., 2012), observations of water masers' orbits (Kuo et al., 2011) and reverberation mapping (Peterson et al., 2004). Such observations lead to the conclusion that most spheroids contain a SMBH.

The fact that every spheroid contains a SMBH leads quickly to the question of why every galaxy is not an active galaxy. The central SMBH powering nuclear activity relies on accreting material to operate. This naturally leads to an epsiodic pattern of activity, with the nucleus lighting up only when material is falling into the black hole. The ubiquity of supermassive black holes and the relative scarcity of active galaxies suggests that every galaxy is potentially active, and is merely waiting for an event that would drive material into the central SMBH. Indeed, Sanders et al. (1988) put observations of ULIRGs into an evolutionary sequence where a major merger induces inflow and activity which is shrouded by dust. This would explain both the infrared emission, because of the dust intercepting and re-radiating the light, and the high luminosity of such systems, because of the supermassive black hole accretion.

In addition to the prevalence of nuclear black holes, observations indicate a link between the black hole and its host galaxy. One such relationship was the M-σ relation (Gebhardt et al., 2000, Ferrarese and Merritt, 2000) which relates the mass of the black hole to the stellar velocity dispersion of the spheroidal components of the host galaxy. The mass of the SMBH is also correlated with the mass of the spheroid (Magorrian et al., 1998, Häring and Rix, 2004), and the luminosity of the bulge (Marconi and Hunt, 2003). Given the interest in these relations it is no surprise that observers continue to refine the correlations as observations improve (Gültekin et al., 2009, Greene et al., 2010). Hopkins et al. (2007) suggests that black holes have a fundamental plane, analogous to the elliptical galaxy fundamental plane, which ties together the two property correlations into a correlation in a higher dimensional space. Whatever form they take, these relationships imply a link between the evolution of the black holes and their host galaxy.

The existence of active galaxies, the strong radiation and feedback processes, and the ubiquity of black holes in spheroids suggest that perhaps it is the effect of the radiation on the surrounding gas that is responsible for the link between the evolution of black holes and galaxies. This coevolution would then naturally manifest itself as correlations of the form seen in the black-hole galaxy relations. But can this suggestive observational picture be put into a theoretical framework?

1.2.2 Theoretical Results

The feedback hypothesis states that the feedback from the active galactic nucleus is what links the evolution of supermassive black holes to their host galaxy. Exactly what form the feedback takes, and the strength of the feedback, is still an open question.

The first model attempting to explain BH-Galaxy relations was Silk and Rees

(1998). In it, they assume that energy from the AGN is deposited into the surroundings, as from Compton heating, and are able to reproduce the relation reported in Magorrian et al. (1998). King (2003) argued that energy deposition, though it may be relevant at large distances from the AGN and thus capable of regulating the intracluster medium, is ineffective at small radii and instead used momentum driven feedback from the AGN to reproduce the observed relationships. Another model (Burkert and Silk, 2001) invokes the star formation in a nuclear disk to regulate the flow of material into the black hole. It is interesting that such different mechanisms can reproduce the observed relationships, and one is left wondering if BH-Galaxy relations are general results of *any* feedback that is sufficiently powerful. However, these models were all relatively simple: they assumed simple symmetries and appealed to a single feedback mechanism. It is likely that it is not just a single process that regulates galaxy growth, and the situation is certainly not spherically symmetric.

Further effort in one dimensional models has improved over the simple results above. Ciotti and Ostriker (1997) and Ciotti and Ostriker (2001) have shown that Compton heating, and photoionization models are sufficient to solve the cooling flow problem (which is that intergalactic gas will cool and condense onto galaxies increasing star formation and overall masses), producing galaxies with a much smaller mass than with a cooling flow alone. Interestingly, they produce an episodic accretion history where the inflowing material heats and is blown out by the AGN where it is able to cool and flow back into the center (Ciotti and Ostriker, 2007). Feedback via momentum and energy separately (Ciotti et al., 2009) and together (Ostriker et al., 2010) has also been modeled in one dimension. The results of these works indicate that one type of feedback is generally insufficient to reproduce observations, and indeed the inclusion of momentum feedback increases the overall efficacy of the AGN's feedback.

In addition to feedback directly from the AGN, regions of elevated star formation are also a source of feedback, which can be significant. Further, in many of the same situations that AGN feedback is important (e.g. mergers) the increase in gas density also drives an increase in star formation leading to a starburst, which can drastically affect the subsequent dynamics of the gas. The potential importance of star formation feedback led Thompson et al. (2005) to consider star formation stabilized disk models as one possible mechanism for AGN fueling. Given such models, the issue of the predominant feedback mechanism is far from clear.

One thing that is certain, however, is that gas needs to be brought to the center of the systems to fuel either the AGN, the starburst, or, what is more likely, both. The primary difficulty is finding a method to remove angular momentum from the gas. Jog and Ostriker (1988) treated giant molecular clouds as essentially billiard balls and found that their interactions caused the clouds to migrate to the center of the galaxy. Another option is the mechanism of 'bars within bars' (Shlosman et al., 1989). In it, they argue that the instability that leads to the large scale bars in disk galaxies can also operate on smaller scales, leading to a hierarchy of bar structures that is able to continuously torque gas to lower angular momentum. Goodman (2003)

finds that thin disks become self-gravitating, and thus fragment due to instabilities, at around 10^{-2} pc, which does not allow enough mass for the observed BH. Though, global torques, as from bars, would get around this problem by replenishing the disk with low angular momentum gas. These and similar considerations led Shlosman et al. (1990) to develop a unified fueling model that relies on a host of mechanisms operating on different length scales.

With the wide range of processes that occur for interstellar gas in galaxies, it is no surprise that a complete theoretical treatment of AGN feedback has not been performed. The range of processes, each with their own scales over which they operate, lead to a complicated and nonlinear problem. Even should a complete description be written down, it is likely that the system of equations would require numerical solution. Further, the ISM is complicated by virtue of its geometry and potentially clumpy nature. The end result of any such study is to appeal to computers to solve the complicated interactions in non-trivial and dynamic geometries. Despite this, theory offers a catalog of potentially important interactions that can be explored numerically.

1.2.3 Numerical Results

Numerical simulation has long been a tool for gaining understanding of astrophysical processes. Much of the benefit of simulation lies in the ability to handle general distributions of matter that would be impossible to treat analytically. Further, it is relatively easy to add more interactions to simulations, so a wide range of possible models and effects can be explored.

Galaxy mergers has been a popular target for numerical simulation in astrophysics since the beginning of scientific computing. Toomre and Toomre (1972) was a pioneering work on the dynamics of major mergers, and despite the low computing power of their day, they found tidal tails and bridges are generic results of merging galaxies. Some years later, Barnes and Hernquist (1991) used the considerably improved computational resources to explain in depth the dynamical processes when both gas and collisionless material are present. In particular, the resulting tidal features are able to effectively torque gas into the center of the merging system.

With the basic picture of the dynamics of merging systems understood, the next step was to begin including the feedback processes that theory has indicated could be dynamically important. The first full three dimensional simulations of mergers with a model for feedback from AGN was Springel et al. (2005a). Their simulations included a new model for star formation treating some related feedback processes (Springel and Hernquist, 2003), and a model for energy deposition into the gas surrounding the black holes. They are able to not only reproduce the $M - \sigma$ relation (Di Matteo et al., 2005), but also produce remnant elliptical galaxies that have little star formation and little AGN activity (Springel et al., 2005b), primarily because the feedback ejects much of the star forming gas to large radii, and thus low density.

With the success of these simulations, many explored the results of their model in other contexts. Hopkins et al. (2005) used the model to explore and refine the picture of quasar evolution presented in Sanders et al. (1988). During the merger gas is torqued to the center and both powers and obscures the quasar. The feedback then blows the gas out of the center and offers a short window during which the quasar is visible before the ejection of gas shuts off activity. Johansson et al. (2009b) and Johansson et al. (2009a) performed a large suite of simulations to test the effect of many galaxy parameters on the resulting BH-Galaxy relation, including orientation, galaxy type, and gas fraction as an attempt to mock up the evolution of the scaling relations over cosmic history. The model was applied to a cosmological context by Khalatyan et al. (2008) who found that feedback was required to form a 'red and dead' central galaxy of a cluster. A larger sample of cosmological simulations by Booth and Schaye (2009) found that galaxies grow black holes onto the $M - \sigma$ no matter where they begin.

In addition to extensions of the Springel et al. (2005a) model, many have developed their own methods and models with the goal of explaining some of the same features as the above. The jet from the AGN was used by Vernaleo and Reynolds (2006) in an attempt to hold back the cooling flow. Kawata and Gibson (2005) include AGN feedback in a single elliptical galaxy and able to reproduce the optical and x-ray luminosities, and are able to shut off star formation. An advanced grid based technique, adaptive mesh refinement, was applied by Kim et al. (2009) to a merger. Though the results are limited, they have made a good proof of concept that AMR can be used in the context of merging galaxies.

With few exceptions, these works share an assumption that should be explored: the feedback is through energy deposited into the surrounding gas. This assumption deserves exploration because dense gas, like what is found in the vicinity of supermassive black holes, has many ways that it can radiate away its energy. Also, Sazonov et al. (2005) find that Compton heating is ineffective out to a large radius. One way around these troubles is to deposit momentum into the surroundings. This would occur in, for example, absorption of light by dust grains. Unlike energy, momentum cannot be radiated away, and so might be important for the dynamics of AGN.

Until very recently, there has been little work in this direction. One early work was Chang et al. (1987) who considered the momentum imparted to the UV absorbing dust. Another numerical effort along these lines (after my own) was Power et al. (2011) who used momentum feedback in their 'Accretion Disk Particle Method.' Also, Ciotti et al. (2009) and Ostriker et al. (2010) consider momentum feedback in their simple one dimensional models.

1.2.4 Contributions

A major portion of this thesis explores numerical models of AGN feedback that operate primarily by the deposition of momentum in the surrounding gas. In spirit,

the work is similar to Springel et al. (2005a), but the details and some major results differ.

In chapters 2 and 3, a sub-grid model of radiation pressure on circumnuclear gas in implemented in full three dimensional hydrodynamic simulations of major mergers of two Milky Way-like galaxies. In these chapters I will show that such a model is able to regulate the growth of the black hole and reproduce the $M - \sigma$ relation, for a certain set of model parameters. However, the star formation in the galaxy is not drastically effected by the model as the feedback operates locally to the black hole.

In chapter 4, I present another model depositing momentum due to AGN activity. Unlike the previous, which deposits momentum shared equally among all the gas in the vicinity, this model instead launches a powerful wind by rapidly bringing some gas to large velocities. By itself, this wind is able to regulate the growth of the black hole, but is also able to shut off star formation in the remnant. This occurs when the wind runs into much slower gas and sweeps up additional material, bringing not only the launched wind, but surrounding material to escape speed. In conjunction with the previous model this model produces remnants with little active star formation and black holes with masses that agree with observations.

1.3 Disk Heating

The picture of the universe that emerges from both theory (Lacey and Cole, 1993) and observation (York et al., 2000) is one of hierarchical structure, starting from the most massive objects, clusters and super-clusters, their smaller constituents, groups of galaxies, with their smaller individual galaxies like the Milky Way, which have a large number of satellites that are smaller still. In this model, a given structure will experience many merger events throughout its history, from the rarer major merger (Stewart et al., 2008), to the much more numerous minor merger events by which much of the halo's mass is accreted (Purcell et al., 2007, Zentner, 2007). Understanding the effects of such a construction history on the baryonic material is vital for understanding the process of galaxy formation as it occurs in the universe.

Major mergers between roughly equal mass objects are relatively rare today (Conselice et al., 2003), but can have very significant effects of the galaxies in question (Bell et al., 2006). Minor mergers, on the other hand, are more frequent (Lotz et al., 2011), and are much less destructive to the larger of the two galaxies. Indeed, most Milky Way like galaxies are host to a large number of satellite galaxies (Guo et al., 2012). Observationally, disk galaxies today are observed to be quite thin (van der Kruit and Freeman, 2011). However, there is some tension between this observation and the fact that most average galaxies are accompanied by a host of smaller galaxies which can ultimately merge and disturb the disk.

These mergers are generally expected to deposit energy into the central galaxy. For example, Toth and Ostriker (1992) looked at the heating in the disk due to satellites

via scattering, and found that the disk gains more energy than is lost by the satellite, and placed some limits on the amount of mass accreted by the Milky Way. Benson et al. (2004) developed a semi-analytic model of disk heating by satellites orbiting the galaxy taking into account the internal structure, mass function and accretion rate of satellites, as well as disk growth. Though they ignore the resonant heating of the disk, and the dynamical effects of bars and spirals, their model agrees broadly with observations. These are only a few models of disk heating, but the general message is that satellites have a number of dynamical mechanisms by which to deposit energy into their host galaxy.

Given that the average history of any galaxy is going to involve many minor mergers, each of which can have an impact on the dynamics of the galaxy, it is somewhat surprising that any thin disk survives to today. Simple analytical estimates can only go so far, and the introduction of numerical techniques is an obvious step to make.

There has been ample prior numerical work on this problem. Sellwood et al. (1998) considered the heating provided to a disk by a small satellite via a resonance between vertical bending waves and stellar orbits. Another early work, Velazquez and White (1999), ran a set of self-consistent simulations of disks and satellites, and found both heating of the disk, and tilting of its plane. Another work studying single minor mergers is Purcell et al. (2009), who found in their set of cosmologically common mergers that the final disk was thicker that that of the Milky Way by a factor of ~ 3. Hopkins et al. (2009) ran simulations of mergers and developed a model characterizing the amount of disk left after such events. The importance of the gaseous component of the disk was pointed out by Moster et al. (2010), who showed that because the gas can absorb some of the impact energy, and can regrow the disk, the final scale heights of Milky Way-like disks can indeed be brought into agreement with observations. Further, in Moster et al. (2011) they show that if a hot gaseous halo is included, the evolution of the thin disk scale height is dominated by the formation of a new stellar disk after a merger event.

However, studies of a single merger event are of limited utility when the full cosmological context of real disks is considered. An average disk will experience many mergers throughout its lifetime, and the effects of multiple mergers should be explored. Bournaud et al. (2007) performed simulations of disks undergoing multiple minor mergers, and found disks which became significantly more elliptical, with little or no disk remaining. Despite their resolution being comparable to the thickness of the thin-disk component of spiral galaxies, these simulations demonstrate that the effect of multiple mergers can be much larger than that of a single merger. Kazantzidis et al. (2008, 2009) performed simulations of a thin disk galaxy subject to a set of satellite mergers whose properties were taken from a cosmological simulation. They find that the final disks suffer a number of dynamical effects resulting from the impactors: the disk thickens, a bar and other non-axisymmetric features develop, and the disk tilts and flares.

This picture is complicated by the fact that other processes can heat disks. In particular, the formation of bars, and the subsequent dynamics can have a large effect on the structure of disks. In a large series of simulations of thin disks, Saha et al. (2010a) found that bars, and transient spiral structure, can heat disks vertically. Sotnikova and Rodionov (2003) also found that the vertical buckling mode of bars plays an important role in disk heating. In a controlled series of experiments focusing on secular evolution, rather than hierarchical assembly, Debattista et al. (2006) found that bar buckling had the largest effect on the vertical structure of the disks. These simulations show that secular effects can also have a large impact on stellar disks, and must be considered in any serious study of the problem.

For the most part, the halos in the previous works are idealized, even though they are motivated by the full cosmological context. To study galaxy formation in the setting in which it actually occurs, the disks will have to be included in the full cosmological setting. One suite of simulations that has provided ripe ground for studying galaxy formation in a realistic context are the Aquarius simulations (Springel et al., 2008). These zoom-in simulations target Milky Way like halos with a lack of recent major mergers and no nearby massive companions in a large cosmological volume, and resimulate the halo at higher resolution. The simulations have provided a very detailed example of halos, including substructure, that can be used as a laboratory to test the effects of various processes on galaxy formation.

Indeed, a fair amount of work had gone into including baryonic material in the Aquarius simulations. Scannapieco et al. (2009) performed resimulations of a number of Aquarius halos including the effects of a realistic multi-phase, star-forming gas and found that while disks form easily, they can be destroyed by mergers or disk instabilities. Tissera et al. (2010) expanded on the previous by focusing on the effects of the baryons on the dark matter halos, finding that the detailed structure of the halo depends on the specifics of how the halo was constructed. Sales et al. (2011), though not using Aquarius, explored the effects of halo parameters on the resulting galaxy and found that the resulting morphology has more to do with the complete accretion history rather than any property of the halo. These works, however, focus on broader issues of disk formation in the cosmological setting.

To answer the question of the effect of the full structure of a realistic dark matter halo on the thickness of disks, a more specialized approach is called for, focusing on the stellar disk and its interaction with the subhalo impactors in the disk's host halo. This avoids any complications of the relatively poorly understood and difficult to model gas physics. Of course, the full story is likely to rely on those physics, but it is worth separating out the simpler collisionless dynamics of stellar disks.

1.3.1 Contributions

Chapter 5 of this thesis presents the first results of a method for including a stellar disk in realistic cosmological simulations. The dark matter halos, taken from

the Aquarius suite of simulations, are adjusted adiabatically by a rigid disk potential before live disk particles are included in the simulations. The disks heat and thicken in general, and though often very strong bars develop which confound the signal, some first steps are taken to link the effects on the dark matter, including halo substructure and frequent substructure mergers, on the evolution of the stellar disk.

Chapter 2

Self-Regulated Black Hole Growth via Momentum Deposition in Galaxy Merger Simulations

We perform hydrodynamical simulations of major galaxy mergers using new methods for calculating the growth of massive black holes (BH) in galactic nuclei and their impact on the surrounding galaxy. We model BH growth by including a subgrid model for accretion produced by angular momentum transport on unresolved scales. The impact of the BHs radiation on surrounding gas is approximated by depositing momentum into the ambient gas, which produces an outward force away from the BH. We argue that these phenomenological models for BH growth and feedback better approximate the interaction between the BH and dense gas in galaxies than previous models. We show that this physics leads to self-regulated black hole growth: during the peak of activity, the accretion rate onto the BH is largely determined by the physics of BH feedback, not the subgrid accretion model. The BH significantly modifies the gas dynamics in the galactic nucleus ($\lesssim 300$ pc), but does not generate large-scale galactic outflows. Integrated over an entire galaxy merger, BH feedback has little effect on the total number of stars formed, but is crucial for setting the BHs mass.

2.1 Introduction

Modern theories of galaxy formation hold that strong feedback processes regulate star formation in galaxies across a wide range of masses. For more massive galaxies, stellar feedback processes appear to become less efficient and feedback from a central massive black hole (BH) begins to dominate. Feedback from an active galactic nucleus (AGN) has been invoked to account for many observational results in galaxy formation, including the $M_{BH} - M_*$ and $M_{BH} - \sigma$ relations and the suppression of

star formation in elliptical galaxies (Silk and Rees, 1998, King, 2003, Di Matteo et al., 2005, Murray et al., 2005, Springel et al., 2005b, Hopkins et al., 2007).

Many recent studies developing numerical models for the effects of BHs on galactic scales have used broadly similar implementations of the uncertain physics of AGN fueling and feedback (e.g., Springel et al. 2005a, Kawata and Gibson 2005, Johansson et al. 2009b). It is, e.g., often assumed that a BH of mass M_{BH} accretes mass from the surrounding interstellar medium (ISM) at a rate proportional to the Bondi rate (Bondi, 1952),

$$\dot{M}_{Bondi} = \frac{4\pi f G^2 M_{BH}^2 \rho}{c_s^3}, \tag{2.1}$$

where ρ is the surrounding gas density, c_s is the sound speed and $f \sim 10 - 100$ takes into account the fact that the sphere of influence of the black hole is not always resolved (Booth and Schaye, 2009). Moreover, these same calculations assume that the black hole's impact on its host galaxy can be approximated by depositing thermal energy released by accretion back into the surrounding gas. There is, however, little detailed motivation or justification for either of these assumptions.

Eq. (2.1) is only applicable when the gas fueling the central BH has very little angular momentum. Otherwise, the transport of angular momentum regulates the accretion rate onto the central BH (e.g., Shlosman et al. 1990). It is generally believed that gas-rich disk galaxies are the progenitors of today's $\gtrsim L^*$ ellipticals and, in particular, that mergers of gas-rich galaxies lead to luminous starbursts and the growth of central massive BHs (Sanders et al., 1988, Hopkins et al., 2005). Most of the gas in disk galaxies, merging galaxies, luminous starbursts (Downes and Solomon, 1998, Tacconi et al., 2006), and nearby luminous AGN (Ho et al., 2008) appears to reside in a rotationally supported disk. There is therefore no strong reason to believe that the spherically-symmetric Bondi accretion rate is a reasonable estimate of the accretion rate onto a BH in gas-rich disk galaxies.

The energy generated by a central AGN can couple to its surroundings in a variety of ways, all of which may have a significant dynamical influence on gas in the host galaxy and in the surrounding intergalactic medium. For example, relativistic jets inject energy into intracluster plasma and may be the key mechanism for suppressing cooling flows in galaxy clusters (McNamara and Nulsen, 2007), although the details of how the energy in the jet couples to the surrounding plasma in a volume-filling way are not fully understood (Vernaleo and Reynolds, 2006). On galactic scales, winds from an accretion disk around the BH may sweep-up and drive gas out of galaxies (e.g., King 2003). And the AGN's radiation can strongly impact the surrounding gas, both via Compton cooling/heating (e.g., Sazonov et al. 2005) and via the momentum imparted as UV radiation is absorbed by dust grains (Chang et al., 1987, Sanders et al., 1988).

The precise physical mechanism(s) responsible for AGN feedback are not fully understood, particularly on galactic scales. For this reason, it is useful to distinguish

between two classes of models: energy and momentum injection. We believe that momentum injection, not energy injection, is likely the dominant form of feedback for the majority of the gas in a galaxy. In most circumstances, jets take the path of least resistance and travel relatively unimpeded out of a galaxy. Furthermore, while radiation from an AGN can, in principle, Compton heat the surrounding gas enough to unbind it, it can only do so for very low density gas. For example, for a BH radiating at $\sim 10^{46}$ erg s^{-1} with a typical quasar spectrum, only gas with $n \lesssim 1\,\mathrm{cm}^{-3}$ can be heated to the Compton temperature within ~ 100 pc. However, the mean gas densities in the central $\sim 100\,\mathrm{pc}$ of ultraluminous infrared galaxies are $\sim 10^4\mathrm{cm}^{-3}$ (Downes and Solomon, 1998). At these densities, the cooling time of the gas is very short and the gas is unable to retain any injected energy. Thus if the radiation from a BH strongly modifies the dynamics of the gas in its immediate vicinity, it must be via the *force* exerted when the radiation is absorbed.

Given the uncertainties in the physics of BH accretion and feedback, it is important to explore a range of models for the impact of BHs on galaxy formation. Towards this end, we have carried out numerical simulations of major galaxy mergers, qualitatively taking into account the physics of accretion induced by angular momentum transport and AGN feedback by momentum injection (radiation pressure). Our accretion and feedback prescriptions both differ from those used in previous numerical simulations of BH growth and feedback. The results in this *Letter* are taken from a larger set of calculations (DeBuhr et. al. in prep.) and represent general features of all the simulations we have carried out.

2.2 Methods

We use a non-public update of the TreeSPH code GADGET-2 (Springel, 2005) to perform simulations of galaxy mergers with feedback from both star formation and central supermassive BHs. The code, provided by V. Springel, includes the effective star formation model of Springel and Hernquist (2003). We describe below the additional modifications that we have implemented to model BH growth and feedback.

The multiphase equation of state of Springel and Hernquist (2003) overpredicts the "sound speed" as compared to observations of the random velocities in galaxies (in atomic or molecular gas). For example, the parameter choices $T_{SN} = 4 \times 10^8$K, $A_0 = 4000$, $t_*^0 = 8.4$Gyr, and $q_{EOS} = 0.5$, which have been used in previous works (Springel et al., 2005a), predicts $dv \sim 30$ km s^{-1} at $n \sim 1\,\mathrm{cm}^{-3}$ and $dv \sim 110$ km s^{-1} for $n \sim 10^3\mathrm{cm}^{-3}$. These are too large by a factor of $\sim 2-3$ compared with the observed values (Downes and Solomon, 1998). To account for this difference, we reduce the pressure everywhere by a constant factor of 10. As in Springel and Hernquist (2003), we assume that $\dot{\rho}_* \sim \rho^{1.5}$ for consistency with observations (Kennicutt, 1988). The normalization of the star formation prescription is chosen so that a Milky Way-like

galaxy has a total star formation rate of about one solar mass per year; for galaxies with different surface densities, the result is also consistent with Kennicutt (1988). By reducing the pressure at fixed ρ by a factor of 10, the gas is more dense in hydrostatic equilibrium. This would increase the star formation rate relative to the observed value. To correct for this, we modify the equation of state parameters to: $t_0^* = 13.86$ Gyr, $\beta = 0.1$, $A_0 = 6600$, $T_{SN} = 6.6 \times 10^8$ K, $T_c = 1000$ K and $q_{EOS} = 0.5$.

The simulations described in this work are all mergers of equal mass galaxies. Each model galaxy consists of a dark matter halo, a rotationally supported disk of gas and stars, a stellar bulge, and a central BH. The galaxy parameters are similar to those in Springel et al. (2005a): each galaxy has a total mass of $1.36 \times 10^{12}\mathrm{M}_\odot$; the mass of the disk is 4.1% of the total, i.e., $5.57 \times 10^{10}\mathrm{M}_\odot$, where 10% of the disk mass is assigned to gas and 90% to stars; the bulge has a mass of $1.86 \times 10^{10}\mathrm{M}_\odot$, i.e., 1/3 of the total disk mass. Each galaxy is made of 8.0×10^5 simulation particles and the gravitational force softening is $\epsilon = 47$ pc. The halo and the bulge have Hernquist density profiles (Hernquist, 1990), where the virial and half-mass radii of the halo are 229 kpc and 102 kpc, respectively (the concentration is 9.0), and the effective radius of the bulge is 1.27 kpc. The gaseous and stellar disks have exponential profiles with scale lengths $R_d = 3.51$ kpc; the scale-height of the stellar disk is 0.7 kpc, while the scale-height of the gaseous disk is determined by hydrostatic equilibrium. The massive BH in each galaxy is modeled using a specially marked collisionless tracer particle.

The initial conditions are generated as in Springel et al. (2005a), except for the decrease in gas pressure described above. The galaxies are placed on a prograde parabolic orbit. The individual spins of the two galaxies are randomly chosen to have a relative angle of about 41 degrees. The galaxies begin at a distance of 142 kpc and the orbit has a pericenter of 14.2 kpc.

We estimate the accretion rate onto the BH from the surrounding gas, due to viscous transport of angular momentum, using

$$\dot{M}_{vis} = 3\pi\alpha\Sigma\frac{c_s^2}{\Omega}\,, \tag{2.2}$$

where Σ is the mean surface density of the gas in the disk, Ω is its angular rotational frequency, and the free parameter α is the dimensionless viscosity; $\dot{M}_{vis}$ is also capped at the Eddington rate. We compute Σ and the sound speed c_s by taking an average of the properties of the individual SPH particles in a spherical region with a radius $R_{acc} = 4\epsilon = 188$ pc centred on the BH. Using velocity information directly from the simulation particles themselves to compute Ω proved to be too noisy; we thus determined Ω using the total mass, M_T, inside R_{acc} through $\Omega^2 = GM_T/R_{acc}^3$.

Note that in our accretion prescription, $\dot{M}_{vis} = 0$ if there is no gas within 4ϵ of the BH. This feature of our model accounts for the fact that our simulations capture the angular momentum transport produced by gravitational torques on large scales ($\gtrsim 4\epsilon = R_{acc}$); we assume, as is physically reasonable but by no means proven, that

these must be sufficient to bring gas close to the BH (within R_{acc}) for significant BH accretion to proceed.

Eq. (2.2) is reminiscent of an alpha prescription of Shakura and Sunyaev (1973), but in this formulation α parameterises both the efficiency of angular momentum transport on scales smaller than our gravitational force softening (by, e.g., gravitational torques) and the uncertainty due to the fraction of the inflowing mass that turns into stars vs. accreting onto the central BH. The physical processes responsible for transporting gas from $\sim$ kpc to ~ 0.1 pc are still not fully understood (Goodman, 2003), but non-axisymmetric gravitational torques are likely responsible (Shlosman et al., 1989). Detailed calculations of the structure of AGN disks from $\sim 0.01-100$ pc, based on transport by spiral waves, show that Eq. (2.2), evaluated at radii $\sim 30-100$ pc, can provide a reasonable estimate of the accretion rate onto the BH in some cases (Thompson et al., 2005). Although Eq. (2.2) is only a crude approximation to the true accretion rate onto the BH, it captures the qualitative physics of accretion induced by angular momentum transport, and is thus, we believe, a more suitable "subgrid" model than Eq. (2.1). Our fiducial choice for α is $\alpha = 0.05$, but we also present results for 0.15 in Sec. 3. In the future, we intend to better calibrate our model of angular momentum transport using simulations that focus on the central ~ 100 pc of galaxies (Hopkins and Quataert, 2010b).

To model the feedback onto the gas surrounding the BH, we have implemented a simple phenomenological model in which the AGN's luminosity L is coupled back into the surrounding gas by depositing momentum radially outward from the BH. Our goal is to account for the radiation pressure produced by the absorption and scattering of the AGN's radiation by dust in the ISM. To accurately do so would require a radiation transport calculation, which is beyond the scope of the current paper. Instead, we model the impact of this radiation on the surrounding galaxy by depositing a total momentum (per unit time) of

$$\tau L/c\,, \quad \text{where} \quad L = \min(\eta \dot{M}_{vis} c^2, L_{Edd}) \tag{2.3}$$

radially away from the BH into every SPH particle within a distance of R_{acc} from the BH; each particle receives the same acceleration. Note that the number of particles that receive this extra force, N, will change with time as particles enter and leave the central region of radius R_{acc}. We assume a radiative efficiency of $\eta = 0.1$. Equation (2.3) models the absorption by the dust of the UV radiation from the AGN (one L/c), and, more importantly, the subsequent diffusion of the far IR photons ($\tau L/c$). In this way, the value of τ determines the total momentum deposited and corresponds to the total far IR optical depth in the nuclear region; we choose $\tau = 10$ in these calculations. This value of τ is consistent with the fact that even the far-infrared radiation produced by dust is optically thick at radii ~ 100 pc during galaxy mergers (e.g., Thompson et al. 2005). In particular, $\tau \sim 10$ is motivated by the surface density of $\Sigma \sim 3$ g cm^{-2} in the inner ~ 100 pc near the peak of accretion, and a FIR opacity of

~ 3 cm^2 g^{-1}. The exact value of τ does not significantly affect our conclusions, but it does normalize the values of $\dot{M}_{vis}$ and M_{BH} (see Eq. 2.4 below).

The strength of the feedback on an individual particle depends not only on the luminosity, but on the number of particles, N, to which the force is being applied in a given timestep. Our results do not depend strongly on N; this is because the momentum is quickly shared with the rest of the gas particles via pressure forces. We carried out a number of test problems on the evolution of gaseous shells with the additional force $\tau L/c$; these explicitly show no dependence on N (DeBuhr et. al. in prep).

Computing the accretion rate onto and the feedback from the BH in the simulations is prone to noise induced by the stochastic motion of the BH particle. To avoid this "Brownian" motion, we choose a mass for the BH tracer particle of $2.8 \times 10^7 \mathrm{M}_\odot$, which is roughly a factor of 100 higher than the other particle masses in the simulation. Note that this mass is an artificial dynamical mass for simulation purposes; in addition to this, we integrate $\dot{M}(t)$ to determine the "true" M_{BH}. Once the two BH tracers have a separation of $4R_{acc}$ or smaller, we consider that they would coalesce to form a single BH. Once the tracers merge, the two values of M_{BH} are summed and one of the BH particles is moved to the center of mass of the two tracers, and the other is removed from the region.

2.3 Results

The top panel of Figure 2.1 shows the viscous accretion rate onto the BH for the fiducial run with $\alpha = 0.05$ (black) and for a run with $\alpha = 0.15$ (blue). For comparison, the Eddington rate $\dot{M}_{Edd} \equiv L_{Edd}/\eta c^2$ is shown in grey, using the BH mass as a function of time from our fiducial simulation. The accretion rate is relatively constant at early times but then peaks during the first close passage of the two galaxies at ~ 0.75 Gyr and then even more strongly as the two galaxies complete their merger at ~ 1.6 Gyr; note that $\dot{M} \ll \dot{M}_{Edd}$ at both early and late times but reaches $\sim \dot{M}_{Edd}$ for ~ 100 Myrs near both first and final passage.

One of the interesting results in Figure 2.1 is that differences in α do not significantly change the accretion rate onto the BH, particularly near the peaks of activity. This is contrary to what one might expect from the fact that $\dot{M}_{vis} \propto \alpha$ (eq. [2.2]). The origin of the weak dependence of $\dot{M}_{vis}$ on α is that when the supply of mass is large, feedback from accretion onto the BH regulates the rate at which the BH accretes. Previous work has shown that there is a critical luminosity L_c at which the outward radiation pressure force due to the central AGN just balances the inward force of gravity. For a simple spherically symmetric problem, this is given by $\tau L_c/c = 4 f_g \sigma^4/G$, where f_g is the gas fraction in the nuclear region and $\sigma^2 = GM_t/2R_{acc}$, with M_t the total mass within R_{acc} (Murray et al., 2005). This in turn implies a critical accretion

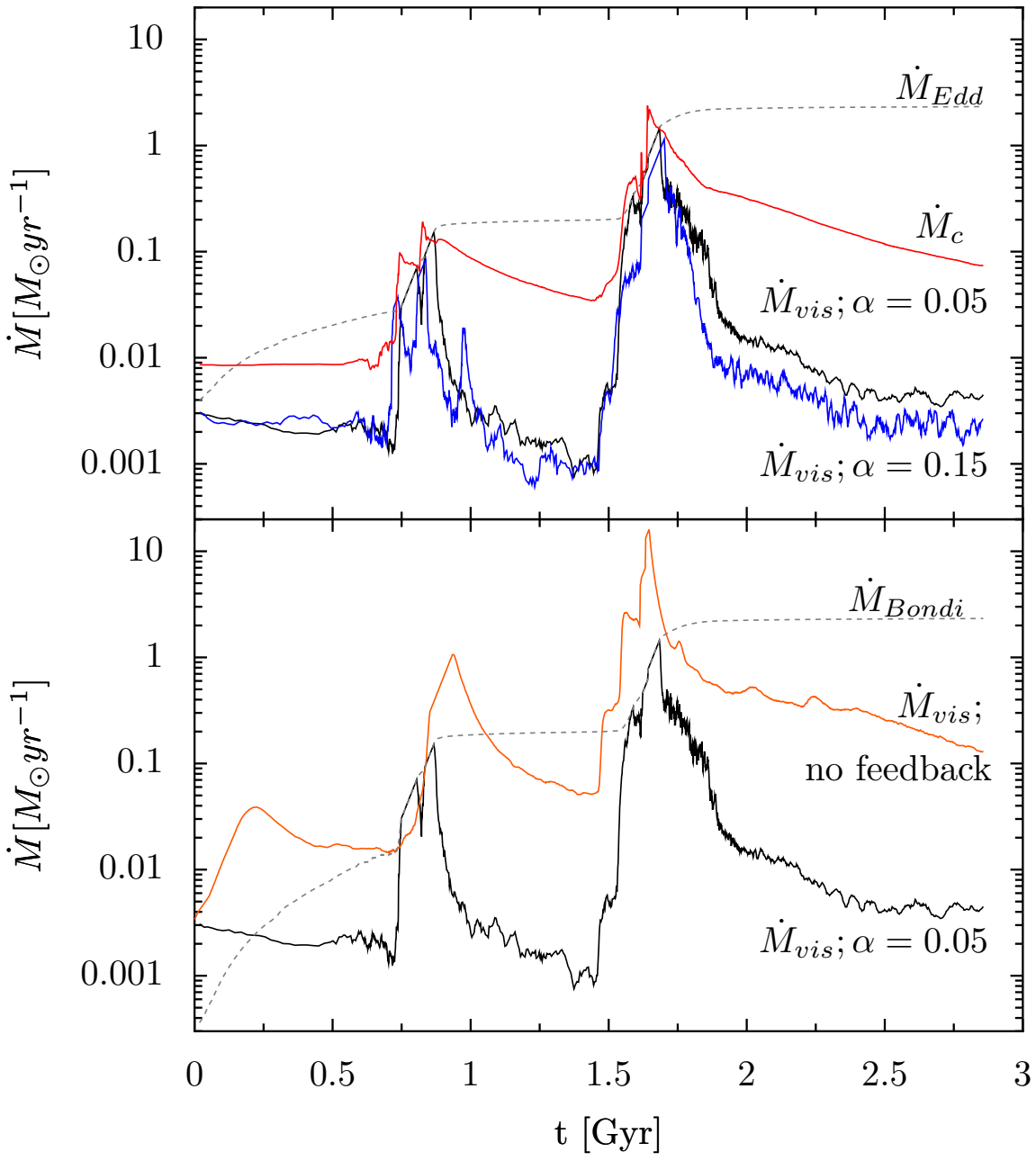

Figure 2.1: *Top panel:* Viscous accretion rate $\dot{M}_{vis}$ onto the black hole (eq. [2.2]) for our fiducial galaxy merger simulation ($\alpha = 0.05$; black), and for a run with three times the viscosity ($\alpha = 0.15$; blue). Also shown is the critical mass accretion rate $\dot{M}_c$ (eq. [2.4]) at which radiation pressure can push gas out of the nuclear region (red), and the Eddington rate $\dot{M}_{Edd}$ (grey). Note that the accretion rate adjusts to $\dot{M}_{vis} \sim \dot{M}_c$ during the peaks of activity, independent of α. *Bottom panel:* Viscous accretion rate for the fiducial simulation (black) as compared to a simulation without feedback (orange; $\alpha = 0.15$); also shown is the Bondi accretion rate using the BH mass from the fiducial simulation. Unlike $\dot{M}_{vis}$, the Bondi rate is $\simeq \dot{M}_{Edd}$ at nearly all times.

rate $\dot{M}_c$

$$\dot{M}_c = \frac{4 f_g}{\tau \eta c G} \sigma^4. \tag{2.4}$$

For $L \gtrsim L_c$, the radiation force on gas in the nuclear region exceeds the inward force of gravity, and thus gas in the vicinity of the BH will be pushed out of the nuclear region. In our model, the accretion rate is determined by the gas properties *within* $R_{acc} \simeq 188$ pc; thus if the gas is largely pushed out of the nuclear region, the accretion rate onto the BH decreases. When $L \lesssim L_c$, gravitational torques can drive gas into the nuclear region towards the BH, thus increasing $\dot{M}_{vis}$. This suggests that the accretion rate may self-adjust such that $\dot{M}_{vis} \sim \dot{M}_c$. To quantify this, the top panel of Figure 2.1 shows $\dot{M}_c$ computed within $2R_{acc}$ of the BH for the fiducial calculation (red). The accretion rate is indeed $\sim \dot{M}_c$ near the peaks of activity. This highlights that although $\dot{M}_{vis} \ll \dot{M}_c$ is certainly possible if there is insufficient gas in the nuclear regions (e.g., after the merger), feedback limits the maximum rate at which the BH can accrete to be $\sim \dot{M}_c$. One point that we return to below is that although feedback does have a strong effect on the gas dynamics in the galactic nuclei, it is *not* strong enough to blow large amounts of gas out of the galaxy as a whole.

The bottom panel of Figure 2.1 compares the accretion rate for the fiducial run (black) and a similar run with no BH feedback (orange; $\alpha = 0.15$). The peak accretion rate is a factor of ~ 10 higher in the case without feedback, and the duration of activity is significantly longer; moreover, $\dot{M}_{vis}$ in the absence of feedback is $\propto \alpha$ and so can be scaled up or down by arbitrary amounts by varying α, unlike in the presence of feedback (top panel). Also shown in the lower panel is the Bondi accretion rate (grey) with the BH mass set by that in the fiducial run (which uses $\dot{M}_{vis}$). For nearly all of the simulation, $\dot{M}_{Bondi} \simeq \dot{M}_{Edd}$, and unlike the simulations of Springel et al. (2005a) or Johansson et al. (2009b), the Bondi rate does not decrease after the final merger, because the ambient gas remains cool and dense.

Figure 2.2 shows the column density of gas in the vicinity of the BH for the case without feedback (right) and the case with feedback (left) both at the same time during the peak of accretion at $t = 1.74$Gyr. The images are 28.5kpc on a side in the top row, and 4.28kpc on a side in the bottom row. In the simulation with feedback, one can see explicitly that the gas has been evacuated from the region near the BH (within $\sim R_{acc}$), as argued above. These images also demonstrate that the feedback from the BH does not produce a large-scale blow-out of matter from the galactic nucleus. More quantitatively, at the end of the simulation, the runs with and without feedback have the same mass of gas outside $4R_d$ to within 10%, and the mass that is at large radii is due to the merger dynamics (e.g., tidal tails) rather than the BH driving a powerful outflow. This is qualitatively consistent with observational evidence for large reservoirs of atomic and molecular gas in nearby luminous AGN and quasars (Scoville et al., 2003), which have relatively normal kinematics (Ho et al., 2008). By contrast, previous simulations using the Bondi accretion rate and thermal feedback find that the BH unbinds the remaining gas in the galaxy near the end of

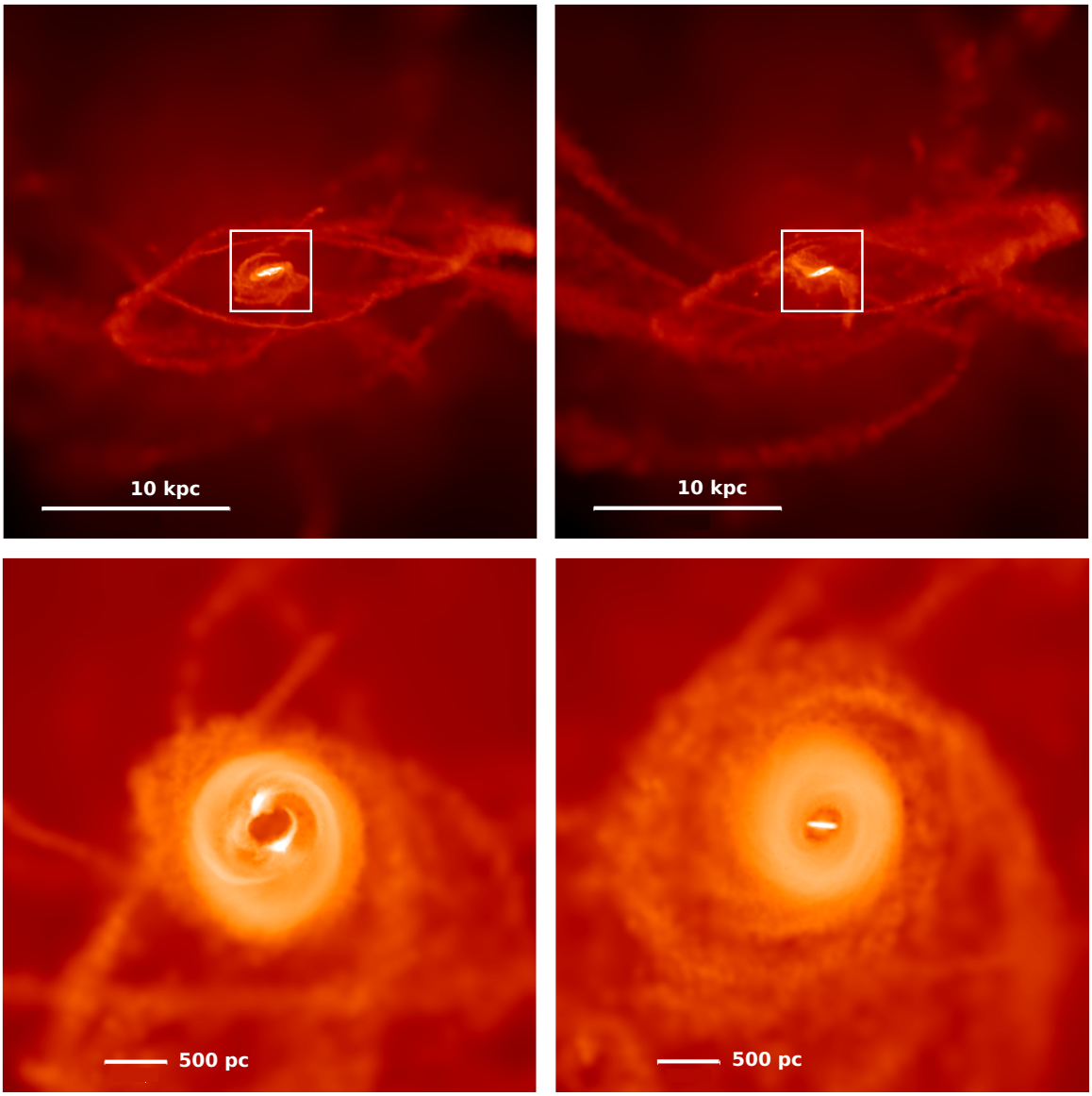

Figure 2.2: Column densities of gas centered on the BH for the run with feedback (left) and without feedback (right), at $t = 1.74$ Gyr during the peak of activity (Fig. 2.1). The colour indicates the column density with brighter colour indicating larger densities. The large scale images are projected onto the orbital plane, whereas the small scale images are viewed along the orbital plane as the nuclear disk has a large inclination. The white box shows the relative scale of the images. Note that the large-scale gas distribution is quite similar in the two cases; the BHs only visible effect is in the nuclear region ($\lesssim 300$ pc), where some of the gas is cleared out in the case with feedback. These images were generated using SPLASH (Price, 2007).

the merger (e.g., Di Matteo et al. 2005) and that this can be important for shutting off star formation in ellipticals (Springel et al., 2005b).

In Figure 2.3 we show the BH mass M_{BH} and the integrated mass of stars formed during the merger (M_*) for the fiducial simulation (black), the run without feedback (orange, dash-dot), and the run with $\alpha = 0.15$ (blue, dash). The addition of feedback changes the total star formation during the merger by less than 1%. In addition, the final BH masses for the two runs with feedback differ by about 30%. This is a further consequence of the self regulated accretion during most stages of the merger. There is, of course, freedom in choosing the initial mass of the BH in our calculations, but so long as this is sufficiently small, it does not significantly change the final mass of the BH. For the simulations without feedback, the final BH mass is larger than in the presence of feedback by a factor of $\simeq 10$, as would be expected from Figure 2.1. In addition, the mass of the BH scales $\propto \alpha$ in this case. Although we have not made a quantitative comparison, the small dispersion in BH mass for different subgrid accretion models in the presence of feedback appears consistent with the small scatter in the $M_{BH} - \sigma$ relation (while models without feedback would produce a larger dispersion in M_{BH}).

2.4 Discussion

The model presented here is a necessarily simplified treatment of the physics occurring in the nuclear regions of galaxies. In particular, the choices of α in the accretion model and of R_{acc} and τ in the model of momentum deposition are somewhat uncertain. Changing these values affects some of details of the gas dynamics. For instance, the accretion history of the BH change modestly as we vary R_{acc} and τ. However, it is encouraging that many of the global results of the simulations are insensitive to these choices. The peak luminosity occurs at the same time and always reaches the Eddington limit. The total stellar mass formed during a merger is essentially independent of these parameters and the final BH mass is relatively insensitive to both R_{acc} and α. Perhaps most interestingly, the peak accretion rate is relatively independent of the subgrid accretion model (α) and is instead set by the structure of the host galaxy and the feedback physics, reaching the critical rate $\sim \dot{M}_c$ at which radiation pressure balances gravity in the nuclear regions of the galaxy (eq. 2.4).

A clear next step in this modeling effort is to perform radiative transfer calculations simultaneously with the SPH calculation in order to more reliably determine the radiation pressure force. This would not only eliminate the need to specify the parameters R_{acc} and τ by hand, but would also provide information about the AGN spectrum as a function of time. Detailed comparisons between these results and observations should allow quantitative tests of the importance of AGN feedback by momentum deposition during BH growth and galaxy formation.

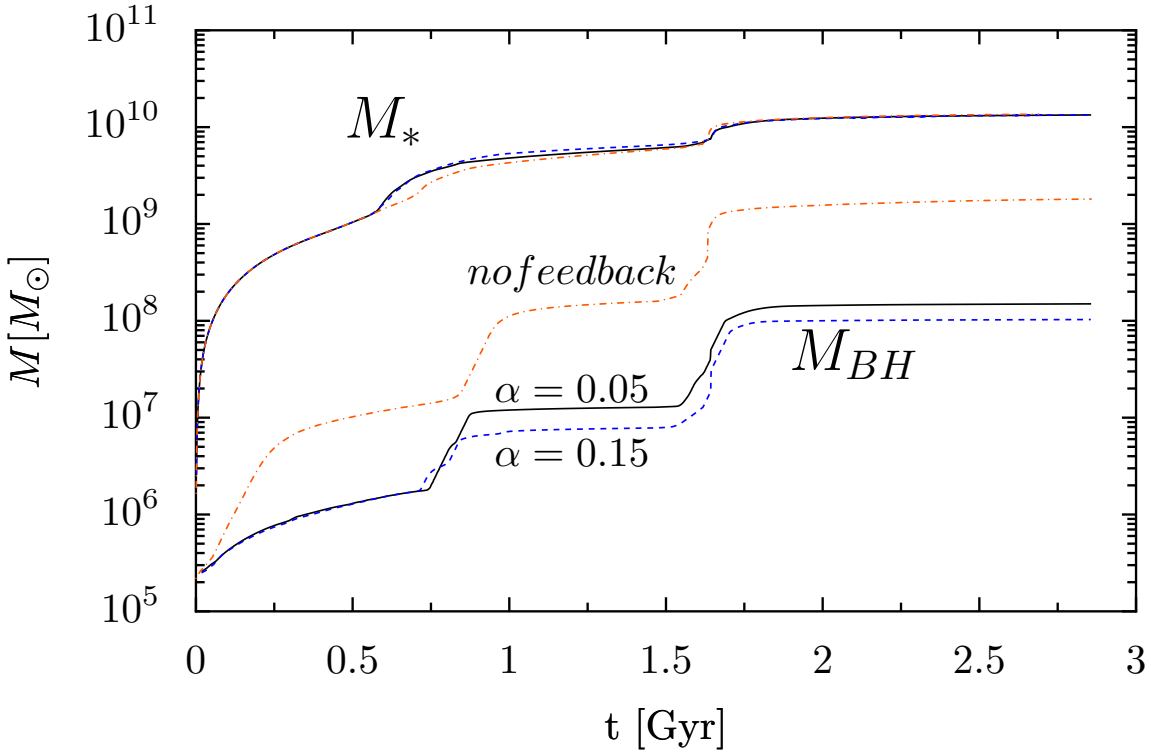

Figure 2.3: The black hole mass M_{BH} (lower three curves) as a function of time during the merger, and the mass of new stars formed during the merger M_*, for three simulations: runs including BH feedback with $\alpha = 0.05$ (black) and $\alpha = 0.15$ (blue, dashed), and the run without BH feedback (orange, dash-dot). Note that BH feedback has little effect on the total stellar mass formed, while it reduces the final BH mass by a factor of ~ 10 compared to the run without feedback. The BH mass is, however, nearly independent of α because the accretion self-regulates as shown in Figure 2.1.

Chapter 3

The Growth of Massive Black Holes in Galaxy Merger Simulations with Feedback by Radiation Pressure

We study the growth of massive black holes (BH) in galaxies using smoothed particle hydrodynamic simulations of major galaxy mergers with new implementations of BH accretion and feedback. The effect of BH accretion on gas in its host galaxy is modeled by depositing momentum at a rate $\sim \tau L/c$ into the ambient gas, where L is the luminosity produced by accretion onto the BH and τ is the wavelength-averaged optical depth of the galactic nucleus to the AGN's radiation (a free parameter of our model). The accretion rate onto the BH is relatively independent of our subgrid accretion model and is instead determined by the BH's dynamical impact on its host galaxy: BH accretion is thus self-regulated rather than "supply limited." We show that the final BH mass and total stellar mass formed during a merger are more robust predictions of the simulations than the time dependence of the star formation rate or BH accretion rate. In particular, the latter depend on the assumed interstellar medium physics, which determines when and where the gas fragments to form star clusters; this in turn affects the fuel available for further star formation and BH growth. Simulations over a factor of ~ 30 in galaxy mass are consistent with the observed $M_{BH} - \sigma$ relation for a mean optical depth of $\tau \sim 25$. This requires that most BH growth occur when the galactic nucleus is optically thick to far-infrared radiation, consistent with the hypothesized connection between ultra-luminous infrared galaxies and quasars. We find tentative evidence for a shallower $M_{BH} - \sigma$ relation in the lowest mass galaxies, $\sigma \lesssim 100\,\mathrm{km\,s^{-1}}$. Our results demonstrate that feedback-regulated BH growth and consistency with the observed $M_{BH} - \sigma$ relation do not require that BH feedback terminate star formation in massive galaxies or unbind large quantities of cold gas.

3.1 Introduction

Feedback from an active galactic nucleus (AGN) has been invoked to resolve a number of observational problems in galaxy formation: (1) to explain the tight observed correlations (Ferrarese and Merritt, 2000, Gebhardt et al., 2000, Häring and Rix, 2004) between central black hole (BH) and galaxy properties, such as the $M_{BH}-\sigma$ and $M_{BH}-M_*$ relations, and the BH "fundamental plane" (Silk and Rees, 1998, King, 2003, Murray et al., 2005, Di Matteo et al., 2005, Sazonov et al., 2005, Hopkins et al., 2007), (2) to shut off star formation in elliptical galaxies (e.g., by blowing gas out of the galaxy), thereby explaining how ellipticals become "red and dead" (e.g., Springel et al. 2005b, Ciotti et al. 2010), (3) to heat the hot intracluster plasma (ICM) in groups and clusters, thereby suppressing cooling and star formation in these environments (e.g., Tabor and Binney 1993, Ciotti and Ostriker 1997, Croton et al. 2006), and (4) to help explain "cosmic downsizing," namely the fact that both star formation and AGN activity reside in progressively lower mass halos at lower redshifts (e.g., Scannapieco et al. 2005).

It is plausible that AGN perform the roles desired of them, but this is by no means certain. Understanding whether this is indeed the case requires developing more sophisticated theoretical models that can be compared quantitatively to observations. There are several key theoretical problems that must be addressed in order to better understand the role of massive BHs in galaxy formation, and to understand the properties of massive BHs themselves. The first is the problem of AGN fueling, i.e., how is gas transferred from galactic scales ($\sim 0.1-1$ kpc) to the vicinity of the massive BH ($\lesssim 0.1$ pc)? A second key problem is the problem of AGN feedback: how do energy and momentum generated by accretion onto a central BH – in the form of radiation and outflows – couple to the surrounding gas, and how does this affect star formation and the growth of the BH itself?

Much of the recent work addressing the impact of BHs on galaxy formation has used qualitatively similar physics (e.g., Springel et al. 2005b, Johansson et al. 2009b). For example, many calculations assume that a BH of mass M_{BH} will accrete mass at a rate proportional to the Bondi rate (Bondi, 1952):

$$\dot{M}_{Bondi} = \frac{4\pi f G^2 M_{BH}^2 \rho}{(c_s^2 + v^2)^{3/2}} \tag{3.1}$$

where ρ is the density of the surrounding gas, c_s is the sound speed of that gas, v is the speed of the black hole through the surrounding medium, and f (typically 100) is a factor taking into account the possible multi-phase structure of the gas and that the sphere of influence of the BH is often not resolved (Booth and Schaye, 2009). There is, however, little justification for using equation 3.1. The Bondi accretion rate estimate assumes that the gas surrounding the BH is spherically symmetric. When the gas is not spherically distributed, the rate of angular momentum transport determines the BH accretion rate (e.g., Shlosman et al. 1990). It is generally believed that the

progenitors of todays $\gtrsim L^*$ ellipticals are gas-rich disk galaxies, the mergers of which lead to luminous starbursts and the growth of the central massive BHs (Sanders et al., 1988, Hopkins et al., 2005). Most of the gas in disk galaxies, merging galaxies, luminous starbursts (Downes and Solomon, 1998, Tacconi et al., 2006), and nearby luminous AGN (Ho et al., 2008) appears to reside in a rotationally supported disk. There is thus no reason to expect that the spherically symmetric Bondi rate provides a good estimate of the BH accretion rate in gas rich galaxies. Even in the central $\sim$ parsec of own galaxy, where the ambient gas *is* hot and pressure supported, the Bondi accretion rate fails by orders of magnitude to predict the accretion rate onto the central BH (Sharma et al., 2007).

There are a number of ways that an AGN can strongly influence its surroundings (e.g., Ostriker et al. 2010). Relativistic jets inject energy into intracluster plasma and may be the primary mechanism suppressing cooling flows in galaxy clusters (McNamara and Nulsen, 2007), even though the details of how the energy in the jet couples to the plasma in a volume filling way are not fully understood (Vernaleo and Reynolds, 2006). On galactic scales, a wind from an accretion disk around the BH can drive gas out of the galaxy (e.g., King 2003) as could cosmic-ray protons produced by a radio loud AGN (Sironi and Socrates, 2010). In addition, the AGN's radiation can strongly affect the surrounding gas, both by Compton heating/cooling (e.g., Sazonov et al. 2005) and by the momentum imparted as UV radiation is absorbed by dust grains (Chang et al., 1987, Sanders et al., 1988, Murray et al., 2005). The presence of hot outflows can increase the ability of the cold gas clouds to absorb momentum from the AGN radiation (Hopkins and Elvis, 2010).

This diversity of feedback mechanisms can be roughly separated into two broad classes: energy and momentum injection. We believe that momentum injection is the dominant mode of feedback for most of the gas in a galaxy, largely because of the very short cooling times of dense gas. For example, if a BH radiates at $\sim 10^{46}$ erg s^{-1} with a typical quasar spectrum, only gas with $n \lesssim 1\,\mathrm{cm}^{-3}$ can be heated to the Compton temperature within ~ 100 pc. However, the mean gas densities in the central $\sim 0.1 - 1\,\mathrm{kpc}$ of luminous star forming galaxies are $\sim 10^{3-5}\mathrm{cm}^{-3}$ (Downes and Solomon, 1998, Tacconi et al., 2006). At these densities, the cooling time of gas is sufficiently short that it is unable to retain much injected energy – be it from the AGN's radiation or from shocks powered by AGN outflows. Thus it is largely the momentum imparted by AGN outflows and by the absorption and scattering of the AGN's radiation that dominates the impact of the AGN on dense gas in galaxies. Since it is the dense gas that fuels star formation and the growth of the BH itself, it is critical to understand the impact of momentum feedback on this gas.[1]

In this paper, we present simulations of major mergers of spiral galaxies using a model for the growth of BHs that includes (1) a BH accretion rate prescription

[1]These conclusions do not apply to dilute plasma in the intracluster or intragroup medium. The densities there are sufficiently low that the plasma can be efficiently heated by an AGN.

motivated by the physics of angular momentum transport and (2) AGN feedback via momentum injection (e.g., radiation pressure). Some results of this model appear in a companion Letter (DeBuhr et al., 2010). The remainder of this paper is organized as follows. Section 3.2 presents a summary of our methods, including a description of the model galaxies (§3.2.1), the model for star formation and the interstellar medium (§3.2.2), our BH accretion and feedback model (§3.2.3) and a summary of our parameter choices (§3.2.4). Section 3.3 shows the results of applying this model to BH growth and star formation in major mergers of gas-rich galaxies. In section 3.4 we show that our model of BH growth and feedback produces a reasonably tight $M_{BH}-\sigma$ correlation similar to that observed. Finally, in section 3.5 we discuss our results and compare our approach to previous models in the literature. Appendix 3.6 presents resolution tests for our fiducial simulation while Appendix 3.7 presents some of the tests used to verify the BH accretion and feedback models that we have implemented.

3.2 Methodology

We use a non-public update of the TreeSPH code GADGET-2 (Springel, 2005) provided by V. Springel to perform simulations of equal-mass mergers of galaxies. This version of the code includes the effective star formation model of Springel and Hernquist (2003) but contains no AGN feedback physics. We modified the code further to implement models for massive BH growth and AGN feedback. The details of the simulations are described in the following subsections. The Appendices present resolution tests and some of the tests we performed to verify our implementation of the BH accretion and feedback model.

3.2.1 Initial Conditions and Galaxy Parameters

Each model galaxy used in our major merger simulations is similar to those in Springel et al. (2005a). They include a spherical halo of collisionless dark matter, a centrifugally supported disk of gas and stars, a stellar bulge, and a central point mass representing a black hole. The code used to generate the initial conditions was provided by V. Springel and is identical to that used in Springel et al. (2005a) except for one change that will be described below.

Table 1 lists the relevant galaxy and simulation parameters for the key merger simulations we focus on in this paper. The simulations are all major mergers of equal mass galaxies. The fiducial simulation (top entry) assumes a mass of $1.94 \times 10^{12} M_{\odot}$ for each merging galaxy, of which 4.1% is assigned to the gas and stars in the disk, 1.36% is assigned to the stars in the bulge, and the rest is in a dark matter halo. The initial mass fraction of gas in the disk is $f_g = 0.1$. This run uses a total of $N_p = 1.6 \times 10^6$ particles with 6×10^5 dark matter particles, 2×10^5 particles each in the gaseous and stellar disk, and 10^5 particles for the stellar bulge. This run has a

Plummer equivalent gravitational force softening of $\epsilon = 47$ pc.

To test the dependence of the results of our fiducial simulation on the model and simulation parameters, we have run a number of additional simulations, varying the gas fraction ($f_g = 0.3$ vs 0.1), bulge-to-disk mass ratio (0.2 vs 0.33), total galaxy mass (from 0.1 to 3 of the fiducial value), simulation particle number (from $N_p = 1.6 \times 10^5$ to 2.4×10^6), force softening ($\epsilon = 22$ to 102 pc), as well as the parameters in the black hole model (described in § 2.4 below).

We use a Hernquist (Hernquist, 1990) density profile for the structure of the dark matter halo:

$$\rho_{halo}(r) = \frac{M_{halo}}{2\pi} \frac{a}{r(r+a)^3}. \tag{3.2}$$

The scale length a of the halo is set by requiring that the halo enclose the same mass within the virial radius as an NFW profile, and that the densities match at small radii. These conditions yield a relationship among the halo scale length, a, the corresponding NFW scale length, r_s, and the concentration of the NFW halo, c (Navarro et al., 1996, Springel et al., 2005a): $a = r_s\{2[\ln(1+c) - c/(1+c)]\}^{1/2}$. The halos used in this work all have a concentration of $c = 9$.

The stellar and gaseous disks both initially have exponential surface density profiles:

$$\Sigma(R) = \frac{M_i}{2\pi R_d^2} \exp\left(-\frac{R}{R_d}\right) \tag{3.3}$$

where M_i is the total mass of the component of interest and R_d is the disk scale length, which is initially the same for the stellar and gaseous disks. The disk scale length for the fiducial simulation is $R_d = 3.5$ kpc, which corresponds to the disk having approximately the same angular momentum per unit mass as a halo with a spin parameter of 0.033. For simulations with different disk masses, we use $R_d \propto M_d^{1/3}$, which is consistent with the observed relation (Shen et al., 2003). The stellar disk's vertical structure is given by the standard $\mathrm{sech}^2(z/z_0)$ profile, where the vertical scale height z_0 is initially set to $z_0 = R_d/5$ at all radii. Unlike the stellar disk, the gaseous disk's vertical structure is determined by hydrostatic equilibrium given the assumed sound speed/equation of state of the gas (discussed below). Setting up this initial vertical hydrostatic equilibrium requires an iterative procedure that is described in Springel et al. (2005a).

The stellar bulges also have Hernquist density profiles. The scale length of the bulge R_b is specified as a fraction of the disk scale length, R_d. In the fiducial simulation, $R_b = R_d/5$. For different bulge masses, we use the scaling relation $R_b \propto M_b^{1/2}$, which is motivated by the observed mass-radius relation of elliptical galaxies (Shen et al., 2003).

In our simulations, two galaxies with identical structure are placed on a prograde orbit. For simulations at our fiducial mass of $1.94 \times 10^{12} M_\odot$ (for each galaxy), the initial separation of the two galaxies' centers is 142.8 kpc. The orbit has approximately zero total energy, which corresponds to an initial velocity for each galaxy of

Table 3.1: Simulation Parameters

Run Name	M_{tot} $[M_{fid}]^a$	$f_{g,0}$	$\frac{M_b}{M_d}$	N_p $[10^6]$	ϵ [pc]	$\frac{R_{acc}}{\epsilon}$	α	τ	$M_{*,new}$ $[10^{10}\mathrm{M}_\odot]$	$M_{BH,f}$ $[10^8\mathrm{M}_\odot]$	$M_{BH,p}$ $[10^8\mathrm{M}_\odot]$	σ_f $[\mathrm{kms}^{-1}]$
fid	1.0	0.1	0.33	1.6	47	4	0.05	10	1.34	1.49	1.33	169
fidNof[b]	1.0	0.1	0.33	1.6	47	4	**0.15**	**0**	1.36	18.1	13.5	170
fid3a	1.0	0.1	0.33	1.6	47	4	**0.15**	10	1.34	1.03	0.90	168
fid6a	1.0	0.1	0.33	1.6	47	4	**0.3**	10	1.35	0.86	0.77	167
fidTau	1.0	0.1	0.33	1.6	47	4	0.05	**3**	1.36	5.05	4.31	163
fidt25	1.0	0.1	0.33	1.6	47	4	0.05	**25**	1.35	0.39	0.35	169
fid8eps	1.0	0.1	0.33	1.6	47	**8**	0.05	10	1.35	2.70	1.76	163
fidafg	1.0	0.1	0.33	1.6	47	4	*[c]	10	1.32	1.21	1.02	169
fidq2[d]	1.0	0.1	0.33	1.6	47	4	0.05	10	1.30	1.40	1.16	168
fidq07[e]	1.0	0.1	0.33	1.6	47	4	0.05	10	1.32	1.52	1.36	164
big	**3.0**	0.1	0.33	1.6	68	4	0.05	10	3.08	6.24	5.27	232
big6a	**3.0**	0.1	0.33	1.6	68	4	**0.3**	10	4.17	7.86	5.15	227
mid	**0.3**	0.1	0.33	1.6	32	4	0.05	10	0.39	0.38	0.26	115
small	**0.1**	0.1	0.33	1.6	22	4	0.05	10	0.13	0.24	0.13	82
small6a	**0.1**	0.1	0.33	1.6	22	4	**0.3**	10	0.13	0.25	0.24	84
smallq07[e]	**0.1**	0.1	0.33	1.6	22	4	0.05	10	0.12	0.06	0.05	81
fg	1.0	**0.3**	0.33	**2.4**	47	4	0.05	10	4.41	7.10	5.53	159
smallfg	**0.1**	**0.3**	0.33	**2.4**	22	4	0.05	10	0.36	0.31	0.23	98
bulge	1.0	0.1	**0.20**	1.6	47	4	0.05	10	1.38	1.44	1.25	161
LRfid	1.0	0.1	0.33	**0.16**	102	4	0.05	10	1.34	1.65	0.93	164
MRfid	1.0	0.1	0.33	**0.48**	70	4	0.05	10	1.35	2.92	2.40	168
MRfidNof[b]	1.0	0.1	0.33	**0.48**	70	4	**0.15**	**0**	1.34	13.5	11.4	167
LRfidNof[b]	1.0	0.1	0.33	**0.16**	102	4	**0.15**	**0**	1.31	13.1	11.4	175
fidvol	1.0	0.1	0.33	1.6	47	**8.62**	0.05	10	1.39	3.22	2.45	164
MRfidvol	1.0	0.1	0.33	**0.48**	70	**5.97**	0.05	10	1.36	3.30	1.92	164

Columns are defined as follows: M_{tot} is the total mass in the simulation, $f_{g,0}$ is the initial gas fraction of the disk, M_b/M_d is the bulge to disk mass ratio, N_p is the total number of particles used in the simulation, ϵ is the Plummer equivalent gravitational force softening, R_{acc}, α and τ are the parameters of the BH accretion and feedback model (§3.2.3), $M_{*,new}$ is the total mass of new stars formed during the simulation, $M_{BH,f}$ and $M_{BH,p}$ are the masses of the BH at the end of the simulation and after the peak of accretion (defined to be when the accretion rate drops to one tenth its maximum value), respectively, and σ_f is the stellar velocity dispersion of the merger remnant (§3.4). Differences from the fiducial simulation are indicated with bold type.

[a] $M_{fid} = 3.88 \times 10^{12}\mathrm{M}_\odot$.

[b] These runs had no AGN feedback.

[c] α was set by the gas fraction within R_{acc} using $\alpha = 3f_g^2$.

[d] The ISM equation of state is defined using $q_{\mathrm{eos}} = 0.2$ (see §3.2.2).

[e] The ISM equation of state is defined using $q_{\mathrm{eos}} = 0.07$ (see §3.2.2).

160 km s^{-1}; the velocity is directed at an angle of 28 degrees from the line connecting the centers of the two galaxies. In order to break the symmetry of the problem, the individual spin axes of the galaxies have a relative angle of about 41 degrees, with one galaxy of the pair having an inclination with respect to the orbital plane of 10 degrees. For the simulations with different overall masses, the orbital parameters are scaled by $M^{1/3}$, so that the time to first passage and the time to final merger are similar to those in the fiducial run.

3.2.2 Interstellar Medium Model

The version of GADGET we use includes Springel and Hernquist (2003)'s sub-resolution model for the interstellar medium (ISM). This model treats the gas as a two phase medium of cold star forming clouds and a hot ISM. When cooling and star formation are rapid compared to the timescale for adiabatic heating and/or cooling (which is nearly always the case in our calculations), the sound speed of the gas is not determined by its true temperature, but rather by an effective sound speed that averages over the multi-phase ISM, turbulence, etc. The effective sound speed as a function of density can be interpolated freely between two extremes using a parameter $q_{\rm eos}$. At one extreme, the gas has an effective sound speed of $10\,{\rm km\,s^{-1}}$, motivated by, e.g., the observed turbulent velocity in atomic gas in nearby spirals; this is the "no-feedback" case with $q_{\rm eos} = 0$. The opposite extreme, $q_{\rm eos} = 1$, represents the "maximal feedback" sub-resolution model of Springel and Hernquist (2003), motivated by the multiphase ISM model of McKee and Ostriker (1977); in this case, 100% of the energy from supernovae is assumed to stir up the ISM. This equation of state is substantially stiffer, with effective sound speeds as high as $\sim 200\,{\rm km\,s^{-1}}$. Varying $q_{\rm eos}$ between these two extremes amounts to varying the effective sound speed of the ISM, with the interpolation

$$c_s = \sqrt{q_{\rm eos}\, c_s^2[q=1] + (1-q_{\rm eos})\, c_s^2[q=0]}\ . \tag{3.4}$$

We do not use the galactic wind feedback of Springel and Hernquist (2003).

In addition to this effective equation of state, GADGET models star formation by stochastically converting gas particles into star particles at a rate determined by the gas density,

$$\dot{\rho}_{SF} = \frac{1-\beta}{t_*^0 \rho_{th}^{1/2}} \rho^{1/2} \rho_c \propto \rho^{3/2} \tag{3.5}$$

where $\beta = 0.1$ is the fraction of the mass of a stellar population returned to the ISM by stellar evolution. The parameter t_*^0 is the characteristic timescale for gas to be converted into stars at the threshold density $\rho_{th} = 0.092$ cm^{-3}; $\rho_c \approx \rho$ is the density of the cold clouds, which is related to the density of the SPH particle by equations (17) and (18) of Springel and Hernquist (2003). For a given gas equation of state, the parameters in equation 3.5 can be adjusted to produce a global star formation law similar to the observed Kennicutt-Schmidt relations (Springel et al., 2005a).

For parameters in the equation of state model that have been used in previous work (Springel et al., 2005a) – $T_{SN} = 4 \times 10^8$ K, $A_0 = 4000$, $t_*^0 = 8.4$ Gyr and $q_{EOS} = 0.5$ – we find that the model overpredicts the sound speed relative to the observed "turbulent" velocities of galaxies, i.e., the non-thermal line widths (see Fig. 1 of Hopkins and Quataert 2010b for a compilation of relevant data). For instance, the above model parameters imply $c_s \sim 30$ km s^{-1} at $n \sim 1$ cm^{-3} and $c_s \sim 110$ km s^{-1} at $n \sim 10^3$ cm^{-3}. These values are too large by a factor of $\sim 2-3$ compared to the random velocities inferred from atomic and molecular line observations (Downes and Solomon, 1998). To account for this, we set $q_{\rm eos} = 0.5$ and then modified GADGET by reducing the pressure everywhere by a factor of 10. This reduces the effective sound speed by a factor of ~ 3 and is thus more consistent with observations. This reduction in ISM pressure is also used in the initial conditions when setting up vertical hydrostatic equilibrium for the gas. Changing the pressure requires changing the equation of state parameters to $T_{SN} = 6.6 \times 10^8$ K, $A_0 = 6600$, and $t_*^0 = 13.86$ Gyr to maintain an average star formation rate of $1\,{\rm M}_\odot$ yr^{-1} for an isolated galaxy with our fiducial Milky Way like mass. In §3.3.3 we compare our fiducial calculations with this reduction in pressure to models with smaller values of $q_{\rm eos}$, 0.07 and 0.2; these also have smaller "sound speeds" more comparable to the observed random velocities of galaxies.

The reduction in the sound speed decreases the Jeans length and mass, making it numerically more prohibitive to resolve these critical scales. For the simulations presented here, we are careful to use sufficient numbers of particles so that the Jeans length and mass are always adequately resolved. The higher gas fraction simulations require a higher particle number as a result (see Table 3.1). The reduction in sound speed also makes it more likely that the gas will fragment by gravitational instability into clumps (ala molecular clouds), as we shall discuss in detail later. This fragmentation is real, not numerical; artificially increasing the sound speed to eliminate it is not necessarily physical and could give incorrect results. On the other hand, we do not include sufficient physics in our ISM model to describe the formation and disruption of molecular clouds so our treatment of the resulting clumping is also not correct. In §3.3.3 we discuss which of our results are the most sensitive to uncertainties related to local gravitational instability in the ISM.

3.2.3 Black Hole Accretion and Feedback

Black Hole Accretion Model

We include a BH as an additional collisionless particle at the center of each galaxy. We model the accretion of the surrounding gas onto the BH, via the transport of angular momentum, using

$$\dot{M}_{visc} = 3\pi\alpha\Sigma\frac{c_s^2}{\Omega} \tag{3.6}$$

where Σ is the mean gas surface density, Ω is the rotational angular frequency, and α is the dimensionless viscosity (a free parameter of our model). We compute Σ and c_s by taking an average of the properties of the SPH particles in a sphere of radius R_{acc} centred on the BH (e.g., $\Sigma = M_g(< R_{acc})/\pi R_{acc}^2$). The radius R_{acc} is typically set equal to four times the gravitational force softening length, i.e., $R_{acc} = 4\epsilon$, although we explore alternate choices as well. We find that estimating the rotation rate using $\Omega^2 \simeq GM(< R_{acc})/R_{acc}^3$ is more numerically robust than actually calculating the rotation and angular momentum of the gas particles within R_{acc}. One important feature of this model is that the region over which the accretion rate is calculated is fixed to be local to the black hole. In previous work (e.g., Springel et al. 2005a), the accretion rate was computed from the nearest N gas particles to the black hole, even if most of those particles were physically rather far away.

Although equation (3.6) is reminiscent of the alpha prescription of Shakura and Sunyaev (1973), in our formulation α characterizes not only the efficiency of angular momentum transport, but also the uncertainty due to the fraction of the inflowing gas that is turning into stars vs. being accreted onto the central BH. The physical mechanisms driving gas from $\sim$ kpc to ~ 0.1 pc are not fully understood, but non-axisymmetric gravitational torques (Shlosman et al., 1989, Hopkins and Quataert, 2010b), turbulence from supernovae (Hobbs et al., 2010), and clumpy stochastic accretion (Levine et al., 2010) may all be important. Using numerical simulations that focus on the nuclei of galaxies (from $\sim 0.1 - 100$ pc) (Hopkins and Quataert, 2010b) simulate the conditions under which there is significant gas inflow to $\lesssim 0.1$ pc. They argue that the net accretion rate is not a strong function of the gas sound speed (unlike *both* eqns 3.1 and 3.6) because non-axisymmetric gravitational perturbations produce orbit crossing and strong shocks in the gas. The resulting inflow rate depends primarily on the non-axisymmetry in the potential, rather than the thermodynamics of the gas. Nonetheless, equation (3.6) evaluated at ~ 100 pc and with $\alpha \sim 0.1$ approximates the accretion rate at small radii in their simulations, albeit with substantial scatter (factor of ~ 10). Given that one of our key results discussed in §3.3 is that the accretion rate is not sensitive to the exact value of α, we believe that equation (3.6) is sufficient for the exploratory calculations in this paper.

Mass of the Black Hole Particle

In our galaxy merger simulations, the two BHs are initially far apart but approach each other in the late stages of the merger. When the BH particles have a separation of less than R_{acc} we consider them to have merged. When this occurs, we sum the individual masses of the two BH particles and set one of the particles to have this mass. This particle is then moved to the center of mass of the two BH system and given the velocity of the center of mass frame. The other BH particle is removed from the region.

The BH particles are subject to stochastic motion due to interaction with the

stellar and gaseous particles, which leads to inaccuracy in the position of the BH and noise in the estimate of the accretion rate. To reduce this numerical "Brownian" motion, the BH particles are given a large "tracer" mass of $2 \times 10^8 M_\odot$ for the fiducial simulation, and scaled with the overall mass for other simulations. As a result, the BH particle is a factor ~ 100 more massive than the halo particles, and a factor $\sim 10^4$ more massive than the stellar and gaseous particles. We artificially increase the BH particle mass solely to reduce numerical relaxation effects. This does not result in spurious dynamical effects on the central stars, gas, and dark matter since the BH's sphere of gravitational influence extends to $\lesssim 10$ pc for the fiducial simulation, which is significantly smaller than our typical force softening of ~ 50 pc.

For the results presented below, the "real" mass of the BH ($\equiv M_{BH}$) is computed by integrating the accretion rate of equation (3.6) in time. The gas particles are not removed as the BH mass increases. Instead, the gas particles have an additional label that tracks whether or not they have been "consumed." We track how much mass the BH should have consumed via accretion at a given time, and the mass of gas that has been consumed. When there is a mis-match, we tag a number of gas particles within R_{acc} (chosen at random) as "consumed" until the total mass accreted by the BH is correct. Particles that have been consumed no longer contribute to the accretion rate estimate, even if they are inside R_{acc}. This implementation prevents any gas particle from providing more than its mass to the integrated mass of the BH.

Feedback from the Black Hole

In our simulations, the AGN is assumed to couple to the surrounding gas by depositing momentum into the gas, directed radially away from the BH. This crudely approximates the effects of (1) strong outflows and/or cosmic-ray pressure produced by the AGN (King, 2003, Sironi and Socrates, 2010) and (2) radiation pressure produced by the absorption and scattering of the AGN's radiation by dust in the ISM (Murray et al., 2005). We focus on the latter when motivating the parameters used in our models.

In reality, the UV radiation from the AGN may well be initially absorbed in the scale of the dusty torus near the central BH (~ 0.01 pc). However, the optical-IR and X-ray radiation, which also carry an appreciable momentum flux, is initially absorbed at larger radii. To accurately account for the impact of the AGN's radiation on gas in its host galaxy would require a radiative transport calculation, which is beyond the scope of the current work. Instead, we model this radiation pressure by depositing a total momentum per unit time of

$$\dot{p} = \tau \frac{L}{c} \quad \text{where } L = min\left(\eta \dot{M}_{visc} c^2, L_{Edd}\right) \tag{3.7}$$

radially away from the BH into the SPH particles within a distance of R_{acc} of the BH particle representing the region over which the IR radiation is absorbed. This

momentum is equally distributed among the particles so that each particle experiences the same acceleration. We use a radiative efficiency of $\eta = 0.1$ in all simulations. The physical picture behind our feedback model in equation (3.7) is that the feedback is produced by the absorption of the ultraviolet light from the AGN by dust in the surrounding gas, and the subsequent reemission of infrared radiation that must diffuse its way out of the nuclear region. As described shortly, the parameter τ is the total infrared optical depth of the nuclear region.

To motivate equation (3.7) in more detail, we note that AGN radiate most of their radiation in the ultraviolet. The opacity of dusty gas to UV radiation is $\kappa_{UV} \sim 10^3$ cm^2 g^{-1}, so that only a surface density of $\sim 10^{-3}$ g cm^{-2} is required to absorb the UV radiation. This is far less than the typical radial column density of gas in the central $\sim 0.1-1$ kpc of luminous star forming galaxies, galaxy mergers, or our simulations (see Fig. 3.2 below). As a result, the UV radiation is efficiently absorbed, except perhaps along polar lines of sight. The absorption and scattering of the UV radiation deposits a momentum per unit time of L/c into the ambient gas, assuming for simplicity that all of the UV radiation is absorbed. If the infrared optical depth is $\gtrsim 1$, the infrared radiation re-emitted by the dusty gas must diffuse out through the nuclear region; doing so deposits an additional momentum per unit time of $\tau L/c$, where $\tau \sim \kappa_{IR}\Sigma$ is the infrared optical depth and $\kappa_{IR} \sim$ few-10 cm^2 g^{-1} is the infrared opacity for the radiation temperatures of interest $\sim 100 - 1000$ K. The net force due to the UV and infrared radiation is thus $\dot{p} \sim (1+\tau)L/c \simeq \tau L/c$, i.e. equation (3.7), for $\tau \gtrsim 1$, which is valid in our calculations near the peak of activity when the BH gains most of its mass.

In our calculations we use a constant value of τ rather than a time variable τ given by $\tau = \kappa_{IR}\Sigma$. Given the simplicity of our feedback model relative to a true radiative transfer calculation, this is not an unreasonable approximation. It is also easier to isolate the effects of varying τ when it is constant in time.

As noted above, we apply the force in equation (3.7) to all particles within a distance R_{acc} of the BH. A more accurate treatment would be to apply the force out to the point where the column is $\sim \kappa_{IR}^{-1}$, i.e., to where the optical depth to infinity is ~ 1. At many times, however, this radius is unresolved. Moreover, it is possible that the photons diffuse primarily along the rotation axis of the gas, rather than in the orbital plane. As a result, the radiation pressure force will be applied primarily at small radii. This is why we apply the force only within R_{acc}. One consequence of this is that the number of SPH particles experiencing the feedback, N, will change as gas moves in and out of R_{acc}. Thus, the strength of feedback felt by an individual particle will change with time. However, because the SPH particles are collisional, they readily share this momentum with neighboring gas particles. In test problems described in Appendix B the effects of our feedback model are essentially independent of N and R_{acc}. The results are not quite so clean in our full simulations (see §3.3.2 and Appendix 3.6), but nonetheless none of our major results depend sensitively on the region over which the feedback force is applied.

One might worry that if the number of particles within R_{acc} were too small, the momentum supplied to a single particle would become large enough to artificially accelerate the particle to the escape velocity. The minimum N required to avoid this is actually quite modest for the range of luminosities in our calculations, and for the simulations presented here this concern is never an issue (although it is for some of the test problems in Appendix B).

3.2.4 Parameter Choices for the Black Hole Model

Our model for BH growth and feedback contains three free parameters: (1) α determines the magnitude of the accretion rate onto the BH; (2) τ determines the total radiation pressure force produced by accretion onto the BH; it is roughly the optical depth to the far IR in the nuclear region; and (3) R_{acc} is the radius of the spherical region within which the accretion rate is determined and the feedback is applied. Our fiducial values for these parameters are $\alpha = 0.05$, $\tau = 10$, and $R_{acc} = 4\,\epsilon$ (where ϵ is the gravitational force softening). We now motivate these particular choices.

The fiducial value of the viscosity used in this work is $\alpha = 0.05$, motivated by the rough consistency between the resulting $\dot{M}$ and Hopkins and Quataert (2010b)'s numerical simulations of gas inflow from $\sim$ 100 pc to $\sim$ 0.1 pc (although there is factor of ~ 10 scatter in the latter that is not captured here). Hopkins and Quataert (2010b)'s calculations in fact require a more complicated subgrid accretion model that depends on additional parameters such as the bulge to disk ratio of the galaxy (because this influences the strength of non-axisymmetric torques); this will be explored in more detail in future work. In addition to $\alpha = 0.05$, we also carried out simulations with $\alpha = 0.15$ and $\alpha = 0.3$, and found no significant differences, for reasons explained below.

We use a constant value (with time) of $\tau = 10$ in most of our simulations. This is motivated by far infrared opacities of $\kappa_{IR} \sim 3 - 10$ cm^2 g^{-1} and surface densities of $\Sigma \sim 1 - 10$ g cm^{-2} within R_{acc} during the peak of activity in our simulations. These surface densities are also consistent with those directly measured in the nuclei of ultraluminous infrared galaxies (Downes and Solomon, 1998). Given the uncertainties associated with the radiative transfer of far infrared photons in galactic nuclei, it is not possible to more accurately estimate the effective value of τ without detailed radiative transfer calculations. As we shall demonstrate explicitly, however, the exact value of τ is also not that critical for the qualitative effects of AGN feedback; the value of τ does, however, strongly affect the final value of the BH mass.

In choosing a value for R_{acc}, we must satisfy $R_{acc} > \epsilon$ in order to avoid numerical artifacts. In addition, we find that the BH particle remains within 4ϵ of the centre of mass of the system at nearly all times, but it can wander around within this region. As a result, 4ϵ is the smallest we can make R_{acc} without having noise induced by the BHs motion. This choice corresponds to several hundred pc in our typical simulation.

Larger values of R_{acc} are unphysical because (1) the accretion rate should only depend on the gas close to the BH; i.e., the transport of gas from, for example, $\sim 8\epsilon$ to $\sim 2\epsilon$ is presumably adequately described by our simulations so we should not try to also account for this in our subgrid model, and (2) the radiation pressure force produced by the AGN (and the re-radiated infrared photons) is likely concentrated at relatively small radii, for the reasons described in §3.2.3.

3.3 Galaxy Merger Simulations

Table 3.1 summarizes the simulations we focus on in this paper, including the resolution, the parameters that specify the initial conditions for the merging galaxies, the parameters that specify the BH accretion and feedback models, and the final properties of the merger remnants (stellar and BH mass and velocity dispersion). We begin by describing the results from our fiducial simulation (top row in Table 3.1) and then discuss simulations that vary a single parameter of the feedback model relative to the fiducial run. We have also performed simulations at different overall galactic mass scales, initial gas fractions, and numerical resolution. The latter resolution tests are presented in Appendix A.

3.3.1 The Fiducial Simulation

The top panel of Fig. 3.1 shows the separation of the BH particles for the fiducial simulation, while the middle panel shows the total star formation rate (in both galaxies) for simulations with (black) and without (red) BH feedback. The first close passage of the two galaxies is around $t = 0.33$ Gyr and the system then undergoes a few short oscillations as the BHs finally settle into a merged state around $t = 1.65$ Gyr. The star formation rate increases following the first passage, with a much larger increase in the star formation rate during the final merger of the galaxies. The bottom panel of Fig. 3.1 shows the BH accretion rate determined from equation 3.6 (black) and the Eddington accretion rate (grey; $\dot{M}_{edd} \equiv L_{edd}/0.1c^2$); the initial BH mass is $1.4 \times 10^5 M_\odot$ but as long as it is not too large $\gtrsim 10^8 M_\odot$, the precise initial BH mass is unimportant for our conclusions. In this and similar plots throughout the paper, the value of $\dot{M}$ plotted before the BHs merge is for the BH in the galaxy with the smaller initial inclination relative to the orbital plane; the BH accretion rate for the other galaxy is comparable to that shown here. The evolution of the accretion rate is similar in many of the simulations we have carried out, with an initial period of activity after the first passage of the merging galaxies, and another period of even higher $\dot{M}$ after the final coalescence of the galaxies and BHs. The latter active episode is when the merged BH gains most of its mass. In particular, the BH reaches the Eddington limit, allowing the mass of the BH to grow exponentially for a few hundred Myr.

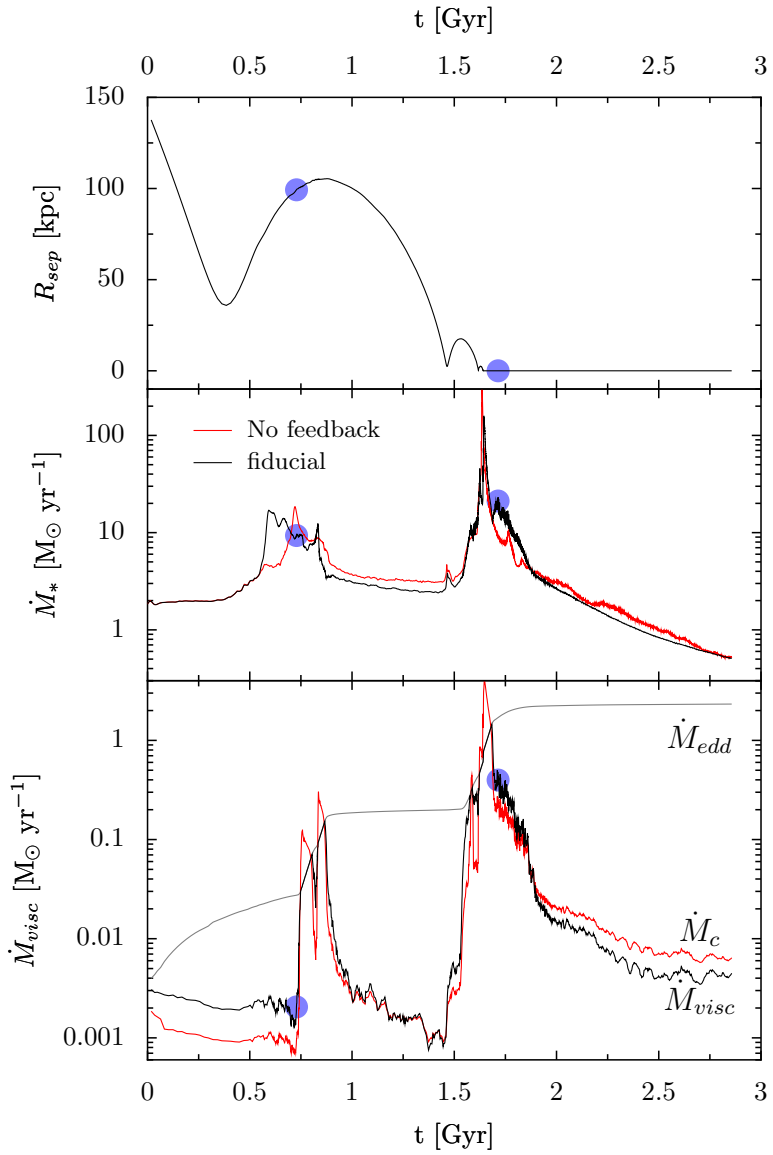

Figure 3.1: *Top:* The separation of the black hole particles as a function of time in the fiducial simulation. The blue circles label the times of the images shown in Figure 3.3. *Middle:* The star formation rate as a function of time for the fiducial simulation (black) and for the run with no feedback (red; run fidNof). *Bottom:* The viscous accretion rate, $\dot{M}_{visc}$ (black), and Eddington rate (grey), as functions of time for the fiducial simulation. The critical $\dot{M}_c$ at which radiation pressure balances gravity (eq. 3.8) is shown within a radius of R_{acc} (red; solid). The increase in star formation and BH accretion after first passage ($t \sim 0.75$ Gyr) is due to the fragmentation and inspiral of large gaseous/stellar clumps (Fig. 3.3), while the much larger increase at final coalescence is due to inflow of diffuse gas caused by non-axisymmetric torques. The latter physics dominates the total stellar and BH mass formed during the merger.

DeBuhr et al. (2010) showed that the BH accretion and feedback model presented in this work leads to self-regulated BH growth, due to a competition between the (inward) gravitational force produced by the galaxy as a whole and the (outward) radiation pressure force produced by the central AGN (eq. 3.7) (Murray et al., 2005). For a spherically symmetric system, equating these two forces leads to $\tau L/c = 4 f_g \sigma^4/G$, where $\sigma^2 = GM_t/2R_{acc}$, M_t is the total mass inside R_{acc}, and we have evaluated these expressions within R_{acc}, where our accretion rate is determined and feedback is implemented. Equivalently, there is a critical accretion rate $\dot{M}_c$, analogous to the Eddington rate, at which the two forces balance:

$$\dot{M}_c = \frac{4 f_g}{\eta \tau G c} \sigma^4. \tag{3.8}$$

The bottom panel of Fig. 3.1 shows $\dot{M}_c$ for our fiducial simulation, evaluated within R_{acc} of the BH (solid red). Comparing $\dot{M}_c$ to the BH accretion rate $\dot{M}_{visc}$ demonstrates that during the peak episodes of accretion $\dot{M}_{visc} \sim \dot{M}_c$, so that radiation pressure becomes dynamically important. Although it is certainly possible to have accretion rates smaller than $\dot{M}_c$ when there is insufficient gas to fuel the AGN, the accretion rate is limited to a maximum value of $\sim \dot{M}_c$.

Fig. 3.2 shows the surface density of gas within $R_{acc} = 4\,\epsilon = 0.19$ kpc for the fiducial simulation and for a higher gas fraction simulation with $f_g = 0.3$. As implied by Fig. 3.1, there are two main epochs during which significant gas is driven into the nuclei of the galaxies: after first passage and at final coalescence. The physical origin of these high nuclear gas densities are, however, somewhat different.

Mihos and Hernquist (1996) showed that the presence of a bulge like that in our simulation suppresses a nuclear starburst after first passage during galaxy mergers, because the bulge inhibits the non-axisymmetric modes that drive inflow. In our fiducial simulation, the majority of the increase in star formation after first passage is due to gravitational instability and fragmentation of the gas, which produces dense regions of rapid star formation. Fig. 3.3 (left panel) shows the gas density in the vicinity of one of the incoming black holes at $t = 0.74$ Gyr, midway through the first peak in star formation; the companion galaxy is well outside of this image. Two knots of dense gas are clearly seen, both of which will soon enter R_{acc}, the BH accretion and feedback region. These two clumps are not the only ones that form after first passage, but they are the only clumps that survive to enter the central region surrounding the BH.[2] Fig. 3.3 (right panel) also shows an image of the gas density in the nuclear region at $t = 1.71$ Gyr, near the peak of star formation and BH accretion and after the galaxies and BHs have coalesced. At this time, the gas density in the nuclear region is significantly higher than at first passage (see also Fig. 3.2) and most of the

[2]In the simulation with a higher initial gas density ($f_g = 0.3$), so many fragments form at large radii and spiral into R_{acc} that the surface density in the central region remains elevated from first passage until the merger completes at $t \sim 1.8$ Gyr (see Fig. 3.2).

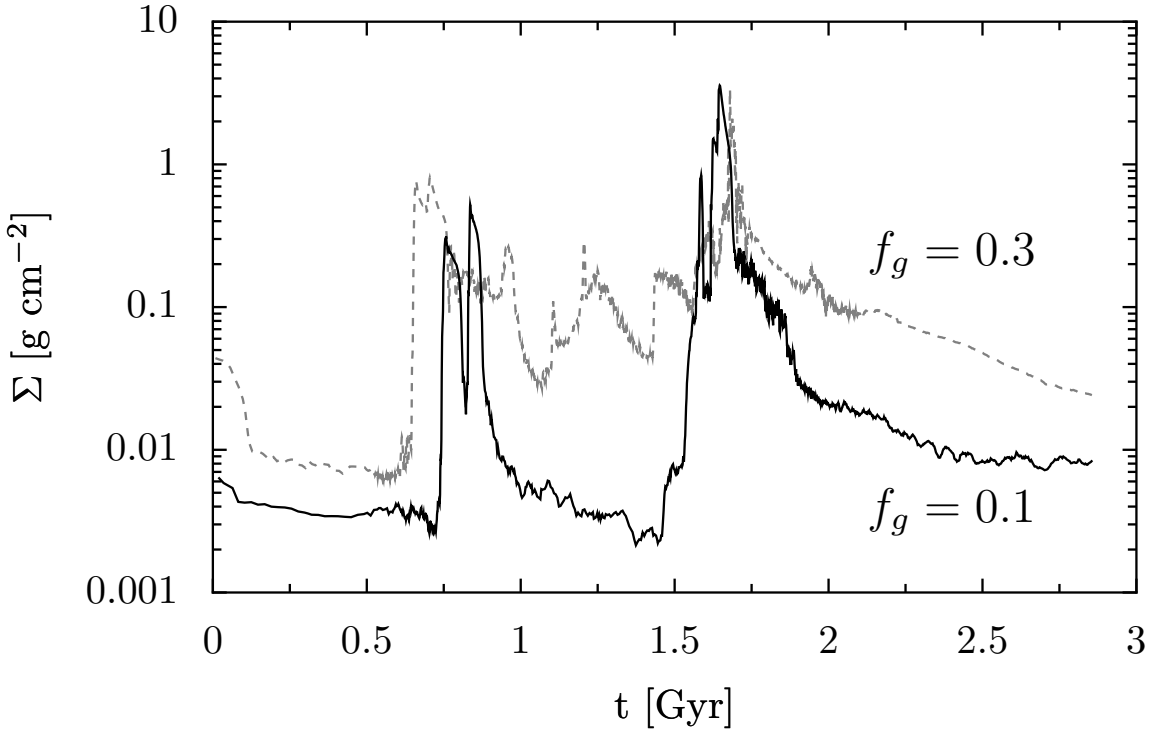

Figure 3.2: The mean gas surface density Σ interior to the accretion radius $R_{acc} = 4\epsilon = 0.19$ kpc for the fiducial simulation with initial gas fraction $f_g = 0.1$ (solid) and for the simulation with $f_g = 0.3$ (dashed; run fg).

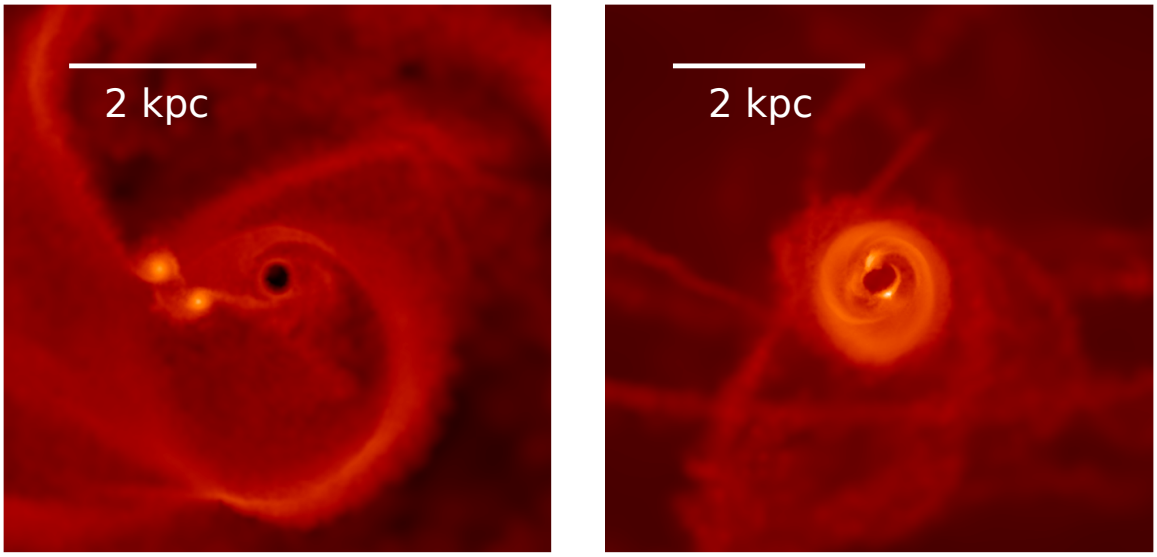

Figure 3.3: Gas density in the vicinity of the BH for the fiducial simulation at $t = 0.73$ Gyr (*left panel*), just prior to the onset of significant BH accretion after the first close passage of the two galaxies, and $t = 1.71$ Gyr (*right panel*), the peak of star formation and BH accretion after the galaxies and BHs have coalesced. The times of these images are labeled with blue circles in Figure 3.1. In the left panel, the image is for the less inclined galaxy and the companion galaxy is well outside the image. The images are 5.7 kpc on a side and brighter color indicates a higher density. The dark region in the center of each image is within R_{acc} of the BH and is evacuated by BH feedback. In the image just after first passage (*left panel*), the two bright white regions are gaseous/stellar clumps that fragmented by Toomre instability during first passage and then spiraled into the nucleus, fueling star formation and BH accretion. At final coalescence (*right panel*), the nuclear gas densities are significantly higher (see also Fig. 3.2) and most of the gas resides in a ~ 1 kpc diameter disk driven into the nucleus by non-axisymmetric stellar torques during the merger. These images were made using SPLASH (Price, 2007).

gas resides in a ~ 1 kpc diameter disk. This nuclear gas concentration is the diffuse ISM driven in from larger radii by non-axisymmetric stellar torques during the merger (e.g., Mihos and Hernquist 1996).

The galaxies in our fiducial simulation are stable when evolved in isolation. The merger itself drives the gas to fragment by locally exceeding the Jeans/Toomre mass. In reality, the gas in such clumps might disperse after $\sim$ a Myr because of stellar feedback not included in our calculations (Murray et al., 2010). This would probably not significantly change our estimate of the star formation rate since we are already normalized to the observed Kennicutt relation; however, such dispersal would lead to little inflow of gas associated with the inspiral of stellar clusters and thus would suppress the first peak in BH accretion (see Hopkins and Quataert 2010b for a more detailed discussion). In §3.3.3 we will return to these issues and show that the total stellar mass and BH mass formed during the merger are relatively insensitive to the details of our assumed ISM model.

Fig. 3.4 shows the surface density of gas in the fiducial simulation (top panel) and for the run without feedback (bottom panel) as a function of distance from the BH at four times: the initial condition ($t = 0$), shortly after the first close passage of the two galaxies ($t = 0.85$ Gyr), near the peak of accretion ($t = 1.71$ Gyr) and at the end of the simulation ($t = 2.85$ Gyr). Once $\dot{M} \sim \dot{M}_c$ at first passage ~ 0.85 Gyr, gas is driven out of the nuclear region by the AGN's radiation pressure. Since at the same time gravitational torques continue to drive gas inwards, the gas begins to pile up at $\sim R_{acc}$. The particular radius at which the pile up occurs of course depends on our choice of R_{acc}, and so the particular size of the evacuated region should not be taken too seriously. Qualitatively, however, the behavior in Fig. 3.4 is reasonable: the AGN pushes on the gas in its neighborhood until it deprives itself of fuel.

Near the peak of activity at $t = 1.71$ Gyr, the gas surface density in the central $R_{acc} \simeq 0.19$ kpc is a factor of $\sim 10 - 30$ larger in the simulations without feedback (bottom panel of Fig. 3.4). However, the gas density at large radii ~ 0.5 kpc is not that different. The radiation pressure force from the BH thus largely affects gas in its immediate environment, rather than the entire gas reservoir of the galaxy. Another indication of this is that the star formation rate is very similar in the simulations with and without feedback (middle panel of Fig. 3.1).

3.3.2 Dependence on Parameters of the BH Model

The models for BH accretion and feedback used here contain uncertain parameters. We have defined the three relevant parameters α, τ, and R_{acc} in §3.2.4 and motivated our fiducial values, but it is important to explore how our results change with variations about our fiducial parameters.

The value of α parameterizes the efficiency with which gas accretes from $\sim R_{acc} \sim$ 190 pc to smaller radii, encapsulating both the efficiency of angular momentum transport and the effects of star formation on unresolved scales. Naively, a higher value of

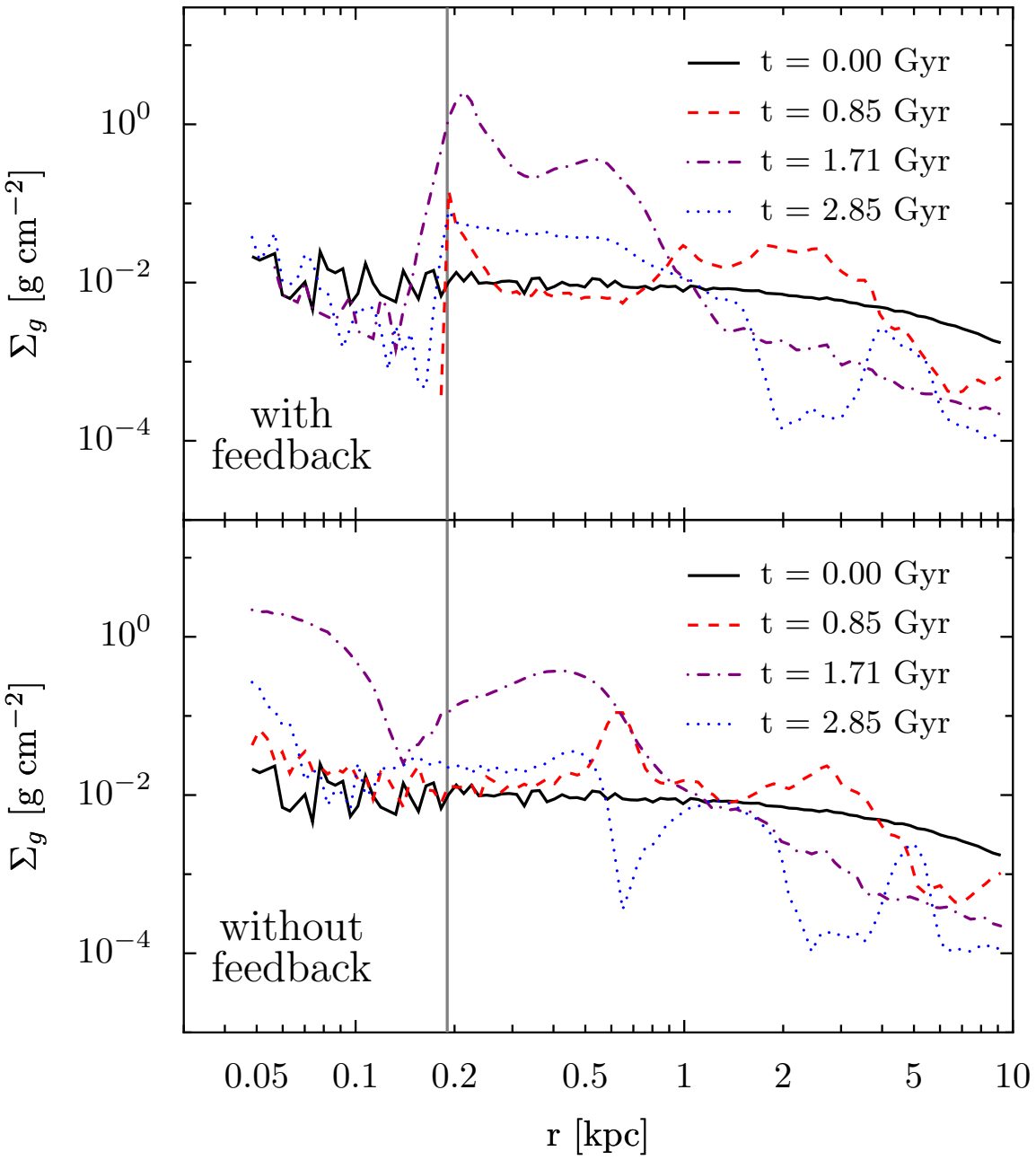

Figure 3.4: Comparison of gas surface density ($\equiv M_g[< r]/\pi r^2$) versus distance from the BH in the fiducial simulation with feedback (top) and without feedback (bottom). Four times are shown: $t = 0$, 0.85 Gyr (first passage), 1.71 Gyr (peak accretion), and 2.85 Gyr (end of simulation). Note that the gas tends to pile up at $R_{acc} = 0.190$ kpc (shown by the vertical line) in the top panel.

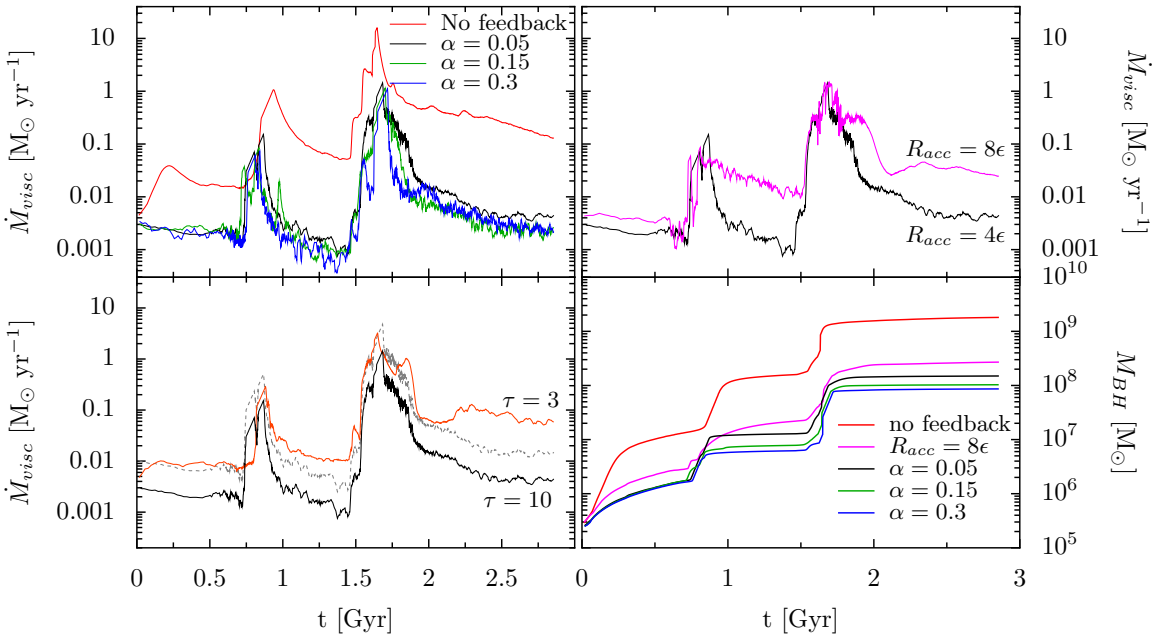

Figure 3.5: *Top Left:* Comparison of the accretion rates for the run without feedback (red; fidNof, $\alpha = 0.15$), and three runs with feedback: the fiducial simulation with $\alpha = 0.05$ (black), the run with $\alpha = 0.15$ (green; fid3a) and the run with $\alpha = 0.3$ (blue; fid6a). *Top Right:* The accretion rate for the fiducial run (black) and the run with $R_{acc} = 8\epsilon$ (magenta; fid8eps). *Bottom Left:* The accretion rate for the fiducial run (black) and the run with $\tau = 3$ (orange; fidTau). Also shown is $\dot{M}_{visc}$ for the fiducial run increased by a factor of 10/3 (dashed line), as expected from eq. (3.8). *Bottom Right:* The integrated black hole masses for all the runs in this Figure with $\tau = 10$.

α would lead to a more massive BH. This is, however, not the case, because during the epochs when the BH gains most of its mass, the accretion rate is set by the efficiency of feedback (eq. 3.8) not by the available mass supply (see Figs 3.1 & 3.4). To demonstrate this more explicitly, the top left panel of Fig. 3.5 compares the BH accretion rates for three simulations with feedback, but differing values of α (0.05, 0.15, and 0.3), to the simulation with no feedback, which has $\alpha = 0.15$. The accretion histories for the three values of α are nearly identical. By contrast, the accretion rate is in general much larger in simulations that neglect feedback (and is $\propto \alpha$). In addition to the constant α runs, we tested a model in which α was time variable, set by the local gas fraction near the BH (fidafg2 in Table 3.1): $\alpha = 3f_g^2$, with f_g determined within R_{acc} (in practice α varied from $\sim 2 \times 10^{-4} - 0.3$). Although this precise functional form is somewhat arbitrary, such a variation is motivated by analytic arguments and numerical simulations which show that instabilities due to self-gravity dominate the transport of gas from ~ 100 pc inward (Shlosman et al., 1990, Hopkins and Quataert, 2010b). For our $\alpha = 3f_g^2$ simulation, we find that the peak accretion rates and final BH mass are very similar to the constant α simulations. This is consistent with our conclusion that in the limit of large fuel supply, feedback, rather than the efficiency of angular momentum transport, sets the rate at which the BH grows.

The parameter τ describes the efficacy of the feedback for a given AGN luminosity. The bottom left panel of Fig. 3.5 compares the BH accretion rate for the fiducial run with $\tau = 10$ (black) and a simulation with a smaller value of $\tau = 3$ (orange). To the extent that the accretion rate is feedback limited and set by $\dot{M}_c$ in equation 3.8, $\dot{M}$ should decrease with increasing τ. Physically, this is because larger τ leads to a larger feedback force, which then requires a smaller accretion rate to provide the luminosity necessary to drive away the surrounding gas. This expectation is borne out by the simulations. To compare the numerical results with the scaling in equation 3.8, the bottom left panel of Fig. 3.5 also shows $\dot{M}$ for the fiducial simulation scaled by a factor of 10/3 (dashed line). This scaled $\dot{M}$ of the fiducial simulation is in reasonably good agreement with the $\tau = 3$ simulation, particularly at the first and second peaks in $\dot{M}$, when most of the BHs mass is accumulated. This demonstrates that the value of τ does not significantly affect any of the qualitative behavior of how the BH grows, although it does determine the overall value of the BH mass.

In the majority of the simulations presented here, the size of the region over which we apply the feedback and average the gas properties to calculate $\dot{M}$, R_{acc}, is set to $4\,\epsilon$. The rationale for this choice was given in §3.2.4, but it is important to consider the effects of changing this value. The top right panel of Fig. 3.5 shows the mass accretion rate for the fiducial simulation and a simulation with $R_{acc} = 8\epsilon = 380$ pc. The peak values of $\dot{M}$ and the time of the first and second peaks are reasonably similar in the two cases. The principle difference is that in the simulations with the larger value of R_{acc}, the feedback is less effective at clearing gas out of the nuclear region (because the force is distributed over a larger number of particles); this allows a higher level of $\dot{M}$ to be maintained after the first passage and final coalescence.

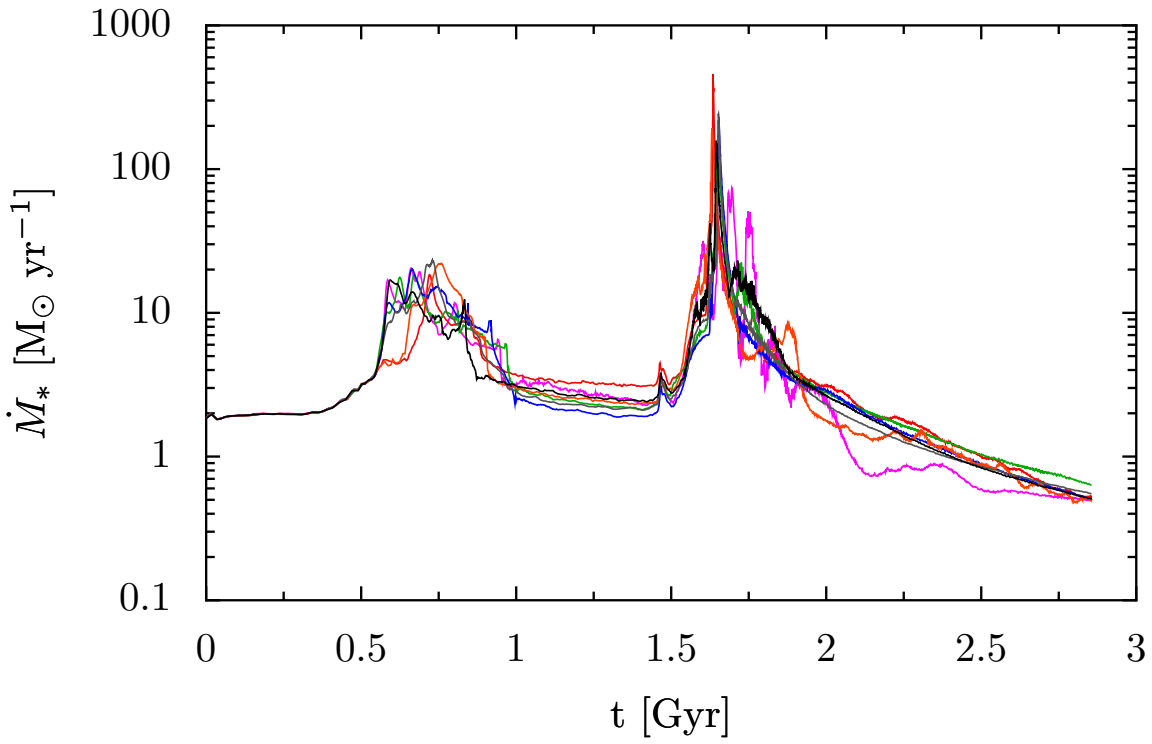

Figure 3.6: The star formation rate for the run with no feedback (red) and for runs with various values of the BH accretion and feedback parameters: $\alpha = 0.05, 0.15, 0.3$ (black, green, blue), $\alpha = 3f_g^2$ (grey), $\tau = 3$ (orange), and $R_{acc} = 8\epsilon$ (magenta). All of these models have very similar star formation histories.

We suspect that the fiducial simulation better approximates what a higher resolution calculation with radiative transfer would find, but this remains to be demonstrated.

The bottom right panel of Fig. 3.5 shows the integrated BH mass as a function of time for the fiducial simulation and for the variations in the feedback/accretion model considered in this subsection that have the same value of τ (but different values of α and/or R_{acc}). The key result is that in the presence of feedback (all but the top curve), there is only a factor of $\simeq 3$ change in the BH mass due to differences in how we treat BH accretion and feedback. A factor of 6 change in α leads to only a 42% change in the final BH mass. This is because most of the BH mass is gained during the final coalescence of the two galaxies, at which point the BH accretion self-regulates and reaches the Eddington-like value in equation (3.8). The run without feedback (top curve), by contrast, has a factor of ~ 10 larger BH mass and the BH mass would scale linearly with the assumed value of α.

The star formation rates for the simulations with different BH feedback parameters are all shown in Fig. 3.6 (this includes the fiducial simulation with and without feedback and the runs with $\alpha = 0.15, 0.3, 3f_g^2$, $\tau = 3$, and $R_{acc} = 8\epsilon$). This figure

demonstrates that the precise parameters of the BH feedback model have little effect on the galaxy-wide properties such as the star formation rate: the total mass of stars formed in simulations with different BH feedback parameters differ by less than 5%.

In previous simulations of BH growth and feedback, AGN feedback acting on dense gas in galaxies has been invoked to quench star formation (Springel et al., 2005b). Our results demonstrate, however, that this is by no means guaranteed (we refer here to 'quasar' feedback on cold dense gas, not the effect of AGN on hot dilute gas in galaxy groups and clusters). In our calculations BH growth is self-regulated and closely connected to the properties of the surrounding galaxy (e.g., eq. 3.8). However, the BHs dynamical influence is centered in the galactic nucleus ($\lesssim 300$ pc); as a result, the BH does not significantly alter the star formation history during a merger. In this scenario, the merger remnant can nonetheless be relatively quiescent ("red and dead") because the burst of star formation uses up much of the available gas.

3.3.3 Effects of the ISM Model

Motivated by observations (e.g., Downes and Solomon 1998), we have reduced the effective sound speed in GADGET's subgrid ISM model (see §3.2.2). There is nonetheless considerable uncertainty in the accuracy of this (or any other) subgrid model. To study in more detail the effects of the ISM model on our results, we performed two additional simulations at our fiducial galaxy mass with the subgrid interpolation parameter $q_{\rm eos} = 0.2$ and 0.07 (see eq. 3.4), and without the factor of 10 reduction in pressure used in our fiducial simulation (an additional simulation with $q_{\rm eos} = 0.07$ at a lower galaxy mass will be discussed in §3.4).[3] The three different ISM models have c_s and Q within a factor of ~ 2 of one another at all radii, with the $q_{\rm eos} = 0.2$ model having the largest values of c_s and Q, and our fiducial model having the smallest values. The parameter Q is initially ~ 3 for our fiducial simulation at the disk scale length R_d, which is why the merger can induce significant fragmentation of the gas (Fig. 3.3). Given the limited physics included in the subgrid model, we do not believe that it is feasible to unambiguously conclude which of these ISM models is more realistic. These models thus provide an indication of the systematic uncertainty introduced by our treatment of the ISM.

Fig. 3.7 compares the BH accretion history (top panel), the star formation rate (middle), and the integrated BH mass and mass of new stars formed during the merger (bottom) for the three runs with differing ISM models. For both the fiducial run and the run with $q_{EOS} = 0.07$ there is significant fragmentation after first passage, which generates the first peak in star formation and BH accretion. By contrast, the run with $q_{EOS} = 0.2$ shows no evidence for gas fragmentation or a pronounced peak in activity at first passage. Despite these differing initial histories, the final result of

[3]We used $T_{SN} = 4 \times 10^8$ K, $A_0 = 4000$ and $t_*^0 = 8.4$ Gyr for these calculations; these values are different from those in our fiducial simulation, and are chosen to fix the total star formation rate for our isolated fiducial galaxy at $1 {\rm M}_\odot$ yr^{-1}.

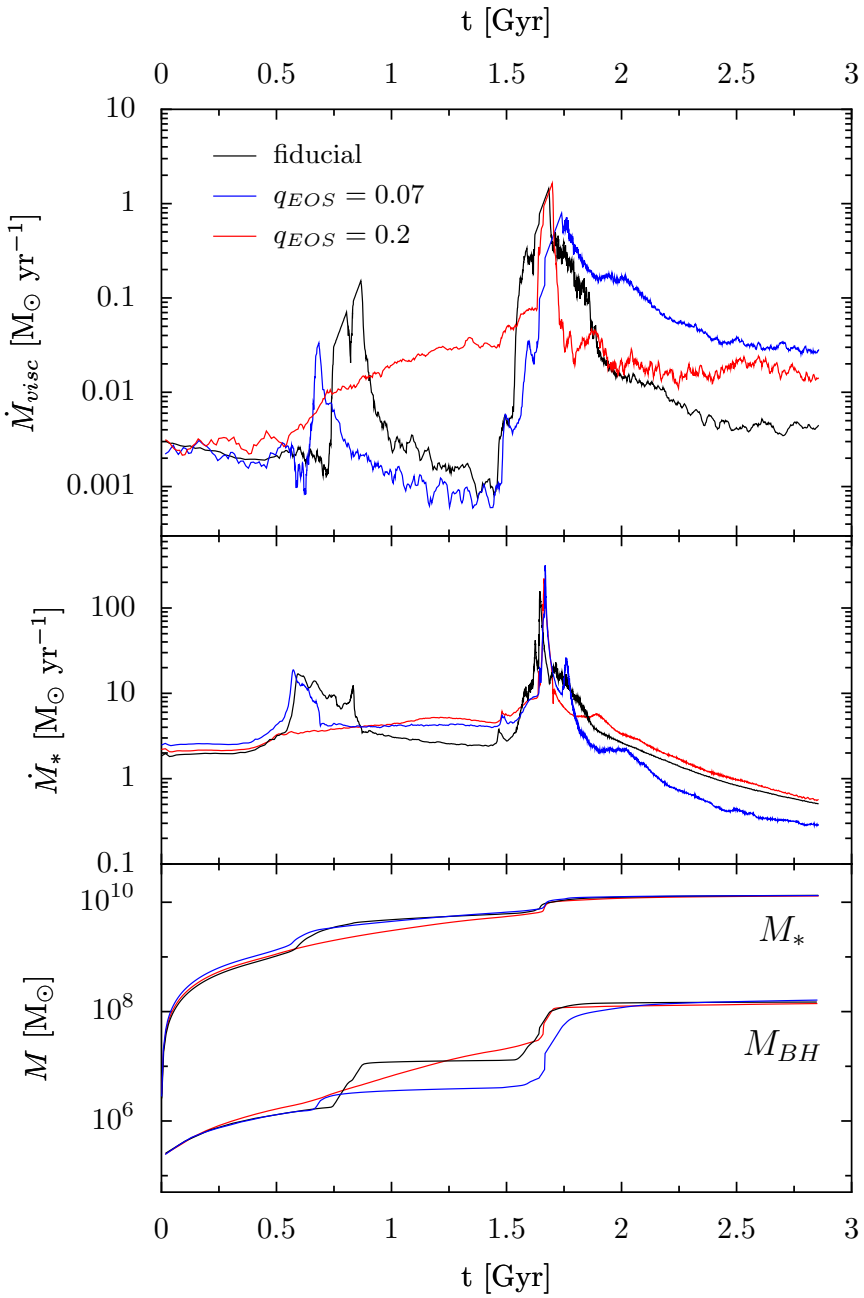

Figure 3.7: Comparison of three simulations that differ only in the ISM models: fiducial (black), $q_{EOS} = 0.2$ (red), and $q_{EOS} = 0.07$ (blue). The panels show the viscous accretion rate (top), star formation rate (middle), and the integrated black hole mass and mass of new stars formed (bottom). The three different ISM models have c_s and Toomre Q within a factor of ~ 2 of one another at all radii; the $q_{\rm eos} = 0.2$ model has the largest values of c_s and Q and our fiducial model has the smallest values.

the merger is very similar in all three cases: the large star formation rates and BH accretion rates coincident with the final coalescence of the two galaxies are not due to fragmentation, but are instead largely due to the inflow of diffuse gas to smaller radii. Moreover, the final BH mass and the total amount of new stars formed during the merger are similar in all three cases. Thus, despite uncertainties in the model of the ISM, we find relatively robust integrated quantities (as did the earlier calculations of Hernquist and Mihos 1995). The precise time dependence of the star formation and BH accretion (i.e., the lightcurves) are, however, significantly more uncertain and sensitive to the details of the model.

3.3.4 Galaxy Parameters

Having shown that the final BH mass and new stellar mass do not depend strongly on the uncertain parameters in our accretion, feedback and ISM models, we now examine how our results vary with galaxy properties such as the total mass, gas fraction, and bulge-to-disk ratio.

Fig. 3.8 shows the BH accretion histories (top panel), star formation rate (middle), and integrated BH mass (bottom) for four runs with different total galaxy mass. The models cover a factor of 30 in galaxy mass, from 0.1-3 times our fiducial mass. The BH and star formation parameters are identical in the four simulations, while the gravitational force softening and structural parameters (e.g., disk scale length, bulge radius) change with the total mass (see §3.2.1).

Fig. 3.8 shows that the BH accretion rates and integrated BH masses increase with galaxy mass as expected from equation 3.8. However, there is a clear difference between the lower and higher mass simulations: the two higher mass simulations show evidence for the first peak in star formation and BH growth that we have shown is due to fragmentation near first passage, while the lower mass runs do not. This is largely a consequence of the fact that observed disks have $R_D \propto M^{1/3}$ (Shen et al., 2003), so that more massive galaxies have higher surface densities and are thus more susceptible to gravitational instability (our ISM model counteracts this slightly, but not enough to stabilize the higher mass disks). It is important to reiterate, however, that modest changes to the subgrid sound speed can change whether or not the gas fragments near first passage (§3.3.3) so it is not clear if the difference as a function of mass in Fig. 3.8 is robust.

In addition to the systematic change in the importance of fragmentation near first passage, Fig. 3.8 also shows differences in the late-time BH accretion between the low and high mass simulations. In particular the two smaller mass runs each show a period of increased accretion after the main peak during the merger. In these cases the new stars formed around final coalescence develop a bar in the inner $\sim R_{acc}$ of the galaxy. This helps drive some of the remaining gas into the accretion region leading to the increased accretion at late times. There is a milder version of this late-time accretion in the fiducial mass $q_{\rm eos} = 0.2$ model without fragmentation in

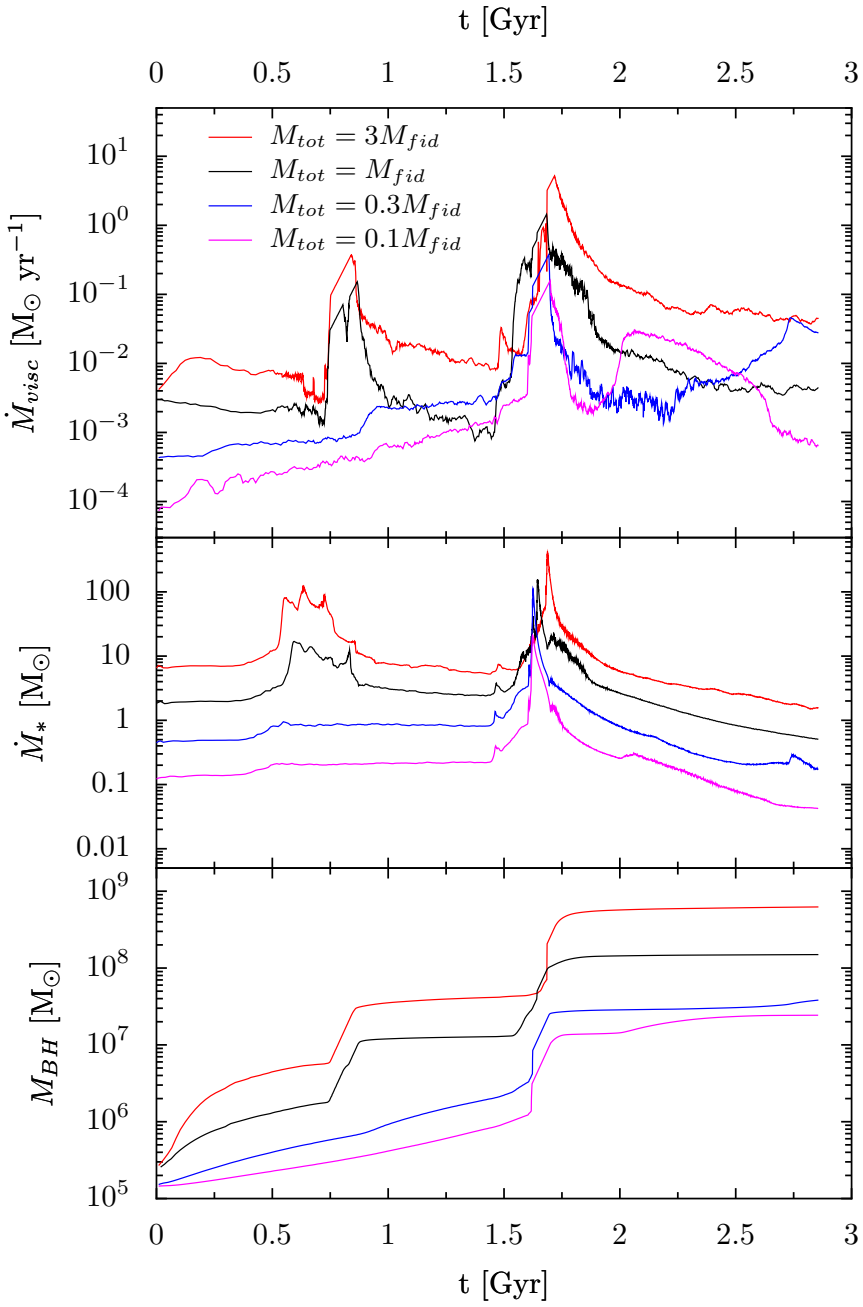

Figure 3.8: Comparison of four simulations that differ only in the total galaxy mass: $M_{fid} = 3.88 \times 10^{12} M_\odot$ (fiducial; black), $3M_{fid}$ (red), $0.3M_{fid}$ (blue), and $0.1M_{fid}$ (magenta). The three panels show the viscous accretion rate (top), star formation rate (middle), and the integrated black hole mass (bottom). The same parameters are used in the BH accretion and feedback models.

Fig. 3.7. Interestingly, there is no analogous late-time inflow of gas to within R_{acc} in our low mass galaxy simulations without BH feedback. The late-time activity is also particularly sensitive to the accretion model at a time when the non-axisymmetry produced by the merger has died away (so that α may in reality decrease significantly). For these reasons, we regard the late time growth in Fig. 3.8 as an interesting deviation from self-similarity in the dynamics, but not necessarily a particularly robust one. One important point that this highlights, however, is that because our implementation of BH growth and feedback does not unbind a significant amount of cold gas at late times (unlike calculations by Springel et al. 2005b), the predictions of our model are more sensitive to the post galaxy coalescence physics.

In addition to the fiducial gas fraction ($f_g = 0.1$) simulations that we have largely focused on, we performed simulations with an initial gas fraction of $f_g = 0.3$ for our fiducial galaxy mass and at one tenth this mass. The qualitative difference in behavior with galaxy mass in Fig. 3.8 persists in the higher gas fraction runs. In particular, in the low mass $f_g = 0.3$ simulation, the gas does not fragment, while it does in the higher mass $f_g = 0.3$ simulation. Fig. 3.2 – discussed in §3.3.1 – explicitly shows the increase in the gas surface density within R_{acc} produced by this at early times.

A final property of the galaxy model that we varied was the bulge to disk mass ratio. The majority of our runs include a bulge with one third the mass of the disk; we also ran one simulation with an initial bulge of one fifth the disk mass, at the fiducial galaxy mass. The final BH mass and total mass of stars formed differ by less than 3% each compared to the fiducial simulation.

3.4 The $M_{BH} - \sigma$ Correlation

Previous numerical studies using models of BH growth and feedback different from those considered here have reproduced a number of the observed correlations between massive BHs and their host galaxies (e.g., Di Matteo et al. 2005, Sazonov et al. 2005, Younger et al. 2008). Younger et al. (2008) argue that the galaxy-BH correlations in simulations (in particular, the BH fundamental plane) are relatively independent of the trigger of BH growth, be it minor mergers, major mergers, or global instabilities of galactic disks. Based on the calculations to date, however, it is unclear to what extent the simulated BH-galaxy correlations depend on the details of the BH feedback or accretion models. In this section we assess this question by quantifying the M_{BH} - σ relation produced in our models.

We define σ of our model galaxies using a method analogous to that of observers: we first project the mass density of the stellar particles into cylindrical bins, and compute the half-mass(light) radius R_e. We then compute the velocity dispersion

weighted by the surface brightness via

$$\sigma^2 = \frac{\int_{R_{min}}^{R_e} \sigma_{los}^2(R) I(R) R dR}{\int_{R_{min}}^{R_e} I(R) R dR} \tag{3.9}$$

where $I(R)$ is the projected 2-d stellar mass profile, σ_{los} is the line of sight velocity dispersion, and $R_{min} = 2\epsilon$ to ensure that there are that no artificial effects introduced by the force softening. We repeat this calculation along 1000 lines of sight with random viewing angles through the center of mass of the merger remnant. The σ quoted in this paper and listed in Table 1 is the median value over the 1000 lines of sight.

Fig. 3.9 shows the correlation between the final BH mass $M_{BH,f}$ and the σ of the merged galaxy for most of the simulations in Table 3.1: different total galaxy masses (black; fid, small, mid, big), different values of the accretion parameter α (red circle; fid3a, fid6a, fidafg, big6a, small6a), alternate ISM models (red x; fidq2, fidq07, smallq07), higher gas fraction (blue square; fg, smallfg), alternate bulge mass (red square; bulge), different values of τ (blue circle; fidTau, fidt25), and the resolution studies in Appendix A (grey; LRfid, MRfid, MRfidvol, fid8eps, fidvol). The solid line indicates the mean relation from the compilation of observational results in Gültekin et al. (2009) while the dotted lines are the $1-\sigma$ error bars. We have linearly rescaled all of our final BH masses to a value of $\tau = 25$, using the fact that both the analytic and numerical results are consistent with $\dot{M}_{visc}$ and $M_{BH,f}$ being $\propto \tau^{-1}$. The value of $\tau = 25$ is chosen so that the rescaled fiducial simulation lies approximately on the $M_{BH} - \sigma$ relation of Gültekin et al. (2009). For our fiducial simulation carried out with $\tau = 3$ and $\tau = 10$, a linear scaling of $M_{BH,f}$ with τ^{-1} is accurate to about 2% (e.g., Table 3.1 and Fig. 3.5). We also carried out our fiducial simulation with $\tau = 25$; this is consistent with a linear scaling of $M_{BH,f}$ from $\tau = 3$ to $\sim 50\%$ (Table 3.1). For nearly all of our simulations, rescaling to $\tau = 25$ amounts to dividing the final BH mass by a factor of 2.5.

Previous analytic arguments were able to reproduce the $M_{BH} - \sigma$ relation with $\tau \sim 1$, rather than requiring $\tau \sim 25$ as we do here (e.g., King 2003, Murray et al. 2005). These calculations, however, assumed $f_g = 0.1$. While perhaps appropriate on average, this is not appropriate in galactic nuclei where the gas densities are higher. The analytic derivations also assumed that BH growth terminated when the system reached the luminosity (accretion rate) at which radiation pressure balances gravity (eq. 3.8). In reality, however, the luminosity must exceed this critical value by a factor of several in order for gas to be efficiently pushed around in the galactic nucleus (as shown explicitly in the test problems in the Appendix). Moreover, the BH continues to accrete some mass even after reaching $\dot{M}_c$. Fig. 3.10 shows this explicitly via the ratio of the final BH mass to the BH mass at the peak of activity for all of the simulations in Fig. 3.9.[4] The net effect of the differences between our simulations and

[4]To account for the fluctuating nature of the BH accretion rate in some of the simulations, we

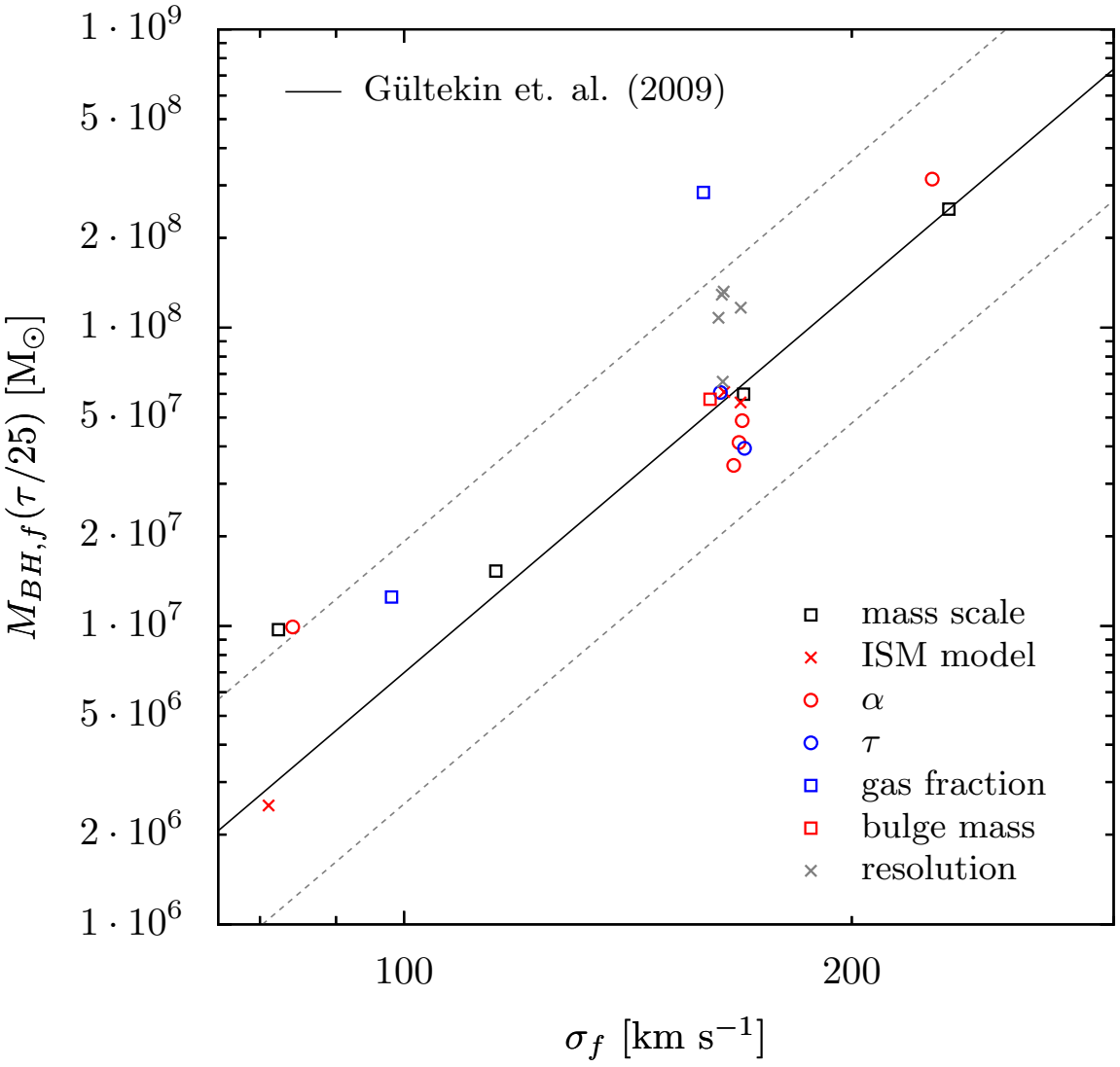

Figure 3.9: The $M_{BH,f}$-σ relation for the simulations in this paper, along with the observed relation (solid) and one sigma scatter (dotted) from Gültekin et al. (2009). The final BH mass $M_{BH,f}$ in all of the simulations has been linearly scaled to $\tau = 25$ from the value used in the simulation (typically $\tau = 10$). The simulations are generally quite consistent with observations; we do find indications of a slight flattening in $M_{BH,f} - \sigma$ at low BH masses.

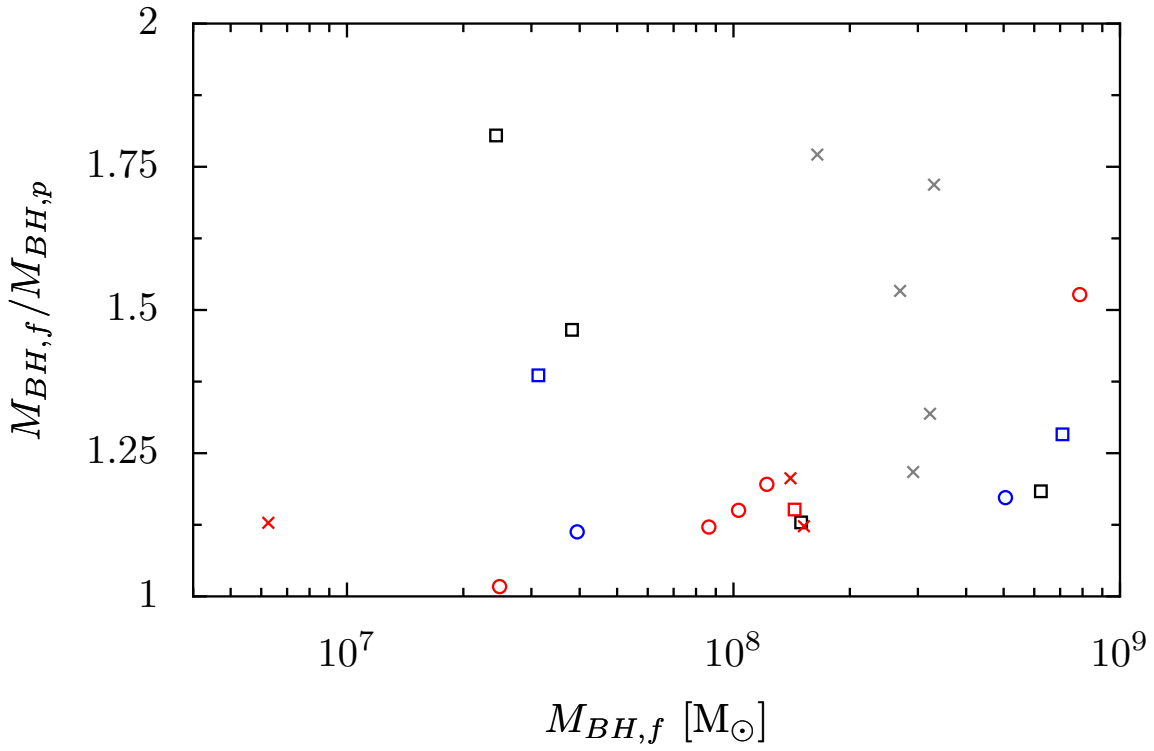

Figure 3.10: The ratio of the final BH mass to the BH mass at the peak of accretion for the simulations in Fig. 3.9, using the same symbol types. This quantifies the extent to which late-time accretion increases the BH mass. The late-time increase in BH mass for many of the lower mass systems produces the slight flattening in $M_{BH} - \sigma$ in Fig. 3.9 at low masses; see the text for a discussion of the robustness of this result.

the simple analytic calculations is that a much larger feedback force per unit BH mass ($\tau \sim 25$, not ~ 1) is required for consistency with the observed $M_{BH} - \sigma$ relation. The physical implications of this larger value of τ for models of AGN feedback will be discussed in § 3.5.

The scatter in BH mass in Fig. 3.9 at our fiducial mass scale of $\sigma \sim 175\,\mathrm{km\,s^{-1}}$ is reasonably consistent with the observed scatter. In the simulations we have varied the BH accretion model (α), the ISM model, numerical resolution, size of the feedback/accretion region R_{acc}, and galaxy properties such as the total mass, gas fraction, and bulge to disk ratio. It is encouraging that all of these simulations produce BH masses within a factor of few of each other. The largest BH mass at $\sigma \sim 175\,\mathrm{km\,s^{-1}}$ is the simulation with an initial gas fraction of $f_g = 0.3$; since this run has a larger gas density at small radii close to the BH (Fig. 3.2), it should probably also have a larger τ, which would reduce the BH mass further, in better agreement with the data. It is difficult to make this comparison to the observed scatter more quantitative given the limitation that our simulations are all equal-mass non-cosmological binary mergers on the same orbit.

The numerical results in Fig. 3.9 suggest a slight flattening of the $M_{BH} - \sigma$ relation at $\sigma \lesssim 100\,\mathrm{km\,s^{-1}}$. This is in large part a consequence of the additional mass gained by the lower mass BHs after their peak of activity (see Figs. 3.8 & 3.10, in particular the fiducial simulations labeled by black squares in Fig. 3.10). This change in behavior at lower masses is primarily due to the fact that the lower mass galaxies are less prone to fragmentation than the more massive galaxies (§3.3.4). Without the fragmentation after first passage, more gas is available to feed the BH at late times leading to the slightly higher BH mass. As discussed in §3.3.4, it is unclear how robust this late time accretion is. In fact, a low mass galaxy simulation with an alternate ISM model ($q_{\rm eos} = 0.07$) does not show significant late-time accretion, leading to a BH mass in good agreement with the extrapolation from higher σ (red x at low mass in Figs. 3.9 & 3.10). We thus regard the case for flattening of $M_{BH} - \sigma$ at low masses in our models as somewhat tentative; our results may instead indicate enhanced scatter at low masses rather than a change in the mean relation. More comprehensive numerical studies of these lower mass systems will be needed to distinguish these two possibilities.

In addition to the $M_{BH} - \sigma$ correlation, the masses of supermassive black holes scale with the stellar mass of their host spheroid (Magorrian et al., 1998). The simulations presented here also produce such a correlation, with a similar slope but offset to smaller black hole masses by a factor of ~ 4. The source of this discrepency is in part related to the fact that the merger remnants do not satisfy the size-mass relation of Shen et al. (2003): the slope of our relation is too shallow. A similar effect was seen in Robertson et al. (2006) for low gas fraction ($\lesssim 0.3$) mergers. By changing the parameters of the galaxy mergers to values appropriate for higher redshift mergers, in particular the gas fraction as a function of galaxy mass, they were able to reproduce

define the BH mass at "peak" to be the mass when $\dot{M}$ drops by a factor of 10 from its peak value.

the Faber-Jackson relation, the size-mass relation, and the fundamental plane of elliptical.

Our simulations generally produce remnants that are too large relative to observations (becasue the gas fraction is small and thus there is not enough stellar mass formed at small radii in the starburst). As a result, the effective σ is small. Because the BH growth is self-regulating and determined by the potential of the galaxy, this leads to black holes that are below the observed $M_{BH} - M_*$ relation. With merger parameters more like those in Robertson et al. (2006), we would end up with physically smaller galaxies (for a given mass) and thus larger values of σ. Because the BH growth is self-regulating, the increase in σ would lead to an increase in M_{BH} along the mean relation in Fig. 3.9.

3.5 Discussion and Conclusions

We have presented a new method for simulating the growth of massive BHs in galaxies and the impact of AGN activity on gas in its host galaxy (see also our related Letter; DeBuhr et al. 2010). In this method, we use a local viscous estimate to determine the accretion rate onto a BH given conditions in the surrounding galaxy (eq. 3.6), and we model the effect of BH feedback on ambient gas by depositing momentum radially away from the BH into the surrounding gas (eq. 3.7).

Our accretion model qualitatively takes into account the angular momentum redistribution required for accretion of cold gas in galaxies and is thus more appropriate than the spherical accretion estimate that has been used extensively in the literature. In our feedback model, the applied force is given by $\tau L/c$, where the AGN's luminosity L is determined by our BH accretion model, and the net efficiency of the feedback is determined by the total optical depth τ of the galactic gas to the AGN's radiation, which is a free parameter of our model. Previous calculations have demonstrated that only when the gas fraction in a galaxy decreases to $\lesssim 0.01$ can the AGN's radiation Compton heat matter to high temperatures (Sazonov et al., 2005). More generally, the cooling times in gas-rich galaxies are so short that the primary dynamical impact of the AGN on surrounding gas is via the momentum imparted by the AGN's outflows or radiation. It is thus not physically well-motivated to model AGN feedback by depositing energy, but not momentum, into surrounding gas, as many calculations have done (e.g., Di Matteo et al. 2005, Springel et al. 2005b, Kawata and Gibson 2005); see Ostriker et al. 2010 for related points.

Throughout this paper, we have focused on BH growth during major mergers of spiral galaxies. As demonstrated in DeBuhr et al. (2010), our model leads to a self-regulated mode of BH accretion in which the BH accretion rate is relatively independent of the details of the BH accretion model (see Fig. 3.5). This is because the accretion rate self-adjusts so that the radiation pressure force is comparable to the inward gravitational force produced by the host galaxy (see eq. 3.8). This self-

regulated mode of BH accretion is a robust feature of all of our simulations during periods of time when there is a significant nuclear gas reservoir – it thus applies precisely when the BH gains most of its mass.

One important consequence of this self-regulated accretion is that AGN feedback does not drive significant large-scale outflows of gas (in contrast to the models of Springel et al. 2005b). For example, the surface density profiles in Fig. 3.4 show that AGN feedback causes gas to pile up at a few hundred pc rather than being completely unbound from the galaxy – this precise radius should not be taken too literally since it is a direct consequence of the fact that we implement feedback and determine the BH accretion rate only within a radius $R_{acc} \sim$ few hundred pc. Nonetheless, we believe that this general result may well be generic: because the BH accretion rate is determined by the gas content close to the BH, the AGN can shut off its own accretion before depositing sufficient energy to unbind all of the gas in the galaxy. If we artificially hold the luminosity of the AGN constant in time at a value exceeding the critical value in equation (3.8), then the AGN *does* eventually unbind all of the surrounding gas (see, e.g., Figs. 3.12 & 3.14 in Appendix B). However, both our isothermal sphere test problem (Fig. 3.17) and our full merger calculations show that when the BH accretion rate is self-consistently determined by the gas properties in the central ~ 100 pc of the galaxy, the AGN simply never stays 'on' long enough to unbind all the gas.

Our results do not, of course, preclude that AGN drive galactic winds. For example, some gas may be unbound by a high speed wind/jet produced by the central accretion disk (which is not in our simulations). In addition, at later stages of a merger or at large radii the gas fraction can be sufficiently low ($\lesssim 0.01$) that gas can be Compton heated to high temperatures and potentially unbound (e.g., Ciotti et al. 2010). This may in fact be sufficient to quench star formation at late times, but only once most of the gas has already been consumed into stars (so that $f_g \lesssim 0.01$). Our results do suggest that AGN feedback does not quench star formation by unbinding a significant fraction of the cold dense gas in a galaxies interstellar medium (in contrast to, e.g., Springel et al. 2005b). In future work it will be important to assess whether variability in the accretion rate on smaller scales than we can resolve (e.g., Hopkins and Quataert 2010b, Levine et al. 2010) modifies this conclusion; such variability could produce some epochs during which AGN feedback has a significantly larger effect on the surrounding gas. Another improvement would be to carry out radiative transfer calculations and assess what fraction of the AGN's radiation is absorbed at large radii in a galaxy ($\sim$ kpc) where the gas has a lower surface density and is thus easier to unbind.

Our simulations cover a factor of ~ 30 in galaxy mass. The final BH mass in our calculations is $\propto \tau^{-1}$ since a larger value of τ corresponds to a larger momentum deposition per unit BH mass. We find reasonable consistency with the normalization of the observed $M_{BH} - \sigma$ relation for $\tau \sim 25$. To compare this result to previous work by Di Matteo et al. (2005), we note that a momentum deposition of $\dot{P}$ corresponds

to an energy deposition rate of $\dot{E} \simeq \dot{P}\sigma$ when the feedback is able to move the gas at a speed comparable to the velocity dispersion σ (which is required for efficient self-regulation of the BH growth). For $\tau \simeq 25$, our results thus correspond to $\dot{E} \simeq 25\,L\,\sigma/c \simeq 0.02\,L\,(\sigma/200\,\mathrm{km\,s^{-1}})$. This is similar to the results of Di Matteo et al. (2005), who found that depositing $\sim 5\%$ of the BH accretion energy in the surrounding gas was required to explain the $M_{BH} - \sigma$ relation. It is encouraging that these two different sets of simulations, with different BH accretion and feedback models, agree at the factor of $\sim 2-3$ level on the energetics required to reproduce the $M_{BH} - \sigma$ relation.

The value of $\tau \sim 25$ required to explain the normalization of the $M_{BH} - \sigma$ relation has strong implications for the dominant physics regulating BH growth. The simplest models of super-Eddington winds from an accretion disk close to the BH are ruled out because they typically have $\tau \sim 1$, i.e., a momentum flux comparable to that of the initial radiation field (King, 2003). Note, however, that observations of broad absorption line quasar outflows suggest values of $\tau \sim 5-10$ in several cases (Moe et al., 2009, Dunn et al., 2010), thought it is unclear how generic these results are. The radiation pressure force produced solely by the scattering and absorption of the AGN's UV radiation by dust corresponds to $\tau \sim 1$ (Murray et al., 2005) and is thus not sufficient to account for the level of feedback required here. Rather, our results suggest that most BH growth happens when the nuclear regions are optically thick to the re-radiated dust emission in the near and far-infrared, so that $\tau \gg 1$. This is consistent with observational evidence in favor of a connection between BH growth, quasars and luminous dust-enshrouded starbursts such as ULIRGs and sub-mm galaxies (e.g., Sanders et al. 1988, Dasyra et al. 2006, Alexander et al. 2008). Quantitatively, the observed *stellar* densities at radii $\sim 1-100$ pc in elliptical galaxies reach ~ 20 g cm^{-2} (Hopkins et al., 2010), implying $\tau \sim 100$ if a significant fraction of the stars were formed in a single gas-rich epoch. It is encouraging that this is within an order of magnitude of (and larger than!) the value of τ we find is required to explain the observed $M_{\rm BH} - \sigma$ relation.

A fixed value of $\tau \sim 25$ independent of galaxy mass produces an $M_{BH} - \sigma$ relation with a slope and scatter in reasonable agreement with observations (see Fig. 3.9). Assessing the scatter more quantitatively will require a wider survey of merger orbits. We do find some tentative evidence for a shallower slope in the $M_{BH} - \sigma$ relation at the lowest galaxy masses, corresponding to $\sigma \lesssim 100\,\mathrm{km\,s^{-1}}$. This range of masses is precisely where the observational situation is particularly unclear, with, e.g., possible differences between the BH-galaxy correlations in classical bulges and pseudo-bulges (Graham, 2008, Hu, 2008, Greene et al., 2008). It is also unclear whether major mergers are the dominant mechanism for BH growth in these lower mass galaxies (e.g., Younger et al. 2008).

Our simulations show that fragmentation of a galactic disk into clumps can be efficiently *induced* by a merger (e.g., Fig. 3.3), even when an isolated galaxy with same properties is Toomre stable (see, e.g., Wetzstein et al. 2007 for related ideas

in the context of dwarf galaxy formation in tidal tails). As Figure 3.7 demonstrates, this fragmentation can produce a significant increase in star formation during the first close passage of galaxies even when there is little inflow of the diffuse ISM (because such inflow is suppressed by a bulge until later in the merger; Mihos and Hernquist 1996). In our simulations we often see a corresponding increase in the BH accretion rate due to the inspiral of dense gas-rich clumps (Fig. 3.3). The inflow of gas by this process may, however, be overestimated: stellar feedback not included in our simulations can unbind the gas in star clusters on a timescale of $\sim$ a Myr, returning most of the gas to the diffuse ISM (e.g., Murray et al. 2010, Hopkins and Quataert 2010b).

Another feedback process that was not included in these simulations was galactic winds. Including this would would reduce the available gas supply at small radii. Our results demonstrate, however, that over a wide range of values of the angular momentum transport efficiency α, the BH accretion rate is nearly independent of α (Fig. 3.5). The self-regulated BH accretion rate (eq. 3.8) is linearly proportional to the gas fraction in the nuclear region. Thus a lower gas fraction due to galactic winds might require a somewhat smaller value of τ for consistency with the $M_{BH} - \sigma$ relation.

Our calculations use subgrid sound speeds motivated by the observed turbulent velocities in galaxies (§3.2.2). We thus believe that our ISM model is physically well-motivated, even though the use of a subgrid sound speed necessarily introduces some uncertainty. Overall, the presence/absence of large-scale clumping of the ISM does not significantly change the final BH mass or the mass of new stars formed in our simulations. It can, however, change the star formation rate and BH accretion rate as a function of time, particularly near the first close passage during a merger.

The tentative change in the $M_{BH} - \sigma$ relation we find for lower mass galaxies is largely due to our treatment of the ISM, rather than our BH feedback or accretion model. For a given gas fraction, lower mass galaxies have a lower gas surface density and thus the ISM is less prone to fragmentation (§3.3.4 and Fig. 3.8). Without the fragmentation after first passage, more gas is available to feed the BH at late times leading to somewhat higher BH mass (Fig. 3.10).

The BH accretion and feedback models used in this paper can be significantly improved in future work, allowing a more detailed comparison to observations. For example, Hopkins and Quataert (2010b) carried out a large number of simulations of gas inflow in galactic nuclei from ~ 100 pc to $\lesssim 0.1$ pc (see, e.g., Levine et al. 2010 for related work). These can be used to provide a more accurate estimate of the BH accretion rate given conditions at larger radii in a galaxy (Hopkins and Quataert, 2010a). Another important improvement would be to use a radiative transfer calculation to self-consistently determine the infrared radiation field produced by a central AGN (and distributed star formation). This could then be used to calculate the radiation pressure force on surrounding gas, eliminating the need for our parameterization of the force in terms of the optical depth τ.

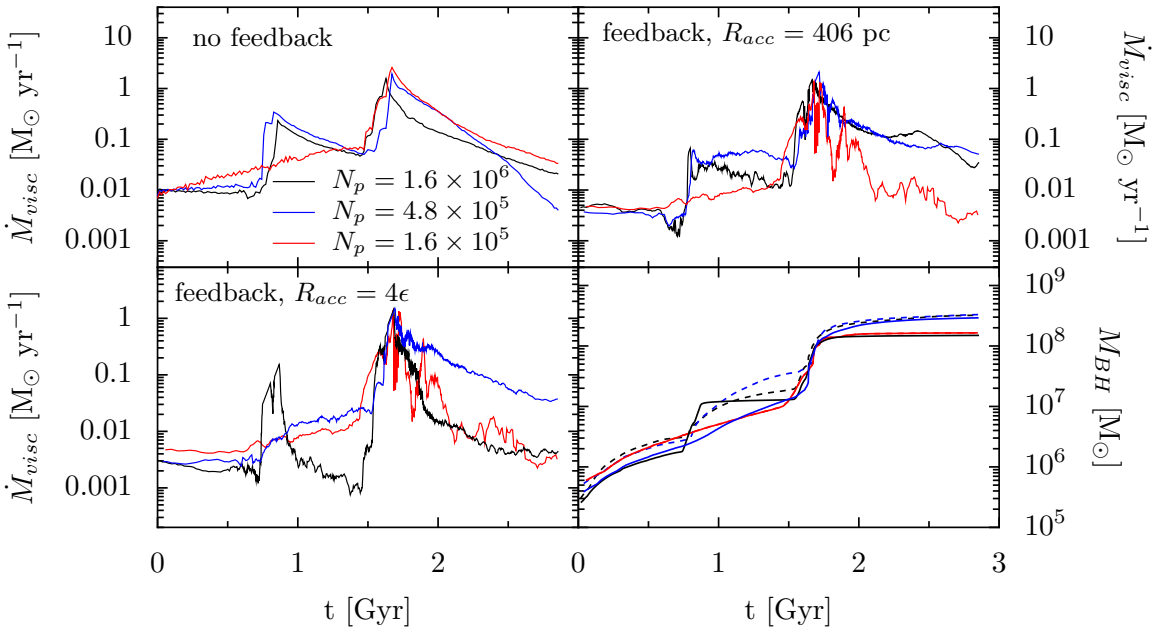

Figure 3.11: *Top left:* BH accretion rate for simulations without feedback at three resolutions (LRfidNof, MRfidNof, fidNof in red, blue and black respectively); $\dot{M}_{visc}$ was computed for $\alpha = 0.05$ and using the same value of $R_{acc} = 406$ pc at all three resolutions (this corresponds to 4ϵ for the lowest resolution). *Top right:* BH accretion rate with feedback at the same three resolutions using $R_{acc} = 406$ pc. *Bottom left:* BH accretion rate with feedback at the same three resolutions using $R_{acc} = 4\epsilon$; here the accretion rate and feedback are calculated in different physical volumes at different resolutions. *Bottom right:* BH masses for all of the runs in this Figure with feedback. Solid lines are for $R_{acc} = 4\epsilon$ while dashed lines are for $R_{acc} = 406$ pc.

3.6 Resolution Studies

In this section, we describe some of our resolution tests both with and without BH feedback. In the absence of feedback, the well-posed questions for resolution studies include both how the gas properties as a function of radius and time depend on the resolution and how integrated properties of the galaxy (e.g., the star formation rate) depend on resolution. However, the feedback, when present, has a nontrivial dependence on the resolution and it is by no means clear that the nonlinear system will in fact converge in a simple way with increasing resolution. Physically, e.g., the AGN's radiation pressure has the strongest effect on the gas that contributes the most to the optical depth, which is largely determined by the column density (the dust opacity being only a relatively weak function of temperature for the conditions of interest). Higher resolution simulations can resolve higher volume and column densities, largely at smaller radii close to the BH, and thus may change some of the

details of the BH feedback. Indeed, Fig. 3.4 shows that the column density increases towards smaller radii in our simulations.

We first consider the question of how the nuclear gas properties depend on numerical resolution *in the absence of feedback*. To this end, the top left panel of Fig. 3.11 shows the BH accretion rate $\dot{M}_{visc}$ calculated for three different particle numbers $N_p = 1.6 \times 10^5, 4.8 \times 10^5$, and 1.6×10^6, with the gravitational force softening $\epsilon \propto N_p^{1/3}$.[5] To make a fair comparison, the accretion rate is evaluated within a fixed volume ($R = 406$ pc) and for $\alpha = 0.05$ for all of the simulations. This choice corresponds to $R = 4\epsilon$ for the lowest resolution run, but is $R \simeq 8.6\epsilon$ for our fiducial resolution simulation. Fig. 3.11 shows that the lowest resolution simulation (red) does not adequately resolve the fragmentation of the gas, and the resulting peak in the accretion rate, near first passage. The medium and higher (= our fiducial) resolution simulations, however, agree reasonably well, except for a slight difference in the slope of $\dot{M}_{visc}(t)$ at late times. Computed over a larger volume ($\sim$ kpc), the agreement between these runs improves.

To assess the convergence in the presence of feedback, the top right panel of Fig. 3.11 shows the BH accretion rate $\dot{M}_{visc}$ evaluated just as in the top left panel, i.e., using a fixed $R_{acc} = 406$ pc, in simulations with the same three particle numbers and force softening. Again the lowest resolution (red) simulation is clearly not adequate, but the medium (blue) and high (black) resolution simulations agree well; the integrated BH mass differs only by 2% in the latter two simulations.

As a final resolution test, the bottom left panel of Fig. 3.11 shows the BH accretion rate as a function of time in simulations with the same three resolutions and force softening, but in which $R_{acc} = 4\epsilon$. Thus in this case the accretion rate is determined, and the feedback applied, on increasingly small spatial scales in the higher resolution simulations. This is probably the most physically realistic (see §3.2.4). This panel shows that the large peak of accretion at final coalescence ($t \sim 1.8$ Gyr) is quite similar in all three cases. This is set by the physics of feedback by momentum deposition and is a robust property of all of our simulations. A corollary of this is that the final BH mass, as shown in the bottom right panel of Fig. 3.11, is the same to within a factor of ~ 2 for the three different resolutions. However, the results in the lower left panel of Fig. 3.11 also clearly demonstrate that the detailed evolution of the accretion rate is sensitive to the resolution. This is not particularly surprising: at fixed resolution, Fig. 3.5 has already demonstrated that the details of $\dot{M}_{visc}(t)$ depend on the value of R_{acc} – although, again, neither the integrated BH mass or star formation rate do. One implication of these results is that it is difficult for current simulations of BH growth to make quantitative predictions about the light curves of AGN activity triggered by mergers.

[5] In Fig. 3.11, $\dot{M}_{visc}$ for the simulations without feedback (upper left) is calculated from the simulation snapshots and the accretion rate is not Eddington limited. The data outputs were relatively infrequent and attempting to integrate the BH mass over such large timesteps was inaccurate.

3.7 Code Verification

We have tested our modifications to GADGET on a number of simplified problems that have answers that can be easily obtained through other methods. §B1 describes tests of the additional momentum feedback force applied to a thin spherical shell of gas. §B2 describes tests in which the force is applied to the gas particles in the central regions of an isothermal sphere. Two ways of implementing the force are tested: to a fixed number of particles around the BH, and to all particles within a fixed region R_{acc} around the BH.

As we are concerned with the performance of our BH accretion and feedback model, in all of the tests presented in this appendix, the multiphase equation of state and star formation model of Springel and Hernquist (2003) are *not* used; instead we use an adiabatic equation of state with $\gamma = 5/3$.

3.7.1 Gas shells

To test that the code is applying the radiation pressure force in equation (3.7) correctly, we have run the code for a simple system containing a black hole particle with a large mass and a thin spherical shell of gas with negligible temperature, pressure and mass. As this gas resides in a thin shell, this problem is more well-posed if we apply the radiation force to a fixed number, N, of gas particles.

This system has a critical luminosity defined by the point at which the radiation force balances the inward pull of gravity. As the gas shell is of low temperature and pressure, we can ignore pressure forces. For a black hole of mass M_{BH} and a gas shell of mass m at a radius r_0 the critical luminosity L_C satisfies (we take $\tau = 1$ for simplicity)

$$L_C = G\frac{M_{BH}m}{r_0^2}c. \tag{3.10}$$

When the luminosity is set to this value, the gas shell should experience no net force. For other values of the luminosity, the expected behaviour can easily be calculated by noting that the gas shell, in the absence of any pressure forces, should have a radius, $r(t)$, that satisfies

$$m\frac{d^2r(t)}{dt^2} = -\frac{GM_{BH}m}{r(t)^2} + \frac{L}{c}. \tag{3.11}$$

This is easily integrated to give the expected behavior of the gas shell.

A number of tests of this system were performed with varying luminosities, parameterized by the ratio of the luminosity applied to the critical luminosity,

$$\lambda = \frac{L}{L_C}. \tag{3.12}$$

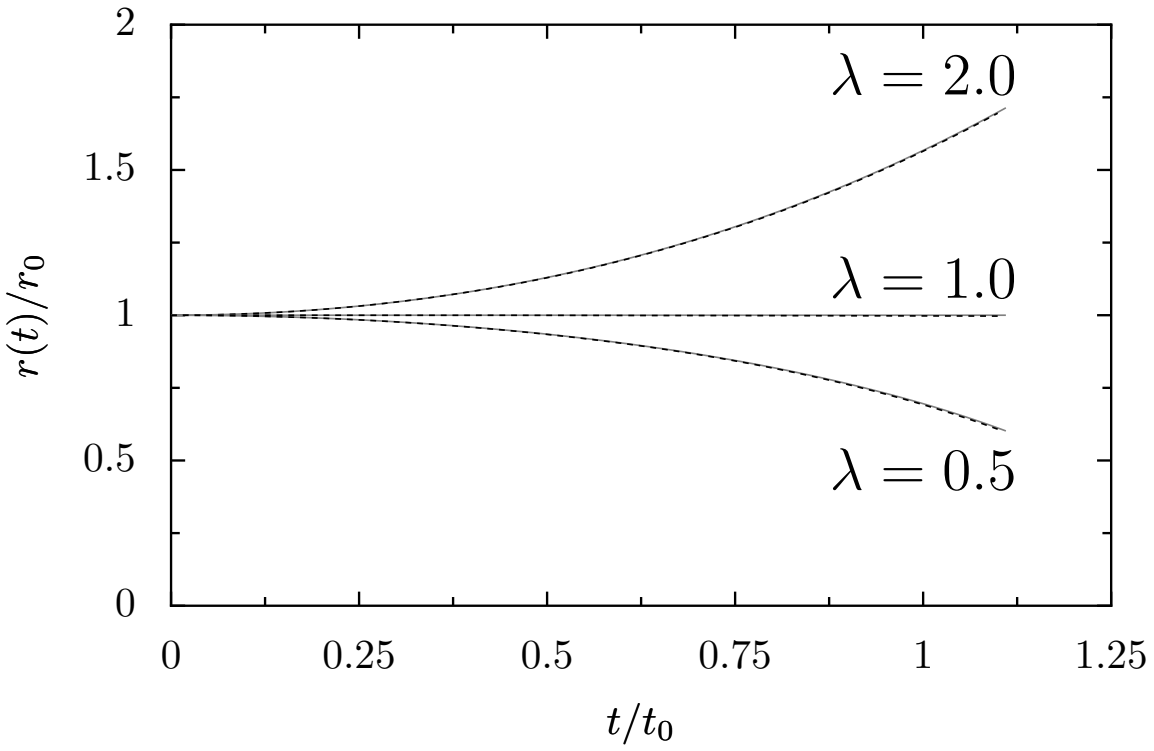

Figure 3.12: Time evolution of the radius of the test shell for three values of radiation force: $\lambda = 0.5, 1.0, 2.0$ (dashed curves). The results match closely with the solutions from integrating eq. (3.11) (superposed grey curves). Here the force is applied to the 25000 innermost gas particles of the 5×10^4 that make up the shell. Time is in units of $t_0 = \sqrt{r_0^3/GM_{BH}}$ and the radius is in units of r_0, where r_0 is the initial radius of the gas shell.

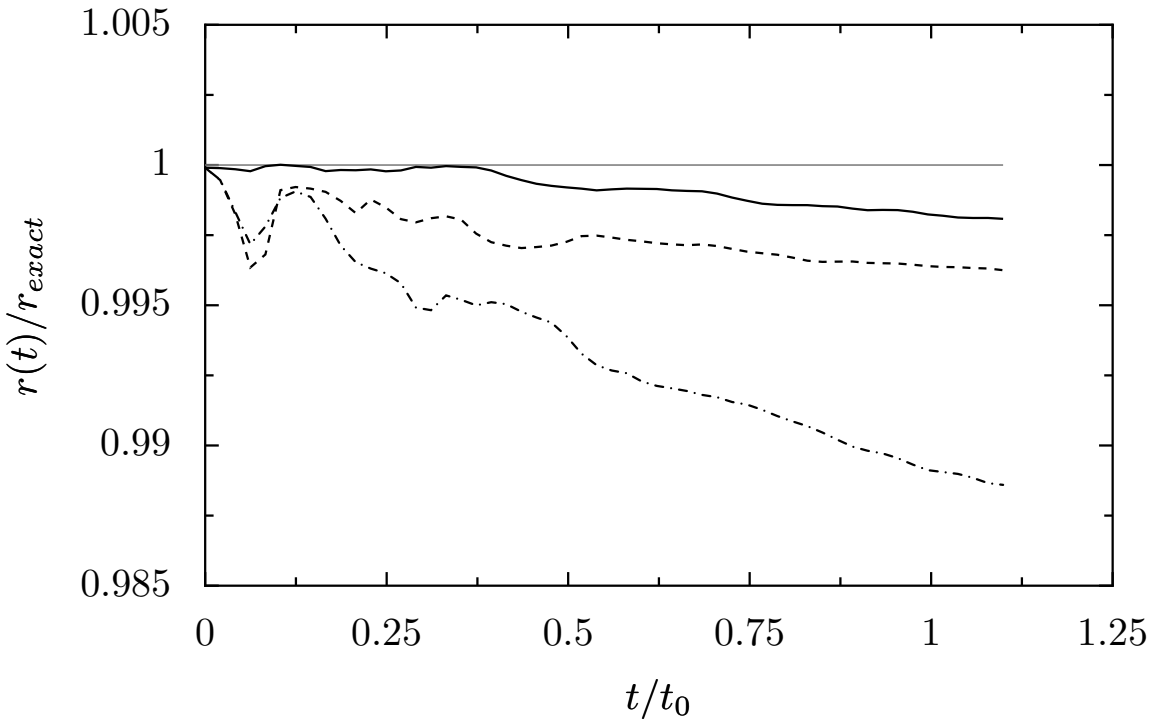

Figure 3.13: Time evolution of the radius of the test shell for three values of N/N_{shell}: 0.5 (solid), 0.25 (dashed), and 0.1 (dot-dashed). The numerical solutions are normalized by the exact solution from eq. (3.11). The radiation force is fixed to be $\lambda = 2.0$. The radius $r(t)$ changes by only about 1% as N is changed, indicating that our results are insensitive to the exact number of particles to which the radiation force is applied.

Fig. 3.12 shows the exact result in grey, with the numerical solution from the modified version of GADGET in black, for runs with $\lambda = 0.5, 1.0$ and 2.0. For these tests the number of particles in the shell is $N_{shell} = 50000$, and the force was applied to $N = 25000$ of them. In all cases, the numerical solution appears indistinguishable from the exact solution of eq. (3.11).

We have also tested the dependence of the results on the value of N/N_{shell}, the fraction of particles that receives the radiation force. Fig. 3.13 shows the ratio of the numerical solution from our code to the exact solution for $N/N_{shell} = 0.5, 0.25$, and 0.1 for the $\lambda = 2.0$ model. This demonstrates that even though the magnitude of the force on an individual particle increases as N decreases, the overall dynamics of the shell is the same, with the radii differing by only $\sim 1\%$ in the three cases. This is primarily due to the fact that the SPH particles are collisional and can thus transfer their motion to their neighbors via pressure forces. The extra momentum imparted to the subset of particles is transferred in part to the outer region of the shell, leading to the overall motion that agrees well with the exact solution. By extension, if N

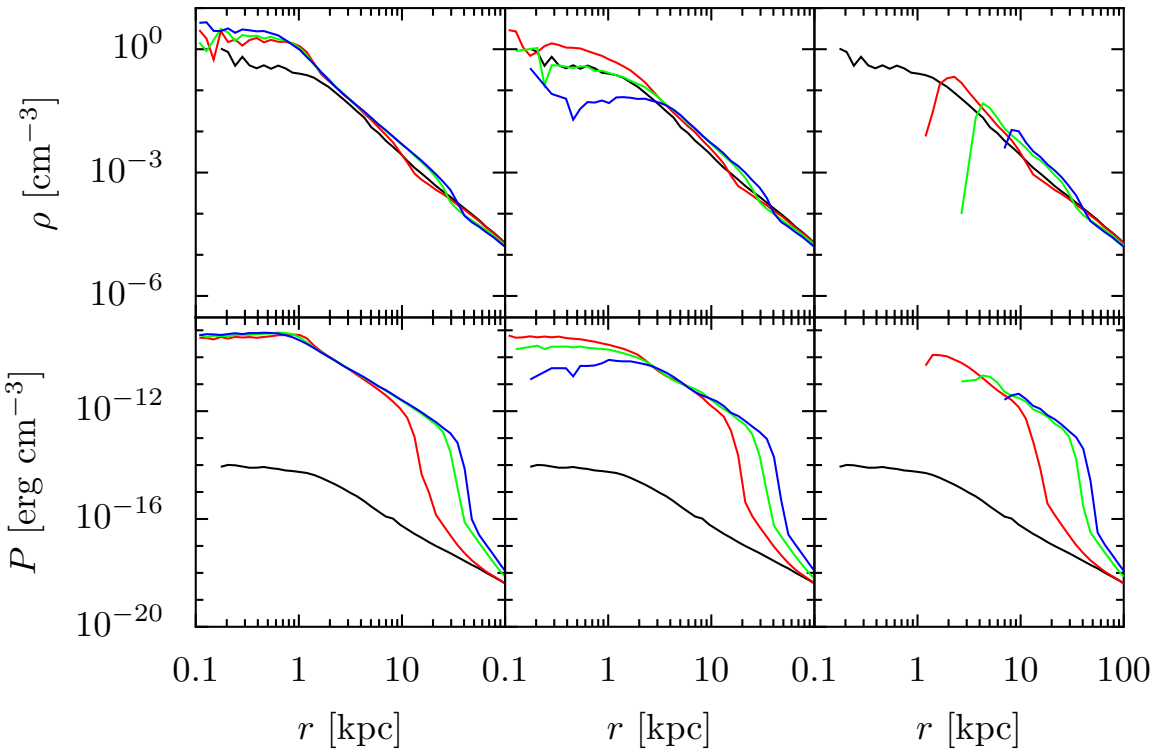

Figure 3.14: The density (top) and pressure profiles (bottom) in simulations of an isothermal sphere of gas embedded in an isothermal King potential. Three different simulations are shown: without feedback from a central black hole, $\lambda = 0.0$ (left), $\lambda = 1.0$ (middle) and $\lambda = 2.0$ (right). Each simulation is shown at four times: the initial profile (black) and $t = 0.16$ (red), 0.32 (green), 0.48 (blue) Gyr.

were to vary over the duration of the simulation, the results would also not depend strongly on the particular value.

3.7.2 Isothermal Sphere

We have performed a second set of tests of the feedback model using an isothermal background given by a King model. The mass of the system is split into two parts. The bulk of the mass makes up the collisionless background that is drawn from the full phase space distribution of the King model. A small fraction of the mass, $f_g = 0.05$, is assigned as collisional SPH particles. These gas particles follow the same spatial profile as the collisionless background but are given zero initial velocities and a very low temperature. Both components are realized with 10^5 particles. Finally, a black hole particle with a small mass is placed at rest at the center of the distribution.

In the absence of feedback, the SPH particles are not in equilibrium by construction and should flow toward the center of the potential provided by the collisionless

background. When the feedback is switched on in the isothermal King potential near the center, the feedback will again have a critical value set by force balance:

$$\frac{L_c}{c} = 4\frac{f_g\sigma^4}{G}. \tag{3.13}$$

When the luminosity is below this value, we expect the extra momentum to be insufficient to clear the gas out of the center. When the luminosity exceeds this value, the feedback should be strong enough to clear the central regions of the distribution. To test this, we apply feedback with a constant luminosity. Again, we parameterize the strength of the feedback as $\lambda = L/L_c$.

We have tested two ways of assigning the radiation force. In the first case, the force is shared (equally) by a fixed number of gas particles nearest to the black hole. In the second case, the force is shared by all gas particles within a fixed radius of the black hole. We discuss the results separately below.

Fixed N

For the tests in this subsection, the radiation force is applied to a fixed number of gas particles: $N = 500$. The King model has $\sigma = 100\text{kms}^{-1}$, $\Psi/\sigma^2 = 12$ and a total mass of $10^{12}\text{M}_\odot$.

Fig. 3.14 compare the density and pressure profiles of three runs with $\lambda = 0$ (i.e. no feedback; left panels), 1 (middle), and 2 (right). Four timesteps are shown: $t = 0$ (black), 0.16 (red), 0.32 (green), and 0.48 Gyr (blue). As expected, the gas flows to the center in the absence of feedback, increasing the density and pressure as the gas begins to equilibrate in the background potential. The middle and right panels show that the feedback clearly has an effect on the gas at the center, providing some support for the incoming gas, allowing the gas to have a lower pressure. For the case with $\lambda = 2$, the feedback is strong enough to effectively clear out the central region.

The nature of the feedback allows a calculation of how the size of the evacuated region should grow with time. Ignoring the thickness of the shell swept up as matter begins to be driven out by the feedback, momentum conservation gives

$$\frac{d}{dt}\left[M_{shell}(r)dr/dt\right] = \frac{L}{c} - \frac{GM_{bg}(r)M_{shell}(r)}{r^2} \tag{3.14}$$

where $M_{shell}(r)$ is the initial mass distribution of gas and $M_{bg}(r)$ is the mass distribution of the background. Near the center of the initial distribution, both the gas and background have an isothermal distribution, for which the mass increases linearly with the distance from the centre. This makes the right hand side of Eq. (3.14) a constant. In this case, the size of the evacuated region, $r(t)$, depends linearly on time:

$$r(t) = \sqrt{2(\lambda-1)(1-f_g)}\sigma t + C \tag{3.15}$$

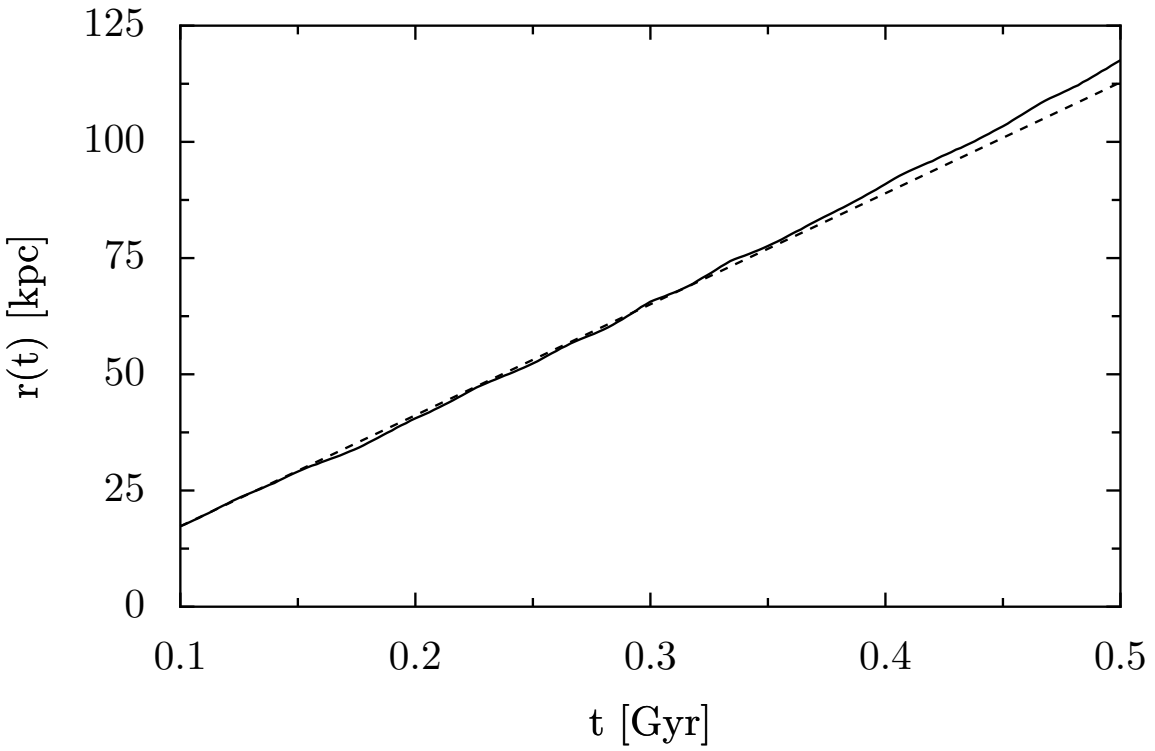

Figure 3.15: Time evolution of the size of the evacuated region for the isothermal sphere test. The $\lambda = 4$ simulation results shown (solid) match well with the analytic solution (Eq. 3.15; dashed).

where C is a constant of integration to account for the finite time required to form the shell of swept up gas.

Fig. 3.15 shows the size of the evacuated region as a function of simulation time for a run with $\lambda = 4$, and the exact solution for a shell moving in an isothermal background (Eq. 3.15) with C chosen to match the position of the shell at $t = 0.1$ Gyr. The size of the evacuated region is defined by the position of the gas particle closest to the black hole. The agreement is very good with only slight deviation at the latest times. For the model employed, the potential is only isothermal near the origin, so when the shell expands sufficiently, the potential shallows and the shell should move faster than the prediction. This is indeed seen at late time in Fig. 3.15.

Fixed R_{acc}

For the galaxy merger simulations, we apply the force inside a fixed R_{acc} throughout the simulation. In this section, we run a similar set of tests as in the previous subsection but we hold R_{acc} fixed. When the number of particles inside R_{acc} becomes small, however, the feedback force exerted on individual particles becomes spuriously

large. We therefore impose an additional condition of minimum N on the feedback. For the tests in this subsection, the feedback is applied to those particles inside R_{acc}, or to the innermost 100 gas particles if there are fewer than this inside R_{acc}. For the simulations in the main paper, typical values of N were 600-800, so there were always enough particles inside the accretion region to avoid the need for a lower bound on N.

Our first test uses a constant $L = 4L_c$, and holds R_{acc} fixed. We use a King model as in the previous section, but with slightly different parameters to connect more closely to the our fiducial simulation: $\sigma = 160\mathrm{kms}^{-1}$, $\Psi/\sigma^2 = 12$ and a total mass of $10^{12}\mathrm{M}_\odot$. We tested this model for three different sizes of the accretion and feedback region: $R_{acc} = 0.7, 1.4$ and 2.8 kpc. The smallest region has initially $N \sim 500$. Note that the values of R_{acc} used here are larger than those used in our galaxy merger simulations in the main text. These values of R_{acc} were necessary to ensure that R_{acc} contains a reasonable number of particles. In the galaxy merger calculations, the overall larger number of particles in the simulation and the high gas density in the central regions imply that smaller values of R_{acc} can be reliably used. They are also more physical, as we argued in §3.2.4.

Fig. 3.16 shows the position of the shell of swept up material for the three runs with $R_{acc} = 0.7, 1.4$ and 2.8 kpc in black, red and blue respectively. Initially, all the gas inside R_{acc} experiences the extra force. As the region becomes more evacuated and the number of particles inside R_{acc} drops, we transition to applying the force to the $N = 100$ particles closest to the BH. The evolution of the shells in this case is quite similar to the evolution in the last section. The model used in this section is smaller in size and so the shell expands past the isothermal core of the King model earlier. As a result, it begins to accelerate outward sooner. However, the tests with different R_{acc} have essentially identical evolution.

Finally, we run a test in which we determine the luminosity from the accretion rate as in Eq. (3.7), and increase the BH mass in time accordingly. This test thus employs the full feedback and accretion model of our galaxy merger simulations. We use the same $\sigma = 160$ km s^{-1} King model, and took $\alpha = 0.1$ and $\tau = 1$ for the feedback parameters. The initial mass of the black hole was $M_{BH,i} = 10^5\mathrm{M}_\odot$.

Fig. 3.17 shows the accretion history of the BH for the runs with $R_{acc} = 0.7, 1.4$, and 2.8 kpc. In each test, the feedback is initially Eddington limited and it is not until about $t = 0.3$ Gyr that the luminosity approaches that required to evacuate the gas out of R_{acc}. At this point, the gas begins to move out of R_{acc} and form a shell of material at $R \sim R_{acc}$. This shell then remains fairly steady as the accretion rate self-regulates around the critical luminosity. As the three values of R_{acc} are all inside the isothermal core of the King model, the critical luminosities (eq. 3.13) are the same, and we would thus expect the accretion rate to self-adjust to the same value at late times. This is indeed borne out in the simulations shown in Fig. 3.17. Of these three runs, only the calculation with $R_{acc} = 0.7$ kpc spends a significant amount of time with fewer than 100 particles inside R_{acc}. Despite the large change in the size

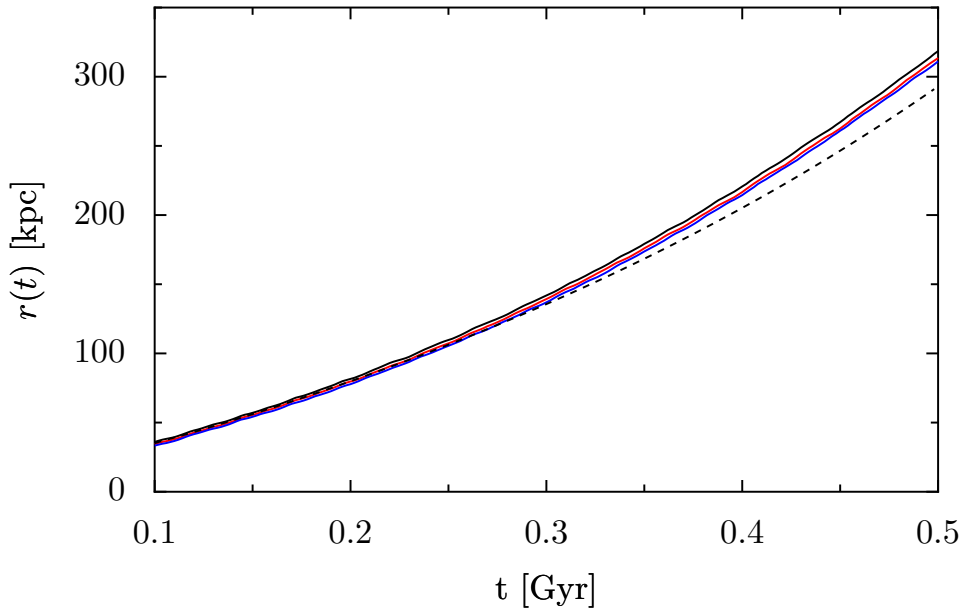

Figure 3.16: Radius of the swept up shell for the isothermal sphere test with $\lambda = 4$ and fixed R_{acc}: 0.7 (black), 1.4 (red), and 2.8 kpc (blue). To avoid numerical problems, the feedback was always applied to at least $N \sim 100$ particles. The numerical results agree well with the dashed curve, which shows a numerical integration of the analytic equation for the shell radius (eq. 3.14).

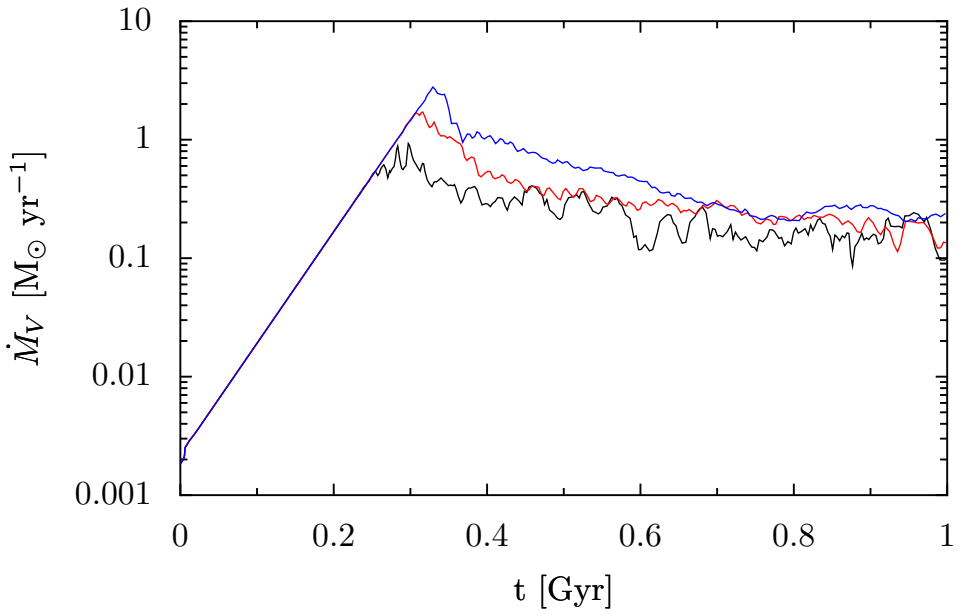

Figure 3.17: The black hole accretion rate for isothermal sphere simulations in which the full black hole accretion and feedback model are used ($\alpha = 0.1$ and $\tau = 1$). Three different values of R_{acc} are shown: $R_{acc} = 0.7$ (black), 1.4 (red), and 2.8 kpc (blue). All three agree well with each other.

of the feedback region, Fig. 3.17 shows that the evolution of the gas is quite similar. The black hole masses for these three runs differ by only a factor of ~ 2 at the end of the simulation.

Chapter 4

Galaxy-Scale Outflows Driven by Active Galactic Nuclei

We present hydrodynamical simulations of major mergers of galaxies and study the effects of winds produced by active galactic nuclei (AGN) on interstellar gas in the AGN's host galaxy. We consider winds with initial velocities $\sim 10,000\,\mathrm{km\,s^{-1}}$ and an initial momentum (energy) flux of $\sim \tau_w L/c$ ($\sim 0.01\,\tau_w\,L$), with $\tau_w \sim 1-10$. The AGN wind sweeps up and shock heats the surrounding interstellar gas, leading to a galaxy-scale outflow with velocities $\sim 1000\,\mathrm{km\,s^{-1}}$, peak mass outflow rates comparable to the star formation rate, and a total ejected gas mass $\sim 3\times10^9\,M_\odot$. Large momentum fluxes, $\tau_w \gtrsim 3$, are required for the AGN-driven galactic outflow to suppress star formation and accretion in the black hole's host galaxy. Less powerful AGN winds ($\tau_w \lesssim 3$) still produce a modest galaxy-scale outflow, but the outflow has little global effect on the ambient interstellar gas. We argue that this mechanism of AGN feedback can plausibly produce the high velocity outflows observed in post-starburst galaxies and the massive molecular and atomic outflows observed in local ultra-luminous infrared galaxies. Moreover, the outflows from local ultra-luminous infrared galaxies are inferred to have $\tau_w \sim 10$, comparable to what we find is required for AGN winds to regulate the growth of black holes and set the $M_{BH}-\sigma$ relation. We conclude by discussing theoretical mechanisms that can lead to AGN wind mass-loading and momentum/energy fluxes large enough to have a significant impact on galaxy formation.

4.1 Introduction

Accretion onto a central massive black hole (BH) in a galactic nucleus produces energy in the form of radiation, relativistic jets, and wider angle (less-collimated) non-relativistic ($v \sim 10^4\,\mathrm{km\,s^{-1}}$) outflows (Krolik, 1999). The coupling of this energy output to gas in galaxies and in the intergalactic medium is believed to play

an important role in galaxy formation, potentially regulating the growth of massive galaxies and the thermal properties of the intracluster medium in galaxy groups and clusters (e.g., Silk and Rees 1998, Croton et al. 2006).

The impact of this 'feedback' on the gas *in* galaxies is particularly uncertain, both because the interstellar (ISM) gas is denser, and thus more difficult to affect dynamically, and because much of the ISM subtends a relatively modest solid angle relative to a central active galactic nucleus (AGN). However, analytic estimates and numerical simulations have demonstrated that if a modest fraction of the energy produced by accretion onto a central BH can couple to the surrounding gas, it can unbind the interstellar gas (e.g., Silk and Rees 1998, Di Matteo et al. 2005). The physical processes most likely to produce such an effect are winds (King, 2003, King et al., 2011), radiation pressure (Murray et al., 2005), and/or Compton heating (Sazonov et al., 2004) from a central AGN. Understanding how this works in detail is one of the major challenges in our understanding of the connection between AGN physics and galaxy formation.

In this paper, we assess the influence of AGN winds on gas in the AGN's host galaxy using three-dimensional numerical simulations. Previous analytic work and one and two-dimensional simulations have demonstrated that AGN winds can in principle sweep up and drive gas out of galaxies, potentially explaining the $M_{BH} - \sigma$ relation and the dearth of gas and ongoing star formation in massive, early-type, galaxies (e.g., King 2005, King et al. 2011, Novak et al. 2011, Ostriker et al. 2010 and references therein).

Observationally, there is strong evidence that AGN indeed drive powerful outflows. Broad-absorption line (BAL) quasars, which show blue-shifted absorption lines in the rest-frame ultraviolet with inferred outflow velocities $\sim 10,000 - 40,000\,\mathrm{km\,s^{-1}}$, represent over $\sim 40\%$ of quasars in infrared selected samples (Dai et al., 2008). A similar fraction of radio-quiet quasars show evidence for high velocity outflows in X-ray absorption line spectroscopy (Tombesi et al., 2010). It is likely that *all* quasars possess such outflows but that they are only observed when the system is viewed modestly edge-on (Murray et al., 1995). However, determining the mass-loss rate from spatially unresolved absorption-line observations is notoriously difficult given uncertainties in the radius of the absorbing gas. In a handful of low-ionization BAL quasars (in particular, FeLoBALs) this degeneracy has been broken, suggesting mass loss rates significantly larger than the black hole accretion rate (Moe et al., 2009, Bautista et al., 2010, Dunn et al., 2010, Faucher-Giguere et al., 2011). These observations trace absorbers at large distances from the BH ($\sim$ kpc), in contrast to most of the high ionization UV and X-ray absorption seen in BAL quasars, which arises at $\lesssim 1$ pc. In addition to these well-characterized outflows, it is possible that quasars drive even more powerful outflows during phases of super-Eddington accretion (King and Pounds, 2003, King et al., 2011) or during obscured phases when the AGN's radiation is trapped in the galactic nucleus, enhancing the force on the ambient gas (DeBuhr et al., 2010, 2011).

To characterize the impact of AGN winds on their host galaxy, we carry out numerical simulations of major galaxy mergers with models for BH growth and feedback. Although it is by no means certain that all quasars are associated with mergers, this provides a convenient and well-posed model in which to study gas inflow in galactic nuclei. It also allows us to readily compare our results to the extensive previous literature on AGN feedback during mergers.

In the next section (§4.2) we summarize our methods, emphasizing our implementation of AGN winds and our treatment of ISM cooling. We then describe our key results in §4.3. We conclude in §4.4 by discussing the implications of our results for models of AGN feedback and for galactic winds driven by AGN. We also compare our results to observations of high-velocity outflows from post-starburst galaxies and ultra-luminous infrared galaxies and summarize the theoretical processes that can produce the large mass-loading and momentum fluxes we find are necessary for AGN winds to have a substantial impact on the surrounding ISM.

4.2 Methodology

We use a modified version of the TreeSPH code GADGET-2 (Springel, 2005) to perform simulations of equal-mass galaxy mergers. This version of the code includes the effective star formation model of Springel and Hernquist (2003) and the radiation pressure AGN feedback model of DeBuhr et al. (2011). As described below, we modified the code further to implement a model of feedback via AGN winds, and to implement a more physical model of how the interstellar gas cools.

4.2.1 Galaxy Models and Initial Conditions

We carry out simulations of major mergers of two equal mass galaxies. We simulate only a single galaxy mass and focus our resources on studying the effects of feedback via AGN winds produced at small radii. Each galaxy model has a rotationally supported disk of gas and stars and a stellar bulge, all embedded in a halo of dark matter. Both the stellar and gaseous disks have an exponential radial profile with a scale length of 3.51 kpc. The vertical profile of the stellar disk is that of an isothermal sheet with a scale height of 702 pc. The vertical structure of the gas disk is set by hydrostatic equilibrium. The halo and stellar bulge both have Hernquist (Hernquist, 1990) profiles with a halo virial and half mass radius of 229 and 102 kpc, respectively (a concentration of 9.0) and with a bulge effective radius of 1.27 kpc. Each galaxy has a total dynamical mass of $1.94 \times 10^{12} \mathrm{M}_{\odot}$, a total disk mass of $7.96 \times 10^{10} \mathrm{M}_{\odot}$ and a bulge of mass $2.66 \times 10^{10} \mathrm{M}_{\odot}$; 10% of the disk mass is gas. We have performed an additional simulation with a disk gas fraction of 30 %; this run gives qualitatively similar results and so is not discussed in detail. The black holes are modeled as additional collisionless particles with initial masses of $10^5 M_{\odot}$.

For our fiducial simulations, each galaxy is formed from 2.4×10^5 particles: the halo has 9×10^4 dark matter particles, the disk has 6×10^4 stellar particles and 6×10^4 gas particles, and the bulge has 3×10^4 stellar particles. The gravitational force softening length is $\epsilon = 70$ pc for the disk and bulge particles and $\epsilon = 176$ pc for the halo particles. We describe resolution tests in § 3.3.

For the merger simulations, the two equal mass galaxies are placed on a prograde orbit with an initial separation of 142.8 kpc and an initial velocity of each galaxy of 160 km s^{-1} directed at an angle of 28° from the line connecting the galaxies. The corresponding orbital energy is approximately zero. The spin of the two galaxies are not aligned with the orbital angular momentum of the system; the relative angle between the spin directions is 41°, with one galaxy's spin making an angle of 10° degrees relative to the orbital angular momentum.

4.2.2 Black Hole Accretion

In this section we briefly review the sub-grid accretion model presented in detail in DeBuhr et al. (2011). The sub-grid accretion rate on scales smaller than our resolution (both gravitational force softening and SPH smoothing) is estimated with a model motivated by the redistribution of angular momentum in the gas. For gas with a surface density Σ, a sound speed c_s and a rotational angular frequency Ω, the mass accretion rate into the nuclear region is:

$$\dot{M}_{visc} = 3\pi\alpha\Sigma\frac{c_s^2}{\Omega}. \tag{4.1}$$

Here α is a free parameter of the model characterizing not only the efficiency of angular momentum transport, but also the amount of gas that turns into stars (on scales below our resolution) instead of falling into the black hole. Our fiducial values of α range from $0.05-0.15$, motivated (at the order of magnitude level) by comparison to the simulations of gas inflow from $\sim 0.1-100$ pc of Hopkins and Quataert (2010b). Over this range of α, there is little dependence of our simulation results on α (see DeBuhr et al. 2011).

To perform the sub-grid estimate of the gas properties in equation (4.1), we take averages of the properties of the SPH particles inside a region of radius $R_{acc} \sim 300$ pc centered on the black hole. For reasons described in DeBuhr et al. (2011) we take this radius to be four times the gravitational force softening, ϵ, of the particles in the simulation.

The BHs in our simulation are modeled as specially marked collisionless particles. To minimize the unavoidable spurious stochastic motion of the BH particles due to gravitational interactions with the stellar and gas particles, we assign the BH particles a (fixed) tracer mass of $2 \times 10^8 M_\odot$, which is $\sim 10^2$-10^4 times more massive than the other particles in the simulation. During each simulation, we also compute separately the 'real' mass of the BH that grows according to the accretion rate at small radii

(with an initial mass of $10^5 M_\odot$). Details of this step were given in § 2.3.2 of DeBuhr et al. (2011).

4.2.3 Radiation Pressure Feedback

The luminosity of the black hole is taken to be a fraction, $\eta = 0.1$, of the rest mass energy of the accreted material:

$$L = \min\Big(\eta \dot{M}_{in} c^2, L_{edd}\Big). \tag{4.2}$$

The net accretion rate $\dot{M}_{\rm in}$ onto the black hole need not equal the viscous inflow rate $\dot{M}_{\rm visc}$ at ~ 100 pc in equation (4.1) if there are significant outflows on scales $\lesssim 100$ pc (roughly our resolution); we return to this point in § 2.4.

In the radiation pressure feedback model introduced in DeBuhr et al. (2011), the accretion luminosity is coupled back into the surrounding gas by adding a total force

$$\dot{p}_{rad} = \tau \frac{L}{c}, \tag{4.3}$$

which is shared equally by all SPH particles inside R_{acc}. The added force is directed radially away from the BH particle. Here τ is a free parameter of the model, representing the optical depth to infrared (IR) radiation in the nuclear region. Our fiducial choice for τ in this work is 20. DeBuhr et al. (2011) showed that $\tau \sim 20$ was required to reproduce the observed normalization of the $M_{\rm BH} - \sigma$ correlation in their simulations.

4.2.4 AGN Wind Feedback

In addition to the radiation pressure feedback described by equation (4.3), accretion onto the black hole can explicitly drive a wind at radii well beneath our resolution. Our treatment of such a wind is motivated in particular by observations of BAL quasars, which have $\sim 10,000\,{\rm km\,s^{-1}}$ outflows launched from near the broad line region at ~ 0.1 pc (e.g., Murray et al. 1995). In our model, the AGN winds at small radii carry a momentum flux given by

$$\dot{p}_w = \tau_w \frac{L}{c}, \tag{4.4}$$

where τ_w is a further parameter of the model representing the total momentum flux in the wind. The wind is launched at a fixed speed v_w. Thus, the rate at which mass is added to the wind is given by

$$\dot{M}_w = \tau_w \frac{L}{c v_w} = \tau_w \eta \frac{c}{v_w} \dot{M}_{in}. \tag{4.5}$$

where we have linked the luminosity of the black hole to the accretion rate as in equation (4.2). In the presence of significant AGN winds, not all of the material entering the nuclear region, $\dot{M}_{visc}$, actually reaches the black hole. Instead, the net accretion rate into the black hole, $\dot{M}_{in}$, must be reduced by the mass of the outflow (see Ostriker et al. 2010): $\dot{M}_{in} = \dot{M}_{visc} - \dot{M}_w$, which implies that the true black hole accretion rate is given by

$$\dot{M}_{in} = \min\left(\frac{\dot{M}_{visc}}{1 + \tau_w \eta c / v_w}, \frac{L_{edd}}{\eta c^2}\right) \tag{4.6}$$

Note that equation (4.6), not equation (4.1), determines the AGN luminosity and thus the magnitude of the feedback in equations (4.3) and (4.4).

To deposit the wind momentum, we give kicks to particles inside R_{acc}. Particles receiving a kick are selected stochastically with each particle having an equal probability of being added to the wind. The probability of a kick is chosen to ensure that the time average of the mass kicked in a given timestep Δt is given by $\dot{M}_w \Delta t$. The kick is implemented by adding a velocity v_w to the current velocity of each selected particle. The direction of this imparted velocity is chosen to be more heavily weighted toward the surrounding disk: if θ is the angle between the imparted momentum and the disk normal, the probability distribution over $x = \cos\theta$ is given by $p(x) = 3(1 - x^2)/4$. For this purpose, the disk normal is defined to be the direction of the total orbital angular momentum about the black hole of all the gas particles inside R_{acc}. This modest equatorial bias in the wind direction is motivated by models of BAL quasars (Murray et al., 1995). Nonetheless, this choice is not that critical: the efficacy of the feedback is largely determined by the outflow momentum/energy flux that is directed within the solid angle subtended by the surrounding ISM. For our fiducial model, $\sim 40\%$ of the momentum flux is directed within one scale-height of the disk at ~ 100 pc. Models with isotropic kicks require slightly large values of τ_w to give results similar to our fiducial model because less of the feedback is directed towards the surrounding ISM.

Despite the similarity between equations (4.3) and (4.4), our two feedback processes affect the gas particles within R_{acc} in different ways. In the case of our simple radiation pressure model, all gas particles within R_{acc} receive an additional acceleration set by equation (4.3) and are pushed outward from the BH. As shown in DeBuhr et al. (2011), this feedback process evacuates the central gas reservoir and lowers the BH accretion rate and the final BH mass, but the velocities of the gas particles are not so large as to produce significant large-scale galactic outflows. In our AGN wind model, by contrast, a small fraction ($\lesssim 5\%$) of gas particles within R_{acc} receives an instantaneous large wind velocity of 3000 to $10,000\,\mathrm{km\,s^{-1}}$. These particles leave R_{acc} within $\lesssim 10^5$ years and, as we show below, can drive a galaxy-scale outflow via their interaction with the ambient ISM.

Our implementation of wind feedback adds two additional input parameters to the simulation. The first, v_w, describes the launch speed of the winds while the second, τ_w,

describes the total momentum flux in the wind. Our default wind speed is motivated in part by observations of BAL quasars and theoretical models of the origin of such winds via line driving in the accretion disk at ~ 0.1 pc (though our model should not be taken as a literal implementation of this physics). Observed wind velocities are $\sim 10,000\,\mathrm{km\,s^{-1}}$. Models of line driving lead to momentum fluxes in the wind of $\lesssim L/c$, i.e., $\tau_w \lesssim 1$ because the lines do not typically completely cover the continuum (Murray et al., 1995). As we show below, however, larger values of τ_w are required for AGN outflows to have a significant effect on the gas dynamics and star formation history in galactic nuclei.

Observationally, momentum fluxes are difficult to infer in most cases because of ambiguities in the absolute density/radial scale at which the absorption occurs. In a handful of low-ionization BALs (in particular, FeLoBALs), this degeneracy has been broken, implying momentum fluxes $\sim 0.3-5L/c$, i.e., $\tau_w \sim 0.3-5$ (with significant uncertainties; see Moe et al. 2009, Bautista et al. 2010, Dunn et al. 2010, Faucher-Giguere et al. 2011). It remains uncertain whether these values of τ_w are representative of the entire BAL-quasar population. We take $\tau_w \simeq 5$ as our fiducial value but also explore the range $1 \leq \tau_w \leq 10$. Our fiducial value of $\tau_w = 5$ was chosen for three reasons that will become clear later in the paper: (1) the AGN wind then leads to a galaxy-scale outflow that significantly influences the surrounding ISM dynamics, (2) the final BH mass in the simulations is reasonably consistent with the observed $M_{\rm BH}-\sigma$ relation for $\tau_w \simeq 5-10$. (3) Observations of high speed atomic and molecular outflows in local ULIRGs suggest $\tau_w \sim 10$ (Feruglio et al., 2010, Chung et al., 2011, Rupke and Veilleux, 2011, Sturm et al., 2011). We discuss physical mechanisms that can produce such powerful AGN winds in §4.4.

4.2.5 ISM Model and Gas Cooling

In the subgrid ISM model of Springel and Hernquist (2003), gas with densities above the star formation threshold approaches an effective thermal energy, u_{eff}, set by a balance between cooling and the feedback from star formation. If processes such as shocks or adiabatic expansion/compression cause the internal energy to deviate from u_{eff}, the differences decay on the timescale given by eq. (12) of Springel and Hernquist (2003). This decay timescale is set by the subgrid model rather than the true cooling time of the gas.

One consequence of Springel and Hernquist (2003)'s ISM model is that sufficiently dense shock heated gas does not cool on its cooling timescale. In this paper we show that AGN winds can shock heat gas in the ISM to above the escape speed – this contributes to driving a galactic wind. To ensure that the cooling of the shock heated gas is correct, we modified the ISM model of Springel and Hernquist (2003) to better match the expected cooling rate for gas with roughly a solar metallicity. To compute the local cooling rate we use a fit to Sutherland and Dopita (1993) for gas with solar metallicity. The fit is essentially eq. (12) of Sharma et al. (2010) but with the cooling

rate increased by a factor of two when the temperature is between $\sim 3 \times 10^4$ K and 3×10^7 K (to account for solar metallicity). From this cooling rate we compute a cooling time, t_{cool}; differences between the thermal energy and the subgrid u_{eff} decay on $t_{relax} = t_{cool}$. For most of the relevant range of temperature and density in our simulations, this cooling time is shorter than the relaxation time of Springel and Hernquist (2003).

In addition to the above modification to the cooling rate, we also consider the role of inverse Compton cooling/heating. To do so, we modify the cooling/relaxation timescale of the gas to be

$$t_{relax}^{-1} = t_{cool}^{-1} + t_C^{-1}. \tag{4.7}$$

where the (non-relativistic) Compton time is given by

$$t_C = 10^7 \mathrm{yr} \left(\frac{R}{300 \text{ pc}} \right)^2 \left(\frac{L}{10^{46} \text{ erg s}^{-1}} \right)^{-1}, \tag{4.8}$$

with R the distance to the BH and L the associated AGN luminosity. We do not consider any radiative transfer effects in this paper, which in reality can modify both the luminosity L seen at a given radius and the local Compton temperature at a given radius. Instead, we take the Compton temperature to be that appropriate for the mean spectrum of luminous AGN, including the effects of obscuration: $T_C \simeq 2 \times 10^7$ K (Sazonov et al., 2004).

In the limit that the Compton timescale is short compared to the two-body cooling time, we no longer relax the thermal energy of the gas to the effective equation of state value for the energy, u_{eff}, but rather to $u_C = 3/2kT_C$. To transition between these two limits, we in general let the thermal energy of gas relax to:

$$u_{relax} = \frac{t_{cool} u_C + t_C u_{eff}}{t_C + t_{cool}}. \tag{4.9}$$

For dense gas, atomic cooling dominates and the gas rather quickly approaches the sound speed associated with the effective equation of state. For gas densities characteristic of the ISM in the central kpc of our model galaxies ($\sim 10 - 10^3$ cm^{-3}) the sound speeds are $\sim 40\,\mathrm{km\,s^{-1}}$ and thus the gas is primarily rotationally supported rather than pressure supported. This justifies our use of the viscous accretion rate in equation 4.1.

4.3 Results

Table 4.1 lists the parameters of the galaxy merger simulations presented in this work. We consider a single galaxy mass and merger orbit (see § 4.2.1), and explore the effects of including AGN wind feedback, both with and without radiation pressure. For the AGN winds, we vary both the total momentum flux in the wind (τ_w) and the wind speed v_w, with fiducial values of $\tau_w = 5$ and $v_w = 10,000\,\mathrm{km\,s^{-1}}$.

Table 4.1: Simulation Parameters

Run Name	τ_w	v_w [$\mathrm{km\,s^{-1}}$]	ISM Model	$M_{BH,f}$ [$10^7 \mathrm{M}_\odot$]	$M_{*,f}$ [$10^9 \mathrm{M}_\odot$]	$M_{*,p}$ [$10^9 \mathrm{M}_\odot$]	$f_{\rm disk}$	$f_{\rm out}$	$M_{\rm out}$ [$10^9 \mathrm{M}_\odot$]	Notes
wo1-10	1	10000	a	56.5	8.67	1.79	0.014	0.343	5.47	wo = wind only
wo3-10	3	10000	a	17.9	7.35	1.05	0.002	0.472	7.52	
wo5-10	5	10000	a	12.2	7.36	1.02	0.002	0.477	7.60	
wo5-7	5	7000	a	5.36	10.7	2.91	0.041	0.175	2.78	
wo5-3	5	3000	a	6.65	12.1	5.23	0.059	0.056	0.89	
wo10-10	10	10000	a	6.20	7.35	0.92	0.002	0.466	7.42	
wo10-7	10	7000	a	2.99	10.8	2.55	0.014	0.191	3.04	
wo10-3	10	3000	a	3.96	12.2	4.70	0.069	0.060	0.96	
wp5-10	5	10000	a	4.38	10.9	3.11	0.006	0.196	3.13	fiducial sim; wp = wind + prad
wp5-7	5	7000	a	5.04	10.9	3.77	0.016	0.175	2.79	
wp5-3	5	3000	a	2.63	12.8	4.02	0.159	0.102	0.36	
wp1-10	1	10000	a	11.8	12.4	3.86	0.006	0.100	1.61	
wp3-10	3	10000	a	6.15	11.9	4.30	0.006	0.149	2.37	
wp10-10	10	10000	a	3.36	10.3	3.21	0.002	0.268	4.26	
wpfg30	5	10000	a	10.2	39.5	4.54	0.003	0.148	7.06	$f_{g,i} = 0.3$
wpsh	5	10000	c	6.14	10.8	3.41	0.002	0.234	3.73	
wpcomp	5	10000	b	6.30	10.8	3.21	0.004	0.276	4.40	
wpcompl	5	10000	b*	5.01	11.4	3.96	0.007	0.181	2.88	
wpinst	5	10000	d	5.90	10.4	2.67	0.018	0.216	3.44	
wplr	5	10000	a	5.28	10.2	4.45	0.004	0.307	4.89	Lower resolution
wphr	5	10000	a	4.77	11.5	3.94	0.012	0.166	2.65	Higher resolution
po	0	0	a	9.33	13.6	4.92	0.051	0.007	0.11	No wind feedback
pofg30	0	0	a	25.9	44.5	6.45	0.028	0.007	0.32	$f_{g,i} = 0.3$, No wind feedback

Model parameters and key quantities in our galaxy merger simulations. The top section lists runs with only the AGN wind feedback model (parametrized by the wind speed v_w and momentum flux τ_w). The bottom section lists runs with both the AGN wind model and the radiation pressure model with $\tau = 20$. ISM model refers to one of four following options: (a) our fiducial cooling model (see §4.2.5), (b) same as (a) but including Compton heating with $T_C = 2 \times 10^7$ K, (b*) same as (a) but including Compton heating with $T_C = 10^6$ K, (c) same as in Springel and Hernquist (2003), and (d) the gas returns to the effective EOS of Springel and Hernquist (2003) instantaneously. Other columns list the key properties of the black holes, stars, and gas in the simulations: $M_{BH,f}$ is the final black hole mass, $M_{*,f}$ is the total mass of new stars formed by the end of the simulation, $M_{*,p}$ is the total mass of new stars formed after the peak of star formation, $f_{\rm disk}$ is the fraction of the gas mass within 3 kpc of the BH at the end of the simulation, $f_{\rm out}$ is the fraction of the gas mass at large distances ($\gtrsim 10$ kpc) above the orbital plane at the end of the simulation, and $M_{\rm out}$ is the corresponding gas mass. $f_{\rm disk}$ is a proxy for how much gas remains in the galaxy at late times while $f_{\rm out}$ is a proxy for the fraction of the gas that is in the outflow at late times; both $f_{\rm disk}$ and $f_{\rm out}$ are normalized to the initial total gas mass of $1.59 \times 10^{10} M_\odot$.

In varying the AGN wind parameters, we are not guaranteed that the resulting BH mass will be consistent with the $M_{BH} - \sigma$ relation. In such cases, the effects of the AGN wind might not be realistic because of the unphysical BH mass. To quantify this, we present results with and without the radiation pressure feedback model explored in DeBuhr et al. (2011). Our simple model of radiation pressure feedback produces model galaxies roughly on the observed $M_{\rm BH} - \sigma$ correlation for $\tau \sim 20$, the value used here (DeBuhr et al., 2011). For the present purposes these calculations are useful primarily because they allow us to study the effects of AGN wind feedback for systems in which the BH is guaranteed to be approximately on the $M_{BH} - \sigma$ relation. We also separately carry out simulations with wind feedback alone.

4.3.1 Effects of AGN Winds

Black hole accretion and star formation rates

Figure 4.1 shows the net accretion rate into the black hole, $\dot{M}_{in}$, and the star formation rate, $\dot{M}_*$, as a function of time (summed over both galaxies) for three different simulations: the fiducial simulation (black curve) with radiation pressure ($\tau = 20$) and AGN wind feedback ($\tau_w = 5$ and $v_w = 10,000\,{\rm km\,s^{-1}}$), a run identical to the fiducial run but without the wind feedback (gray), and a run with both wind and radiation pressure feedback that includes Compton heating/cooling in the thermodynamics of the gas (blue). We first describe the effects of the AGN wind and later return to the role of Compton heating/cooling.

The inclusion of the wind feedback has little effect on either the accretion or star formation rate before the final coalescence of the two galaxies at $t \sim 1.7$ Gyr. This is *a priori* surprising because equation (4.6) implies that for a given set of conditions at large radii (that determines $\dot{M}_{\rm visc}$) the BH accretion rate at small radii is a factor of $1+\tau_w \eta c/v_w = 16$ smaller for the simulation with AGN winds than for the run with just radiation pressure. After a small number of time steps, however, the feedback due to radiation pressure is so effective in all of the simulations in Figure 4.1 that the physical conditions at small radii quickly adjust so that there is a balance between radiation pressure and gravity. This sets the BH accretion rate $\dot{M}_{in}$ to be $\sim f_g \sigma^4/(\tau \eta c G)$ (DeBuhr et al., 2010) independent of the presence of the AGN wind removing mass from the nuclear region (where f_g and σ are the gas fraction and velocity dispersion at small radii, respectively).

Although the AGN wind feedback has little effect on the early time star formation and BH accretion, Figure 4.1 shows that after final coalescence both the BH accretion rate and the star formation rate decrease significantly more rapidly with the inclusion of the AGN wind. The effects of the BHs feedback are maximized at and after final coalescence because this is when the BH reaches its final mass (to within a factor of a few) and when the BH accretion rate is largest. Thus, the dynamics at and after

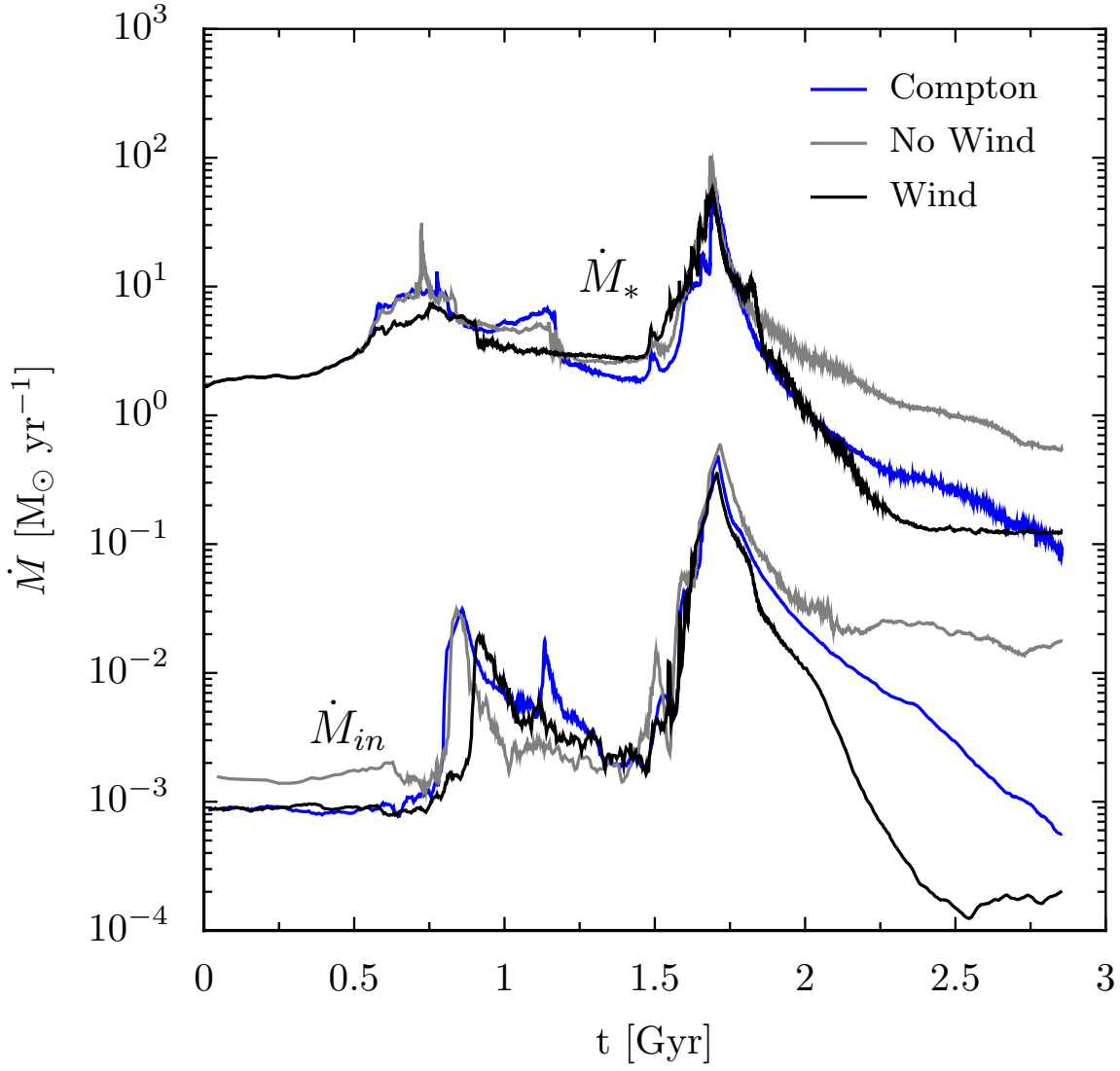

Figure 4.1: The star formation rate, $\dot{M}_*$, and accretion rate into the black hole, $\dot{M}_{in}$, as a function of time for the fiducial simulation with both AGN wind and radiation pressure feedback (run 'wp5-10' in Table 1; black), the run with only the radiation pressure feedback (run 'po'; gray), and the run that included Compton heating (run 'wpcomp'; blue).

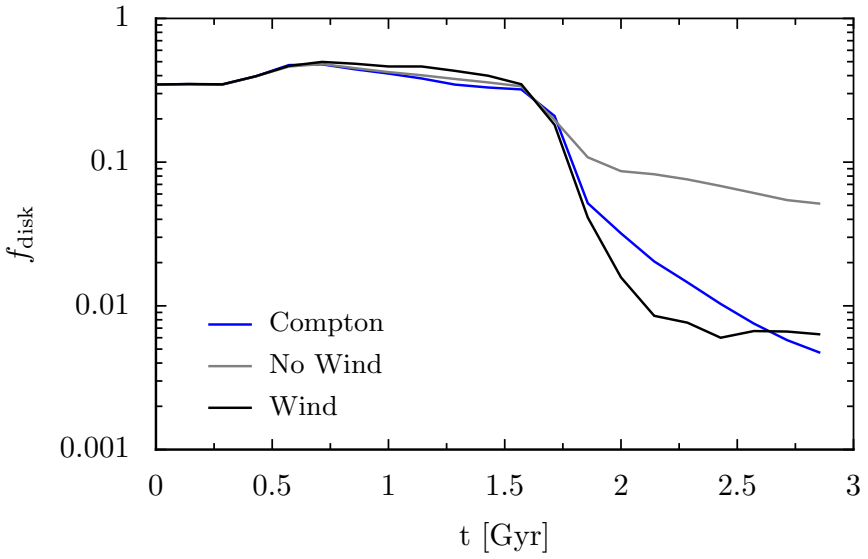

Figure 4.2: The fraction of the total gas mass inside a sphere of radius 3 kpc (relative to the total *initial* gas mass) centered on the black hole for the same three runs shown in Fig. 1. When the AGN wind model is included, the central material is rapidly ejected after final coalescence ($t \sim 1.7$ Gyr).

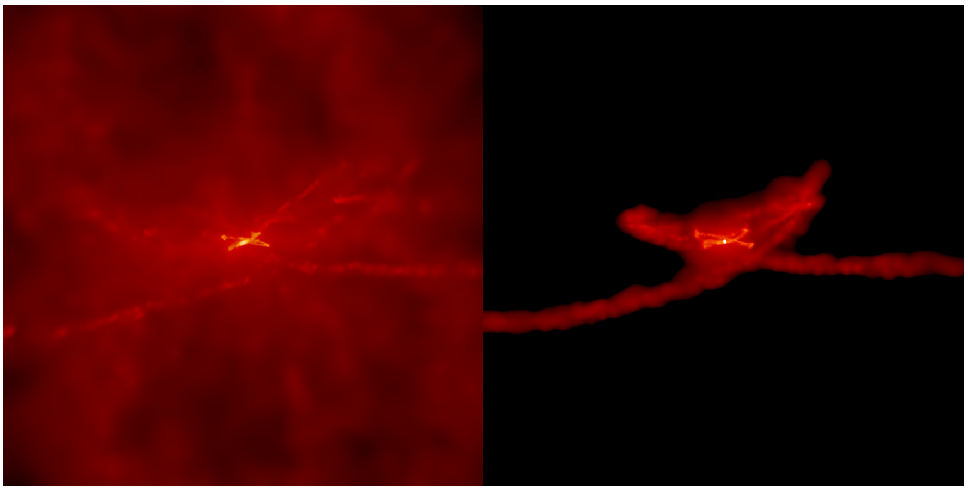

Figure 4.3: The projected gas density for the fiducial simulation (left) and the run without AGN wind feedback (right) at a time just after the final merger ($t = 1.71$ Gyr). Brighter color corresponds to higher density. The images are edge-on to the plane of the orbit and the box size is 280 kpc. While both simulations have material at large distance in tidal tails, there is significantly more material out of the orbital plane with AGN wind feedback. These images were generated using SPLASH (Price, 2007).

final coalescence is the most sensitive to the details of the feedback physics.

To assess why the late-time accretion and star formation are suppressed by the inclusion of the AGN wind, Figure 4.2 shows the gas mass fraction (normalized to the gas mass at the start of the simulation) within 3 kpc of the BH as a function of time, for the same three simulations as in Figure 4.1.[1] Tidal interactions drive gas into the center of the two galaxies (or the merged remnant) after the first close passage ($t \sim 0.5$ Gyr) and at final coalescence ($t \sim 1.7$ Gyr), maintaining a large nuclear gas fraction in spite of the intense star formation. The resulting increase in the BH accretion rate (seen also in Fig. 4.1) significantly increases the strength of the AGN feedback. In the simulation including AGN winds, this feedback efficiently removes material from the central regions of the galaxy, reducing the amount of gas inside the central 3 kpc of the merged system by a factor of ~ 10 relative to the simulation without explicit AGN winds.

Figure 4.3 shows images of the projected gas density for the fiducial simulation (*left*) and the corresponding simulation without the AGN wind (*right*) at $t = 1.71$ Gyr, shortly after final coalescence. The images are 280 kpc on a side and show a roughly edge-on view of the orbital plane of the two galaxies. While there is material at large distances in the simulation without the AGN wind, these features are the tidal tails generated during the merger and most of this material is near the orbital plane. Thus our simple implementation of radiation pressure feedback is not efficient at unbinding gas from the galaxy, though it is very effective at regulating the growth of the BH itself (DeBuhr et al., 2011). By contrast, in the simulation with the AGN wind, Figure 4.3 (left panel) shows that there is significantly more material blown out of the galaxy, especially in the directions perpendicular to the orbital plane. Quantitatively, at the end of the simulation the mass of gas at large distances ($|z| > 10$ kpc) from the orbital plane is $\simeq 3 \times 10^9 M_\odot$ in the simulation including the AGN wind, about 20 times larger than in the simulation with only radiation pressure feedback (see Table 4.1 and Fig. 4.6 below). A corollary of this efficient removal of gas by the AGN wind is that the total stellar mass formed during the simulation is $\sim 20\%$ smaller in the case with the AGN wind; most of this suppression in star formation happens at late times, after the final coalescence of the two galaxies (see Fig. 4.1).

Impact on the ISM

The evacuation of the central part of the galaxy by the AGN wind would not be surprising if the majority of the material ejected was explicitly added to the wind by our deposition of momentum (i.e., if the unbound mass was primarily material that was explicitly 'kicked'). We find that this is not the case. At the end of the fiducial simulation ($t = 2.85$ Gyr), of the 33,028 gas particles at large transverse position ($|z| > 10$ kpc), only 8,904 of the particles have been explicitly kicked. The other 72%

[1]The precise choice of 3 kpc is somewhat arbitrary but the results in Figure 4.2 are relatively robust to changes in this choice.

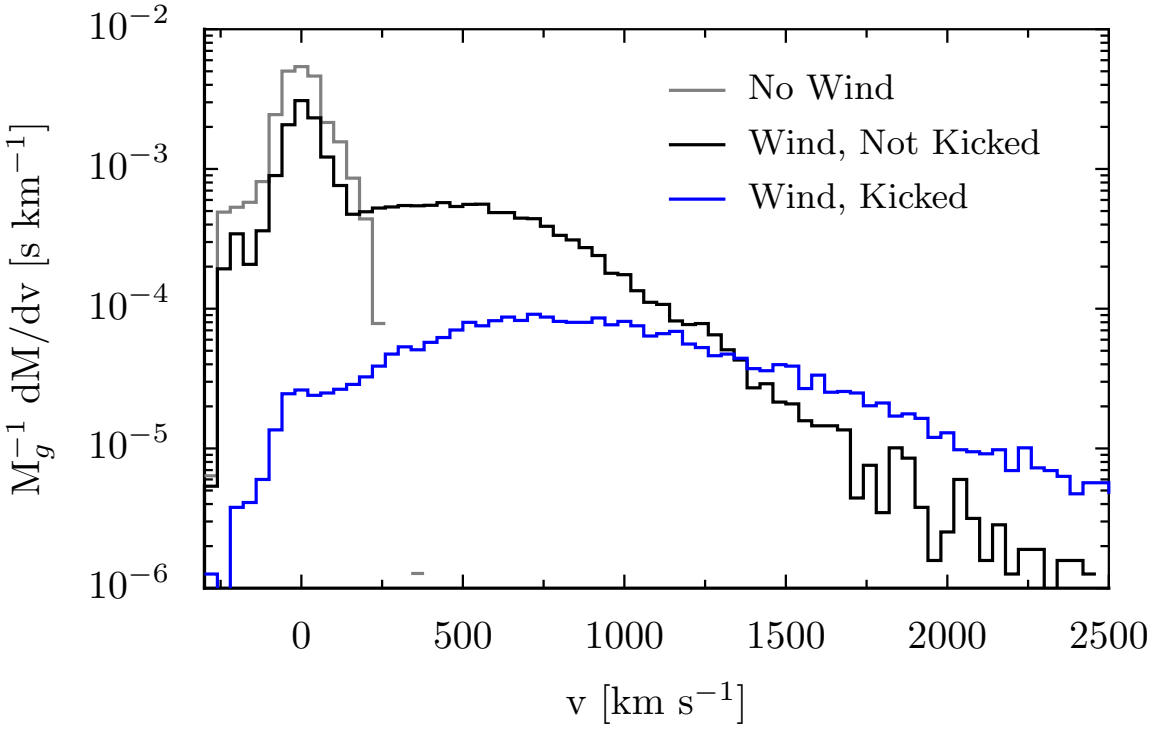

Figure 4.4: Effects of AGN winds on the distribution of radial velocities of the gas particles (relative to the black hole) at the end of the simulation. Few gas particles have velocities greater than $\sim 200\,\mathrm{km\,s^{-1}}$ in the run with only radiation pressure (run 'po'; grey). By contrast, in the fiducial simulation with the AGN wind, a significant fraction of the particles have velocities above a few 100 $\mathrm{km\,s^{-1}}$. About 25% of these outflowing particles were explicitly added to the wind and kicked with an initial wind velocity of 10,000 $\mathrm{km\,s^{-1}}$ (blue), while the rest were not explicitly added to the wind (black) initially but were accelerated due to hydrodynamic interactions with the 'kicked' high-speed particles.

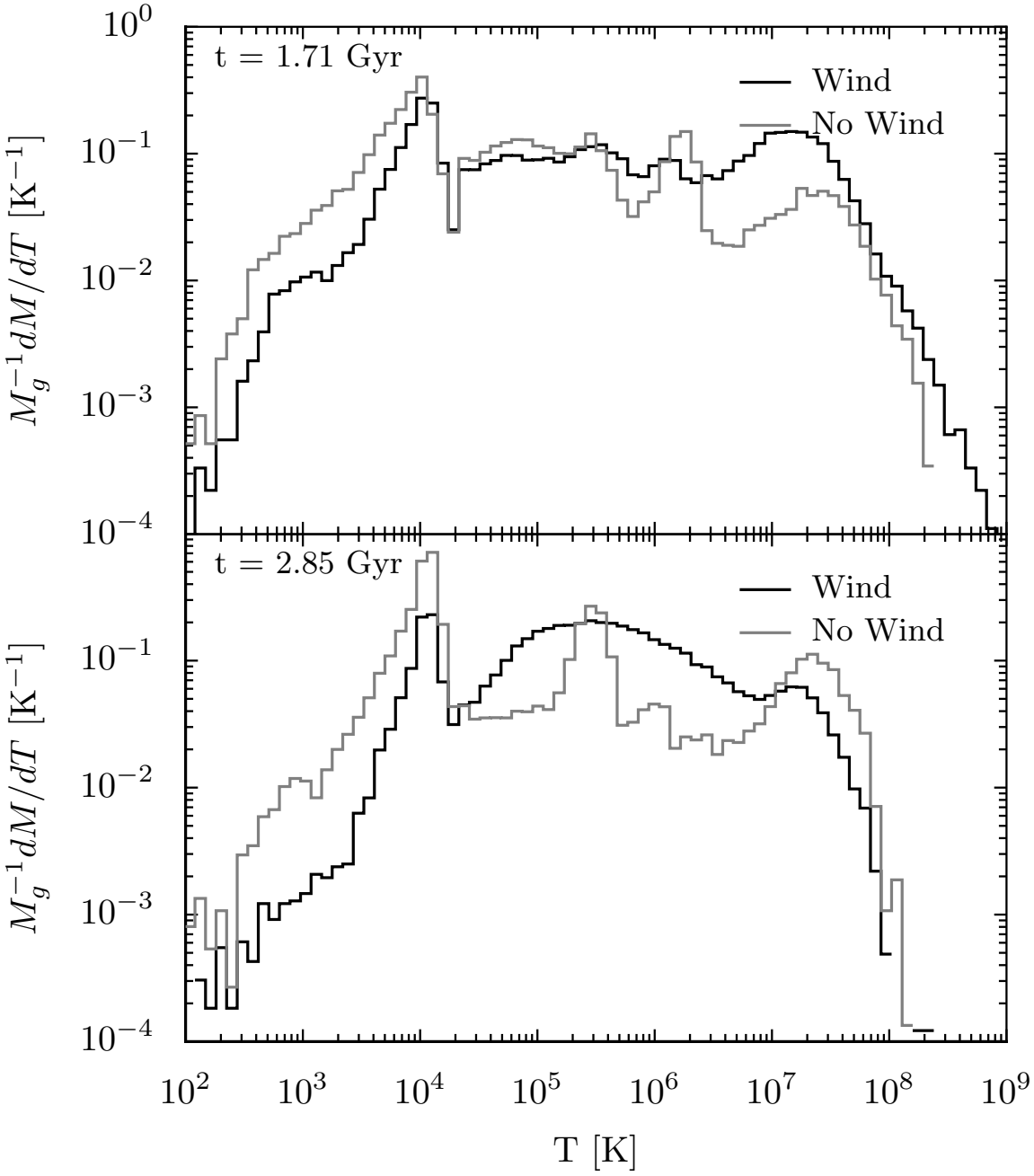

Figure 4.5: Effects of AGN winds on the mass weighted distribution of gas temperatures. The same two simulations as in Fig. 4 are shown at two times: near the peak of accretion at 1.71 Gyr (*top*), and at the end of the simulation at 2.85 Gyr (*bottom*). The temperature distributions are normalized to have a unit area. The excess of gas at high temperatures near the peak of BH accretion (*top*) in the case with wind feedback is due to the shock heating of the ISM gas.

(82% by mass) have been ejected because of hydrodynamic interactions with wind material. In addition, at any time only a small fraction $\sim 5\%$ of the gas inside R_{acc} (the accretion/feedback region) has been explicitly added to the wind. These results demonstrate that the majority of the galactic outflow arises self-consistently due to the interaction between the AGN wind that we initialize and the surrounding ISM.

Figure 4.4 illustrates this point in a different way: here we show the radial velocities (relative to the BH) of the gas particles at the end of the simulation, without (gray) and with (black and blue) wind feedback. Those particles that *have not* been explicitly kicked and added to the wind are shown in black while those that have been explicitly kicked are shown in blue. In the case with the AGN wind, there is a significant fraction of the gas with velocities $\sim 300 - 1000\,\mathrm{km\,s^{-1}}$, larger than *any* of the gas in the simulation without the wind feedback (gray). Moreover, the outflow velocities are similar for particles that have, and have not, been explicitly kicked. The particles that are explicitly kicked receive initial impulses of $v_w = 10,000\,\mathrm{km\,s^{-1}}$ and yet have final speeds of a few thousand $\mathrm{km\,s^{-1}}$. This result indicates that the wind we initialize sweeps up a significant amount of material in the ISM of the surrounding galaxy, driving additional gas out of the galaxy at high velocities $\sim 300-1000\,\mathrm{km\,s^{-1}}$.

Figure 4.5 shows the mass weighted temperature distribution (normalized to the total gas mass) near the peak of accretion ($t = 1.71$ Gyr; *top*) and at the end of the simulation (t = 2.85 Gyr; *bottom*) for the run with AGN wind feedback (black) and without (gray). The presence of the AGN wind leads to a significant amount of mass heated to above $\sim 10^7$ K when the BH is near its peak accretion rate (*top* panel in Fig. 4.5). This is due to gas that has been shock heated by the AGN wind. Much of this shock heated gas is ultimately able to escape the host galaxy – this gas expands outwards and cools adiabatically, leading to the large excess of $\sim 10^{5-6}$ K gas at the end of the simulation with the AGN wind (*bottom*).

In our calculations that include a simple treatment of inverse Compton scattering off of the AGN's radiation field, we take the Compton temperature to be $T_C = 2\times10^7$ K, the average observed value (Sazonov et al., 2004). This is similar to the peak in the temperature distribution we find in simulations without Compton scattering (*top* panel of Fig. 4.5). As a result Compton scattering mildly suppresses the high temperature tail of the gas shock heated by the AGN wind. This in turn suppresses the amount of mass blown out of the inner regions of the galaxy at late times (see Fig. 4.2). Nonetheless, there is still a factor of $\sim 3-10$ times less gas in the inner 3 kpc in the simulation with the AGN wind and Compton cooling relative to the simulation without the AGN wind. In addition, the star formation rate and BH accretion rate are significantly lower at late times even when Compton cooling is taken into account (Fig. 4.1).

4.3.2 Dependence on Feedback Model Parameters

In the previous section we demonstrated that an AGN wind generated at small radii can produce a galaxy-wide outflow that unbinds several $10^9\,M_\odot$ of gas and suppresses star formation in its host galaxy. In this section we explore in more detail how this phenomenon depends on the properties of the AGN wind.

To quantify the effects of the AGN wind, we calculate the following quantities in all of our simulations and list the results in Table 4.1: (1) the final BH mass $M_{BH,f}$, (2) the total mass of new stars formed by the end of the simulation, $M_{*,f}$, (3) the total mass of new stars formed after the peak of star formation,[2] $M_{*,p}$, (4) the fraction of the gas mass within 3 kpc of the BH at the end of the simulation, $f_{\rm disk} = M_{g,r<3{\rm kpc}}/M_{g,tot}$, and (5) the fraction of the gas mass at large distances ($\gtrsim 10$ kpc) above the orbital plane at the end of the simulation, $f_{\rm out} = M_{g,|z|>10{\rm kpc}}/M_{g,tot}$. The fractions $f_{\rm disk}$ and $f_{\rm out}$ are both normalized to the *initial* total gas mass of $1.59 \times 10^{10} M_\odot$ (from both galaxies); $f_{\rm disk}$ is a proxy for how much gas remains in the galaxy while $f_{\rm out}$ is a proxy for the fraction of the gas that is in the outflow at late times. Table 4.1 also quotes $M_{\rm out}$, the absolute mass in the outflow at the end of the simulation.

Figure 4.6 compares these key quantities for simulations utilizing only the AGN wind feedback model (triangles) and for simulations with both radiation pressure and AGN wind (crosses). For comparison, we also show the results of the simulation with only radiation pressure feedback, taking $\tau = 20$ (dotted lines). In the *left* set of panels, we fix $\tau_w = 5$ and vary the wind speed from $3,000 - 10,000\,{\rm km\,s^{-1}}$. In the *right* set of panels, we fix $v_w = 10,000\,{\rm km\,s^{-1}}$ and vary τ_w from $1 - 10$.

Figure 4.6 (*left* panel) shows that the final BH mass is relatively independent of the speed of the AGN wind for a given value of τ_w. By contrast, for simulations with the AGN wind model alone, the *right* panel shows that the final BH mass decreases by a factor of ~ 10 as τ_w increases from $1 - 10$.[3] This is consistent with the analytic results of King (2003) and Murray et al. (2005), and the numerical results of DeBuhr et al. (2011), in which the final BH mass decreases linearly with the total momentum supplied by the AGN, be it in the form of a wind or radiation. In particular, when the accretion rate is Eddington limited, the net force associated with the feedback is $\propto \tau_w L_{edd} \propto \tau_w M_{BH}$ (eq. 4.4). Thus the BH mass at which feedback is able to overcome the gravity of the gas in the galactic nuclei scales as $M_{BH} \propto \tau_w^{-1}$.

Although the BH mass is only a weak function of v_w at fixed τ_w, the properties of the gas at the end of the simulation depend strongly on v_w (bottom, left panels in Fig. 4.6). Specifically, a larger wind speed v_w at fixed τ_w leads to more efficient blow out of gas from the galaxy at late times (smaller $f_{\rm disk}$ and larger $f_{\rm out}$). For a given value of τ_w, the momentum flux in the outflow ($\dot{p}_w = \tau_w L/c$; eq. 4.4) is independent

[2] We distinguish between $M_{*,p}$ and $M_{*,f}$ because Figure 4.1 shows that the AGN wind's largest effect on the star formation history is at late times, after the peak of BH accretion and star formation.

[3] The same effect is much less evident in the simulations with radiation pressure and the AGN wind (crosses in the *right* panels) because the former largely sets the BH mass.

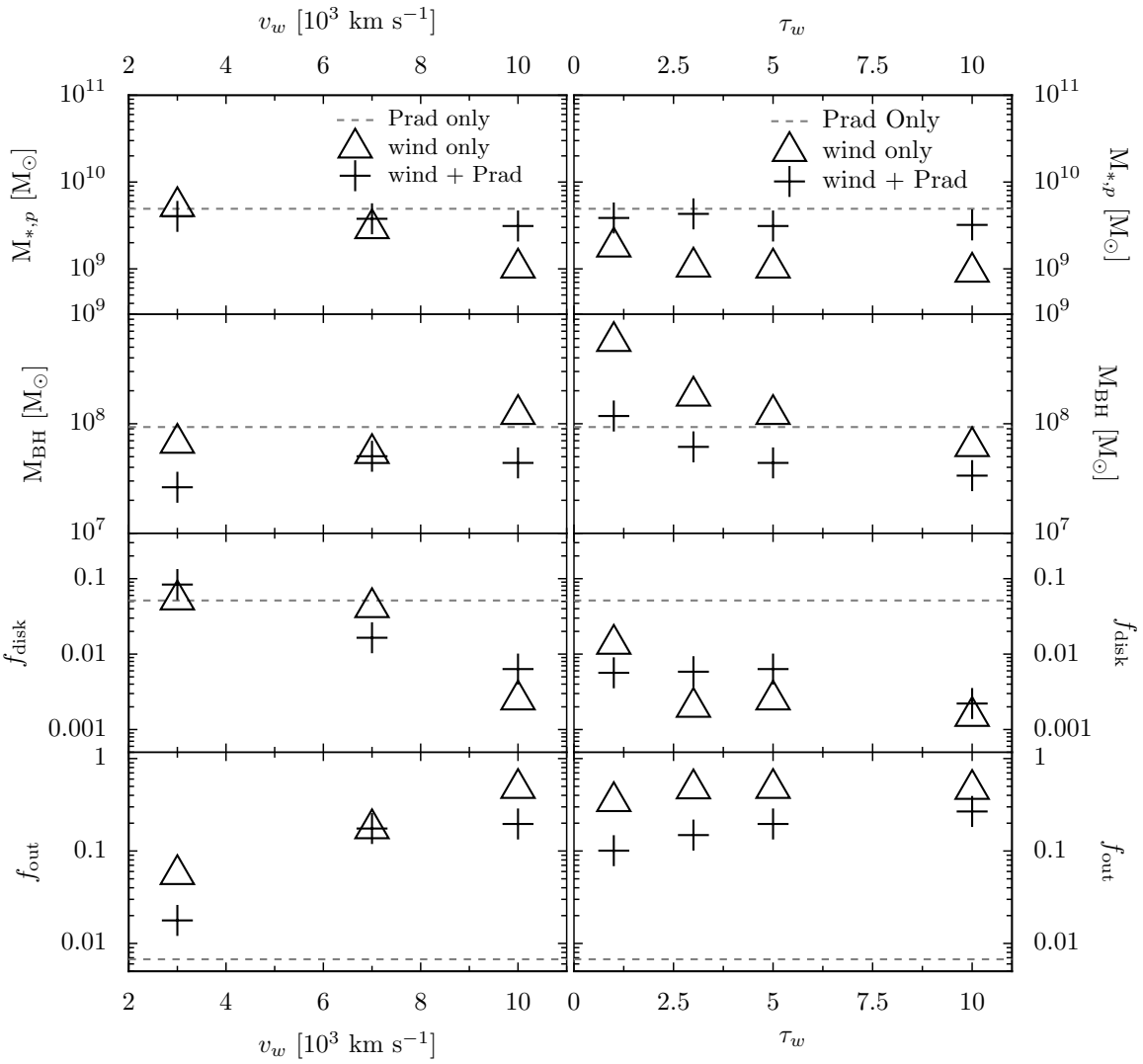

Figure 4.6: Key quantities characterizing the effects of the AGN wind model as a function of wind speed v_w (left column) and momentum flux τ_w (right column); see Table 1 for more details. These results quantify describe how the properties of the galaxy merger remnant at the end of the simulation depend on the parameters characterizing the AGN wind at small radii. In each panel, the triangles label the runs with only the AGN wind feedback, the crosses label the runs with both AGN wind and radiation pressure feedback, and the dashed line is for the simulation with only radiation pressure feedback. The four rows (from top to down) show: the mass $M_{*,p}$ of new stars formed after the peak of star formation during the simulation; the final black hole mass $M_{BH,f}$; the mass fraction $f_{\rm disk}$ of gas at the end of the simulation within 3 kpc of the black hole, and the gas mass fraction $f_{\rm out}$ at the end of the simulation that is at large distances from the orbital plane: $|z| > 10$ kpc . Both $f_{\rm disk}$ and $f_{\rm out}$ are normalized to the total initial gas mass in the system.

of v_w. By contrast, the energy flux in the outflow ($\dot{E}_w = \dot{p}_w v_w$) increases for a larger wind speed. Thus a larger wind speed leads to more efficient shock heating of the gas in the galactic nucleus. A larger value of τ_w has a similar effect, increasing both the momentum and energy fluxes in the wind, and producing a more powerful galaxy-scale outflow (bottom, right panels in Fig. 4.6).

Overall, then, the galaxy-wide outflow is a consequence of both the wind launched from small radii sweeping up and driving out ambient gas and the wind generating a shock that heats and unbinds ambient gas. This is why the gas content in the outflow – as measured by $f_{\rm out}$ in Figure 4.6 – increases with both increasing v_w and increasing τ_w. In general the simulations with AGN wind feedback alone have somewhat higher outflow rates than the simulations with AGN winds and radiation pressure. The reason is that the feedback is then provided entirely by the wind, enabling it to be more effective and unbind a larger amount of gas.

The mass of new stars formed in our simulations decreases for larger v_w and/or τ_w (top panels in Fig. 4.6). This is a simple consequence of the galaxy-scale outflow being more powerful for larger v_w and/or τ_w. The net effect of the outflow on the stellar mass formed in the simulation is, however, relatively modest (typically $\sim 10 - 20\%$). The AGN wind's most prominent effect on the star formation history is that it can suppress the late-time star formation, as highlighted in Figure 4.1. It is also important to note, however, that the outflow does not always have this effect. For example, the top left panel of Figure 4.6 shows that simulations with outflows having $\tau_w = 5$ and $v_w = 3000\,{\rm km\,s^{-1}}$ form a very similar amount of new stars (both in total and after the peak of star formation) to simulations with the radiation pressure feedback model alone. This is consistent with the fact that for these parameters, the outflow does not appreciably change the gas content in the galactic disk ($f_{\rm disk}$ in Fig. 4.6), although it does unbind a modest amount of additional gas $\sim 3 \times 10^8 {\rm M}_\odot$ (see $f_{\rm out}$ in Fig. 4.6 and M_{out} in Table 4.1).

4.3.3 Numerical Tests

We argued in §4.3.1 and 4.3.2 that the galactic outflow seen in our simulations is a consequence of both the AGN wind sweeping up ambient gas (momentum conservation) and the AGN wind shock heating ambient gas and unbinding it (energy conservation). The former mechanism does not depend sensitively on the thermodynamics of the gas, while the latter does. As described in §4.2.5 we modified the ISM equation of state of Springel and Hernquist (2003) in order to include two-body cooling at solar metallicity; we also included a simple treatment of inverse Compton scattering off of the AGN's radiation field in some of our simulations (see Fig. 4.1).

To further assess the sensitivity of our results to the thermodynamics of the gas, we carried out a number of additional tests. In particular, two extremes are to use the Springel and Hernquist (2003) model as is (in which gas that deviates from the equilibrium equation of state relaxes back on a timescale different from, and typically

Table 4.2: Resolution Test

Property	High	Fid	Low
$M_{*,t}$ $[10^9 \mathrm{M}_\odot]$	11.5	10.9	10.2
$M_{BH,f}$ $[10^7 \mathrm{M}_\odot]$	4.77	4.38	5.28
f_{disk}	0.012	0.006	0.004
f_{out}	0.166	0.196	0.307
M_{out} $[10^9 \mathrm{M}_\odot]$	2.65	3.13	4.89

Simulation properties are the same as those of the fiducial simulation in Table 1. The three simulations differ only in the mass resolution, with a total of 1.6×10^5 (low), 4.8×10^5 (fid), and 1.6×10^6 (high) particles.

longer than, the true cooling time), or to force gas to return to the effective equation of state of Springel and Hernquist (2003) instantaneously (thus removing the possibility of strong shock heating unbinding gas). The results of these calculations with our standard AGN wind parameters are given in Table 4.1, labeled wpsh and wpinst, respectively. In both cases, the AGN wind drives a galaxy-scale outflow with an ejected mass $\sim 3 \times 10^9 \mathrm{M}_\odot$, very similar to our fiducial simulation. However, these 'extreme' ISM models have effects that are not surprising: Springel and Hernquist (2003)'s equation of state (in which the gas effectively cools more slowly) is more effective at suppressing star formation and clearing gas out of the nucleus (wpsh), while the simulation with instantaneous cooling (wpinst) retains a larger nuclear gas disk at the end. Overall, however, these differences are modest – they are smaller, e.g., than the uncertainties introduced by the relatively poor current constraints on the total momentum/energy flux in AGN winds (τ_w). This test demonstrates that our treatment of the ISM thermodynamics is probably sufficiently accurate to assess the impact of AGN winds at the order of magnitude level. However, future calculations that incorporate a more realistic multi-phase, turbulent ISM (e.g., Hopkins et al. 2011) will be very valuable.

Recently, Durier and Dalla Vecchia (2011) showed that after injection of energy, either thermally or kinetically, inaccuracies can arise in the subsequent evolution of the SPH particles when each is assigned a separate timestep, as occurs in GADGET. To ascertain if our feedback is subject to the innacuracies they report, we reran the fiducial simulation with an implementation of their timestep limiter. All of our key qualitative conclusions are unchanged, though there is a modest (~ 30 %) change in the post merger star formation and disk fraction (f_{disk}).

Figure 4.7 shows the radial velocities of the SPH particles (relative to the BH) at the end of the simulation for three runs that differ only in the mass resolution with 1.6, 4.8, and 16.0 $\times 10^5$ particles, respectively. For the two higher resolution simulations, the distributions are quite similar for the bulk of the disk ($v \sim 0$) and outflow ($v \sim 500 - 1000\,\mathrm{km\,s^{-1}}$), though the high velocity tails differ somewhat. Table 4.2 compares the integrated quantities shown in Figure 4.6. The biggest difference

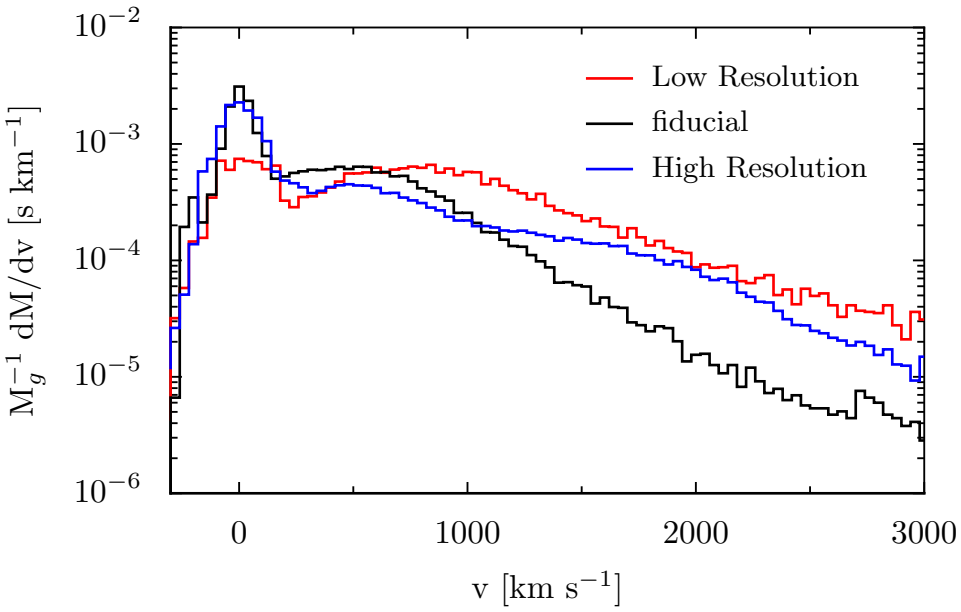

Figure 4.7: The distribution of radial velocities relative to the black hole for the gas particles in the fiducial simulation (black), the simulation at lower resolution (red) and the simulation at higher resolution (blue).

is that the highest resolution simulation retains more mass in a nuclear disk at late times. However, the mass in the outflow and the fraction of the mass in the outflow at late times are reasonably converged. The total mass of new stars formed and the final BH mass also do not change appreciably with resolution. We conclude that the effects of this model are reasonably well resolved at the fiducial resolution employed.

4.4 Discussion and Conclusions

We have carried out three-dimensional SPH simulations of the interaction between a high-speed outflow produced by an AGN and interstellar gas in the AGN's host galaxy. We show that this interaction can drive a large-scale galactic outflow that in some cases unbinds a significant fraction of the ISM of the host galaxy (see, e.g., King 2005 for closely related arguments). The AGN-driven galactic winds found here provide a possible explanation for the high velocity outflows observed in some post-starburst galaxies (Tremonti et al., 2007) and for the massive atomic and molecular outflows with $v \sim 1,000\,\mathrm{km\,s^{-1}}$ seen in local ultra-luminous infrared galaxies (ULIRGs) (Feruglio et al., 2010, Chung et al., 2011, Rupke and Veilleux, 2011, Sturm et al., 2011). We return to this below. Our specific calculations assume that AGN activity is triggered by major mergers of galaxies (as seen, for example, by Koss et al. 2010), but we suspect that the results presented here are much more general and ap-

ply relatively independent of the physical mechanism(s) that drive gas into the central ~ 100 pc of galaxies. The physically-motivated model utilized here for AGN wind feedback is easy to implement (§4.2.4) and could readily be applied in other contexts, including high resolution simulations of galactic nuclei and cosmological simulations of BH growth and evolution.

Our results provide a quantitative mapping between the properties of an AGN wind in the vicinity of the BH and the resulting large-scale galaxy-wide outflow (Table 4.1 and Fig. 4.6). We have parametrized the AGN wind at small radii in terms of its speed v_w and momentum flux $\dot{p}_w = \tau_w L/c$ – the corresponding energy flux in the wind is $\dot{E}_w = 0.5\,\dot{p}_w\,v_w = 0.5\,\tau_w(v_w/c)\,L$.

We find that an AGN wind with $v_w \sim 10,000\,\mathrm{km\,s^{-1}}$ – typical of, e.g., broad-absorption line quasars – produces a galactic outflow with velocities $\sim 1,000\,\mathrm{km\,s^{-1}}$. This reduction in velocity is a consequence of the AGN wind sweeping up and driving out $\sim 5-10$ times as much mass as was in the wind initially (e.g., Fig. 4.4). Quantitatively, we find that the AGN-driven galactic outflow unbinds $\sim 1-5\times10^9 M_\odot$ of gas, $\sim 10-40\%$ of the initial gas in the two merging galaxies (which are Milky Way-like spirals in our calculations). This is true for a wide range of outflow models, covering $\tau_w \sim 1-10$, $v_w \sim 7,000-10,000\ \mathrm{km\,s^{-1}}$, and with and without the radiation pressure feedback model from DeBuhr et al. (2010, 2011). Not surprisingly, AGN winds with larger momentum and energy fluxes (larger τ_w and v_w) are more effective at driving galaxy-scale outflows (Fig. 4.6).

The mass outflow rate from the vicinity of the galaxy is somewhat noisy and thus difficult to directly measure in the simulations. The average outflow rate relative to the star formation rate can, however, be readily estimated by comparing the total unbound mass ($M_{\rm out}$ in Table 4.1) with the mass in new stars formed in the simulation ($M_{*,f}$ and $M_{*,p}$ in Table 4.1, where $M_{*,f}$ is the total mass of new stars formed and $M_{*,p}$ is the mass of new stars formed after the peak of star formation). This comparison implies that the average mass outflow rate is typically comparable to the star formation rate; after the peak of star formation in the merger, which is when the BH reaches its final mass, the average outflow rate often exceeds the corresponding star formation rate by factors of a few.

Physically, we find that the properties of the galaxy-wide outflow are determined by both the momentum and energy fluxes in the AGN wind at small radii. A larger momentum flux implies that more mass can be swept out of the galaxy while a larger energy flux in the wind (e.g., larger v_w at fixed $\dot{p}_w$) leads to more shock heating of the ambient ISM. This shocked gas partially cools but retains enough thermal energy to contribute to driving the galaxy-wide outflow. For quantitatively accurate results we find that it is necessary to modify the Springel and Hernquist (2003) equation of state to properly include metal-line cooling and Compton heating/cooling as processes by which gas relaxes back to the effective equation of state that is used to calculate the ISM pressure (see §4.2.5).

To produce a galaxy at the end of the simulation that is on the $M_{BH}-\sigma$ relation

using only feedback by our AGN wind model, we require $\tau_w \gtrsim 5-10$ (see Table 4.1 and Fig. 4.6; the velocity dispersion of the remnant galaxy is $\simeq 170\,\mathrm{km\,s^{-1}}$ so that $M_{BH} \simeq 7\times10^7 M_\odot$ for galaxies on the mean $M_{BH}-\sigma$ relation). This required momentum flux is comparable to, although somewhat smaller than, the required momentum flux of $\dot{p}\sim 20\,L/c$ that DeBuhr et al. (2011) found using a simple model of radiation pressure feedback in which all particles in the vicinity of the BH feel a force $\propto \tau\,L/c$. The energy flux corresponding to $\tau_w\sim 5-10$ and $v_w\sim 10,000\,\mathrm{km\,s^{-1}}$ is $\dot{E}\sim 0.1\,L$, similar to the energy injection rate of $\sim 0.05\,L$ that Di Matteo et al. (2005) found was required to reproduce the $M_{BH}-\sigma$ relation (although they deposited thermal energy into ambient gas while we supply kinetic energy to a wind).

One important distinction that we find is between AGN driving galactic outflows and AGN outflows regulating the growth of the BH. For example, in our models with $\tau_w = 1$ and $v_w = 10,000\,\mathrm{km\,s^{-1}}$, the final BH mass is a factor of ~ 10 above the mean $M_{BH}-\sigma$ relation in calculations that only include AGN wind feedback. Also including the simple radiation pressure feedback model from DeBuhr et al. (2011) in the simulation resolves this discrepancy; the same AGN wind model then unbinds $\sim 10^9 M_\odot$ of gas, $\sim 10\%$ of the initial gas mass in the system. However, in spite of this outflow, the AGN wind neither regulates the BH growth nor has a significant effect on the average star formation in the system. This demonstrates that very powerful AGN outflows with $\tau_w\sim 3-10$ are required for the BH to have a substantial effect on either its own accretion history or the star formation in the surrounding galaxy. This conclusion is similar to that of Silk and Nusser (2010), who required a comparable momentum to eject gas from their model galaxies, and to that of Kaviraj et al. (2011), who found that simple models for the color evolution of early type galaxies required feedback similar in strength ($\dot{E}$ of a few percent) and duration (~ 200 Myr) to what we find here.

The galactic outflows found in our simulations with $v_w\sim 10,000\,\mathrm{km\,s^{-1}}$ and $\tau_w \gtrsim 3$ have properties broadly similar to those observed in some massive post-starburst galaxies (Tremonti et al., 2007) and in local ULIRGs (Feruglio et al., 2010, Chung et al., 2011, Rupke and Veilleux, 2011, Sturm et al., 2011). Moreover, it is striking that Sturm et al. (2011) inferred $\dot{p}_w\sim 10\,L/c$, i.e., $\tau_w\sim 10$, for the molecular outflows in local ULIRGs (these values are uncertain at the factor of ~ 3 level; see, e.g., Sturm et al. 2011 for more details). This is comparable to the outflow momentum flux we find is required to both suppress late time star formation during galaxy mergers and produce remnants approximately on the observed $M_{BH}-\sigma$ relation. This correspondence is encouraging, though it does not directly address the question of what mechanism powers such outflows in the first place. The relative role of star formation and AGN in powering the $\sim 1000\,\mathrm{km\,s^{-1}}$ molecular outflows is also unclear, with Sturm et al. (2011) presenting evidence from OH observations in favor of AGN, while Chung et al. (2011) argue that star-formation is the dominant power source based on their CO observations. In addition, in some samples of post-starburst galaxies, the observed outflows appear consistent with those driven by star formation

(Coil et al., 2011).

From the theoretical perspective, the biggest uncertainty in applying our results is the uncertainty in the absolute momentum/energy flux in AGN outflows at small radii. This uncertainty remains even for the most well-characterized outflows, those of broad-absorption line (BAL) quasars. In theoretical models in which BAL outflows are produced by radiation pressure on lines in the vicinity of the broad-line region, the predicted momentum flux is typically $\lesssim L/c$, i.e., $\tau_w \lesssim 1$ (Murray et al., 1995). This follows from the fact that (observationally) the lines do not cover the entire continuum and thus cannot absorb the entire continuum momentum flux. This constraint is less clear for low-ionization BALs (in which the lines cover more of the continuum), but probably remains reasonably accurate. One way out of this conclusion is if magnetic fields contribute to accelerating BAL outflows (as in, e.g., Proga 2003) since this can increase both the mass flux and terminal velocity of the outflow. There are observational estimates that the momentum flux in some low-ionization BAL outflows may indeed be $\gtrsim L/c$ (Moe et al., 2009, Bautista et al., 2010, Dunn et al., 2010), though these are difficult observations to interpret and they have complicated selection effects.

In addition to line-driven winds, it is possible that even more powerful outflows are driven during evolutionary phases distinct from optically bright quasars. The two most promising from our point of view are: (1) outflows driven by radiation pressure on dust during phases when the ISM around the AGN is optically thick to far-infrared radiation (Murray et al., 2005, DeBuhr et al., 2010). In this case the momentum flux in a small-scale AGN wind can in principle reach $\sim \tau L/c$, where τ is the infrared optical depth of the galactic nucleus. Such an outflow is not directly seen in DeBuhr et al. (2011)'s simple implementation of radiation pressure feedback. However, this could easily be a limitation of the lack of a proper treatment of the infrared radiative transfer. Indeed, we expect that radiation pressure will inevitably drive a high-speed outflow off of the nuclear disk ('torus') at $\sim 1-10$ pc. (2) An additional source of powerful high-speed outflows can be produced if the fueling rate of the central AGN significantly exceeds Eddington (e.g., King 2003). In this case, the accretion disk becomes radiatively inefficient and much of the nominally inflowing mass is likely unbound (e.g., Blandford and Begelman 1999). The disparity in spatial scales between the horizon and where the AGN accretion rate is set ($\sim 1-10$ pc; e.g., Hopkins and Quataert 2010b) implies that it is very likely that there is a phase of super-Eddington fueling. The critical question is whether this phase lasts long enough to dominate the integrated properties of a black hole's outflow.

All of the calculations presented in this paper utilize the effective equation of state model of Springel and Hernquist (2003) (modified as in §4.2.5) to pressurize the ISM and prevent runaway gravitational fragmentation. This is a very simplistic treatment of ISM physics and in the future it is important to study the interaction between a central AGN and the surrounding ISM using more realistic models that approximate the turbulent, multi-phase structure of the ISM (e.g., Dobbs et al. 2011, Hopkins

et al. 2011).

Chapter 5

Stellar Disks in Aquarius Dark Matter Haloes

We investigate the evolution of stellar disks inserted into Aquarius dark matter halos and evolved in a full cosmological environment. We introduce the stellar disks into the Aquarius halos by first evolving the halo under the influence of a growing rigid disk potential from $z = 1.3$ to $z = 1.0$. The rigid potential is then replaced with live particles and evolved in the dark matter halo to $z = 0.0$. Regardless of the initial orientation of the disk, the inner parts of the halos contract under the action of the disk and change from prolate to oblate as the disk grows to the full size, We find that the majority of the stellar disks form bars that dominate the dynamics of the disk within the inner few scale radii. The disks heat continuously throughout the simulation and suffer a sharp increase in thickness and vertical velocity dispersion when the massive bars buckle. The heating signal is confounded by the bar, and no strong statements can be made linking the disk evolution to the halo substructure.

5.1 Introduction

The Aquarius suite of simulations (Springel et al., 2008) have proved very useful for numerical explorations of galaxy formation. Scannapieco et al. (2009) performed resimulations of a number of Aquarius halos including the effects of a realistic multi-phase, star-forming gas and found that disks form easily, but can be destroyed by mergers or disk instabilities. Expanding on the previous by focusing on the effects of the baryons on the dark matter halos, Tissera et al. (2010) found that the detailed structure of the halo depends on the specifics of how the halo was constructed. A new method of including idealized disks Aumer and White (2012), starting with a collapsing spherical cloud of cooling, star-forming gas, has recently been developed and applied to the Aquarius halos. Though not using Aquarius, Sales et al. (2011) used similarly selected dark matter halos to explore the effects of halo parameters on

the resulting galaxy, and found that the resulting galaxy morphology had more to do with the complete history of accretion rather than any property of the dark matter halo.

However, many of these studies have difficulty in reproducing galaxies as observed today. The simulated galaxies often end with too large a mass (Guo et al., 2010), or without the right amount of star formation (Scannapieco et al., 2009). Further, substructure can easily destroy disks, leaving too little mass in a disk component. Observationally, disk galaxies are thin (van der Kruit and Freeman, 2011). Numerically, however, they are startling easy to destroy or thicken (Purcell et al., 2009, Velazquez and White, 1999, Hopkins et al., 2009). Given the ease of destroying disks, one is left wondering how any disks survive to today, especially when the frequent impact of halo substructure is taken into account.

In this paper, we present simulations of stellar disks inserted into a number of the Aquarius halos. Rather than focusing on the full growth of the disk throughout the history of the halo, we consider the effects of the realistic setting of the Aquarius halos on a stellar disk that has already formed. The method presented can be thought of as a means to test the evolution of disk properties as they relate to the specific history of the dark matter halo in which they are embedded.

Much earlier work has studied stellar disks in a cosmological setting. Dark matter halos in ΛCDM cosmologies are found numerically to be generally triaxial (see, e.g., Bullock 2002, Allgood et al. 2006). This asymmetry in the halo can trigger the formation of bars (Heller et al., 2007a,b), which have important effects on the subsequent evolution of the disk. Bars can also form as a result of interactions with substructure (Romano-Díaz et al., 2008). Given this, it is no surprise that a large number of works easily produce bars. In a series of papers Curir et al. (2006) investigated disks, comprised of stars both with and without a gas component inserted into a cosmological context, albeit at a resolution lower than what we employ in this work, and find their model generically grows a bar. Both the effect of a stellar bar on the halo's evolution (Berentzen and Shlosman, 2006), and the effect of the halo on a stellar bar's evolution (Berentzen et al., 2006) have been considered in realistic dark matter halos. Including a live dark matter halo supports (rather than suppresses) bar formation (Athanassoula, 2002). Machado and Athanassoula (2010) consider the growth of bars in both circular and elliptical disks inserted into dark matter halos and the resulting loss of triaxiality in the halo. Stellar bars are also susceptible to the buckling instability, which has a dramatic effect on the dynamics of disks (Debattista et al., 2006, Martinez-Valpuesta et al., 2006, Martinez-Valpuesta and Shlosman, 2004).

Bars are not the only possible source of disk heating. Simulations of isolated halos with single mergers (Velazquez and White, 1999, Purcell et al., 2009, Hopkins et al., 2009, Moster et al., 2010), for cosmologically motivated histories of multiple mergers (Bournaud et al., 2007, Kazantzidis et al., 2008, 2009), and also including gas dynamics (Moster et al., 2010, 2011) all lead to the conclusion that substructure is

Run Name	Halo	Disk Orientation	M_d [10^{10}M$_\odot$]	R_d [kpc]	z_d [kpc]	Notes
AMinor	A5	Minor	5.00	3.00	0.60	
AMajor	A5	Major	5.00	3.00	0.60	
AMinorHalf	A5	Minor	2.50	2.38	0.48	
AMinorThird	A5	Minor	1.67	2.08	0.42	
AMinorGas	A5	Minor	5.00	3.00	0.60	initial gas fraction of 0.4
AMinorHR	A5	Minor	5.00	3.00	0.60	5×10^5 particles in disk
ANoDisk	A5	-	-	-	-	No disk
BMinor	B5	Minor	5.00	3.00	0.60	
BMajor	B5	Major	5.00	3.00	0.60	
BNoDisk	B5	-	-	-	-	No disk
CMinor	C5	Minor	5.00	3.00	0.60	
CMajor	C5	Major	5.00	3.00	0.60	
CMinorHalf	C5	Minor	2.50	2.38	0.48	
CMinorThird	C5	Minor	1.67	2.08	0.42	
CMinorGas	C5	Minor	5.00	3.00	0.60	initial gas fraction of 0.4
CNoDisk	C5	-	-	-	-	No disk
DMinor	D5	Minor	5.00	3.00	0.60	
DMajor	D5	Major	5.00	3.00	0.60	
DNoDisk	D5	-	-	-	-	No disk

Table 5.1: Simulation Parameters: Halo refers to the Aquarius halo (and resolution level) used in the simulation. If the disk normal was initially aligned with the halo minor axis or major axis the Orientation is Minor or Major respectively. M_d is the total mass of the disk model. R_d is the scale length of the disk and z_d is the scale height of the initial disk.

an effective source of disk heating. Transient spiral density waves can also heat disks (Fuchs, 2001, Minchev and Quillen, 2006), though this mechanism operates largely in the radial direction.

This work has some common features with the previous works, and will, thus, reflect some of their results. However, the Aquarius suite of simulations provides one of the most realistic settings, including well resolved substructure, in which to study galaxy evolution. The organization of this paper is as follows. Described in section 5.2 is the methodology used to insert the stellar disk into the halo. Section 5.2.4 gives the details of the simulations. The effects of the ramping procedure on the halo is given in section 5.3. In section 5.4 and 5.4.4 the main results of our fiducial disk model are given. Alternative disk models are explored in section 5.5. Finally, in section 5.7, we conclude with a discussion of the results.

5.2 Methods

To study the evolution of stellar disks in a full cosmological environment, we begin with a suite of dark matter haloes from the Aquarius simulations (Springel et al., 2008). We then add a stellar disk to each Aquarius halo in two phases. During the first phase – starting at $z = 1.3$ and ending at $z = 1.0$ – the dark matter is allowed to react to a rigid disk potential whose mass increases from zero at $z = 1.3$ to the desired final mass at $z = 1$. At the start of the second 'live' phase (at $z = 1.0$), the rigid disk is replaced with live simulation particles. This live disk is then evolved self-consistently along with all the dark matter particles to $z = 0$. Below we describe each step in detail.

5.2.1 Dark Matter Haloes

The high-resolution zoom-in simulations of dark matter haloes in the Aquarius project are chosen from a cosmological box that assumed a ΛCDM universe with $\Omega_\Lambda = 0.75$, $\Omega_m = 0.25$, $\Omega_b = 0.04$, $\sigma_8 = 0.9$ and $H_0 = 73\,\mathrm{km\,s^{-1}Mpc^{-1}}$.

In this work we select haloes A, B, C and D at the resolution level 5. This resolution level corresponds to dark matter particle masses of $\approx 3 \times 10^6 \mathrm{M}_\odot$, and a comoving gravitational force softening length of 685 pc. The virial mass of the four dark matter haloes at $z = 0$ is $1.49 \times 10^{12} M_\odot, 7.11 \times 10^{11} M_\odot, 1.61 \times 10^{12} M_\odot$, and $1.49 \times 10^{12} M_\odot$, respectively. Despite their comparable final masses, the four haloes have different merger histories. While each halo has a fair number of small subhalo mergers, the level of activity for infalling satellites above one tenth the disk mass M_d (chosen to be $5 \times 10^{10} M_\odot$ for the fiducial disk model) varies from halo to halo. Haloes A and B are relatively quiet after $z \sim 0.7$ when a subhalo of mass $\sim 0.3 M_d$ impacts in each. Halo C has a number of larger subhaloes in the latter part of our simulation ($z < 0.5$), where the most two massive subhaloes have masses of $0.22 M_d$ and $0.16 M_d$. Halo D has the most active history, with appreciable encounters spread throughout the simulation.

Scannapieco et al. (2009) resimulated these haloes with gas and found the $z = 0$ disk-to-bulge ratios to vary significantly. Halo C and D each had a disk-to-bulge ratio of around 0.25, whereas halos A and B had a ratio of less than 0.1 at the end of their simulations because of extended periods of strong mis-alignment between the cold gaseous and stellar components. These values were based on kinematic decompositions; a photometric decomposition generally gives larger values.

5.2.2 Phase 1: Adding a Rigid Disk

We modified a version of GADGET-2 (Springel, 2005) to add a rigid stellar disk potential to the existing dark matter particles. The potential corresponds to an

exponential disk of the density:

$$\rho(R,z,t) = \frac{M_d(t)}{4\pi R_d^2 z_d} e^{-R/R_d} \operatorname{sech}^2\left(\frac{z}{z_d}\right), \tag{5.1}$$

where R_d and z_d are the scale length and scale height of the disk, respectively, and $M_d(t)$ is the mass of the disk. The mass of the disk is increased linearly in the scale factor, which is approximately linear in time, from zero at $z = 1.3$ to the total mass, M_d, at $z = 1.0$.

The center of the disk is initially placed at the minimum of the gravitational potential of the main Aquarius halo at $z = 1.3$. The initial velocity of the disk is set to the velocity of the potential minimum. To orient the disk, we first determine the principal axes of the gravitational potential of the dark matter halo. To do this, we construct equipotential surfaces of the dark matter particles and fit ellipsoids to them. The disk normal is chosen to be aligned with either the minor or major axis of the halo at $z = 1.3$. We refer to these two disk orientations as "Minor" and "Major" in the rest of the paper.

During this phase of the simulation, each dark matter particle feels a force from this rigid potential in addition to the normal gravitational interactions with all the dark matter particles. These extra forces are applied in a self-consistent manner, with the disk center experiencing the third-law force pairs from each dark matter particle. This procedure assures that linear momentum is conserved and the disk center moves with the center of the main halo.

The orientation of the rigid potential is fixed during this phase. This choice appears appropriate since the dark matter haloes do not rotate much between $z = 1.3$ and 1.0. We do find, however, that the principal axes of the haloes can drift by up to 20 degrees between $z = 1.3$ and 1.0. This drift implies that if our disk's normal is initially aligned with one of the halo's axes at $z = 1.3$, it may become slightly misaligned by $z = 1.0$. We have performed test runs and found this slight offset to have no qualitative effect on the results of these simulations.

5.2.3 Phase 2: Live Disk

Phase 1 above allows the dark matter particles to respond adiabatically to the presence of a growing rigid disk potential between $z = 1.3$ and 1.0. Phase 2 begins at $z = 1.0$ when we add live disk particles to the simulations.

The initial conditions of the live disk particles are generated by creating a model of the full potential of the system, and finding an approximate solution to the Jeans equations. The potential of the disk is easily computed from the model density, but for the halo potential we perform a fit to the dark matter particle potentials at the end of phase 1 at $z = 1$ (excluding the contribution to the potential from the rigid disk). The halo particles are projected into coordinates centered on the disk with the

z axis aligned with the disk normal. The potential values of the halo particles are fit to the following functional form:

$$\Phi = v_c^2 \ln \left[1 + \frac{u^2}{R_c^2} \right] \tag{5.2}$$

where u is a similar ellipsoidal coordinate defined by

$$u^2 = z^2 + \frac{x^2 + y^2}{a_3^2}. \tag{5.3}$$

Here v_c, R_c and a_3 are parameters of the fit. This definition of u forces the description of the background halo potential to have one of its principle axes along the disk normal. This is a good assumption for the evolved halo in both the major and minor orientation. This definition also assumes a potential axisymmetric with respect to the disk normal direction.

Once the live disk particles are added at $z = 1$, the rigid disk potential is turned off and both the stellar and dark matter particles are allowed to evolve self-consistently until $z = 0$.

To test the stability of the live disks generated with this method, we have evolved the disk particles in isolation subject to a static background potential equal to the fitted halo potential in equation (5.2). The generated disks are stable over a long time and develop no significant structure.

5.2.4 Disk Parameters

We have run a suite of simulations with a range of disk parameters and properties to assess the robustness of our results. The main parameters of the simulations are summarized in Table 5.1.

Our fiducial disk model assumes a stellar disk mass of $M_d = 5 \times 10^{10} \mathrm{M}_\odot$, a scale length of $R_d = 3$ kpc, and a scale height of $z_d = 0.6$ kpc. These values are chosen to resemble the Milky Way's disk today (Jurić et al., 2008, McMillan, 2011). This is also a reasonable choice for $z = 1.0$ as disk size does not exhibit strong evolution between $z \sim 1.0$ and 0 (Trujillo et al., 2006). Each realization of the disk uses 2×10^5 stellar particles. The disk particles each has a comoving gravitational force softening of 137 pc. For each halo, we run two separate simulations for two disk orientations, in which the initial disk normal is either aligned with the minor or major axis of the halo at $z = 1.3$.

For a direct comparison between simulations without and with a disk, we run dark-matter-only simulations with the particle positions and velocities from the Aquarius $z = 1$ snapshot as initial conditions (labeled with 'NoDisk' in Table 5.1). Although the subsequent particle positions and velocities will not be identical to those in the original Aquarius runs due to differences in machine and numerical details, the properties of the haloes are very similar.

To quantify the dependence of our results on the assumed disk mass, we run additional simulations with one half and one third the fiducial disk mass in the minor orientation in the A and C halos (labeled 'Half' and 'Third'). The scale lengths are reduced consistent with the observed relation, $R_d \propto M_d^{1/3}$ (Shen et al., 2003).

Two additional simulations are performed with haloes A and C that include a gaseous component with initial gas fraction of $f_g = 0.4$. This component is comprised of 10^5 SPH particles. The gas particles are initialized with the same radial profile as the stellar component, but the vertical structure is initialized in hydrostatic equilibrium. The gas used in these runs is not star forming and does not cool. The motivation for including such a gaseous component is to bracket the ends of possible disk models.

Finally, to determine if our results are converged with respect to the stellar disk particle number, we perform a simulation of the AMinor disk with 5×10^5 instead of 2×10^5 stellar particles. This run is listed as 'AMinorHR' in Table 5.1.

5.3 Effects of Rigid Stellar Disks on Dark Matter Haloes

In this section we discuss the effects of the rigid disk potential on the shapes and orientations of the dark matter haloes during the disk growing phase of the simulations ($z = 1.3$ to 1). By comparing our simulations with the original Aquarius dark-matter-only haloes, we can quantify how the presence of stellar disks in more realistic simulations alter the distributions of the dark matter.

To quantify the triaxiality of each halo, we determine the principal axes by constructing equipotential surfaces near the center of the halo with the procedure discussed in Sec 2. In general, the equipotential surfaces are fit well by ellipsoids, failing to be ellipsoidal only in the presence of significant substructure. In haloes B and D, there are significant subhaloes near the position of the disk initially, so the fit to an ellipsoid fail for a few potential bins. Nevertheless, for most of the potential bins (which translate roughly into values of the radius) and for most times, the fit performs very well.

Figs. 5.1 and 5.2 illustrate the effects of the rigid disk on the triaxiality of the dark matter haloes. Fig. 5.1 shows the surface density of dark matter particles in the inner 40 kpc of haloes B (top) and D (bottom) at the initial time $z = 1.3$ (left column), and at $z = 1.0$ for runs without the disk (middle column) and with the disk (right column). Fig. 5.2 plots the time evolution of the axial lengths determined from equipotential surfaces at ~ 5 kpc; the results are representative of the other equipotential surfaces. The axial lengths and orientations are computed at each snapshot.

Without stellar disks, Figs. 5.1 (left two panels) and 5.2 (dashed curves) show that the inner parts of all four dark matter haloes from the Aquarius simulations are

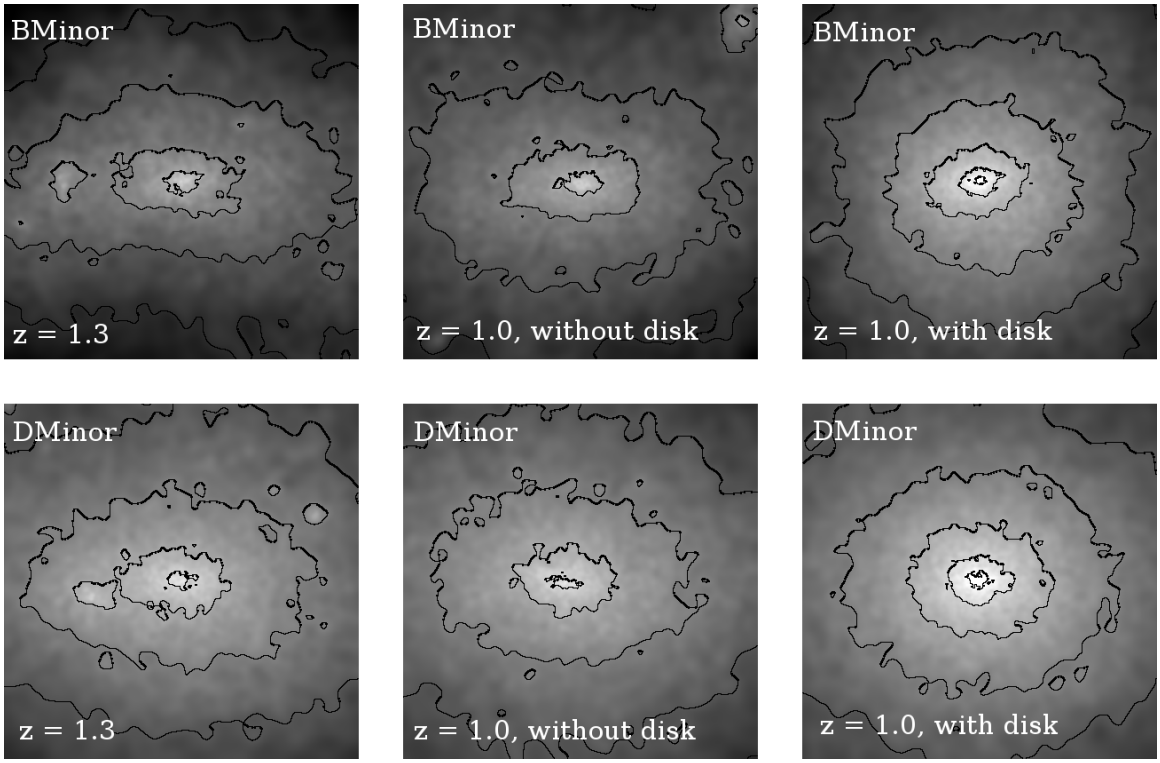

Figure 5.1: Surface density of the dark matter particles in halo B (top) and halo D (bottom), projected along their minor axes. The images are 40 kpc across. In the pure dark matter run without a disk (left and middle columns), the haloes are prolate (in the inner 40 kpc) and the shapes evolve little from $z = 1.3$ to 1.0. However, when a rigid disk is introduced (with disk normal aligned with the minor axis) adiabatically between $z = 1.3$ and 1.0 (right column), the dark matter haloes are symmetrized in the disk plane and become oblate by $z = 1.0$.

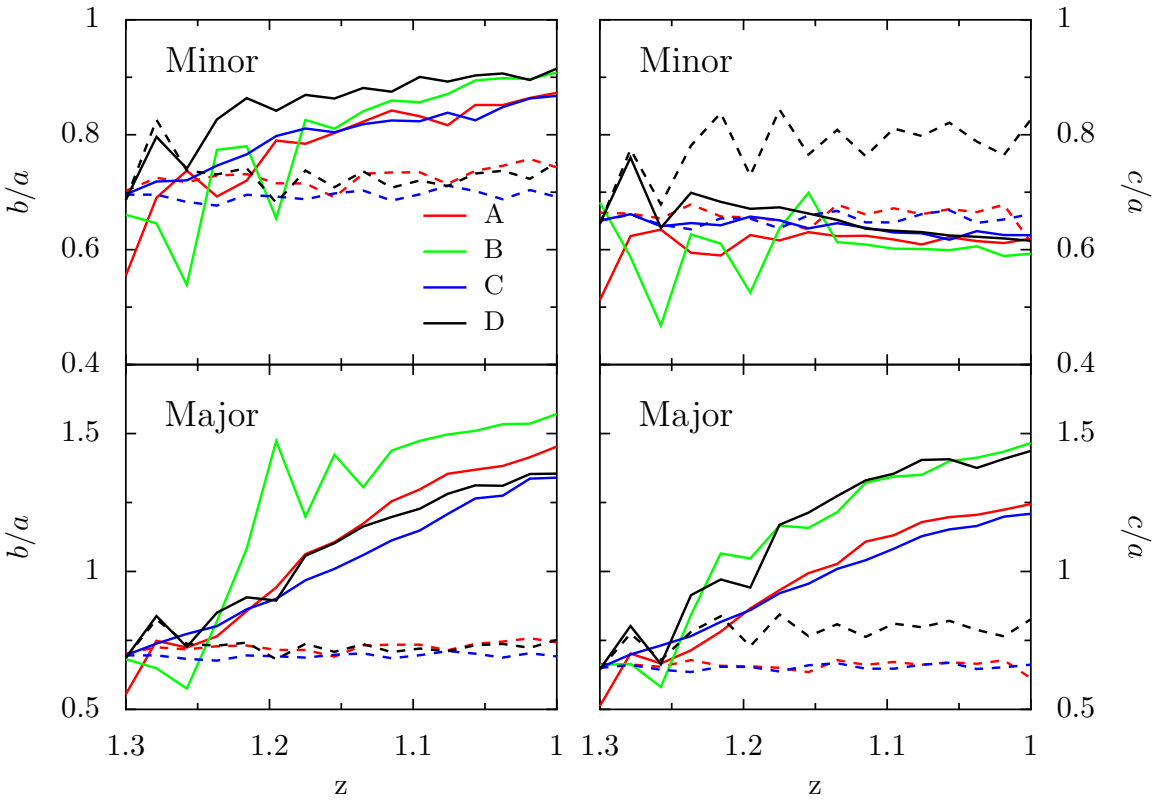

Figure 5.2: Effects of stellar disks on the shapes of dark matter haloes. The dashed curves show the axial ratios for the original Aquarius haloes A (red), B (green), C (blue), and D (black) between $z = 1.3$ and 1.0. The ratios stay nearly constant with $c \sim b \sim 0.7a$. The solid curves show how the insertion of a growing rigid disk between $z = 1.3$ and 1.0 modifies the axial ratios of the dark matter haloes. The modifications depend on if the disk normal is initially aligned with the minor (top panels) or major (bottom panels) axis of the halo at $z = 1.3$. Since the axial lengths of the haloes change with time, the initial major and minor axes may not stay as the major and minor axes at all times. For ease of comparison, we name the principal axes a, b, c (with $a \geq b \geq c$) at $z = 1.3$ and plot the subsequent evolution of the *same* axes. The ratios b/a and c/a can therefore become greater than 1 at later times. The axial ratios for the original halo B are very noisy and are not plotted because a nearby subhalo twists its major axis as it falls into the halo.

prolate with axial ratios of $c \sim b \sim 0.7a$. The ratios stay quite constant between $z = 1.3$ and 1.0.

How the halo responds to the disk depends on the orientation of the disk. When the disk normal is initially aligned with the minor axis of the halo, we find the presence of the disk to nearly symmetrize the axial ratio of the dark matter halo in the disk plane, as shown by the rounder contours in the right panels of Fig. 5.1. The solid curves in the upper two panels of Fig. 5.2 show the corresponding evolution in the axial ratios: b/a evolves from ~ 0.7 towards 0.9, while c/a remains relatively constant at ~ 0.6 to 0.7 between $z = 1.3$ and 1.0. The inner ~ 50 kpc of the haloes therefore change from being prolate to nearly oblate in the presence of a disk in the minor orientation.

When the disk normal is initially aligned with the major axis of the halo, the halo in the disk plane starts out quite symmetric since $b \sim c$ at $z = 1.3$. As the solid curves in the lower panels of Fig. 5.2 show, the presence of the disk significantly increases b/a and c/a as the initial major axis a contracts, but the ratio of b/c is relatively constant. The haloes become nearly spherical at $z \sim 1.2$, after which the initial major axis becomes the minor axis as b/a and c/a both exceed unity. Note that for ease of comparison, we name the principal axes a, b, c (with $a \geq b \geq c$) at $z = 1.3$ and plot the subsequent evolution of the *same* axes. The haloes therefore again evolve from being prolate to oblate in the presence of a disk in the major orientation. The difference here is the disk normal that was initially aligned with the halo's major axis at $z = 1.3$ ends up being aligned with the halo's minor axis at $z = 1$, and this occurs because of changes in the axial lengths of the halo rather than re-orientation of the disk.

Our results for the shapes of haloes without and with a stellar disk are in broad agreement with previous work. Dark matter haloes in N-body simulations generally have a range of shapes with a preference for prolateness over oblateness (Bett et al., 2007). The shapes can also depend on the radius, exhibiting a variation from prolate in the inner regions to triaxial or oblate in the outer parts (Vera-Ciro et al., 2011). To study the effects of disks on haloes, Kazantzidis et al. (2010) use mergers of idealized haloes to create an initially triaxial halo and find that a triaxial or prolate halo becomes more spherical under the effects of the rigid disk potential. Their disks in the major orientation end up more spherical than oblate as in our case, but that could be an effect of having an isolated halo. Infalling material in a fully cosmological simulation such as the Aquarius can easily modify the results. Berentzen and Shlosman (2006) performed simulations of disks growing in a cosmological setting, and also found that the growing disk washed out the prolateness of the halo. Interestingly, while the change in halo shape was sensitive to the total disk mass, it was not sensitive to how the mass was introduced, be it gradually or abruptly.

In addition to changes in the axial ratios, adding a stellar disk can also reorient the halo's equipotential surfaces between $z = 1.3$ and 1.0. Comparing the haloes in our simulations with disks and those in the original Aquarius simulations, we find

that with the exception of halo B, the major axis of the halo does not experience significant reorientation in the presence of a growing disk. In halo B, a subhalo is visible at ~ 15 kpc from the disk center at $z = 1.3$ in Fig. 5.1. In the original Aquarius halo, this subhalo twists the major axis of halo B as it falls into the halo. The axial length for halo B is therefore quite noisy and is not plotted in Fig. 5.2. When a stellar disk is added, we find the major axis to be more stable due to the influence of the rigid disk.

5.4 Live Stellar Disks and Bar Formation

In this section we present the results for the evolution of the live stellar disks in the Aquarius dark matter haloes from $z = 1.0$ to 0.

5.4.1 Structural Properties of Live Disks

Images of the final ($z = 0$) surface densities of the live disks are plotted in Fig. 5.3. For completeness, we show both the face-on and edge-on views of each disk in the four haloes. The left two columns show the disks that are initially aligned with the minor axis of the halo; the right two columns show the major axis runs. The images (43 kpc on a side) clearly show that a bar extending to at least $2R_d$ has formed in each disk, with halo C containing the weakest bar. We will further quantify the bar strength and evolution in § 4.2.

The edge-on images of the disks in Fig. 5.3 reveal a large variation in the amount of material outside the disk plane. The CMinor, DMinor, AMajor, and CMajor haloes contain a prominent diffuse component of stars extending to tens of kpc outside the disk plane, whereas this component is nearly absent in the other four haloes. We will examine the kinematic properties of these stars in § 4.3 and their correlation with outer warps of the disk plane in § 4.4.

Fig. 5.4 shows snapshots of the disk surface density (left) and mean vertical height (middle) between $z = 1$ and 0, and the $z = 0$ vertical profile (right) for the four "Minor" disks (from top down). Fig. 5.5 shows the same quantities for the four "Major" disks. The central surface density of the disk in the left column is seen to increase with time when a stellar bar forms. In addition, there is a slight enhancement at large radii in each case. This effect is most pronounced in the B disks and least pronounced in the C disks. The increase of material at large radii tends to increase the best fit scale length R_d of the disk, but we find the effect to be at most at the $\sim 20\%$ level: R_d increases from the initial value of 3 kpc at $z = 1$ to ~ 3.4, 3.7, and 3.3 kpc at $z = 0$ for haloes A, B, and D, respectively. The scale length for halo C, by contrast, stays quite constant. We note, however, that the surface density profiles of BMajor and BMinor in Figs. 5.4 and 5.5 exhibit noticeable deviations from the initial exponential form by the end of the simulation.

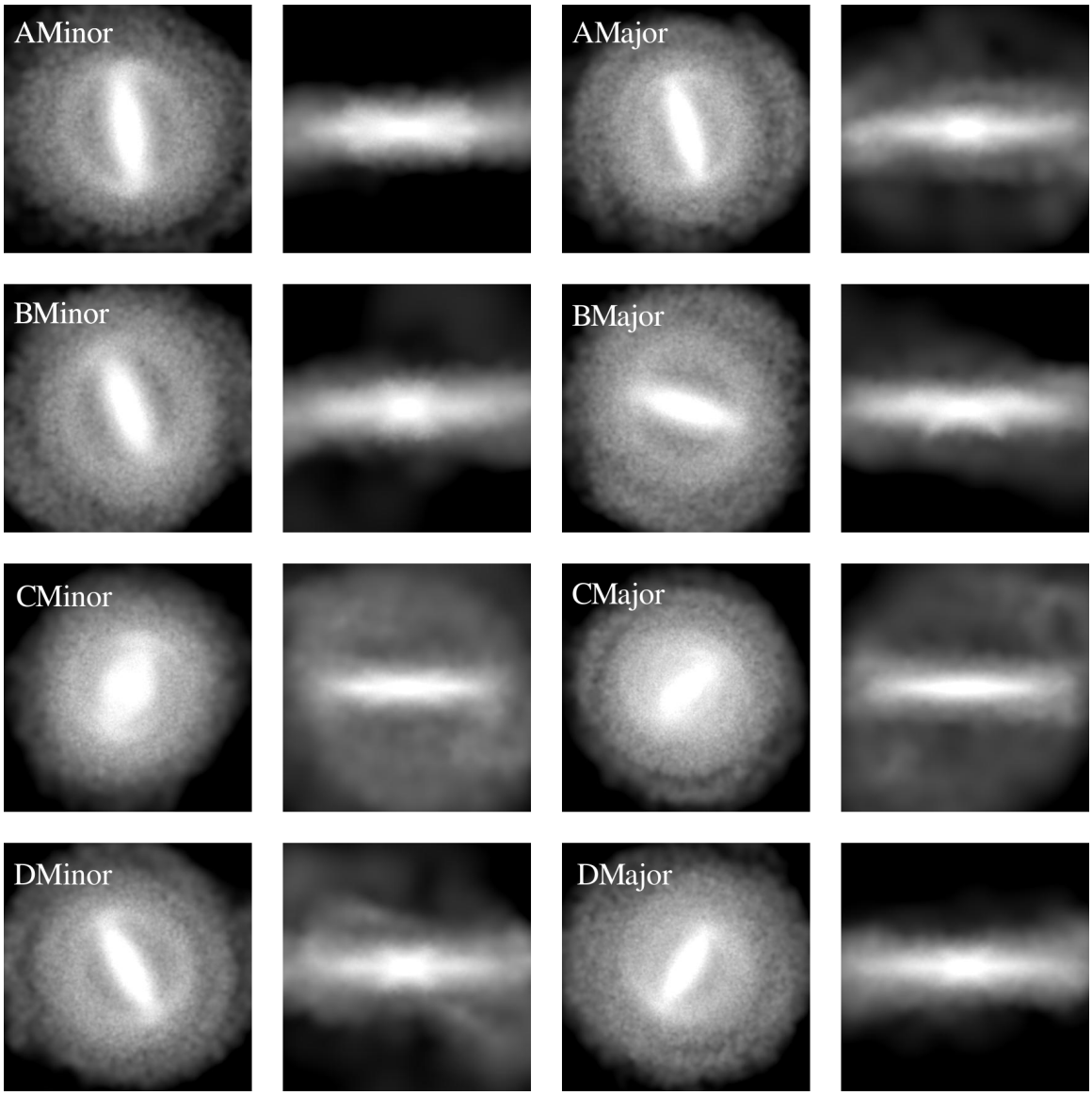

Figure 5.3: Surface density of the $z = 0$ stellar disk, viewed faced-on (columns 1 and 3) and edge-on (columns 2 and 4), for haloes A, B, C and D (from top down). Each image is 43 kpc on a side. "Minor" and "Major" indicate whether the disk normal is initially aligned with the minor or major axis of the dark matter halo at $z = 1.3$.

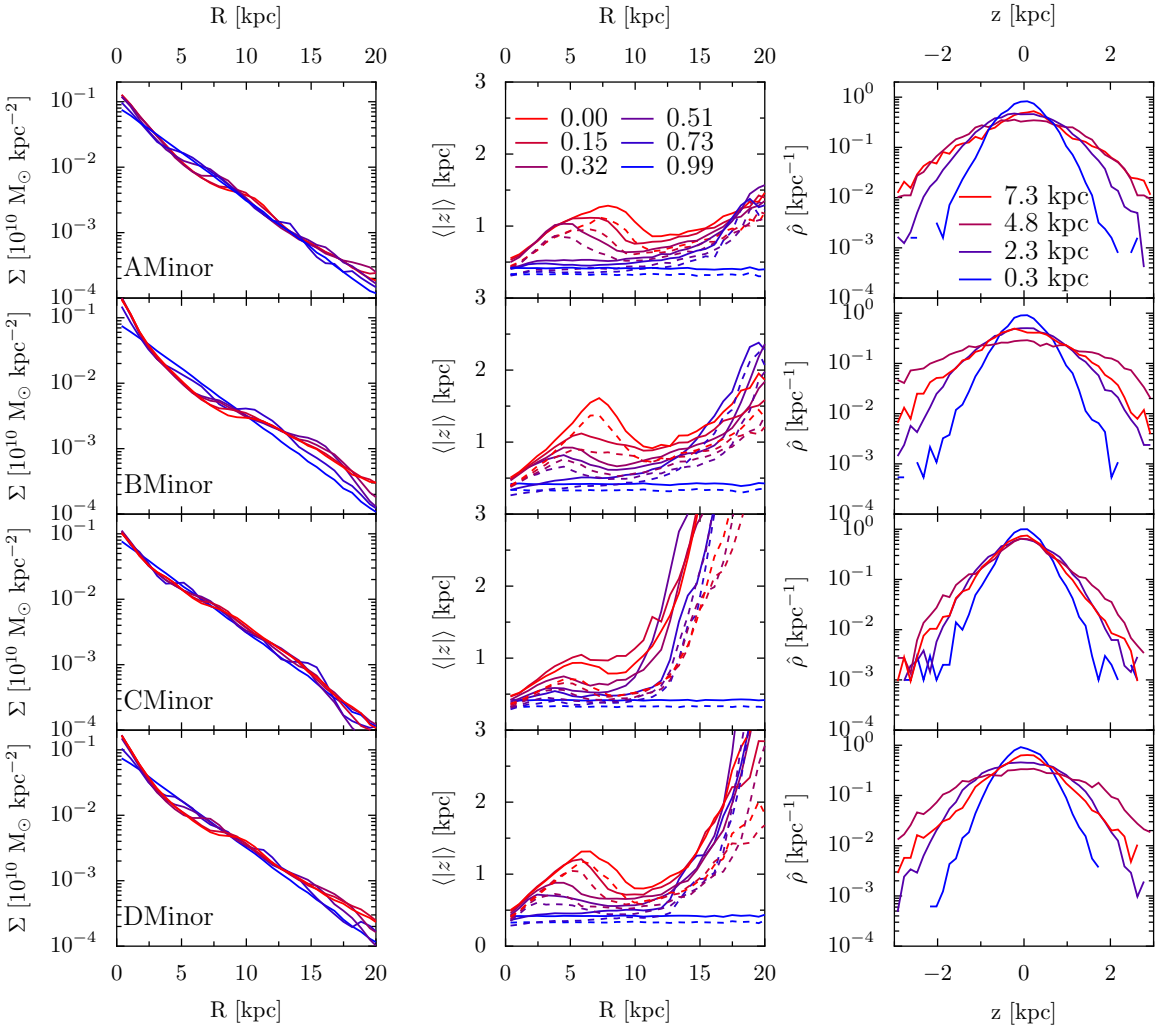

Figure 5.4: Structural properties of the disks in the minor orientation for haloes A, B, C, and D (top down). The projected surface density of the disk as a function of radius (left column) is quite stable between $z = 0.99$ (blue) and 0.0 (red), with a steepening in the inner few kpc due to the stellar bars. The middle column shows two measures of the height of the disk, the mean (solid) and median (dashed) distance of the disk particles from the disk plane, as a function of radius for six redshifts during the simulations. The vertical profiles of the disk at $z = 0$ (right column) become broader with increasing radii.

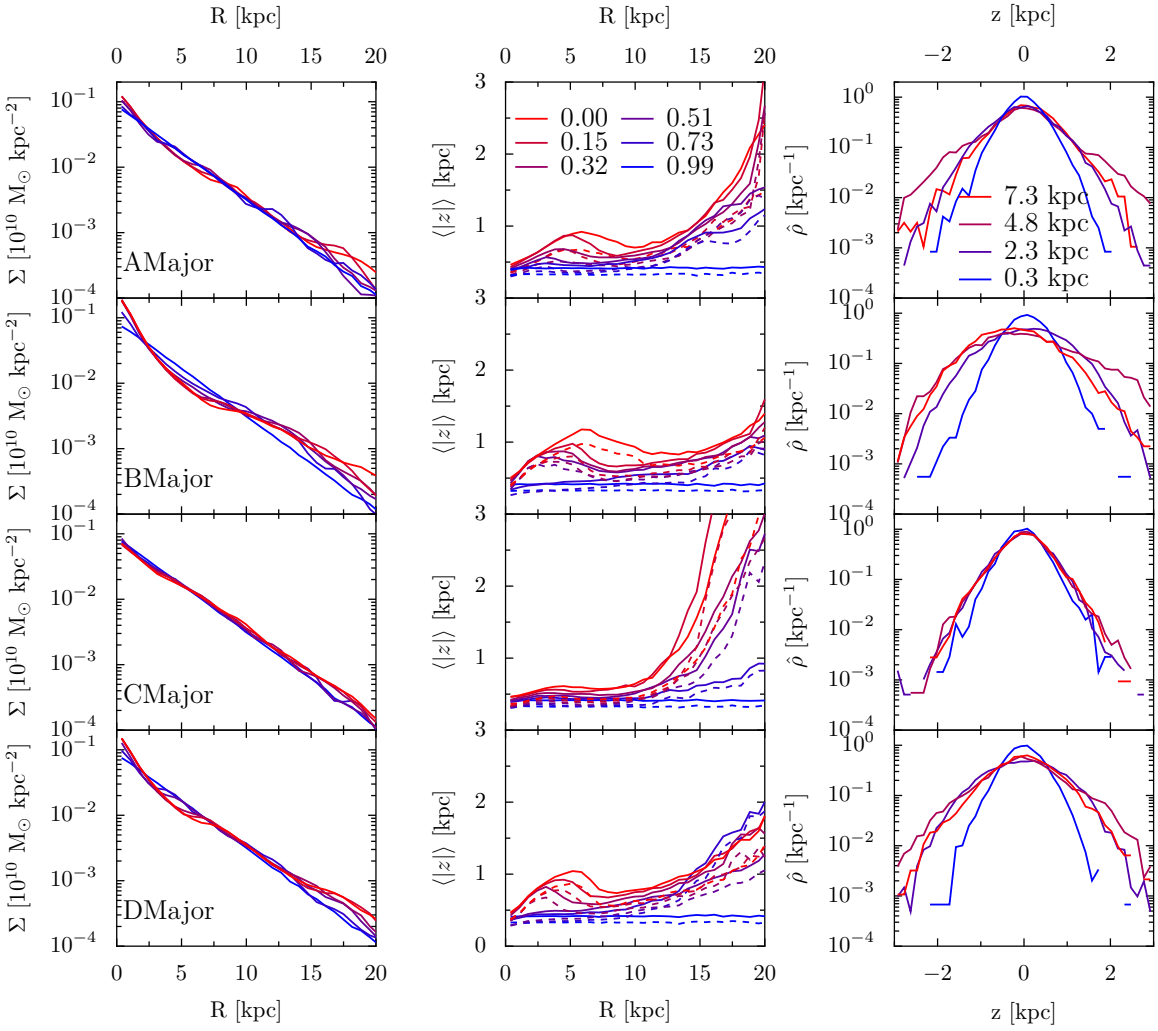

Figure 5.5: Structural properties of the disks in the major orientation for haloes A, B, C, and D (top down). The projected surface density of the disk as a function of radius (left column) is quite stable between $z = 0.99$ (blue) and 0.0 (red), with a steepening in the inner few kpc due to the stellar bars. The right column shows two measures of the height of the disk, the mean (solid) and median (dashed) distance of the disk particles from the disk plane, as a function of radius for six redshifts during the simulations. The vertical profiles of the disk at $z = 0$ (right column) become broader with increasing radii.

The middle and right columns of Figs. 5.4 and 5.5 show the vertical structures of the disks. The radial profile of the mean and median vertical height $|z|$ is flat at the first two snapshots ($z = 0.99$ and 0.73) for all eight disks, but a broad bump develops at $R \sim 5$ kpc in the later snapshots for disks A, B, D as a bar forms. The outer profile of $|z|$ at $R > 10$ kpc also varies greatly from disk to disk. A dramatic rise in $|z|$ is seen in the outer parts of C Minor, DMinor and CMajor, and to a lesser extent, AMajor. This rise correlates directly with the amount of material out of the disk plane in Fig. 5.3. Throughout the simulation, the disk plane changes orientation, and while most of this reorientation is a coherent tumbling motion of the disk, some of the outermost material gets 'left behind,' creating streams that are on a different plane than the bulk of the disk mass. More discussion of this issue will be presented in § 4.4. These features in the vertical structure have been seen before, especially in the simulations of Kazantzidis et al. (2008) and Machado and Athanassoula (2010), and also to a lesser extent in Moster et al. (2010).

The CMajor disk is remarkable in that among the eight disks, it has the least amount of vertical thickening in the inner 10 kpc of the disk but the largest amount of diffuse material outside the disk plane at large radii. These results strongly suggest that the features at the centers of these disks and the material out of the plane of the disk are formed from separate mechanisms. This realization is present in the other panels of Figs. 5.4 and 5.5, but it is most striking for CMajor. We present evidence below that the thickening at the center of the disk is due to a large bar that develops, and the material out of the plane is due to torques by changes in the disk orientation as a function of radius.

5.4.2 Stellar Bars

To quantify the bars that formed in the central regions of the disks, we compute the strength of the $m = 2$ Fourier amplitude of the surface density in each disk. The particles in the disk are binned radially in the disk plane, and the following coefficients are computed for each bin:

$$\begin{aligned} a_m &= \sum_i \cos(m\theta_i) \qquad m = 0, 1, ... \\ b_m &= \sum_i \sin(m\theta_i) \qquad m = 1, 2, ... \end{aligned} \tag{5.4}$$

where the sum is carried out over all the disk particles (labeled by i and assumed to have equal mass) in the radial bin, and θ_i is the azimuthal position of that particle in the disk plane. The strength of a given mode is $c_m = \sqrt{a_m^2 + b_m^2}$. To give a collective notion about the strength of the $m = 2$ mode for the whole disk, we compute the

relative mode strength A_2 by integrating c_2 over the inner two scale radii:

$$A_2 = \frac{\int_0^{2R_d} c_2(R) R dR}{\int_0^{2R_d} c_0(R) R dR}. \tag{5.5}$$

Fig. 5.6 shows the value of A_2 computed over the inner $2R_d$ for disks in both the minor orientation (top) and the major orientation (bottom). The strength of the $m = 2$ mode matches the expectation from examining the images in Fig. 5.3. In particular, the bar is weakest in the CMajor halo, with $A_2 < 0.17$ throughout the simulation. The CMinor disk is also distinctly stable, in which A_2 stays nearly a constant at ≈ 0.2 after a rapid initial rise from 0 to 0.22.

By contrast, the bar strengths A_2 for haloes A, B, and D show a rapid initial rise from zero, followed by a ~ 20 to 30% drop in amplitude at a redshift that differs from disk to disk, and then a late time growth leading to a final value as high as $A_2 \sim 0.5$ at $z = 0$ (for haloes A and B). The qualitative trends of A_2 resemble those reported in earlier N-body simulations, e.g., the idealized disk and halo systems of Dubinski et al. (2009), the constrained cosmological run of Villa-Vargas et al. (2009). The dips in A_2 after initial bar formation have been attributed to bar buckling instability in these papers. For our disks in the initial minor orientation (top panel in Fig. 5.6), BMinor shows the earliest dip at $z \approx 0.65$; the dips in A_2 for DMinor and AMinor start to occur at $z \approx 0.5$. For our disks in the initial major orientation, only BMajor and DMajor exhibit noticeable dips in A_2 at $z \approx 0.55$ and 0.45.

It is worth noting that (Berentzen et al., 2006) found that bars cannot survive in halos that are very triaxial. The evolution of the halo shape during the ramping phase of our simulations is important for setting up the conditions in which a bar could form and survive until today.

To quantify the bar buckling instability further, we discuss in the next subsection and show in Fig. 5.7 the corresponding vertical heating measured by the relative disk velocity dispersion in the vertical direction in the inner $2R_d$ of the disk. For the five disks AMinor, BMinor, DMinor, BMajor, and DMajor, there is a clear sharp rise in disk heating at the redshift at which A_2 dips in Fig. 5.6.

The formation of bars in these disks is not entirely unexpected based on the criterion of Efstathiou et al. (1982). According to this criterion, the disk will be stable against developing a bar if

$$Q_{bar} = \frac{v_M}{\sqrt{M_d G / R_d}} > 1.1\,, \tag{5.6}$$

where v_M is the maximum velocity of the rotation curve, and M_d and R_d are the disk mass and scale length, respectively. For the initial live disks in our simulations at $z = 1$, we find $Q_{bar} = 0.98, 0.83, 1.03$, and 0.93 for haloes A, B, C, and D, respectively, and the value of Q_{bar} is largely independent of the initial disk orientation. These disks

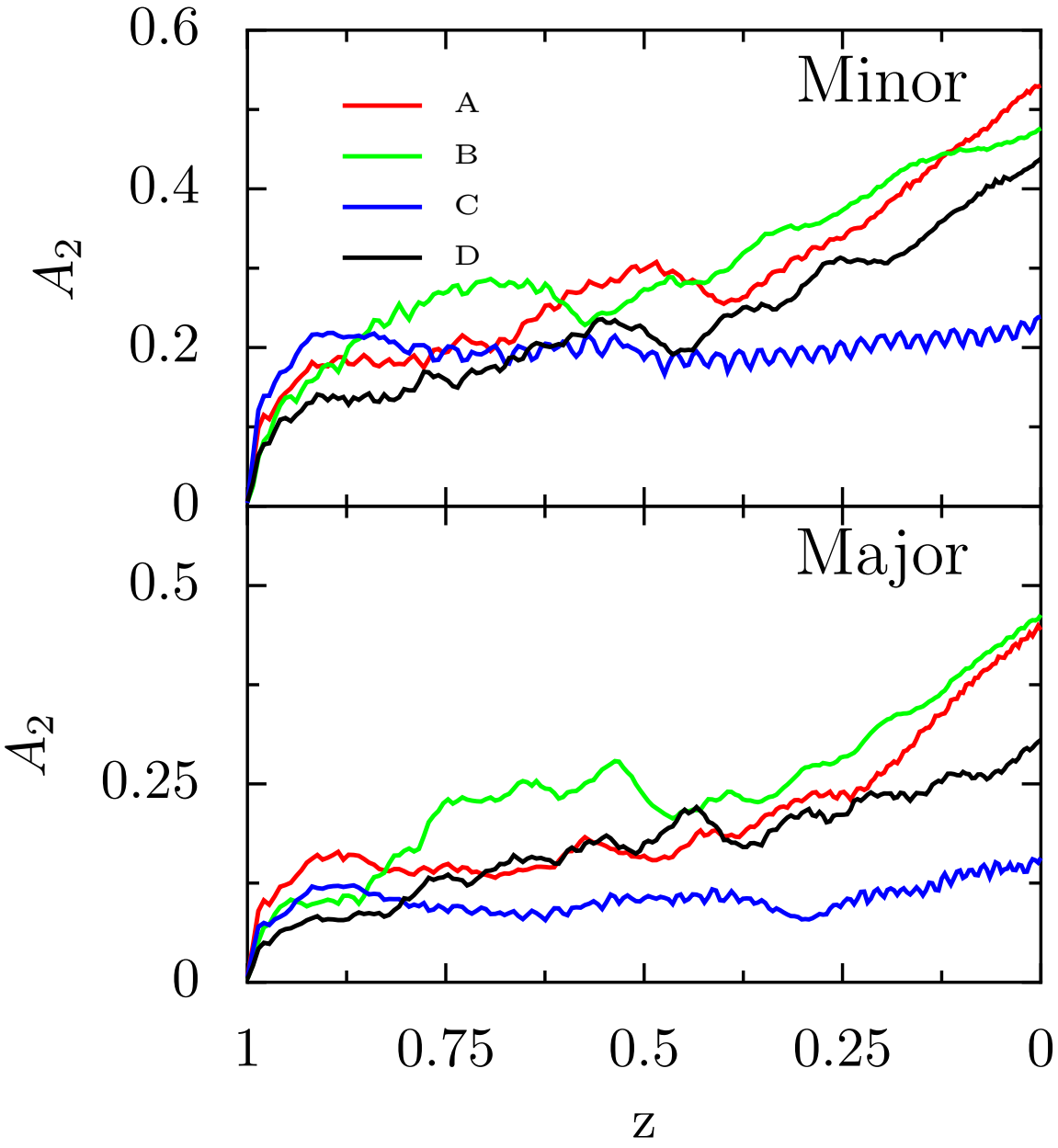

Figure 5.6: Strengths of stellar bars measured by the $m = 2$ mode, A_2, in the inner $2R_d$ for the disks in each halo for the minor (top) and major (bottom) orientations. Halo C (blue) develops the weakest bar, while the $m = 2$ mode grows with time for haloes A (red), B (green), and D (black).

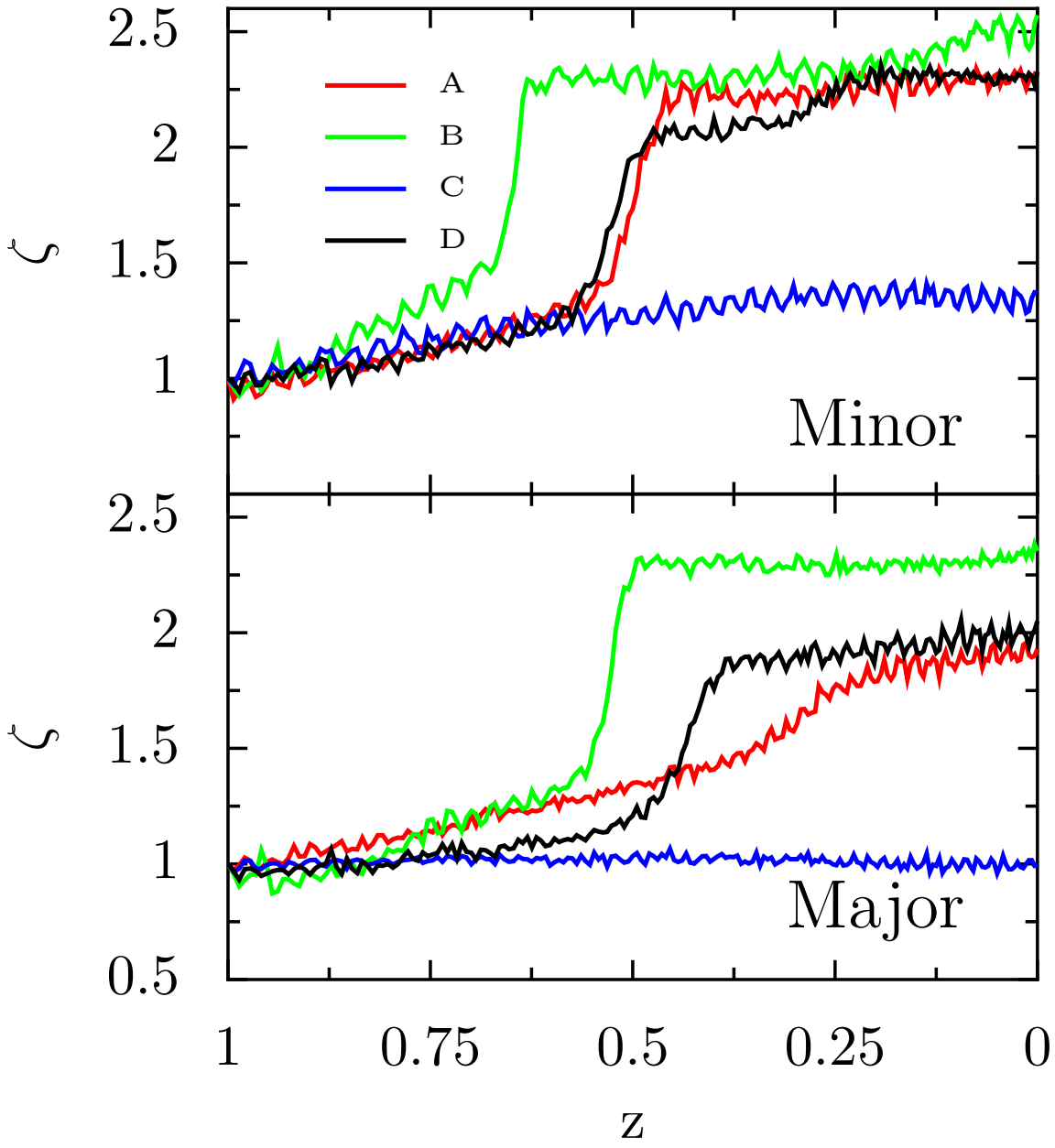

Figure 5.7: Evolution of ζ for the disks in the minor (top) and major (bottom) orientations. The disks which form a strong bar, which eventually buckles, all show a large jump in ζ during buckling. The C halo, in both orientations, shows the least heating.

are therefore unstable against a bar forming, as seen in Fig. 5.3. Moreover, halo C has the weakest bar since its Q_{bar} value is closest to the threshold for stability.

In comparison, we find Q_{bar} to be greater than 1.1 in our simulations in which the disk masses are lowered by a factor of 2 and 3 (see Sec 5 below); the corresponding Q_{bar} is 1.13 and 1.23 for halo A, and 1.15 and 1.26 for halo C. The increase in Q_{bar} for decreasing disk mass indicates stronger stability against bar formation in lower mass disks. These smaller disks indeed appear mostly free of bars, as shown below in Fig. 5.12. The $m = 2$ coefficient is also small, with $A_2 < 0.2$ (right panels of Fig. 5.13).

We note that equation (5.6) is approximate since it treats only the self-gravity of the disk and does not consider the velocity dispersion (Athanassoula, 2008). For the disks studied here, however, equation (5.6) appears to work well.

5.4.3 Disk Heating and Velocity Profiles

In addition to the shape of the disk, the velocity structure of the disk evolves during the simulation. We define the following quantity to characterize the vertical heating of the disk. For a cumulative radial disk mass profile $M(R)$ and a vertical velocity dispersion profile $\sigma_z(R)$, we use

$$\zeta = \frac{\int_0^{2R_d} \frac{dM}{dR}\sigma_z^2(R)dR}{\int_0^{2R_d} \frac{dM_0}{dR}\sigma_{z,0}^2(R)dR} \tag{5.7}$$

where subscript "0" in the denominator denotes that these quantities are evaluated for the initial redshift of the live phase ($z = 1.0$). The limit of integration is set to twice the scale radii, the same as in the A_2 definition above.

The evolution of ζ with redshift is given in Fig. 5.7 for disks in the minor (top) and major (bottom) orientations. The halo-to-halo variation is striking. Once again, vertical heating is negligible in the CMajor disk, in which ζ stays at unity throughout the simulation. The CMinor disk experiences a gradual increase of only $\sim 30\%$ in ζ between $z = 1$ and 0. By contrast, ζ jumps from 1 to 2-2.5 suddenly at $z \sim 0.5$ to 0.7 for the disks in the other three haloes. This jump in ζ is accompanied by a dip in the bar strength A_2 at a similar redshift, as a result of bar buckling (see Fig. 5.6 and previous subsection). Similar jumps in the velocity structure of barred disks have been reported before (e.g., Fig. 6 of Martinez-Valpuesta et al. 2006, Sotnikova and Rodionov 2003), taking place over a similar timescale as seen in our simulations.

The complete set of profiles of the stellar velocity dispersions in three directions about the disk plane is shown in Fig. 5.8 and 5.9 for the disks in the minor and major orientation, respectively. In each figure, the three columns show the azimuthal (left), radial (middle), and vertical (right) components of the stellar velocity dispersion. Within each panel, six snapshots between $z = 1$ and 0 are plotted.

In the vertical direction, jumps in σ_z are clearly seen between $z \sim 0.7$ and 0.5 for the five disks AMinor, BMinor, DMinor, BMajor and DMajor, as was shown in

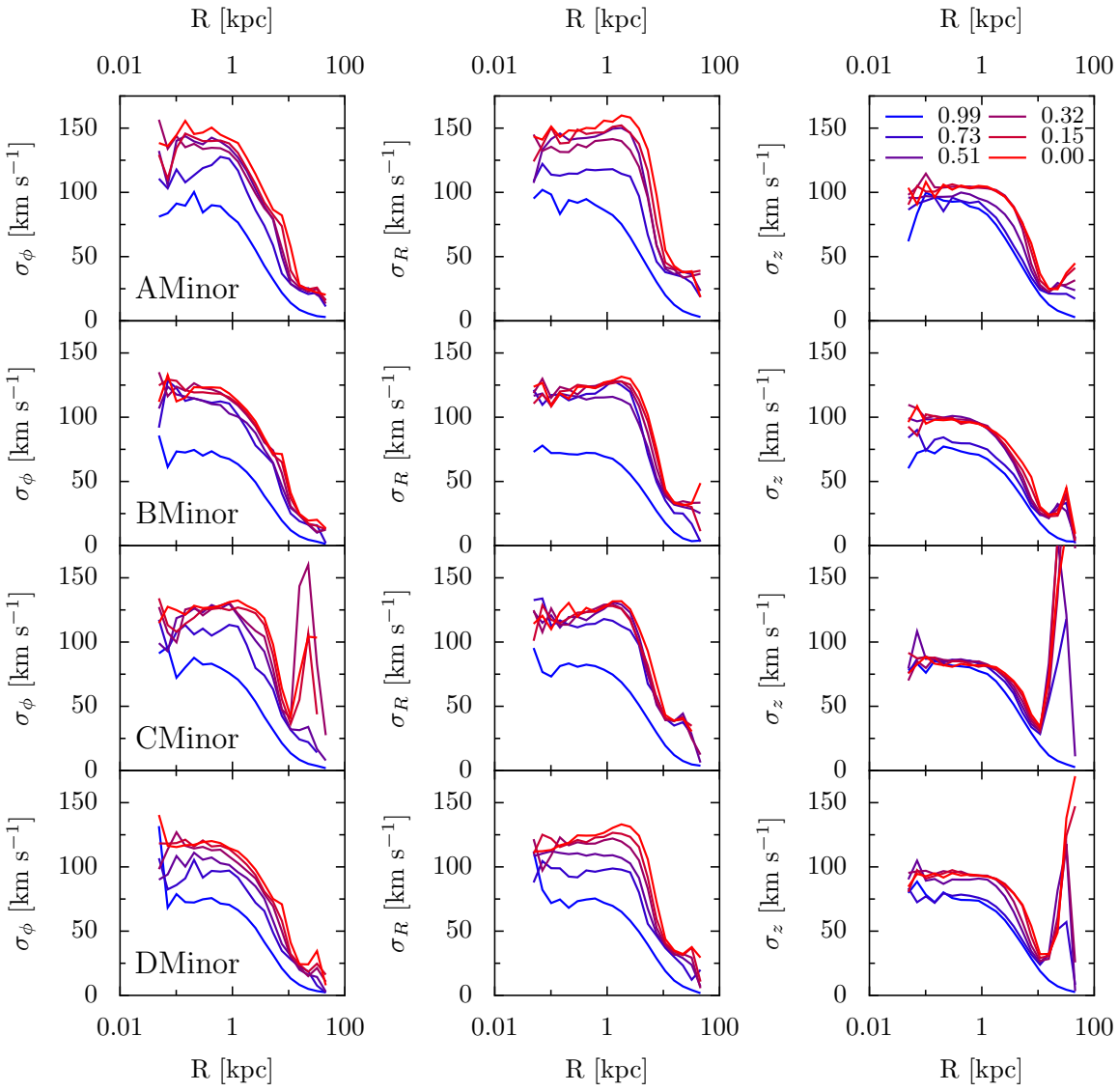

Figure 5.8: Velocity dispersion profiles of the minor disks in haloes A, B, C and D (from top to bottom). The three columns show the three velocity components defined by the disk: azimuthal (left), radial (middle), and vertical (right). In each panel, the different curves show six outputs ranging from $z = 0.99$ (blue) to 0.0 (red).

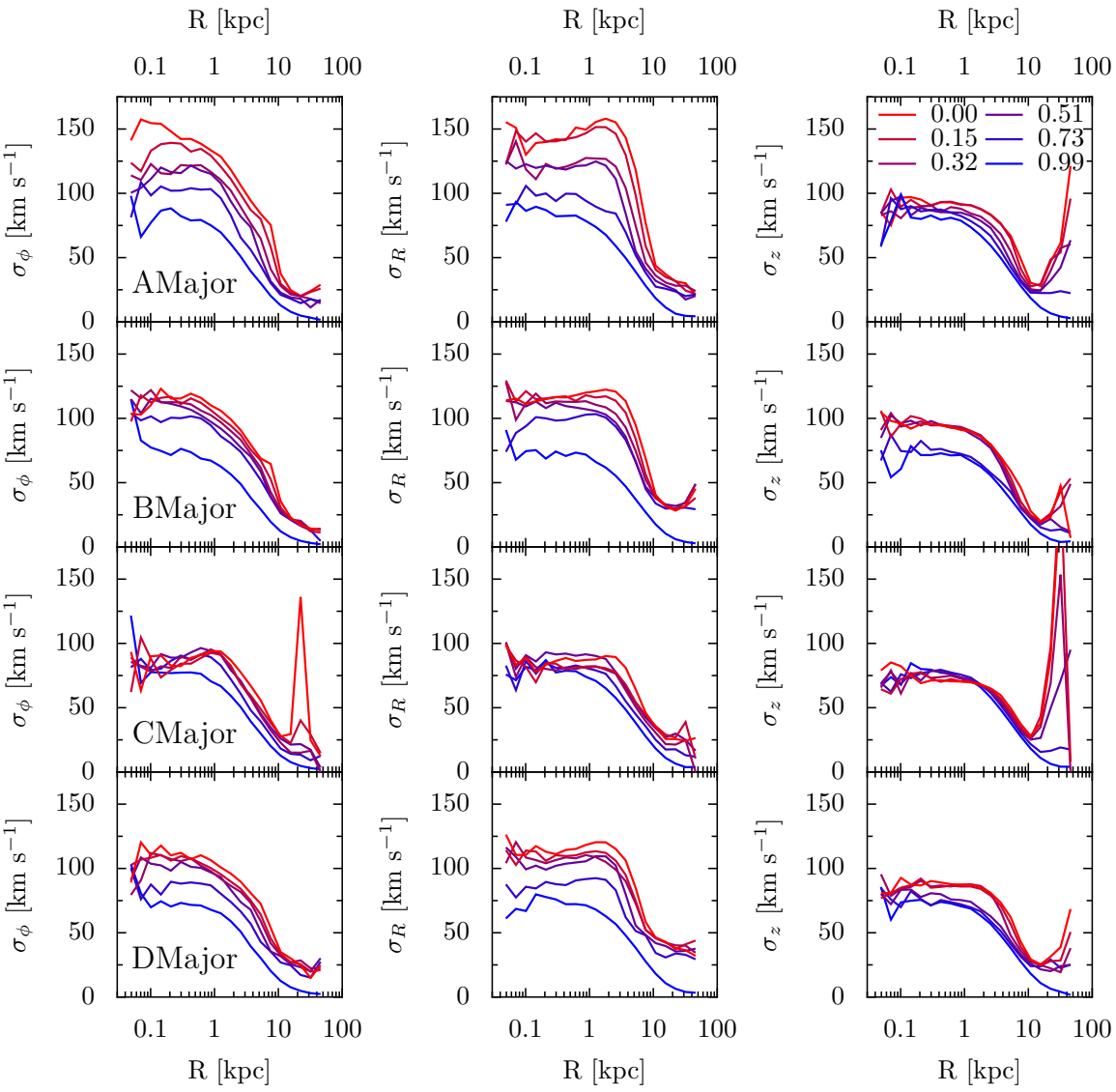

Figure 5.9: Same as Fig. 5.8 but for the four disks in the major orientation.

Fig. 5.7. For the other three disks, AMajor's σ_z increases more gradually without a sudden jump, while σ_z stays nearly constant for CMajor and CMinor, which do not form a significant bar. This behavior is again consistent with Fig. 5.7. Similar results have been seen in simulations by Saha et al. (2010b), who found heating both due to the bar buckling, and a slower overall heating before and after the buckling.

The streams of stellar particles visible in Figs. 5.3 – 5.5 are responsible for the rise in σ_z at radii beyond 10 kpc in Figs. 5.8 and 5.9. The rise is particularly prominent for the three disks CMinor, DMinor, and CMajor, in which σ_z reaches > 150 km/s at $R \sim 20$ to 40 kpc. The edge-on images in Fig. 5.3 indeed show that these three disks contain an extended diffuse component of stars outside the disk plane, spreading to tens of kpc. This component gives rise to the sharp increase in the mean vertical height in the three objects in Figs. 5.4 and 5.5. The AMajor disk also exhibits a similar behavior to a lesser extent.

In the radial and azimuthal directions, Figs. 5.8 and 5.9 show two phases of heating. Between the first two snapshots at $z = 0.99$ (blue curves) and 0.73 (light purple curves), which precedes any bar formation, σ_R and σ_ϕ increase for all eight disks, with a larger jump for the disks in the minor orientation. In comparison, there is almost no vertical heating as evidenced by the nearly identical σ_z at these snapshots. Similar trends are reported in an idealized model for the halo and disk of M31, in which the changes in σ_R and σ_Φ are attributed to transient spiral features present early in the simulations (Gauthier et al., 2006).

A second phase of heating in the radial and azimuthal directions can be seen in a subset of disks in the inner ~ 10 kpc in the $z < 0.73$ snapshots of Figs. 5.8 and 5.9. It is tempting to attribute this phase of heating to bar activities, e.g., σ_R and σ_Φ are nearly unchanged between $z = 0.73$ and 0.0 for CMinor and CMajor that have very weak bars, whereas they increase by up to 50% for AMinor and AMajor that have strong bars. Fig. 6 of Gauthier et al. (2006) illustrates similar heating and explains it by the stellar bars that have formed in their runs with dark matter subhalos. We note, however, that the BMinor disk (and BMajor to a lesser extent) contains a strong bar, but its σ_R and σ_Φ stay nearly constant after $z = 0.73$. However, figures 5.7 and 5.6 show that the bar in halo B forms earlier than in the other halos, giving a transition time from early transient features to bar growth significantly before $z = 0.73$.

5.4.4 Disk Reorientation

Once the stellar disk goes live at $z = 1.0$ in our simulations, the orientation of the disk is free to change. To determine the disk normal, the disk particles are binned in radius, and an imaginary plane is drawn through the center of mass of the entire disk. The sum of the squared distances of each particle in the given bin to the plane is computed, and the normal to the plane is varied to minimize this sum. In this way, we find a disk normal for each radial bin of the disk. This process is performed for each output and a history of the disk's orientation is constructed.

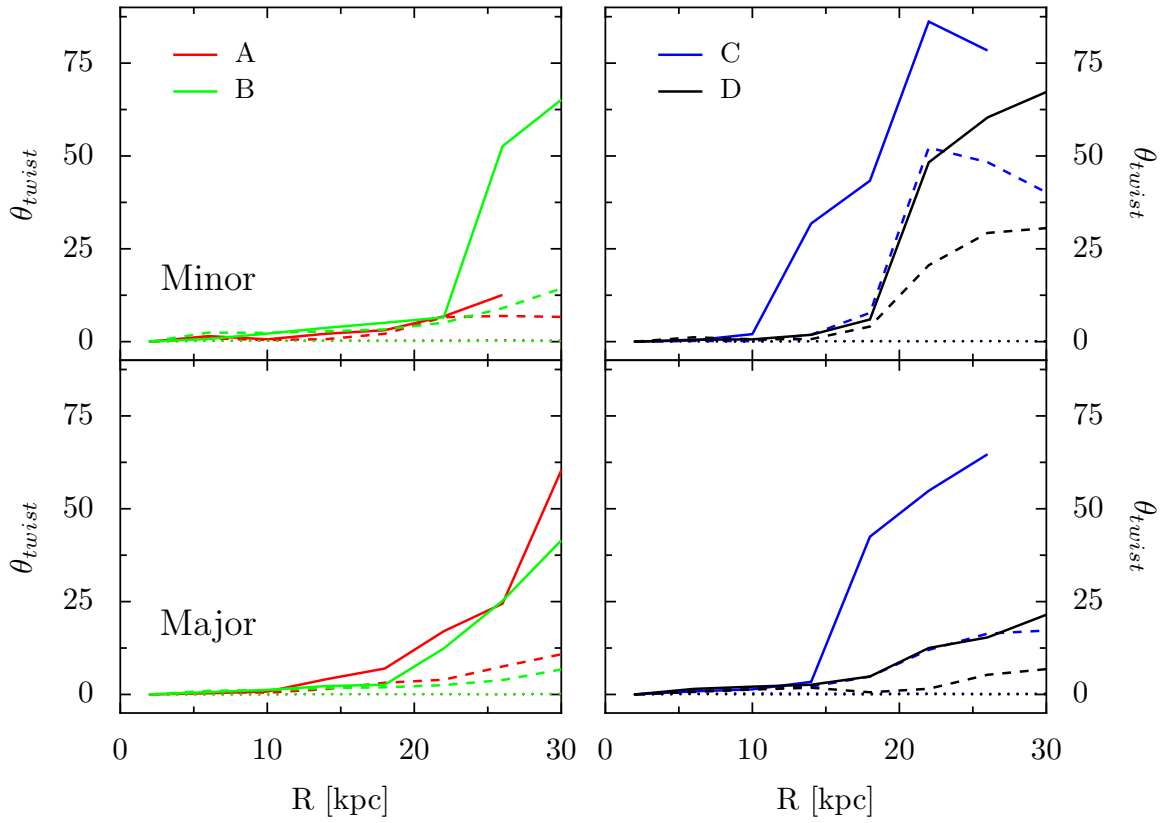

Figure 5.10: The twist angle for the Minor (top row) and Major (bottom row) disks as a function of radius at three different times (z = 1.0, 0.5, 0.0 as dotted, dashed and solid respectively).

In practice, we find this procedure to produce disk normals that are nearly identical in the central bins of the disk, even though the outer-most bins can have a very different orientation. The average of the innermost bins' normal directions are taken as the disk normal for each output of each disk.

The angle, θ_d, between the disk normal at a given redshift z and the initial disk normal at $z = 1.0$ is plotted in Fig. 5.11 for each disk in the minor (top) and major (bottom) orientations. In each case, the disk experiences some reorientation, with the disk in the CMinor case showing the largest change. For the most part, the disks reorient coherently, with each radial bin experiencing the same change in normal. The exception to this is the outer edges of the disks, which can lag behind and perhaps create the streams seen in Fig. 5.3. Indeed, comparing Figs. 5.11 and 5.3, we see that the greater the change in the orientation of the disk, the more apparent is the material out of the disk plane.

The disk normals computed at each radial bin can be used to characterize the relative twist of the edges of the disk as compared to the center. We define the twist

angle, $\theta_{twist}(R)$, as the angle between the normal for the central bin and the normal for the bin at radius R. Figure 5.10 shows this twist angle as a function of radius for each of the halos, in both the Minor (top row) and Major (bottom row) versions, at three different redshifts. Initially ($z = 1.0$; dotted lines), the disk is completely coherent and θ_{twist} is zero at all radii. As the disk evolves to $z = 0.5$ (dashed lines) and $z = 0.0$ (solid lines) the edges of the disk can develop a significant difference in normal direction. The trends in figure 5.10 match the expectation from figures 5.3, 5.4 and 5.5. The larger the value of θ_{twist}, the more material will appear out of the plane of the disk, and the larger the increase in the disk height at large radii will be. Of particular note are CMinor and CMajor: both runs shows significant twist between the center of the disk and the edges.

We have performed a visual inspection of the material at large radius, and it should be noted that the material is largely in the form of rings of material concentric with the disk, but with a plane that is offset. This assures that the fit to the orientation of the material at large radius is accurately measuring the orientation of the extremities of the disk. If, for example, the material was not in ring-like structures, the fit to orientation would not correspond so directly to the plane in which the bulk of material is orbiting the potential center. Similar out-of-plane structures have been seen in previous simulations. Kazantzidis et al. (2008) found streams in their simulations of disks subjected to multiple subhalo impacts. In a numerical study of extended HI disks, Roškar et al. (2010) found significant warps which appear quite similar in structure to the streams in our stellar disks.

We have also computed the relative orientation between the disk and the halo at a given time. The halo orientation is computed by binning the halo particles in potential and fitting ellipsoids to those surfaces. The directions of the principle axes can then be taken from the best fit ellipsoid. This procedure is repeated at each bin in potential, which correspond roughly to different radii. In nearly all cases, the axes show very little twist over the inner 50 kpc. When the disk orientation is compared with the halo's principle axes, we find very little relative reorientation. Therefore while the disk is reorienting, as seen in Fig. 5.11, it is doing so with the halo.

The tumbling of the halo has been shown to not only induce bar formation, but also to generate warps (Dubinski and Chakrabarty, 2009). Further, misalignment between the disk and halo angular momentum is a source of both disk tumbling, and misalignment between the inner and outer regions of the disk (Debattista and Sellwood, 1999). Perturbations from satellites can also produce misalignment in disks (Weinberg and Blitz, 2006). The exact mechanism that produces the misalignment in our simulations is unclear; a closer examination of this issue is a target for future study.

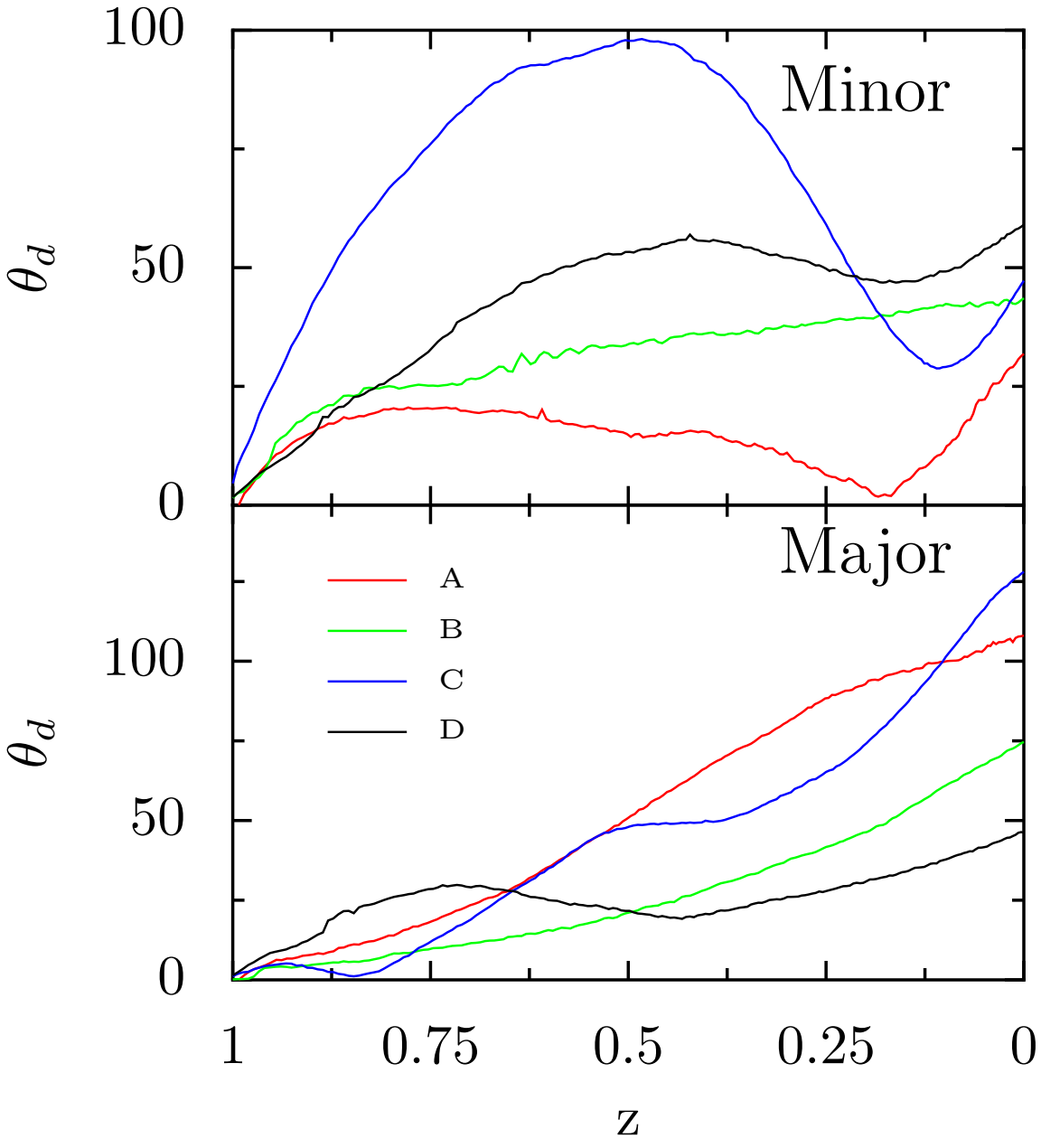

Figure 5.11: Angle (in degrees), θ_d, between the disk normal at a given redshift and the disk normal at $z = 1.0$ for haloes A (red), B (green), C (blue), and D (black). The disk normal is aligned with the minor (top) and major (bottom) axis of each halo at $z = 1.3$.

5.5 Alternate Disk Models

To quantify the dependence of the disk structures on the assumed disk mass, we have performed additional runs for halos A and C, in which the disk mass is reduced from the fiducial value of $5 \times 10^{10} M_{\odot}$ by a factor of 2 and 3. The scale radius of the disk is reduced according to the observed scaling relation $R_d \propto M_d^{1/3}$ (Shen et al., 2003). These runs are labeled "Half" and "Third" in Table 1. The change of disk mass required the disk growing phase between $z = 1.3$ and 1.0 to be redone for each case since the dark matter haloes would be responding to the potential of a smaller disk.

We have also performed test runs with haloes A and C in which the disk is assumed to have an initial gas fraction of $f_g = 0.4$. These runs are labeled AMinorGas and CMinorGas. The total baryonic mass is the same as in the fiducial run, i.e. $5 \times 10^{10} M_{\odot}$; the disk mass in stars is therefore reduced to $3 \times 10^{10} M_{\odot}$. The gas has the same radial profile as the stellar particles, but is set up to be in vertical hydrostatic equilibrium. For simplicity it does not form stars or cool. We include this component to test if a gas component helps stabilize the stars in a disk. A more realistic simulation will turn most of the gas at $z = 1$ into stars by $z = 0$, thereby bracketing our results for the AMinorGas run and the fiducial run AMinor. Indeed, the resulting central mass concentration produced from star forming gas has been shown to correlate with many bar properties (Villa-Vargas et al., 2010, Berentzen et al., 2007).

We find large reductions in the bar strengths as the disk mass is lowered. Fig. 5.12 shows the $z = 0$ face-on surface density of the inner 21 kpc by 21 kpc region of four different disk for halo A. The right panels of Fig. 5.13 show the time evolution of the coefficient A_2 of the $m = 2$ mode that characterizes the bar strength for haloes A and C (see Sec 4.2). These figures show a clear decrease in bar strengths as the disk mass is reduced. Halo AMinor with the largest mass disk has a growing $m = 2$ mode throughout the simulation, while the other three smaller disks all have $A_2 < 0.2$. The smaller mass disks in the C haloes also end with smaller values of A_2, but the overall decrease is smaller as the disk in the CMinor halo shows at most a weak bar to begin with. As discussed in Sec 4.2, the approximate bar instability criterion given by equation (5.6) requires $Q_{bar} < 1.1$ for bar formation. The disks with the fiducial mass of $5 \times 10^{10} M_{\odot}$ satisfy this condition and indeed developed bars by $z = 0$ (see Fig. 3). By contrast, the disks with reduced masses all have $Q_{bar} > 1.1$ and $A_2 < 0.2$ and show no strong bars.

The middle panels of Fig. 5.13 show the mean particle distance from the disk plane as a function of radius for these same simulations at $z = 0$. Both quantities are given relative to the initial disk size to aid in the comparison. Unlike the original disk, the low-mass AMinor disks show a significantly reduced bar feature. The low-mass disks in the C halo show similar behavior, but the initial bar in the CMinor disk is weak to begin with, so the reduction is somewhat less dramatic. However, the outer edges of

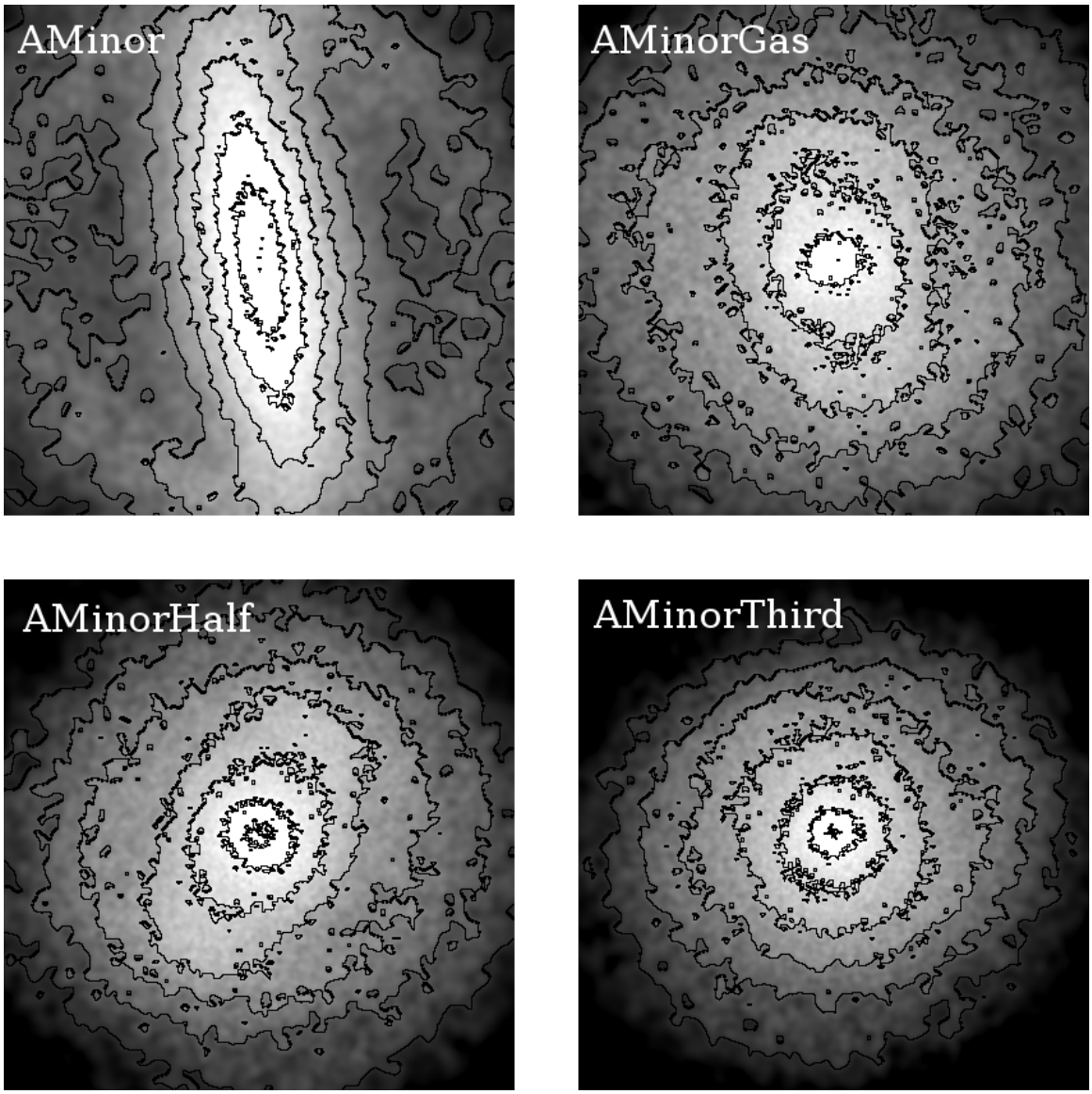

Figure 5.12: Surface density of the stellar disk at $z = 0$, viewed faced-on, for four disk models for halo A. The four models differ in the assumed disk masses: $5 \times 10^{10}, 3 \times 10^{10}, 2.5 \times 10^{10}$ and $1.67 \times 10^{10} M_{\odot}$ for AMinor, AMinorGas, AMinorHalf, and AMinorThird, respectively. Reducing the disk mass helps stabilize the disk against bar formation. The images are 21 kpc on a side, and contours have been added to highlight the shape of the disks. The brightness of the image is logarithmic in the surface density, with all four images having the same scale.

the smaller mass disks are more easily brought out of the central disk plane, leading to streamers that are originally closer in to the center of the disk. Indeed, since the original mass CMinor disk show the most of this material, the low mass C halos were worse, showing almost a complete shell at large radii comprised of stars that began in the outer reaches of the initial disks.

In contrast to the strong dependence of bar strengths on disk mass, we find that a factor of 3 reduction in the disk mass hardly affects the dark matter halo between $z = 1.3$ and 1.0 as the rigid disk is introduced. The left panels of Fig. 5.13 show that the axial ratio b/a for both haloes A and C is driven towards unity, while c/a is largely preserved as the rigid disk is brought to its final mass, nearly symmetrizing the halo in the disk plane. The effects on the halo shape do not weaken as the final disk mass is reduced by a factor of three. The axial ratios are shown for a particular equipotential surface, chosen to be about five kpc from the center of the disk.

The alternate mass disks also reorient themselves during the evolution. All four AMinor disks have similar reorientation histories, showing at most a 12 degree offset between the disk orientations. The alternate CMinor runs, however, had more divergent reorientation histories. The angle between the original CMinor disk normal and the disk normal in the alternate CMinor runs was typically around 30 degrees, rising as high as 60-80 temporarily near $z \sim 0.7$.

The runs that include gas show drastically reduced signatures of bars, and the associated heating. The strong effect of this massive gas component is expected because the gas offers support against self-gravity via its pressure. The extra support provided in these simulations in likely an overestimate, as realistic gas cools and forms stars, but the ability of a simple gas model to suppress the bar points to the need to include a realistic gas component. The lack of a strong bar also means that the subsequent bar buckling cannot occur and the central thickness of the disk is smaller at the end of the simulation.

To assess the degree of convergence of these results with the resolution of the stellar disk particles, we have run a disk in the AMinor orientation with 5×10^5 particles instead of 2×10^5, labeled AMinorHR in Table 5.1. The results of this simulation, e.g., the values of A_2 and ζ, agree to within 5% of the run at our fiducial resolution. A similar degree of convergence is also reported in the detailed study of Dubinski et al. (2009). Quantities such as the bar strength, pattern speed, and halo response to disk in their simulation with 10^6 dark matter particles and 1.8×10^5 disk particles are very similar to those in runs with 10 and 100 times more particles.

5.6 Subhalos of Aquarius

To link the evolution of the disks in these simulations to the history of subhalo impactors on the Aquarius halos, a catalog of subhalo properties is needed. To get an initial feel for the level of activity in the four halos used, we examined the outputs

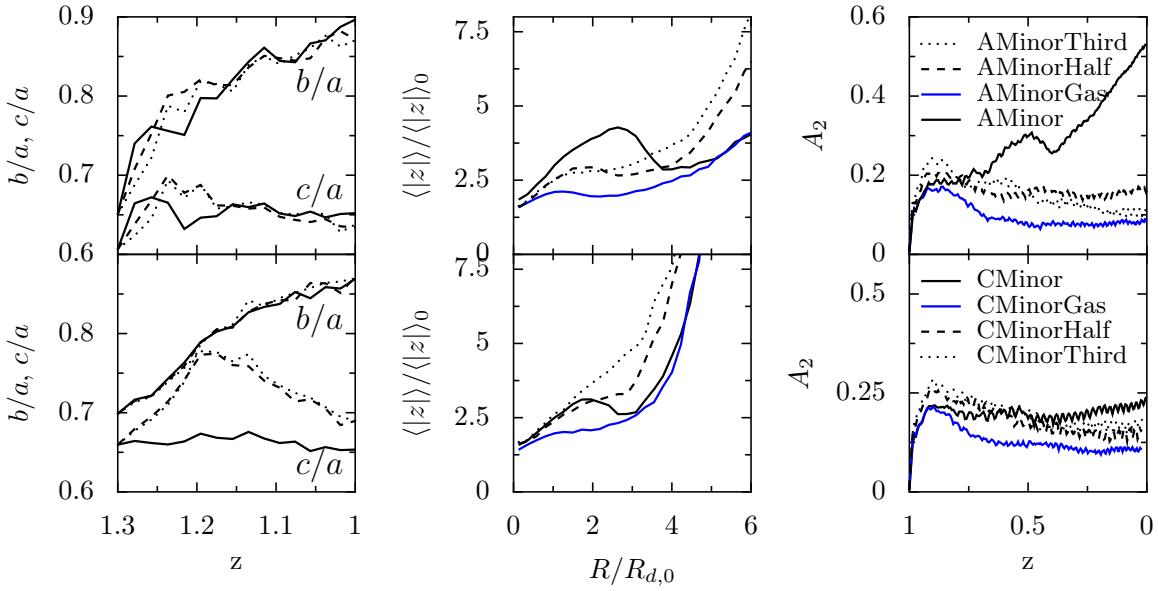

Figure 5.13: Comparison of four disk models for halo A (top row) and halo C (bottom row). The four models differ in the assumed disk mass: $5 \times 10^{10}, 3 \times 10^{10}, 2.5 \times 10^{10}$ and $1.67 \times 10^{10} M_{\odot}$ for runs labeled Minor, MinorGas, MinorHalf, and MinorThird, respectively. *Left:* The axial ratios of the dark matter haloes between $z = 1.3$ and 1.0 hardly depend on the disk mass. *Middle:* Mean vertical distance $|z|$ of the stellar particles from the disk plane as a function of disk radius at $z = 0$. Among these runs, only the AMinor and CMinor disks (black solid curves) form stellar bars, which produce a bump in $|z|$ at a radius of ~ 2 - 3 R_d. *Right:* Bar strengths measured by the $m = 2$ coefficient A_2 as a function of redshift. Reducing the disk mass stabilizes the disk against bar formation. Note that the runs including gas are not included in the left panels because before the disk goes live, their evolution is identical to the original 'Minor' runs.

of SUBFIND (Springel et al., 2001) for the original Aquarius halos A5, B5, C5 and D5 and created a merger history for all the subhalos in these catalogs. More detailed statements about the effects of the substructure on the disks, or the disks on the substructure require a halo finder to be run on the actual results of the simulation. These two approaches are described below.

5.6.1 SUBFIND halos

In this section we describe the results of the original SUBFIND outputs for the Aquarius simulation. We construct merger histories, and identify subhalos that are capable of affecting the stellar disk.

The SUBFIND algorithm (Springel et al., 2001) identifies substructure of a halo in two steps. The first is to run a normal friends-of-friends halo finder to identify particle groups. These groups are then given as inputs to the subhalo finding procedure. Subhalos are identifies as gravitationally bound sets of particles which are locally over-dense. This algorithm assigns each dark matter particle to one substructure and detailed information about the merger history of the halo and its substructure can easily be generated.

The SUBFIND outputs provide a list of all subhalos present in the Aquarius simulations, at each output redshift. But not all of these subhalos will be interesting for our purposes; those that are far away or those that are very low in mass can not have a significant impact on the disk. Further, the SUBFIND catalogs give only instantaneous information about the subhalos, and will not, in general, include the distance of closest approach as the subhalos move in the potential of the host halo. Determining if a given subhalo is interesting then requires the construction of its history over the entire simulation time.

The main problem is to associate each halo at a time t_1 to halos at a later time t_2, and thereby creating a history for each subhalo in the relevant volume of our simulation. For each subhalo that is within ten disk radii, and which is larger than one thousandth the disk mass, we construct a history both forward and backward in time in the following way.

For the subhalo of interest, the overlap between particle membership at the current time is computed with each subhalo in the next SUBFIND output. The halo with the largest number of particles common to the initial subhalo is taken to be the descendant of the initial subhalo. This process is then repeated at the subsequent output. The result of this procedure, applied to each subhalo which passes the proximity and mass cuts, is a tree structure that links each subhalo at time t_1 to a subhalo at a later time.

In will be the case that multiple progenitor halos can have the same descendant. Indeed, this is exactly the result when two subhalos merge, or when, as is more common, a subhalo merges with the main halo. By tracing through this tree, a history of the halos' position and mass can be constructed.

In a few cases, the matching forward in time is difficult to achieve because subhalos

might temporarily pass close to a much larger structure, and lose their resolution. For most of these cases, matching the current subhalo to a subhalo two snapshots removed will solve the issue, as the subhalo often will move out of the central regions of the massive object and be counted as a separate object once more. Another difficulty is that the process of tidal stripping can often lead to very low overlap between a halo and its descendant. These cases are relatively easy to handle by also performing the matching backwards in time, as often the central core of the subhalo survives close passages intact, and it is only the outer edges of the subhalo that are stripped.

Once each interesting subhalo has a history, the times where the subhalo makes a close passage to the central halo, and thus the stellar disk, can be examined more closely. For each subhalo passing within 10 disk radii of the center, we compute orbital parameters of the halo's trajectory. The position of the subhalo at the three times nearest to each close passage of the center are used to construct orbital parameters for the subhalo. The method is general enough to find elliptical, parabolic or hyperbolic orbits. The distance of closest approach can then easily be found for the given orbit fit. The history of each main Aquarius halo is constructed from the collection of these fits, and a picture of the main events involving halo substructure develops.

Figures 5.14-5.17 show the most massive subhalo impactors in each of the four Aquarius halos used in this work. Each figure gives the distance of the subhalo from the disk center (in units of the initial disk scale length), the mass of the subhalo (in units of the disk mass) and the path of the subhalo relative to the disk position, projected into the disk plane.

Figures 5.18-5.21 give another view of the subhalo merger history. Each figure shows the pericenter distance and mass of the major subhalo events for each Aquarius halo. As can be seen in the previous figures, a subhalo can have many close passages of the disk. The symbols in these figures show each such passage. To aid in comparison, the colors in these figures match the colors in the previous figures.

The picture that develops from these figures is that the level of activity in the halos hosting our disk simulations vary significantly in the level and strength of their substructure impact history. In halos A and B, the most significant close passages have only a mass of a few percent of the stellar disk mass. Halos C and D, on the other hand, each have an encounter with a body larger than one tenth of the disk mass. Such encounters are cosmologically common and can destroy a disk (Purcell et al., 2009) for some values of the subhalo orbital parameters. By far, halo D has the most active history between $z = 1.0$ and today.

In addition to the subhalos having an effect on the disk, the simulations also allow interactions in the other direction, with the disk influencing the subhalos. The subhalo histories above are constructed from the SUBFIND outputs of the original unmodified Aquarius simulations, and will not strictly apply in the presence of the disk. However, the particles in the subhalos in these original SUBFIND catalogs can be easily found in the simulations including the disk, and the resulting structures can be examined. In only a few cases are the SUBFIND halos completely disrupted in

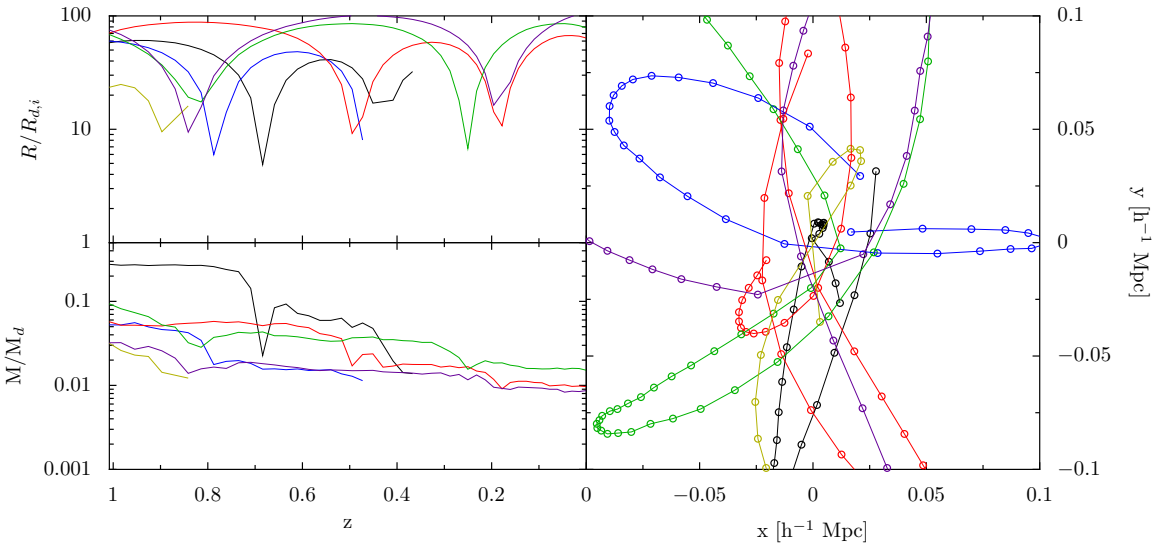

Figure 5.14: The history of massive subhalos for Aquarius A5. Shown in the top left panel is the distance of each halo from the disk center (in units of the disk scale length). In the bottom left is the mass history of the subhalo (in units of the disk mass). The right panel shows the orbit of the subhalos with respect to the disk center projected onto the plane of the disk.

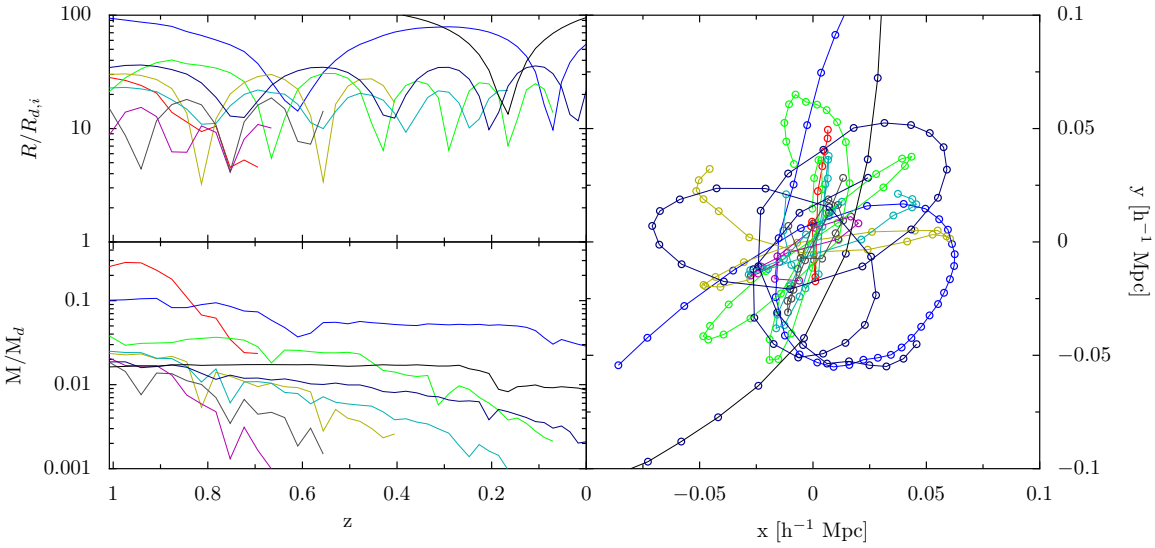

Figure 5.15: As figure 5.14 for Aquarius halo B5.

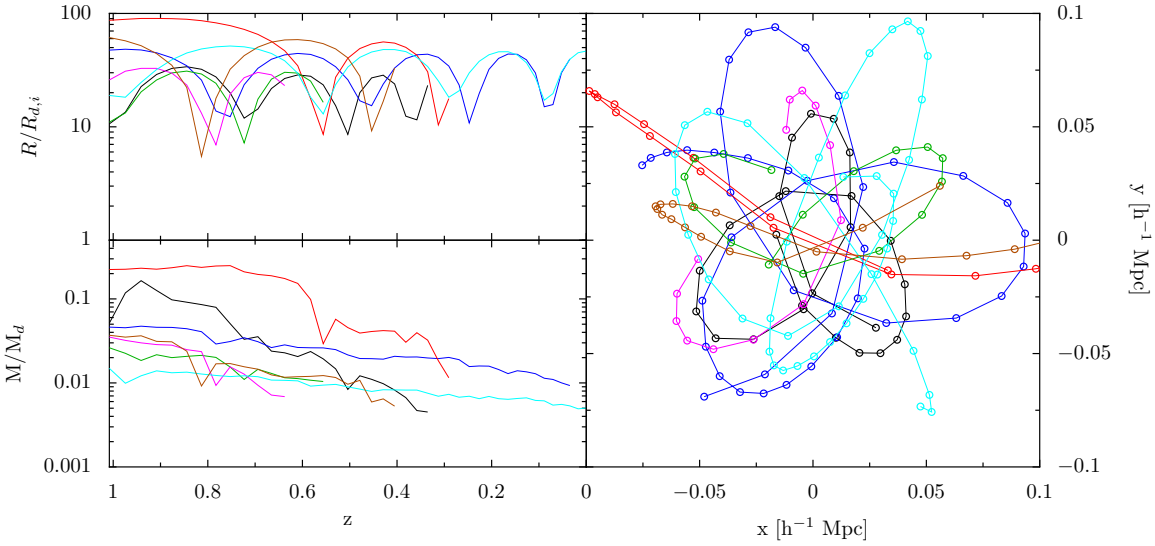

Figure 5.16: As figure 5.14 for Aquarius halo C5.

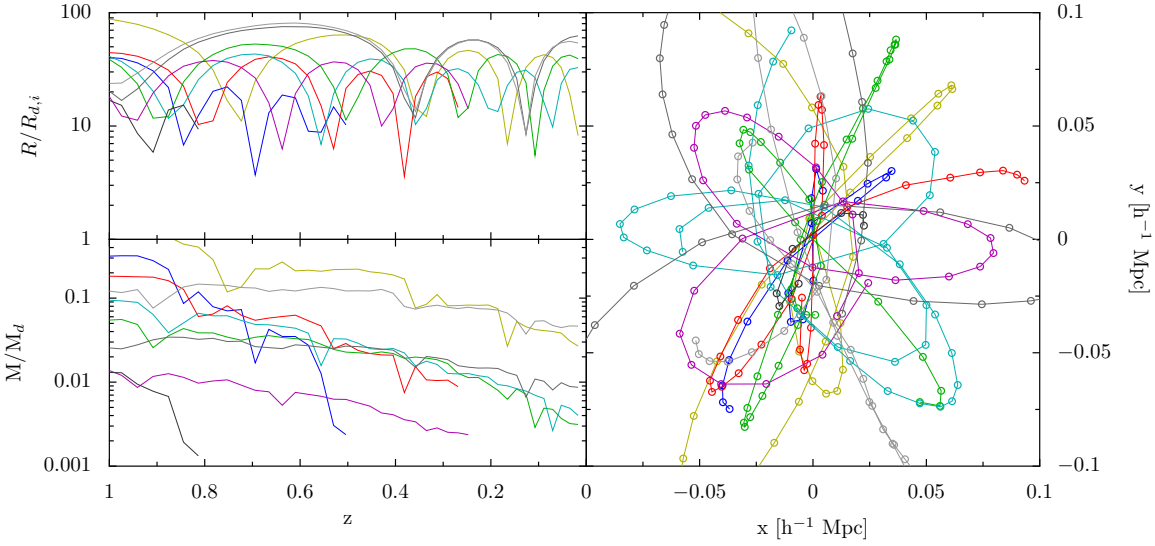

Figure 5.17: As figure 5.14 for Aquarius halo D5.

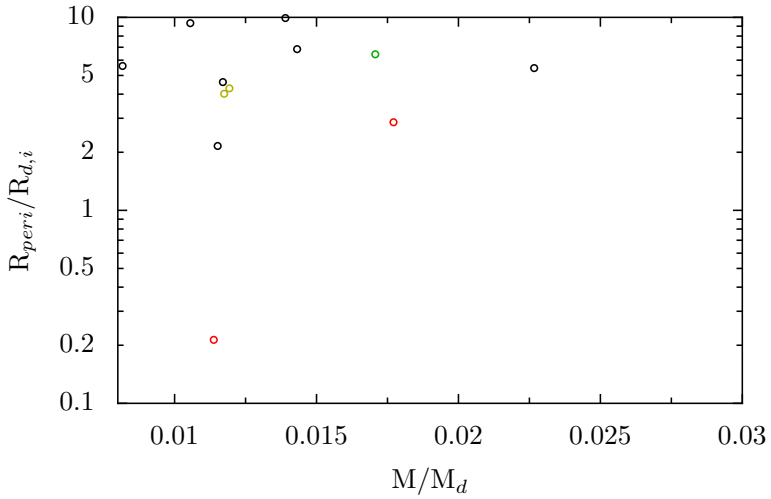

Figure 5.18: Pericentric distances and subhalo masses for the close passages of substructure in Aquarius halo A5. The colors are chosen to match those of figure 5.14, for those subhalos that make multiple passes of the halo center. Those subhalos that have only one close passage are shown in black.

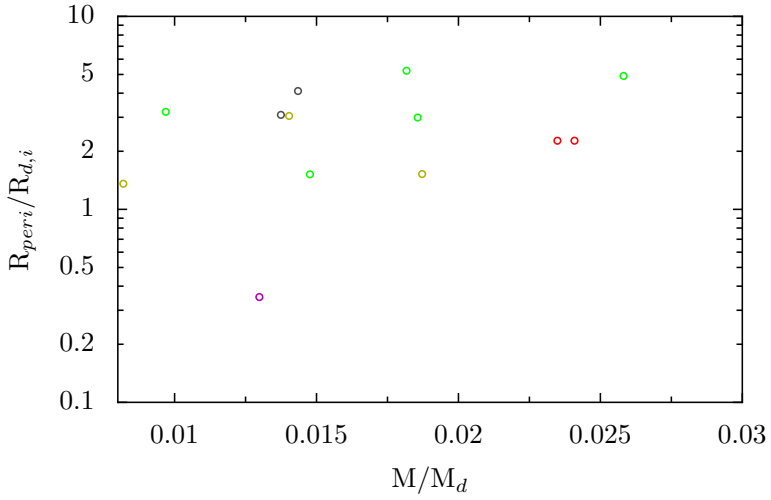

Figure 5.19: As figure 5.18 but for Aquarius halo B5.

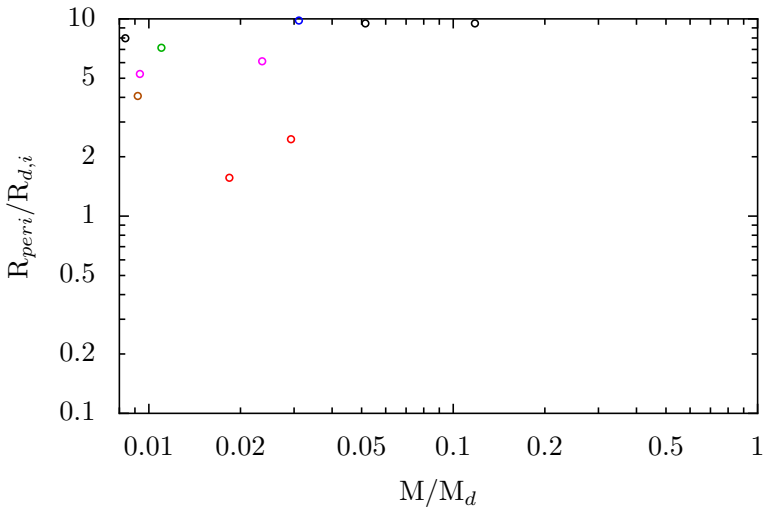

Figure 5.20: As figure 5.18 but for Aquarius halo C5.

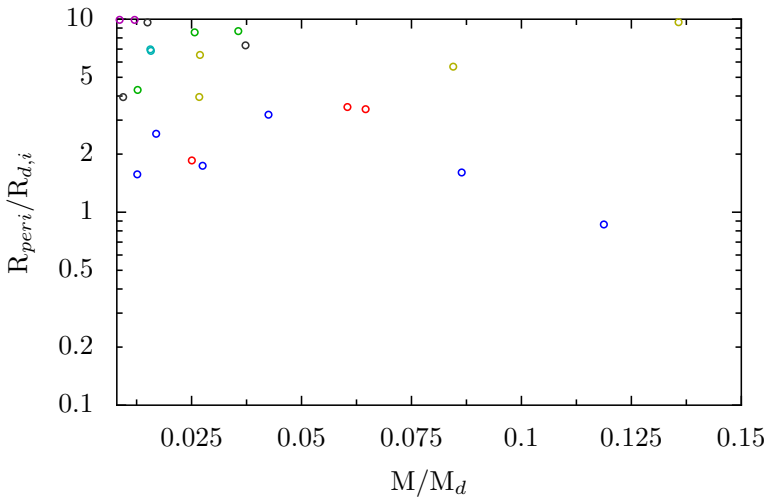

Figure 5.21: As figure 5.18 but for Aquarius halo D5.

the simulations with disks included. More often, there is a central core of the original subhalo that survives, and the other members in the original catalog form long tidal tails. Three example halos from the AMinor simulation are shown in figure 5.22, which demonstrates the three major results of applying this ID matching procedure. The halo marked with green points retains essentially all of its compact nature. The halo particles marked in blue show a concentrated core, but also tidal tails that extend quite far from the center. The red halo, though there is some concentration of particles in the lower right, is essentially fully disrupted.

To determine the effect of the disk on the substructure, we used the following procedure to identify structures that survive to $z = 0.0$ for each halo, without disks and with disks in both orientations. The particles in our simulations that have the same ID's as those in the original SUBFIND outputs are collected and examined. For each, the center of mass is computed using an iterative procedure that shrinks the sphere in which the calculation is performed at each step, terminating after a fixed number of steps. The changes in center of mass position in the final two steps were always on the order of a few parsecs, so the centers found are well converged. Then, the half mass radius of each collection of particles is found. This gives a notion of how compact the collection of particles is. For a group of particles which still form a reasonable subhalo, the half mass radius should be small, even if there are some tidal tails, as the bulk of the mass is still centrally located.

Upon examination of the results numerically and visually, the best metric for the survival of the subhalo in our simulations was if the half mass radius was smaller than 25 kpc. This procedure is only necessary because we did not have access to SUBFIND, and only had the outputs for the original Aquarius runs for halos A5, B5, C5 and D5. Just like some particles that were associated with a given structure in the original Aquarius simulation are part of long tidal tails in our modified simulations, some particles that were not members are likely to become members. So this procedure cannot find accurate halo masses or other integral properties. Instead, it provides a picture of where substructures can be found with respect to the disk.

Figure 5.23 shows the main result of this procedure. The cumulative number of substructures as a function of radius from the disk is shown for the unmodified halo simulations (ANoDisk and similar from table 5.1) in black, the minor orientation runs in red, and the major orientation runs in blue. These curves give the sum for all four halos in each category. As before, halos with small mass are removed. The solid line shows only halos with a mass larger than 0.1% of the disk mass. To see how the results varied with this mass cut, also shown are the counts for halos more massive that 5% of the disk (dashed) and the counts for halos more massive than 10% of the disk mass.

The inclusion of the disk in the simulations leads to fewer substructures over almost the entire range explored. There are three mechanisms that could account for such a deficit: tidal stripping of the substructures, tidal heating of the substructure by the host halo, and disk shocking as substructures pass through the disk(D'Onghia

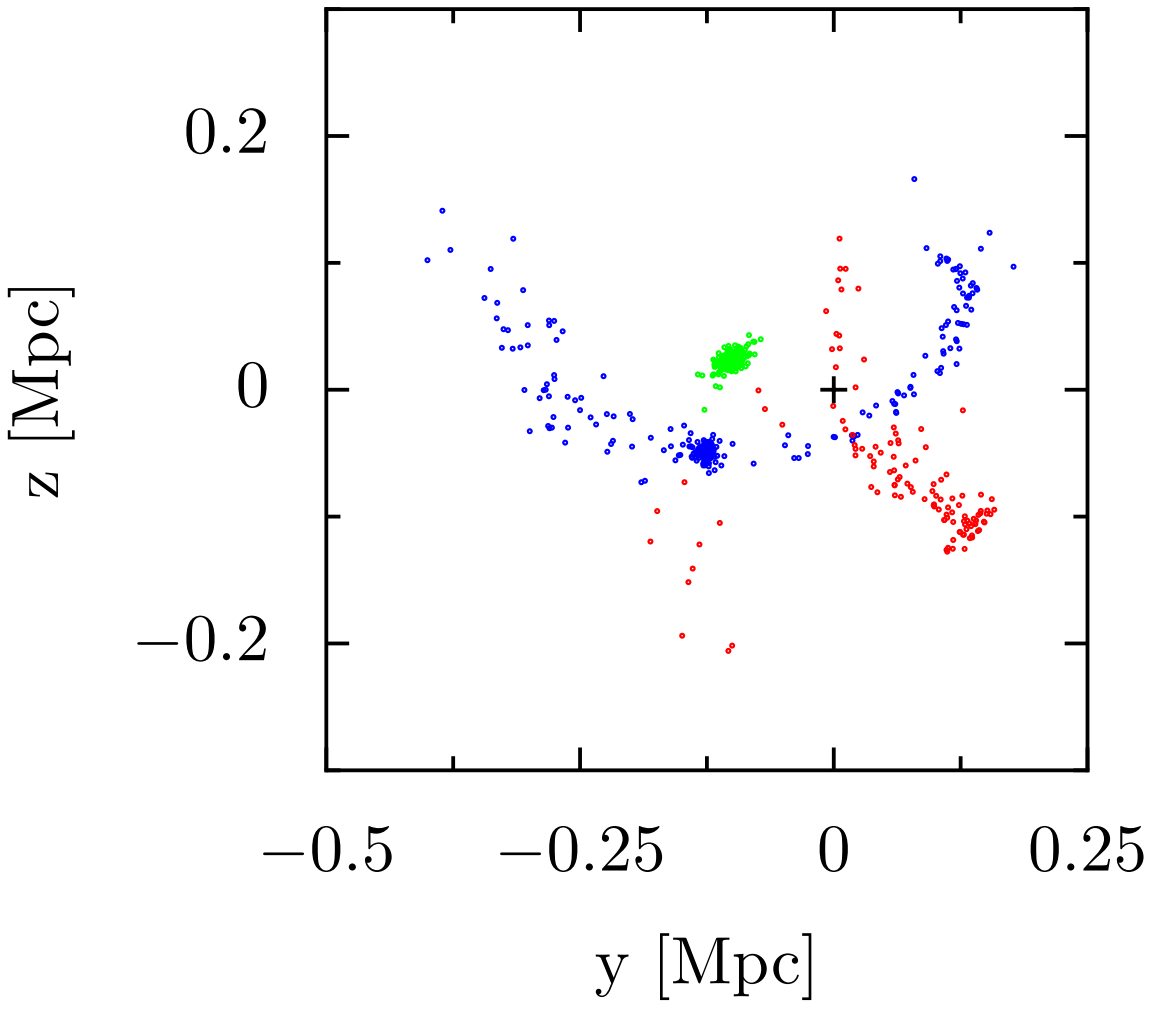

Figure 5.22: Positions of three example subhalos from the SUBFIND catalog. Shown are the positions of the member particles in the AMinor simulation projected onto the coordinate axes. The central halo's location is marked with a '+'. Each of the main cases are shown: the green halo survives relatively intact; the blue halo has long tidal tails, but has a core that remains; the red halo is disrupted with only a hint of a remaining core.

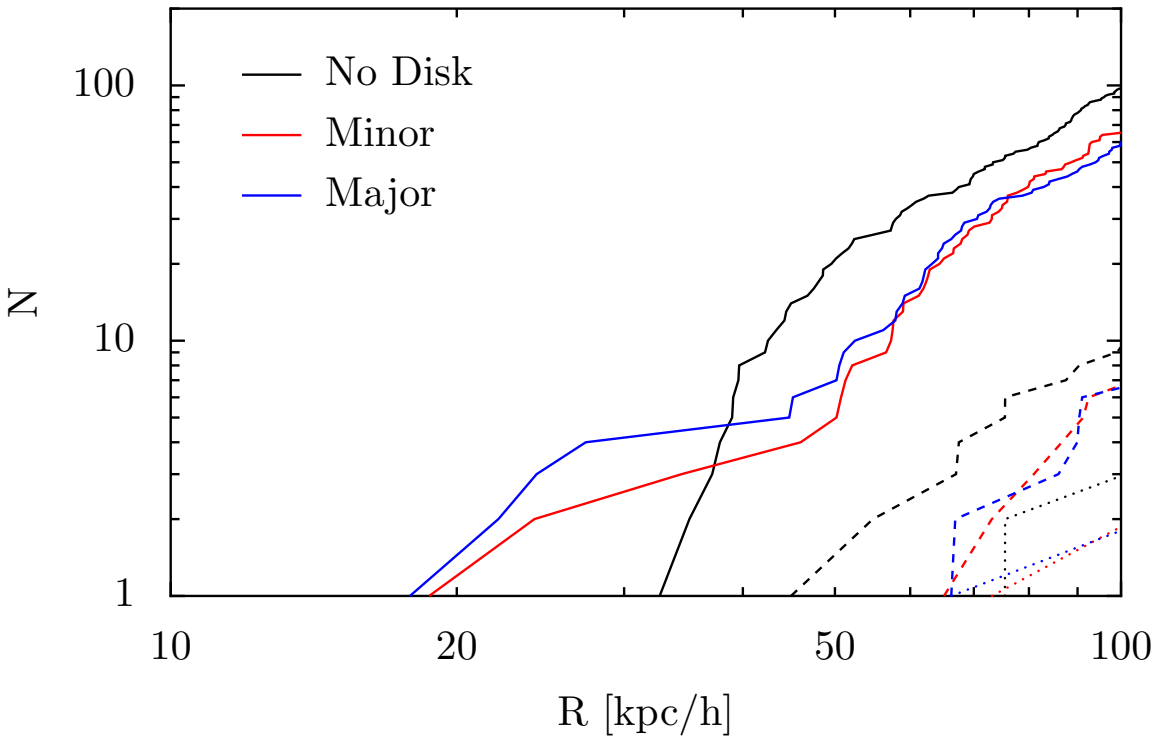

Figure 5.23: The cumulative number density of substructure with radius for the simulations without disks (black), with disks in the minor orientation (red) and with disks in the major orientation (blue). Each curve is the sum over each Aquarius halo for the given type of simulation. Solid lines count halos that are at least one thousandth the disk mass, dashed lines count halos that are at least 5% of the disk mass, and the dotted line shows only those halos greater than 10% of the disk mass.

et al., 2010). The first two mechanisms are present in both runs with and without disks, though they can be exacerbated by the alterations to the main halo's potential with a disk included. Disk shocking can only occur in the runs with a disk, and it would be interesting to do a more careful study of the subhalos' interaction with the disk. However, without access to SUBFIND, any such attempt would be fraught with difficulty. Several publicly available halo finders exist, but comparison to the canonical results from the original Aquarius simulations would be made more difficult.

5.7 Discussion and Conclusions

5.7.1 Summary of Results

We have presented the results of simulation of live stellar disks in the fully cosmological setting of the Aquarius simulations. The simulations take place in two phases, first by preparing the halo for the live disk with a rigid disk potential, and then by inserting a live disk of particles which are evolved to today. We explored a range of halos, and multiple disk models.

Generically, the halos are initially triaxial and symmetrize during the ramping, and subsequent live phases of the evolution. Similar results have been seen in both isolated halos (Berentzen et al., 2006) and in cosmological settings (Berentzen and Shlosman, 2006, Machado and Athanassoula, 2010). During the ramping phase, the halos do not experience significant reorientation, though in the B and D halos substructure impacts twist the unmodified halo.

With the exception of the disks in the C halo, the live disks form massive bars that dominate the dynamics of the star particles. The bars, which grow throughout the simulation, eventually buckle and demonstrate the typical x-shaped structure (Martinez-Valpuesta et al., 2006). The disk scale length grows in the disks with a bar, primarily as a result of a single component model no longer applying. In every disk the scale height increased during the evolution, and for those disks with bars there was a significant increase in disk height near the center of the disk after the bar buckles.

In every disk there was a gradual overall vertical heating, and for those disks with bars, a relatively sudden increase in vertical velocity dispersion. The appearance of a strong bar also heats the stellar particles in the plane of the disk.

In addition to the change in structure of each disk, the disk normal evolves during the simulation. The reorientation of the disk follows the change in orientation of the halo figure axes. So while the disk does reorient, it does so in a way that is consistent with the dark matter halo. As the disk reorients, the extremities of the disk are left behind and end up as streams that are significantly out of the plane of the central disk. These streams show up in the height of the disk at large radius, and in the vertical and azimuthal velocity dispersions at large radius.

Alternate disk models were able to stabilize the disk against the bar by decreasing the mass of the stellar component. The primary reason for this stabilization is that the drop in mass reduces the self-gravity of the disk, and the halo's potential can then dominate the disk's dynamics. Including a gaseous component of the disk allows stabilization without reducing the mass of the disk. However, the gas in this work included no star formation, cooling or feedback, so the support provided by this gas is an over-estimate. The purely stellar disk and the disks with an initial gaseous component can be thought of as two ends bracketing the results for a more realistic gas model.

5.7.2 Comparison to Observations

The disks presented in these simulations share many features with observed disk galaxies. Though our statistics are not good enough to perform detailed comparisons, there are some general features of disk galaxies in the local universe captured by our simulations.

By construction, the mass of the disk models presented agrees with recent measurements of the mass of the Milky Way (McMillan, 2011). Also by construction, we agree with measurements of the scale length and scale height of the Milky Way (McMillan, 2011, Jurić et al., 2008). With these relatively few data as inputs, our simulations were able to reproduce a number of observations of real galaxies.

In the local universe, observations indicate that as many as 2/3 of disk galaxies host a bar (Knapen et al., 2000, Marinova and Jogee, 2007). With only a few exceptions, our simulations easily form bars, and most of the simulated disks host a bar as early as $z \sim 0.75$. Though the evolution of the bar fraction with redshift is still a subject of ongoing debate (e.g., Jogee et al. 2004, Sheth et al. 2008), the fraction of barred disks is non-negligible out to $z \sim 1$. In addition to the prevalence of bars, observations indicate a large number of galaxies with x-shaped structures, or peanut-shaped bulges (Bureau and Freeman, 1999, Bureau et al., 2006, Kuijken and Merrifield, 1995, Whitmore and Bell, 1988). One explanation for these features, which are also seen in our simulations (e.g., figure 5.3) is the buckling of a bar (Raha et al., 1991).

One conspicuous feature of our simulations is the misalignment between the orientation of the inner portions of the disk with the outer portions. By eye, the structures appear very much like observed warps in disk galaxies (Sancisi, 1976), which are quite common in the local universe, as seen in optical surveys (Reshetnikov and Combes, 1998, Sanchez-Saavedra et al., 1990) and neutral hydrogen, both in our own (Weinberg and Blitz, 2006, Levine et al., 2006) and other galaxies (García-Ruiz et al., 2002).

Some features of the velocity structure of our disks are also broadly in agreement with measurements of the Milky Way. The circular velocity of the Milky Way is $\sim 230\,\mathrm{km\,s^{-1}}$ near a radius of 10 kpc (McMillan, 2011, Xue et al., 2008), which is in rough agreement with the disks in our simulations. Also, our disks heat in the

vertical direction continuously, consistent with measurements done on local stars in Milky Way (Aumer and Binney, 2009). This heating should be distinguished from the rapid increase in σ_z seen as a result of the bar buckling. In particular, the CMajor disk showed no evidence of a bar and still showed gradual heating at the solar radius (see figure 5.9).

However, there are some shortcomings to the modeling employed here. Disk galaxies often show a thick-thin disk decomposition (Jurić et al., 2008). Our simulated galaxies showed no strong evidence for a thick-thin decomposition. Though, there is evidence that the thin disk stars are a different population than those of the thick disk (for example, chemically Navarro et al. 2011), leading one to suspect that a proper treatment of star formation is required to reproduce both a thick and thin disk in simulations. Further, most disks have roughly constant vertical scale height with radius van der Kruit and Searle (1981), Comerón et al. (2011), which ours fail to have (e.g., figures 5.4 and 5.5).

5.7.3 Conclusions

The stellar disks we have evolved in four Aquarius halos reproduced many of the features of local disk galaxies. However, while the Aquarius halos are a very realistic setting in which to explore numerically issues in galaxy formation, their realism can also confound analysis.

There are a number of ways to generate bars, be it halo triaxiality (Heller et al., 2007a,b), the tumbling of the halo figure (Dubinski and Chakrabarty, 2009) or perturbations from substructure (Kazantzidis et al., 2008). The presence of all of these phenomena makes determining which is the primary mechanism difficult. Similarly, the heating experienced by the disk can come from many sources: the intrinsic heating of the stellar particles by the bar (Saha et al., 2010b, Sotnikova and Rodionov, 2003), transient spiral structure (Fuchs, 2001, Minchev and Quillen, 2006) or from substructure impact (Benson et al., 2004, Toth and Ostriker, 1992). Like real galaxies, the disks in this work showed warps, but like other morphological features, there are a number of mechanisms that can support their growth. Halo tumbling can torque the stellar disk (Dubinski and Chakrabarty, 2009), misalignment between the disk and halo angular momentum can cause warps (Debattista and Sellwood, 1999), and substructure can also bring material out of the plane of the disk (Weinberg and Blitz, 2006).

The profound effect of the formation of a bar on the stellar disk precludes any strong statement from being made linking the evolution of these model disks to the properties of the host halo, be it the main halo itself, or the substructure which impacts on the disk. In the future, one extension of this work is to begin with disk models that are stable against bar formation. Though such disks might not be the most realistic, it would allow a test of the effect of a realistic pattern of substructure impact on a stellar disk, eliminating any heating from bar generation in the disk.

Another possible extension of this work is to include a realistic gas component which is star forming. The simple exploration of an inert gas component in this work showed that it is possible that the gas will stabilize the disk, both from the increased pressure support and the fact that gas can absorb some of the impact energy (Moster et al., 2010). However, correctly modeling the physics of star forming gas is difficult, and so our focus on the stellar components of the disk does not have to contend with any of the uncertainty in star formation feedback physics.

Bibliography

D. M. Alexander, W. N. Brandt, I. Smail, A. M. Swinbank, F. E. Bauer, A. W. Blain, S. C. Chapman, K. E. K. Coppin, R. J. Ivison, and K. Menéndez-Delmestre. Weighing the Black Holes in z ˜ 2 Submillimeter-Emitting Galaxies Hosting Active Galactic Nuclei. AJ, 135:1968–1981, May 2008. doi: 10.1088/0004-6256/135/5/1968.

B. Allgood, R. A. Flores, J. R. Primack, A. V. Kravtsov, R. H. Wechsler, A. Faltenbacher, and J. S. Bullock. The shape of dark matter haloes: dependence on mass, redshift, radius and formation. MNRAS, 367:1781–1796, April 2006. doi: 10.1111/j.1365-2966.2006.10094.x.

E. Athanassoula. Bar-Halo Interaction and Bar Growth. ApJ, 569:L83–L86, April 2002. doi: 10.1086/340784.

E. Athanassoula. Disc instabilities and semi-analytic modelling of galaxy formation. MNRAS, 390:L69–L72, October 2008. doi: 10.1111/j.1745-3933.2008.00541.x.

M. Aumer and J. J. Binney. Kinematics and history of the solar neighbourhood revisited. MNRAS, 397:1286–1301, August 2009. doi: 10.1111/j.1365-2966.2009.15053.x.

M. Aumer and S. D. M. White. Idealized models for galactic disk formation and evolution in 'realistic' LambdaCDM haloes. *ArXiv e-prints*, March 2012.

J. E. Barnes and L. E. Hernquist. Fueling starburst galaxies with gas-rich mergers. ApJ, 370:L65–L68, April 1991. doi: 10.1086/185978.

M. A. Bautista, J. P. Dunn, N. Arav, K. T. Korista, M. Moe, and C. Benn. Distance to Multiple Kinematic Components of Quasar Outflows: Very Large Telescope Observations of QSO 2359-1241 and SDSS J0318-0600. ApJ, 713:25–31, April 2010. doi: 10.1088/0004-637X/713/1/25.

E. F. Bell, S. Phleps, R. S. Somerville, C. Wolf, A. Borch, and K. Meisenheimer. The merger rate of massive galaxies. *astro-ph/0602038*, February 2006.

A. J. Benson, C. G. Lacey, C. S. Frenk, C. M. Baugh, and S. Cole. Heating of galactic discs by infalling satellites. MNRAS, 351:1215–1236, July 2004. doi: 10.1111/j.1365-2966.2004.07870.x.

I. Berentzen and I. Shlosman. Growing Live Disks within Cosmologically Assembling Asymmetric Halos: Washing Out the Halo Prolateness. ApJ, 648:807–819, September 2006. doi: 10.1086/506016.

I. Berentzen, I. Shlosman, and S. Jogee. Stellar Bar Evolution in Cuspy and Flat-cored Triaxial CDM Halos. ApJ, 637:582–597, February 2006. doi: 10.1086/498493.

I. Berentzen, I. Shlosman, I. Martinez-Valpuesta, and C. H. Heller. Gas Feedback on Stellar Bar Evolution. ApJ, 666:189–200, September 2007. doi: 10.1086/520531.

P. Bett, V. Eke, C. S. Frenk, A. Jenkins, J. Helly, and J. Navarro. The spin and shape of dark matter haloes in the Millennium simulation of a Λ cold dark matter universe. MNRAS, 376:215–232, March 2007. doi: 10.1111/j.1365-2966.2007.11432.x.

R. D. Blandford and M. C. Begelman. On the fate of gas accreting at a low rate on to a black hole. MNRAS, 303:L1–L5, February 1999. doi: 10.1046/j.1365-8711.1999.02358.x.

H. Bondi. On spherically symmetrical accretion. MNRAS, 112:195–+, 1952.

C. M. Booth and J. Schaye. Cosmological simulations of the growth of supermassive black holes and feedback from active galactic nuclei: method and tests. MNRAS, 398:53–74, September 2009. doi: 10.1111/j.1365-2966.2009.15043.x.

F. Bournaud, C. J. Jog, and F. Combes. Multiple minor mergers: formation of elliptical galaxies and constraints for the growth of spiral disks. A&A, 476:1179–1190, December 2007. doi: 10.1051/0004-6361:20078010.

A. H. Bridle and R. A. Perley. Extragalactic Radio Jets. ARA&A, 22:319–358, 1984. doi: 10.1146/annurev.aa.22.090184.001535.

J. S. Bullock. Shapes of Dark Matter Halos. In P. Natarajan, editor, *The Shapes of Galaxies and their Dark Halos*, pages 109–113, March 2002.

M. Bureau and K. C. Freeman. The Nature of Boxy/Peanut-Shaped Bulges in Spiral Galaxies. AJ, 118:126–138, July 1999. doi: 10.1086/300922.

M. Bureau, G. Aronica, E. Athanassoula, R.-J. Dettmar, A. Bosma, and K. C. Freeman. K-band observations of boxy bulges - I. Morphology and surface brightness profiles. MNRAS, 370:753–772, August 2006. doi: 10.1111/j.1365-2966.2006.10471.x.

A. Burkert and J. Silk. Star Formation-Regulated Growth of Black Holes in Protogalactic Spheroids. ApJ, 554:L151–L154, June 2001. doi: 10.1086/321698.

C. A. Chang, A. V. R. Schiano, and A. M. Wolfe. The effect of a quasi-stellar object on its host galaxy - Dynamical and physical processes in the interstellar medium around a quasi-stellar object. ApJ, 322:180–200, November 1987. doi: 10.1086/165714.

A. Chung, M. S. Yun, G. Naraynan, M. Heyer, and N. R. Erickson. Evidence for 1000 km s^{-1} Molecular Outflows in the Local ULIRG Population. ApJ, 732:L15+, May 2011. doi: 10.1088/2041-8205/732/1/L15.

L. Ciotti and J. P. Ostriker. Cooling Flows and Quasars: Different Aspects of the Same Phenomenon? I. Concepts. ApJ, 487:L105+, October 1997. doi: 10.1086/310902.

L. Ciotti and J. P. Ostriker. Cooling Flows and Quasars. II. Detailed Models of Feedback-modulated Accretion Flows. ApJ, 551:131–152, April 2001. doi: 10.1086/320053.

L. Ciotti and J. P. Ostriker. Radiative Feedback from Massive Black Holes in Elliptical Galaxies: AGN Flaring and Central Starburst Fueled by Recycled Gas. ApJ, 665: 1038–1056, August 2007. doi: 10.1086/519833.

L. Ciotti, J. P. Ostriker, and D. Proga. Feedback from Central Black Holes in Elliptical Galaxies. I. Models with Either Radiative or Mechanical Feedback but not Both. ApJ, 699:89–104, July 2009. doi: 10.1088/0004-637X/699/1/89.

L. Ciotti, J. P. Ostriker, and D. Proga. Feedback from Central Black Holes in Elliptical Galaxies. III. Models with Both Radiative and Mechanical Feedback. ApJ, 717: 708–723, July 2010. doi: 10.1088/0004-637X/717/2/708.

A. L. Coil, B. J. Weiner, D. E. Holz, M. C. Cooper, R. Yan, and J. Aird. Outflowing Galactic Winds in Post-starburst and Active Galactic Nucleus Host Galaxies at $0.2 < z < 0.8$. ApJ, 743:46, December 2011. doi: 10.1088/0004-637X/743/1/46.

S. Comerón, B. G. Elmegreen, J. H. Knapen, H. Salo, E. Laurikainen, J. Laine, E. Athanassoula, A. Bosma, K. Sheth, M. W. Regan, J. L. Hinz, A. Gil de Paz, K. Menéndez-Delmestre, T. Mizusawa, J.-C. Muñoz-Mateos, M. Seibert, T. Kim, D. M. Elmegreen, D. A. Gadotti, L. C. Ho, B. W. Holwerda, J. Lappalainen, E. Schinnerer, and R. Skibba. Thick Disks of Edge-on Galaxies Seen through the Spitzer Survey of Stellar Structure in Galaxies (S^4G): Lair of Missing Baryons? ApJ, 741:28, November 2011. doi: 10.1088/0004-637X/741/1/28.

C. J. Conselice, M. A. Bershady, M. Dickinson, and C. Papovich. A Direct Measurement of Major Galaxy Mergers at z ¡ 3. AJ, 126:1183–1207, September 2003. doi: 10.1086/377318.

D. J. Croton, V. Springel, S. D. M. White, G. De Lucia, C. S. Frenk, L. Gao, A. Jenkins, G. Kauffmann, J. F. Navarro, and N. Yoshida. The many lives of active galactic nuclei: cooling flows, black holes and the luminosities and colours of galaxies. MNRAS, 365:11–28, January 2006. doi: 10.1111/j.1365-2966.2005.09675.x.

A. Curir, P. Mazzei, and G. Murante. Bar instability in cosmological halos. A&A, 447:453–463, February 2006. doi: 10.1051/0004-6361:20053418.

X. Dai, F. Shankar, and G. R. Sivakoff. 2MASS Reveals a Large Intrinsic Fraction of BALQSOs. ApJ, 672:108–114, January 2008. doi: 10.1086/523688.

K. M. Dasyra, L. J. Tacconi, R. I. Davies, R. Genzel, D. Lutz, T. Naab, D. B. Sanders, S. Veilleux, and A. J. Baker. Probing for evolutionary links between local ULIRGs and QSOs using NIR spectroscopy. *New Astronomy Review*, 50:720–724, November 2006. doi: 10.1016/j.newar.2006.06.079.

V. P. Debattista and J. A. Sellwood. Warped Galaxies from Misaligned Angular Momenta. ApJ, 513:L107–L110, March 1999. doi: 10.1086/311913.

V. P. Debattista, L. Mayer, C. M. Carollo, B. Moore, J. Wadsley, and T. Quinn. The Secular Evolution of Disk Structural Parameters. ApJ, 645:209–227, July 2006. doi: 10.1086/504147.

J. DeBuhr, E. Quataert, C.-P. Ma, and P. Hopkins. Self-regulated black hole growth via momentum deposition in galaxy merger simulations. MNRAS, 406:L55–L59, July 2010. doi: 10.1111/j.1745-3933.2010.00881.x.

J. DeBuhr, E. Quataert, and C.-P. Ma. The growth of massive black holes in galaxy merger simulations with feedback by radiation pressure. MNRAS, 412:1341–1360, April 2011. doi: 10.1111/j.1365-2966.2010.17992.x.

J. DeBuhr, E. Quataert, and C.-P. Ma. Galaxy-scale outflows driven by active galactic nuclei. MNRAS, 420:2221–2231, March 2012. doi: 10.1111/j.1365-2966.2011.20187.x.

T. Di Matteo, V. Springel, and L. Hernquist. Energy input from quasars regulates the growth and activity of black holes and their host galaxies. Nature, 433:604–607, February 2005. doi: 10.1038/nature03335.

C. L. Dobbs, A. Burkert, and J. E. Pringle. The properties of the interstellar medium in disc galaxies with stellar feedback. MNRAS, 417:1318–1334, October 2011. doi: 10.1111/j.1365-2966.2011.19346.x.

E. D'Onghia, V. Springel, L. Hernquist, and D. Keres. Substructure Depletion in the Milky Way Halo by the Disk. ApJ, 709:1138–1147, February 2010. doi: 10.1088/0004-637X/709/2/1138.

D. Downes and P. M. Solomon. Rotating Nuclear Rings and Extreme Starbursts in Ultraluminous Galaxies. ApJ, 507:615–654, November 1998. doi: 10.1086/306339.

J. Dubinski and D. Chakrabarty. Warps and Bars from the External Tidal Torques of Tumbling Dark Halos. ApJ, 703:2068–2081, October 2009. doi: 10.1088/0004-637X/703/2/2068.

J. Dubinski, I. Berentzen, and I. Shlosman. Anatomy of the Bar Instability in Cuspy Dark Matter Halos. ApJ, 697:293–310, May 2009. doi: 10.1088/0004-637X/697/1/293.

J. P. Dunn, M. Bautista, N. Arav, M. Moe, K. Korista, E. Costantini, C. Benn, S. Ellison, and D. Edmonds. The Quasar Outflow Contribution to AGN Feedback: VLT Measurements of SDSS J0318-0600. ApJ, 709:611–631, February 2010. doi: 10.1088/0004-637X/709/2/611.

F. Durier and C. Dalla Vecchia. Implementation of feedback in SPH: towards concordance of methods. *ArXiv e-prints*, May 2011.

G. Efstathiou, G. Lake, and J. Negroponte. The stability and masses of disc galaxies. MNRAS, 199:1069–1088, June 1982.

C. . Faucher-Giguere, E. Quataert, and N. Murray. A Physical Model of FeLoBALs: Implications for Quasar Feedback. *ArXiv e-prints*, August 2011.

L. Ferrarese and D. Merritt. A Fundamental Relation between Supermassive Black Holes and Their Host Galaxies. ApJ, 539:L9–L12, August 2000.

C. Feruglio, R. Maiolino, E. Piconcelli, N. Menci, H. Aussel, A. Lamastra, and F. Fiore. Quasar feedback revealed by giant molecular outflows. A&A, 518:L155+, July 2010. doi: 10.1051/0004-6361/201015164.

B. Fuchs. Density waves in the shearing sheet - III. Disc heating. MNRAS, 325: 1637–1642, August 2001. doi: 10.1046/j.1365-8711.2001.04549.x.

I. García-Ruiz, R. Sancisi, and K. Kuijken. Neutral hydrogen and optical observations of edge-on galaxies: Hunting for warps. A&A, 394:769–789, November 2002. doi: 10.1051/0004-6361:20020976.

J.-R. Gauthier, J. Dubinski, and L. M. Widrow. Substructure around M31: Evolution and Effects. ApJ, 653:1180–1193, December 2006. doi: 10.1086/508860.

K. Gebhardt, R. Bender, G. Bower, A. Dressler, S. M. Faber, A. V. Filippenko, R. Green, C. Grillmair, L. C. Ho, J. Kormendy, T. R. Lauer, J. Magorrian, J. Pinkney, D. Richstone, and S. Tremaine. A Relationship between Nuclear Black Hole Mass and Galaxy Velocity Dispersion. ApJ, 539:L13–L16, August 2000.

A. M. Ghez, S. Salim, N. N. Weinberg, J. R. Lu, T. Do, J. K. Dunn, K. Matthews, M. R. Morris, S. Yelda, E. E. Becklin, T. Kremenek, M. Milosavljevic, and J. Naiman. Measuring Distance and Properties of the Milky Way's Central Supermassive Black Hole with Stellar Orbits. ApJ, 689:1044–1062, December 2008. doi: 10.1086/592738.

J. Goodman. Self-gravity and quasi-stellar object discs. MNRAS, 339:937–948, March 2003. doi: 10.1046/j.1365-8711.2003.06241.x.

A. W. Graham. Fundamental Planes and the Barless M_{bh}-σ Relation for Supermassive Black Holes. ApJ, 680:143–153, June 2008. doi: 10.1086/587473.

J. E. Greene, L. C. Ho, and A. J. Barth. Black Holes in Pseudobulges and Spheroidals: A Change in the Black Hole-Bulge Scaling Relations at Low Mass. ApJ, 688:159–179, November 2008. doi: 10.1086/592078.

J. E. Greene, C. Y. Peng, M. Kim, C.-Y. Kuo, J. A. Braatz, C. M. Violette Impellizzeri, J. J. Condon, K. Y. Lo, C. Henkel, and M. J. Reid. Precise Black Hole Masses from Megamaser Disks: Black Hole-Bulge Relations at Low Mass. ApJ, 721:26–45, September 2010. doi: 10.1088/0004-637X/721/1/26.

K. Gültekin, D. O. Richstone, K. Gebhardt, T. R. Lauer, S. Tremaine, M. C. Aller, R. Bender, A. Dressler, S. M. Faber, A. V. Filippenko, R. Green, L. C. Ho, J. Kormendy, J. Magorrian, J. Pinkney, and C. Siopis. The M-σ and M-L Relations in Galactic Bulges, and Determinations of Their Intrinsic Scatter. ApJ, 698:198–221, June 2009. doi: 10.1088/0004-637X/698/1/198.

Q. Guo, S. White, C. Li, and M. Boylan-Kolchin. How do galaxies populate dark matter haloes? MNRAS, 404:1111–1120, May 2010. doi: 10.1111/j.1365-2966.2010.16341.x.

Q. Guo, S. Cole, V. Eke, and C. Frenk. Satellite Galaxy Number Density Profiles in the Sloan Digital Sky Survey. *ArXiv e-prints*, January 2012.

N. Häring and H. Rix. On the Black Hole Mass-Bulge Mass Relation. ApJ, 604: L89–L92, April 2004.

C. H. Heller, I. Shlosman, and E. Athanassoula. Structure Formation inside Triaxial Dark Matter Halos: Galactic Disks, Bulges, and Bars. ApJ, 671:226–242, December 2007a. doi: 10.1086/523260.

C. H. Heller, I. Shlosman, and E. Athanassoula. Induced Nested Galactic Bars inside Assembling Dark Matter Halos. ApJ, 657:L65–L68, March 2007b. doi: 10.1086/513104.

L. Hernquist. An analytical model for spherical galaxies and bulges. ApJ, 356:359–364, June 1990. doi: 10.1086/168845.

L. Hernquist and J. C. Mihos. Excitation of Activity in Galaxies by Minor Mergers. ApJ, 448:41–+, July 1995. doi: 10.1086/175940.

L. C. Ho, J. Darling, and J. E. Greene. Properties of Active Galaxies Deduced from H I Observations. ApJ, 681:128–140, July 2008. doi: 10.1086/588207.

A. Hobbs, S. Nayakshin, C. Power, and A. King. On the role of supernovae-driven turbulence in the feeding of supermassive black holes. *ArXiv e-prints*, January 2010.

P. F. Hopkins and M. Elvis. Quasar feedback: more bang for your buck. MNRAS, 401:7–14, January 2010. doi: 10.1111/j.1365-2966.2009.15643.x.

P. F. Hopkins and E. Quataert. An Analytic Model of Angular Momentum Transport by Gravitational Torques: From Galaxies to Massive Black Holes. *ArXiv e-prints*, July 2010a.

P. F. Hopkins and E. Quataert. How do massive black holes get their gas? MNRAS, 407:1529–1564, September 2010b. doi: 10.1111/j.1365-2966.2010.17064.x.

P. F. Hopkins, L. Hernquist, T. J. Cox, T. Di Matteo, P. Martini, B. Robertson, and V. Springel. Black Holes in Galaxy Mergers: Evolution of Quasars. ApJ, 630: 705–715, September 2005. doi: 10.1086/432438.

P. F. Hopkins, L. Hernquist, T. J. Cox, B. Robertson, and E. Krause. An Observed Fundamental Plane Relation for Supermassive Black Holes. ApJ, 669:67–73, November 2007. doi: 10.1086/521601.

P. F. Hopkins, T. J. Cox, J. D. Younger, and L. Hernquist. How do Disks Survive Mergers? ApJ, 691:1168–1201, February 2009. doi: 10.1088/0004-637X/691/2/1168.

P. F. Hopkins, N. Murray, E. Quataert, and T. A. Thompson. A maximum stellar surface density in dense stellar systems. MNRAS, 401:L19–L23, January 2010. doi: 10.1111/j.1745-3933.2009.00777.x.

P. F. Hopkins, E. Quataert, and N. Murray. Self-regulated star formation in galaxies via momentum input from massive stars. MNRAS, 417:950–973, October 2011. doi: 10.1111/j.1365-2966.2011.19306.x.

J. Hu. The black hole mass-stellar velocity dispersion correlation: bulges versus pseudo-bulges. MNRAS, 386:2242–2252, June 2008. doi: 10.1111/j.1365-2966.2008.13195.x.

C. J. Jog and J. P. Ostriker. The velocity dispersion of the giant molecular clouds - A viscous origin. ApJ, 328:404–426, May 1988. doi: 10.1086/166302.

S. Jogee, F. D. Barazza, H.-W. Rix, I. Shlosman, M. Barden, C. Wolf, J. Davies, I. Heyer, S. V. W. Beckwith, E. F. Bell, A. Borch, J. A. R. Caldwell, C. J. Conselice, T. Dahlen, B. Häussler, C. Heymans, K. Jahnke, J. H. Knapen, S. Laine, G. M. Lubell, B. Mobasher, D. H. McIntosh, K. Meisenheimer, C. Y. Peng, S. Ravindranath, S. F. Sanchez, R. S. Somerville, and L. Wisotzki. Bar Evolution over the Last 8 Billion Years: A Constant Fraction of Strong Bars in the GEMS Survey. ApJ, 615:L105–L108, November 2004. doi: 10.1086/426138.

P. H. Johansson, A. Burkert, and T. Naab. The Evolution of Black Hole Scaling Relations in Galaxy Mergers. ApJ, 707:L184–L189, December 2009a. doi: 10.1088/0004-637X/707/2/L184.

P. H. Johansson, T. Naab, and A. Burkert. Equal- and Unequal-Mass Mergers of Disk and Elliptical Galaxies with Black Holes. ApJ, 690:802–821, January 2009b. doi: 10.1088/0004-637X/690/1/802.

M. Jurić, Ž. Ivezić, A. Brooks, R. H. Lupton, D. Schlegel, D. Finkbeiner, N. Padmanabhan, N. Bond, B. Sesar, C. M. Rockosi, G. R. Knapp, J. E. Gunn, T. Sumi, D. P. Schneider, J. C. Barentine, H. J. Brewington, J. Brinkmann, M. Fukugita, M. Harvanek, S. J. Kleinman, J. Krzesinski, D. Long, E. H. Neilsen, Jr., A. Nitta, S. A. Snedden, and D. G. York. The Milky Way Tomography with SDSS. I. Stellar Number Density Distribution. ApJ, 673:864–914, February 2008. doi: 10.1086/523619.

S. Kaviraj, K. Schawinski, J. Silk, and S. S. Shabala. A simple model for AGN feedback in nearby early-type galaxies. MNRAS, 415:3798–3806, August 2011. doi: 10.1111/j.1365-2966.2011.19002.x.

D. Kawata and B. K. Gibson. Self-regulated active galactic nuclei heating in elliptical galaxies. MNRAS, 358:L16–L20, March 2005. doi: 10.1111/j.1745-3933.2005.00018.x.

S. Kazantzidis, J. S. Bullock, A. R. Zentner, A. V. Kravtsov, and L. A. Moustakas. Cold Dark Matter Substructure and Galactic Disks. I. Morphological Signatures of Hierarchical Satellite Accretion. ApJ, 688:254–276, November 2008. doi: 10.1086/591958.

S. Kazantzidis, A. R. Zentner, A. V. Kravtsov, J. S. Bullock, and V. P. Debattista. Cold Dark Matter Substructure and Galactic Disks. II. Dynamical Effects of Hierarchical Satellite Accretion. ApJ, 700:1896–1920, August 2009. doi: 10.1088/0004-637X/700/2/1896.

S. Kazantzidis, M. G. Abadi, and J. F. Navarro. The Sphericalization of Dark Matter Halos by Galaxy Disks. ApJ, 720:L62–L66, September 2010. doi: 10.1088/2041-8205/720/1/L62.

R. C. Kennicutt, Jr. Properties of H II region populations in galaxies. I - The first-ranked H II regions. ApJ, 334:144–158, November 1988. doi: 10.1086/166825.

A. Khalatyan, A. Cattaneo, M. Schramm, S. Gottlöber, M. Steinmetz, and L. Wisotzki. Is AGN feedback necessary to form red elliptical galaxies? MNRAS, 387:13–30, June 2008. doi: 10.1111/j.1365-2966.2008.13093.x.

J.-h. Kim, J. H. Wise, and T. Abel. Galaxy Mergers with Adaptive Mesh Refinement: Star Formation and Hot Gas Outflow. ApJ, 694:L123–L127, April 2009. doi: 10.1088/0004-637X/694/2/L123.

A. King. Black Holes, Galaxy Formation, and the M_{BH}-σ Relation. ApJ, 596:L27–L29, October 2003. doi: 10.1086/379143.

A. King. The AGN-Starburst Connection, Galactic Superwinds, and M_{BH}-σ. ApJ, 635:L121–L123, December 2005. doi: 10.1086/499430.

A. R. King and K. A. Pounds. Black hole winds. MNRAS, 345:657–659, October 2003. doi: 10.1046/j.1365-8711.2003.06980.x.

A. R. King, K. Zubovas, and C. Power. Large-scale outflows in galaxies. MNRAS, 415:L6–L10, July 2011. doi: 10.1111/j.1745-3933.2011.01067.x.

J. H. Knapen, I. Shlosman, and R. F. Peletier. A Subarcsecond Resolution Near-Infrared Study of Seyfert and "Normal" Galaxies. II. Morphology. ApJ, 529:93–100, January 2000. doi: 10.1086/308266.

M. Koss, R. Mushotzky, S. Veilleux, and L. Winter. Merging and Clustering of the Swift BAT AGN Sample. ApJ, 716:L125–L130, June 2010. doi: 10.1088/2041-8205/716/2/L125.

J. H. Krolik. *Active galactic nuclei : from the central black hole to the galactic environment*. Princeton University Press, 1999.

K. Kuijken and M. R. Merrifield. Establishing the connection between peanut-shaped bulges and galactic bars. ApJ, 443:L13–L16, April 1995. doi: 10.1086/187824.

C. Y. Kuo, J. A. Braatz, J. J. Condon, C. M. V. Impellizzeri, K. Y. Lo, I. Zaw, M. Schenker, C. Henkel, M. J. Reid, and J. E. Greene. The Megamaser Cosmology Project. III. Accurate Masses of Seven Supermassive Black Holes in Active Galaxies with Circumnuclear Megamaser Disks. ApJ, 727:20, January 2011. doi: 10.1088/0004-637X/727/1/20.

C. Lacey and S. Cole. Merger rates in hierarchical models of galaxy formation. MNRAS, 262:627–649, June 1993.

A. Laor and H. Netzer. Massive thin accretion discs. I - Calculated spectra. MNRAS, 238:897–916, June 1989.

E. S. Levine, L. Blitz, and C. Heiles. The Vertical Structure of the Outer Milky Way H I Disk. ApJ, 643:881–896, June 2006. doi: 10.1086/503091.

R. Levine, N. Y. Gnedin, and A. J. S. Hamilton. Measuring Gas Accretion and Angular Momentum Near Simulated Supermassive Black Holes. ApJ, 716:1386–1396, June 2010. doi: 10.1088/0004-637X/716/2/1386.

J. M. Lotz, P. Jonsson, T. J. Cox, D. Croton, J. R. Primack, R. S. Somerville, and K. Stewart. The Major and Minor Galaxy Merger Rates at z ¡ 1.5. ApJ, 742:103, December 2011. doi: 10.1088/0004-637X/742/2/103.

R. E. G. Machado and E. Athanassoula. Loss of halo triaxiality due to bar formation. MNRAS, 406:2386–2404, August 2010. doi: 10.1111/j.1365-2966.2010.16890.x.

J. Magorrian, S. Tremaine, D. Richstone, R. Bender, G. Bower, A. Dressler, S. M. Faber, K. Gebhardt, R. Green, C. Grillmair, J. Kormendy, and T. Lauer. The Demography of Massive Dark Objects in Galaxy Centers. AJ, 115:2285–2305, June 1998.

A. Marconi and L. K. Hunt. The Relation between Black Hole Mass, Bulge Mass, and Near-Infrared Luminosity. ApJ, 589:L21–L24, May 2003. doi: 10.1086/375804.

I. Marinova and S. Jogee. Characterizing Bars at z ˜ 0 in the Optical and NIR: Implications for the Evolution of Barred Disks with Redshift. ApJ, 659:1176–1197, April 2007. doi: 10.1086/512355.

I. Martinez-Valpuesta and I. Shlosman. Why Buckling Stellar Bars Weaken in Disk Galaxies. ApJ, 613:L29–L32, September 2004. doi: 10.1086/424876.

I. Martinez-Valpuesta, I. Shlosman, and C. Heller. Evolution of Stellar Bars in Live Axisymmetric Halos: Recurrent Buckling and Secular Growth. ApJ, 637:214–226, January 2006. doi: 10.1086/498338.

N. J. McConnell, C.-P. Ma, J. D. Murphy, K. Gebhardt, T. R. Lauer, J. R. Graham, S. A. Wright, and D. O. Richstone. Dynamical Measurements of Black Hole Masses in Four Brightest Cluster Galaxies at 100 Mpc. *ArXiv e-prints*, March 2012.

C. F. McKee and J. P. Ostriker. A theory of the interstellar medium - Three components regulated by supernova explosions in an inhomogeneous substrate. ApJ, 218:148–169, November 1977. doi: 10.1086/155667.

P. J. McMillan. Mass models of the Milky Way. MNRAS, 414:2446–2457, July 2011. doi: 10.1111/j.1365-2966.2011.18564.x.

B. R. McNamara and P. E. J. Nulsen. Heating Hot Atmospheres with Active Galactic Nuclei. ARA&A, 45:117–175, September 2007. doi: 10.1146/annurev.astro.45.051806.110625.

J. C. Mihos and L. Hernquist. Gasdynamics and Starbursts in Major Mergers. ApJ, 464:641–+, June 1996. doi: 10.1086/177353.

I. Minchev and A. C. Quillen. Radial heating of a galactic disc by multiple spiral density waves. MNRAS, 368:623–636, May 2006. doi: 10.1111/j.1365-2966.2006.10129.x.

M. Moe, N. Arav, M. A. Bautista, and K. T. Korista. Quasar Outflow Contribution to AGN Feedback: Observations of QSO SDSS J0838+2955. ApJ, 706:525–534, November 2009. doi: 10.1088/0004-637X/706/1/525.

B. P. Moster, A. V. Macciò, R. S. Somerville, P. H. Johansson, and T. Naab. Can gas prevent the destruction of thin stellar discs by minor mergers? MNRAS, 403: 1009–1019, April 2010. doi: 10.1111/j.1365-2966.2009.16190.x.

B. P. Moster, A. V. Maccio', R. S. Somerville, T. Naab, and T. J. Cox. The effects of a hot gaseous halo on disc thickening in galaxy minor mergers. *ArXiv e-prints*, August 2011.

N. Murray, J. Chiang, S. A. Grossman, and G. M. Voit. Accretion Disk Winds from Active Galactic Nuclei. ApJ, 451:498–+, October 1995. doi: 10.1086/176238.

N. Murray, E. Quataert, and T. A. Thompson. On the Maximum Luminosity of Galaxies and Their Central Black Holes: Feedback from Momentum-driven Winds. ApJ, 618:569–585, January 2005. doi: 10.1086/426067.

N. Murray, E. Quataert, and T. A. Thompson. The Disruption of Giant Molecular Clouds by Radiation Pressure & the Efficiency of Star Formation in Galaxies. ApJ, 709:191–209, January 2010. doi: 10.1088/0004-637X/709/1/191.

J. F. Navarro, C. S. Frenk, and S. D. M. White. The Structure of Cold Dark Matter Halos. ApJ, 462:563–+, May 1996. doi: 10.1086/177173.

J. F. Navarro, M. G. Abadi, K. A. Venn, K. C. Freeman, and B. Anguiano. Through thick and thin: kinematic and chemical components in the solar neighbourhood. MNRAS, 412:1203–1209, April 2011. doi: 10.1111/j.1365-2966.2010.17975.x.

H. Netzer. Ionized gas in active galactic nuclei. New A Rev., 52:257–273, August 2008. doi: 10.1016/j.newar.2008.06.009.

G. S. Novak, J. P. Ostriker, and L. Ciotti. Feedback from Central Black Holes in Elliptical Galaxies: Two-dimensional Models Compared to One-dimensional Models. ApJ, 737:26, August 2011. doi: 10.1088/0004-637X/737/1/26.

J. P. Ostriker, E. Choi, L. Ciotti, G. S. Novak, and D. Proga. Momentum Driving: Which Physical Processes Dominate Active Galactic Nucleus Feedback? ApJ, 722: 642–652, October 2010. doi: 10.1088/0004-637X/722/1/642.

B. M. Peterson, L. Ferrarese, K. M. Gilbert, S. Kaspi, M. A. Malkan, D. Maoz, D. Merritt, H. Netzer, C. A. Onken, R. W. Pogge, M. Vestergaard, and A. Wandel. Central Masses and Broad-Line Region Sizes of Active Galactic Nuclei. II. A Homogeneous Analysis of a Large Reverberation-Mapping Database. ApJ, 613: 682–699, October 2004. doi: 10.1086/423269.

C. Power, S. Nayakshin, and A. King. The accretion disc particle method for simulations of black hole feeding and feedback. MNRAS, 412:269–276, March 2011. doi: 10.1111/j.1365-2966.2010.17901.x.

D. J. Price. splash: An Interactive Visualisation Tool for Smoothed Particle Hydrodynamics Simulations. *Publications of the Astronomical Society of Australia*, 24: 159–173, October 2007. doi: 10.1071/AS07022.

D. Proga. Numerical Simulations of Mass Outflows Driven from Accretion Disks by Radiation and Magnetic Forces. ApJ, 585:406–417, March 2003. doi: 10.1086/345897.

C. W. Purcell, J. S. Bullock, and A. R. Zentner. Shredded Galaxies as the Source of Diffuse Intrahalo Light on Varying Scales. ApJ, 666:20–33, September 2007. doi: 10.1086/519787.

C. W. Purcell, S. Kazantzidis, and J. S. Bullock. The Destruction of Thin Stellar Disks Via Cosmologically Common Satellite Accretion Events. ApJ, 694:L98–L102, April 2009. doi: 10.1088/0004-637X/694/2/L98.

N. Raha, J. A. Sellwood, R. A. James, and F. D. Kahn. A dynamical instability of bars in disk galaxies. Nature, 352:411, August 1991. doi: 10.1038/352411a0.

V. Reshetnikov and F. Combes. Statistics of optical WARPS in spiral disks. A&A, 337:9–16, September 1998.

B. Robertson, T. J. Cox, L. Hernquist, M. Franx, P. F. Hopkins, P. Martini, and V. Springel. The Fundamental Scaling Relations of Elliptical Galaxies. ApJ, 641: 21–40, April 2006. doi: 10.1086/500360.

E. Romano-Díaz, I. Shlosman, C. Heller, and Y. Hoffman. Disk Evolution and Bar Triggering Driven by Interactions with Dark Matter Substructure. ApJ, 687:L13–L16, November 2008. doi: 10.1086/593168.

R. Roškar, V. P. Debattista, A. M. Brooks, T. R. Quinn, C. B. Brook, F. Governato, J. J. Dalcanton, and J. Wadsley. Misaligned angular momentum in hydrodynamic cosmological simulations: warps, outer discs and thick discs. MNRAS, 408:783–796, October 2010. doi: 10.1111/j.1365-2966.2010.17178.x.

D. S. N. Rupke and S. Veilleux. Integral Field Spectroscopy of Massive, Kiloparsec-scale Outflows in the Infrared-luminous QSO Mrk 231. ApJ, 729:L27+, March 2011. doi: 10.1088/2041-8205/729/2/L27.

K. Saha, Y.-H. Tseng, and R. E. Taam. The Effect of Bars and Transient Spirals on the Vertical Heating in Disk Galaxies. ApJ, 721:1878–1890, October 2010a. doi: 10.1088/0004-637X/721/2/1878.

K. Saha, Y.-H. Tseng, and R. E. Taam. The Effect of Bars and Transient Spirals on the Vertical Heating in Disk Galaxies. ApJ, 721:1878–1890, October 2010b. doi: 10.1088/0004-637X/721/2/1878.

L. V. Sales, J. F. Navarro, T. Theuns, J. Schaye, S. D. M. White, C. S. Frenk, R. A. Crain, and C. Dalla Vecchia. The Origin of Disks and Spheroids in Simulated Galaxies. *ArXiv e-prints*, December 2011.

M. L. Sanchez-Saavedra, E. Battaner, and E. Florido. Frequency of Warped Spiral Galaxies at Visible Wavelengths. MNRAS, 246:458, October 1990.

R. Sancisi. Warped HI Disks in Galaxies. A&A, 53:159, December 1976.

D. B. Sanders. Infrared Emission from AGN. In Y. Terzian, E. Khachikian, & D. Weedman, editor, *Activity in Galaxies and Related Phenomena*, volume 194 of *IAU Symposium*, page 25, 1999.

D. B. Sanders, B. T. Soifer, J. H. Elias, B. F. Madore, K. Matthews, G. Neugebauer, and N. Z. Scoville. Ultraluminous infrared galaxies and the origin of quasars. ApJ, 325:74–91, February 1988. doi: 10.1086/165983.

D. B. Sanders, E. S. Phinney, G. Neugebauer, B. T. Soifer, and K. Matthews. Continuum energy distribution of quasars - Shapes and origins. ApJ, 347:29–51, December 1989. doi: 10.1086/168094.

S. Y. Sazonov, J. P. Ostriker, and R. A. Sunyaev. Quasars: the characteristic spectrum and the induced radiative heating. MNRAS, 347:144–156, January 2004. doi: 10.1111/j.1365-2966.2004.07184.x.

S. Y. Sazonov, J. P. Ostriker, L. Ciotti, and R. A. Sunyaev. Radiative feedback from quasars and the growth of massive black holes in stellar spheroids. MNRAS, 358: 168–180, March 2005. doi: 10.1111/j.1365-2966.2005.08763.x.

C. Scannapieco, S. D. M. White, V. Springel, and P. B. Tissera. The formation and survival of discs in a ΛCDM universe. MNRAS, 396:696–708, June 2009. doi: 10.1111/j.1365-2966.2009.14764.x.

E. Scannapieco, J. Silk, and R. Bouwens. AGN Feedback Causes Downsizing. ApJ, 635:L13–L16, December 2005. doi: 10.1086/499271.

N. Z. Scoville, D. T. Frayer, E. Schinnerer, and M. Christopher. The Host Galaxies of Optically Bright Quasi-stellar Objects: Molecular Gas in z ¡ 0.1 Palomar-Green Quasi-stellar Objects. ApJ, 585:L105–L108, March 2003. doi: 10.1086/374544.

J. A. Sellwood, R. W. Nelson, and S. Tremaine. Resonant Thickening of Disks by Small Satellite Galaxies. ApJ, 506:590–599, October 1998. doi: 10.1086/306280.

N. I. Shakura and R. A. Sunyaev. Black holes in binary systems. Observational appearance. A&A, 24:337–355, 1973.

P. Sharma, E. Quataert, G. W. Hammett, and J. M. Stone. Electron Heating in Hot Accretion Flows. ApJ, 667:714–723, October 2007. doi: 10.1086/520800.

P. Sharma, I. J. Parrish, and E. Quataert. Thermal Instability with Anisotropic Thermal Conduction and Adiabatic Cosmic Rays: Implications for Cold Filaments in Galaxy Clusters. ApJ, 720:652–665, September 2010. doi: 10.1088/0004-637X/720/1/652.

S. Shen, H. J. Mo, S. D. M. White, M. R. Blanton, G. Kauffmann, W. Voges, J. Brinkmann, and I. Csabai. The size distribution of galaxies in the Sloan Digital Sky Survey. MNRAS, 343:978–994, August 2003. doi: 10.1046/j.1365-8711.2003.06740.x.

S. Shen, S. D. M. White, H. J. Mo, W. Voges, G. Kauffmann, C. Tremonti, and S. F. Anderson. The soft X-ray properties of quasars in the Sloan Digital Sky Survey. MNRAS, 369:1639–1653, July 2006. doi: 10.1111/j.1365-2966.2006.10463.x.

K. Sheth, D. M. Elmegreen, B. G. Elmegreen, P. Capak, R. G. Abraham, E. Athanassoula, R. S. Ellis, B. Mobasher, M. Salvato, E. Schinnerer, N. Z. Scoville, L. Spalsbury, L. Strubbe, M. Carollo, M. Rich, and A. A. West. Evolution of the Bar Fraction in COSMOS: Quantifying the Assembly of the Hubble Sequence. ApJ, 675:1141–1155, March 2008. doi: 10.1086/524980.

I. Shlosman, J. Frank, and M. C. Begelman. Bars within bars - A mechanism for fuelling active galactic nuclei. Nature, 338:45–47, March 1989. doi: 10.1038/338045a0.

I. Shlosman, M. C. Begelman, and J. Frank. The fuelling of active galactic nuclei. Nature, 345:679–686, June 1990. doi: 10.1038/345679a0.

J. Silk and A. Nusser. The Massive-black-hole-Velocity-dispersion Relation and the Halo Baryon Fraction: A Case for Positive Active Galactic Nucleus Feedback. ApJ, 725:556–560, December 2010. doi: 10.1088/0004-637X/725/1/556.

J. Silk and M. J. Rees. Quasars and galaxy formation. A&A, 331:L1–L4, March 1998.

L. Sironi and A. Socrates. The Eddington Limit in Cosmic Rays: An Explanation for the Observed Lack of Low-Mass Radio-Loud Quasars and The M-M_{sstarf} Relation. ApJ, 710:891–902, February 2010. doi: 10.1088/0004-637X/710/2/891.

N. Y. Sotnikova and S. A. Rodionov. Mechanisms of the Vertical Secular Heating of a Stellar Disk. *Astronomy Letters*, 29:321–335, May 2003. doi: 10.1134/1.1573281.

V. Springel. The cosmological simulation code GADGET-2. MNRAS, 364:1105–1134, December 2005. doi: 10.1111/j.1365-2966.2005.09655.x.

V. Springel and L. Hernquist. Cosmological smoothed particle hydrodynamics simulations: a hybrid multiphase model for star formation. MNRAS, 339:289–311, February 2003. doi: 10.1046/j.1365-8711.2003.06206.x.

V. Springel, S. D. M. White, G. Tormen, and G. Kauffmann. Populating a cluster of galaxies - I. Results at [formmu2]z=0. MNRAS, 328:726–750, December 2001.

V. Springel, T. Di Matteo, and L. Hernquist. Modelling feedback from stars and black holes in galaxy mergers. MNRAS, 361:776–794, August 2005a. doi: 10.1111/j.1365-2966.2005.09238.x.

V. Springel, T. Di Matteo, and L. Hernquist. Black Holes in Galaxy Mergers: The Formation of Red Elliptical Galaxies. ApJ, 620:L79–L82, February 2005b. doi: 10.1086/428772.

V. Springel, J. Wang, M. Vogelsberger, A. Ludlow, A. Jenkins, A. Helmi, J. F. Navarro, C. S. Frenk, and S. D. M. White. The Aquarius Project: the subhaloes of galactic haloes. MNRAS, 391:1685–1711, December 2008. doi: 10.1111/j.1365-2966.2008.14066.x.

K. R. Stewart, J. S. Bullock, R. H. Wechsler, A. H. Maller, and A. R. Zentner. Merger Histories of Galaxy Halos and Implications for Disk Survival. ApJ, 683:597–610, August 2008. doi: 10.1086/588579.

E. Sturm, E. González-Alfonso, S. Veilleux, J. Fischer, and J. et. al. Graciá-Carpio. Massive Molecular Outflows and Negative Feedback in ULIRGs Observed by Herschel-PACS. ApJ, 733:L16+, May 2011. doi: 10.1088/2041-8205/733/1/L16.

A. A. Suchkov, R. J. Hanisch, W. Voges, and T. M. Heckman. Sloan Digital Sky Survey Active Galactic Nuclei with X-Ray Emission from ROSAT PSPC Pointed Observations. AJ, 132:1475–1484, October 2006. doi: 10.1086/506563.

J. W. Sulentic, P. Marziani, and D. Dultzin-Hacyan. Phenomenology of Broad Emission Lines in Active Galactic Nuclei. ARA&A, 38:521–571, 2000. doi: 10.1146/annurev.astro.38.1.521.

R. A. Sunyaev and L. G. Titarchuk. Comptonization of X-rays in plasma clouds - Typical radiation spectra. A&A, 86:121–138, June 1980.

R. S. Sutherland and M. A. Dopita. Cooling functions for low-density astrophysical plasmas. ApJS, 88:253–327, September 1993. doi: 10.1086/191823.

G. Tabor and J. Binney. Elliptical Galaxy Cooling Flows Without Mass Drop-Out. MNRAS, 263:323–+, July 1993.

L. J. Tacconi, R. Neri, S. C. Chapman, R. Genzel, I. Smail, R. J. Ivison, F. Bertoldi, A. Blain, P. Cox, T. Greve, and A. Omont. High-Resolution Millimeter Imaging of Submillimeter Galaxies. ApJ, 640:228–240, March 2006. doi: 10.1086/499933.

T. A. Thompson, E. Quataert, and N. Murray. Radiation Pressure-supported Starburst Disks and Active Galactic Nucleus Fueling. ApJ, 630:167–185, September 2005. doi: 10.1086/431923.

P. B. Tissera, S. D. M. White, S. Pedrosa, and C. Scannapieco. Dark matter response to galaxy formation. MNRAS, 406:922–935, August 2010. doi: 10.1111/j.1365-2966.2010.16777.x.

F. Tombesi, M. Cappi, J. N. Reeves, G. G. C. Palumbo, T. Yaqoob, V. Braito, and M. Dadina. Evidence for ultra-fast outflows in radio-quiet AGNs. I. Detection and statistical incidence of Fe K-shell absorption lines. A&A, 521:A57+, October 2010. doi: 10.1051/0004-6361/200913440.

A. Toomre and J. Toomre. Galactic Bridges and Tails. ApJ, 178:623–666, December 1972.

G. Toth and J. P. Ostriker. Galactic disks, infall, and the global value of Omega. ApJ, 389:5–26, April 1992. doi: 10.1086/171185.

C. A. Tremonti, J. Moustakas, and A. M. Diamond-Stanic. The Discovery of 1000 km s^{-1} Outflows in Massive Poststarburst Galaxies at z=0.6. ApJ, 663:L77–L80, July 2007. doi: 10.1086/520083.

I. Trujillo, N. M. Förster Schreiber, G. Rudnick, M. Barden, M. Franx, H.-W. Rix, J. A. R. Caldwell, D. H. McIntosh, S. Toft, B. Häussler, A. Zirm, P. G. van Dokkum, I. Labbé, A. Moorwood, H. Röttgering, A. van der Wel, P. van der Werf, and L. van Starkenburg. The Size Evolution of Galaxies since z˜3: Combining SDSS, GEMS, and FIRES. ApJ, 650:18–41, October 2006. doi: 10.1086/506464.

P. C. van der Kruit and K. C. Freeman. Galaxy Disks. ARA&A, 49:301–371, September 2011. doi: 10.1146/annurev-astro-083109-153241.

P. C. van der Kruit and L. Searle. Surface photometry of edge-on spiral galaxies. I - A model for the three-dimensional distribution of light in galactic disks. A&A, 95: 105–115, February 1981.

H. Velazquez and S. D. M. White. Sinking satellites and the heating of galaxy discs. MNRAS, 304:254–270, April 1999.

C. A. Vera-Ciro, L. V. Sales, A. Helmi, C. S. Frenk, J. F. Navarro, V. Springel, M. Vogelsberger, and S. D. M. White. The shape of dark matter haloes in the Aquarius simulations: evolution and memory. MNRAS, 416:1377–1391, September 2011. doi: 10.1111/j.1365-2966.2011.19134.x.

J. C. Vernaleo and C. S. Reynolds. AGN Feedback and Cooling Flows: Problems with Simple Hydrodynamic Models. ApJ, 645:83–94, July 2006. doi: 10.1086/504029.

J. Villa-Vargas, I. Shlosman, and C. Heller. Dark Matter Halos and Evolution of Bars in Disk Galaxies: Collisionless Models Revisited. ApJ, 707:218–232, December 2009. doi: 10.1088/0004-637X/707/1/218.

J. Villa-Vargas, I. Shlosman, and C. Heller. Dark Matter Halos and Evolution of Bars in Disk Galaxies: Varying Gas Fraction and Gas Spatial Resolution. ApJ, 719:1470–1480, August 2010. doi: 10.1088/0004-637X/719/2/1470.

Y. Wadadekar. Radio emission from AGN detected by the VLA FIRST survey. A&A, 416:35–40, March 2004. doi: 10.1051/0004-6361:20034244.

M. D. Weinberg and L. Blitz. A Magellanic Origin for the Warp of the Galaxy. ApJ, 641:L33–L36, April 2006. doi: 10.1086/503607.

M. Wetzstein, T. Naab, and A. Burkert. Do dwarf galaxies form in tidal tails? MNRAS, 375:805–820, March 2007. doi: 10.1111/j.1365-2966.2006.11360.x.

B. C. Whitmore and M. Bell. IC 4767 (the 'X-galaxy') - The missing link for understanding galaxies with peanut-shaped bulges? ApJ, 324:741–748, January 1988. doi: 10.1086/165933.

X. X. Xue, H. W. Rix, G. Zhao, P. Re Fiorentin, T. Naab, M. Steinmetz, F. C. van den Bosch, T. C. Beers, Y. S. Lee, E. F. Bell, C. Rockosi, B. Yanny, H. Newberg, R. Wilhelm, X. Kang, M. C. Smith, and D. P. Schneider. The Milky Way's Circular Velocity Curve to 60 kpc and an Estimate of the Dark Matter Halo Mass from the Kinematics of ˜2400 SDSS Blue Horizontal-Branch Stars. ApJ, 684:1143–1158, September 2008. doi: 10.1086/589500.

D. G. York, J. Adelman, J. E. Anderson, Jr., S. F. Anderson, J. Annis, N. A. Bahcall, J. A. Bakken, R. Barkhouser, S. Bastian, E. Berman, W. N. Boroski, S. Bracker, C. Briegel, J. W. Briggs, J. Brinkmann, R. Brunner, S. Burles, L. Carey, M. A. Carr, F. J. Castander, B. Chen, P. L. Colestock, A. J. Connolly, J. H. Crocker, I. Csabai, P. C. Czarapata, J. E. Davis, M. Doi, T. Dombeck, D. Eisenstein, N. Ellman, B. R. Elms, M. L. Evans, X. Fan, G. R. Federwitz, L. Fiscelli, S. Friedman, J. A. Frieman, M. Fukugita, B. Gillespie, J. E. Gunn, V. K. Gurbani, E. de Haas, M. Haldeman, F. H. Harris, J. Hayes, T. M. Heckman, G. S. Hennessy, R. B. Hindsley, S. Holm, D. J. Holmgren, C.-h. Huang, C. Hull, D. Husby, S.-I. Ichikawa, T. Ichikawa, Ž. Ivezić, S. Kent, R. S. J. Kim, E. Kinney, M. Klaene, A. N. Kleinman, S. Kleinman, G. R. Knapp, J. Korienek, R. G. Kron, P. Z. Kunszt, D. Q. Lamb, B. Lee, R. F. Leger, S. Limmongkol, C. Lindenmeyer, D. C. Long, C. Loomis, J. Loveday, R. Lucinio, R. H. Lupton, B. MacKinnon, E. J. Mannery, P. M. Mantsch, B. Margon, P. McGehee, T. A. McKay, A. Meiksin, A. Merelli, D. G. Monet, J. A. Munn, V. K. Narayanan, T. Nash, E. Neilsen, R. Neswold, H. J. Newberg, R. C. Nichol, T. Nicinski, M. Nonino, N. Okada, S. Okamura, J. P. Ostriker, R. Owen, A. G. Pauls, J. Peoples, R. L. Peterson, D. Petravick, J. R. Pier, A. Pope, R. Pordes, A. Prosapio, R. Rechenmacher, T. R. Quinn, G. T. Richards, M. W. Richmond, C. H. Rivetta, C. M. Rockosi, K. Ruthmansdorfer, D. Sandford, D. J. Schlegel, D. P. Schneider, M. Sekiguchi, G. Sergey, K. Shimasaku, W. A. Siegmund, S. Smee, J. A. Smith, S. Snedden, R. Stone, C. Stoughton, M. A. Strauss, C. Stubbs, M. SubbaRao, A. S. Szalay, I. Szapudi, G. P. Szokoly, A. R. Thakar, C. Tremonti, D. L. Tucker, A. Uomoto, D. Vanden Berk, M. S. Vogeley, P. Waddell, S.-i. Wang, M. Watanabe, D. H. Weinberg, B. Yanny, and N. Yasuda. The Sloan Digital Sky Survey: Technical Summary. AJ, 120:1579–1587, September 2000. doi: 10.1086/301513.

J. D. Younger, P. F. Hopkins, T. J. Cox, and L. Hernquist. The Self-Regulated

Growth of Supermassive Black Holes. ApJ, 686:815–828, October 2008. doi: 10.1086/591639.

A. R. Zentner. The Excursion Set Theory of Halo Mass Functions, Halo Clustering, and Halo Growth. *International Journal of Modern Physics D*, 16:763–815, 2007. doi: 10.1142/S0218271807010511.